

Computational Intelligence & Neuroscience

# Processing of Brain Signals by Using Hemodynamic and Neuroelectromagnetic Modalities

Guest Editors: Laura Astolfi, Sara Gonzalez Andino,  
Fabrizio De Vico Fallani, and Fabio Babiloni





---

# **Processing of Brain Signals by Using Hemodynamic and Neuroelectromagnetic Modalities**

# **Processing of Brain Signals by Using Hemodynamic and Neuroelectromagnetic Modalities**

Guest Editors: Laura Astolfi, Sara Gonzalez Andino, Fabrizio De Vico Fallani, and Fabio Babiloni



Copyright © 2010 Hindawi Publishing Corporation. All rights reserved.

This is a special issue published in volume 2010 of “Computational Intelligence and Neuroscience.” All articles are open access articles distributed under the Creative Commons Attribution License, which permits unrestricted use, distribution, and reproduction in any medium, provided the original work is properly cited.

## Editor-in-Chief

Andrzej Cichocki, RIKEN Brain Science Institute, Japan

## Advisory Editors

Shun-ichi Amari, Japan  
Remi Gervais, France  
Johannes Pantel, Germany

## Associate Editors

Fabio Babiloni, Italy  
Sylvain Baillet, France  
Theodore W. Berger, USA  
Vince D. Calhoun, USA  
Seungjin Choi, South Korea  
S. Antonio Cruces-Alvarez, Spain  
Justin Dauwels, USA  
Deniz Erdogmus, USA

Simone G. O. Fiori, Italy  
Shangkai Gao, China  
Pasi A. Karjalainen, Finland  
Karim G. Oweiss, USA  
Rodrigo Quian Quiroga, UK  
Saeid Sanei, UK  
Hiroshige Takeichi, Japan  
Fabian Joachim Theis, Japan

Shiro Usui, Japan  
Marc Van Hulle, Belgium  
Francois B. Vialatte, Japan  
Yoko Yamaguchi, Japan  
Li Yuanqing, China  
Liqing Zhang, China

# Contents

**Processing of Brain Signals by Using Hemodynamic and Neuroelectromagnetic Modalities,**

Laura Astolfi, Sara Gonzalez Andino, Fabrizio De Vico Fallani, and Fabio Babiloni

Volume 2010, Article ID 934180, 2 pages

**A Neural Mass Model to Simulate Different Rhythms in a Cortical Region,** M. Zavaglia, F. Cona,  
and M. Ursino

Volume 2010, Article ID 456140, 8 pages

**A Semantic Model to Study Neural Organization of Language in Bilingualism,** M. Ursino, C. Cuppini,  
and E. Magosso

Volume 2010, Article ID 350269, 10 pages

**Crossmodal Links between Vision and Touch in Spatial Attention: A Computational Modelling Study,**

Elisa Magosso, Andrea Serino, Giuseppe di Pellegrino, and Mauro Ursino

Volume 2010, Article ID 304941, 13 pages

**Realistic and Spherical Head Modeling for EEG Forward Problem Solution: A Comparative  
Cortex-Based Analysis,** Federica Vatta, Fabio Meneghini, Fabrizio Esposito, Stefano Mininel,  
and Francesco Di Salle

Volume 2010, Article ID 972060, 11 pages

**The Influence of Age and Skull Conductivity on Surface and Subdermal Bipolar EEG Leads,**

Katrina Wendel, Juho Väisänen, Gunnar Seemann, Jari Hyttinen, and Jaakko Malmivuo

Volume 2010, Article ID 397272, 7 pages

**Determination of Neural Fiber Connections Based on Data Structure Algorithm,**

Dilek Göksel Duru and Mehmed Özkan

Volume 2010, Article ID 251928, 6 pages

**Simultaneous EEG-fMRI in Patients with Unverricht-Lundborg Disease: Event-Related  
Desynchronization/Synchronization and Hemodynamic Response Analysis,** Elisa Visani,  
Ludovico Minati, Laura Canafoglia, Isabella Gilioli, Lucia Salvatoni, Giulia Varotto, Patrik Fazio,  
Domenico Aquino, Maria Grazia Bruzzone, Silvana Franceschetti, and Ferruccio Panzica

Volume 2010, Article ID 164278, 5 pages

**Cross-Correlation of Motor Activity Signals from dc-Magnetoencephalography, Near-Infrared  
Spectroscopy, and Electromyography,** Tilmann H. Sander, Stefanie Leistner, Heidrun Wabnitz,  
Bruno-Marcel Mackert, Rainer Macdonald, and Lutz Trahms

Volume 2010, Article ID 785279, 8 pages

**Improvement of EEG Signal Acquisition: An Electrical Aspect for State of the Art of Front End,**

Ali Bulent Usakli

Volume 2010, Article ID 630649, 7 pages

**DTI Parameter Optimisation for Acquisition at 1.5T: SNR Analysis and Clinical Application,**

M. Laganà, M. Rovaris, A. Ceccarelli, C. Venturelli, S. Marini, and G. Baselli

Volume 2010, Article ID 254032, 8 pages

**Exploring Cortical Attentional System by Using fMRI during a Continuous Performance Test,**

M. G. Tana, E. Montin, S. Cerutti, and A. M. Bianchi

Volume 2010, Article ID 329213, 6 pages

**EEG Analysis of the Brain Activity during the Observation of Commercial, Political, or Public Service Announcements,** Giovanni Vecchiato, Laura Astolfi, Alessandro Tabarrini, Serenella Salinari, Donatella Mattia, Febo Cincotti, Luigi Bianchi, Domenica Sorrentino, Fabio Aloise, Ramon Soranzo, and Fabio Babiloni

Volume 2010, Article ID 985867, 7 pages

**On the Use of Electrooculogram for Efficient Human Computer Interfaces,** A. B. Usakli, S. Gurkan, F. Aloise, G. Vecchiato, and F. Babiloni

Volume 2010, Article ID 135629, 5 pages

**Online Detection of P300 and Error Potentials in a BCI Speller,** Bernardo Dal Seno, Matteo Matteucci, and Luca Mainardi

Volume 2010, Article ID 307254, 5 pages

**Independent Component Analysis for Source Localization of EEG Sleep Spindle Components,**

Erricos M. Ventouras, Periklis Y. Ktonas, Hara Tsekou, Thomas Paparrigopoulos, Ioannis Kalatzis, and Constantin R. Soldatos

Volume 2010, Article ID 329436, 12 pages

**Music Composition from the Brain Signal: Representing the Mental State by Music,** Dan Wu, Chaoyi Li,

Yu Yin, Changzheng Zhou, and Dezhong Yao

Volume 2010, Article ID 267671, 6 pages

## Editorial

# Processing of Brain Signals by Using Hemodynamic and Neuroelectromagnetic Modalities

**Laura Astolfi,<sup>1,2</sup> Sara Gonzalez Andino,<sup>3</sup> Fabrizio De Vico Fallani,<sup>1,4</sup> and Fabio Babiloni<sup>1,4</sup>**

<sup>1</sup>IRCCS Fondazione Santa Lucia, Via Ardeatina 306, 00179 Roma, Italy

<sup>2</sup>Department of Computer Science and System, Faculty of Engineering, Via Ariosto 25, University of Rome "Sapienza", 00185 Rome, Italy

<sup>3</sup>Electrical Neuroimaging Group, Department of Clinical Neuroscience, University of Geneva, 1211 Geneva 14, Switzerland

<sup>4</sup>Department of Physiology and Pharmacology, University of Rome "Sapienza", 00185 Rome, Italy

Correspondence should be addressed to Fabio Babiloni, [fabio.babiloni@uniroma1.it](mailto:fabio.babiloni@uniroma1.it)

Received 9 February 2010; Accepted 9 February 2010

Copyright © 2010 Laura Astolfi et al. This is an open access article distributed under the Creative Commons Attribution License, which permits unrestricted use, distribution, and reproduction in any medium, provided the original work is properly cited.

Human neocortical processes involve temporal and spatial scales spanning several orders of magnitude, from the rapidly shifting somatosensory processes characterized by a temporal scale of milliseconds and a spatial scale of few square millimeters to the memory processes, involving time periods of seconds and spatial scale of square centimeters. Information about the brain activity can be obtained by measuring different physical variables arising from the brain processes, such as the increase in consumption of oxygen by the neural tissues or a variation of the electric potential over the scalp surface. All these variables are connected in direct or indirect way to the neural ongoing processes, and each variable has its own spatial and temporal resolution. The different neuroimaging techniques are then confined to the spatiotemporal resolution offered by the monitored variables. For instance, it is known from physiology that the temporal resolution of the hemodynamic deoxyhemoglobin increase/decrease lies in the range of 1-2 seconds, while its spatial resolution is generally observable with the current imaging techniques at few millimeter scale. Today, no neuroimaging method allows a spatial resolution on a millimeter scale and a temporal resolution on a millisecond scale. Nevertheless, the issue of several temporal and spatial domains is critical in the study of the brain functions, since different properties could become observable, depending on the spatiotemporal scales at which the brain processes are measured.

It is well known that the electroencephalography (EEG) and magnetoencephalography (MEG) are useful techniques for the study of brain dynamics, due to their

high temporal resolution. However, it has been said that the spatial resolution of the EEG is rather low, due to the different electrical conductivities of brain, skull, and scalp that markedly blur the EEG potential distributions, making the localization of the underlying cortical generators problematic. In the last ten years, a body of mathematical techniques, known as high-resolution EEG, was developed to estimate precisely the cortical activity from noninvasive EEG measurements. Such techniques include the use of a large number of scalp electrodes, realistic models of the head derived from magnetic resonance images (MRIs), and advanced processing methodologies related to the solution of the so-called "inverse problem," that is, the estimation of the brain activity (i.e., electromagnetic generators) from the EEG/MEG measurements. The approach implies both the use of thousands of equivalent current dipoles as a source model and the realistic head models, reconstructed from magnetic resonance images, as the volume conductor medium. The use of geometrical constraints on the position of the neural source or sources within the head model generally reduces the solution space (i.e., the set of all possible combinations of the cortical dipoles strengths). An additional constraint is to force the dipoles to explain the recorded data with a minimum or a low amount of energy (minimum-norm solutions). The solution space can be further reduced by using information deriving from hemodynamic measures (i.e., fMRI-BOLD phenomena) recorded during the same task. The rationale of a multimodal approach is that neural activity, modulating neuronal firing and generating EEG/MEG potentials, increases glucose and

oxygen demands. This results in an increase in the local hemodynamic response that can be measured by functional magnetic resonance images (fMRIs). Hence, fMRI responses and cortical sources of EEG/MEG data can be spatially related, and the fMRI information can be used as a prior in the solution of the inverse problem. As a result of all these computational approaches, it is possible to estimate the cortical activity with a spatial resolution of few millimeters and with a temporal resolution of milliseconds from noninvasive EEG measurements.

In the framework of a COST Action BM0601 NeuroMath, there was organized a workshop in Rome in 2009 on the themes of the processing of neuroelectromagnetic and hemodynamic signals. Selected papers from this conference were subjected to standard peer-review and compiled in this special issue. With this issue we want to illustrate ongoing and emerging research in the development and application of mathematical methods to the recording, analysis, integration, and modeling of neural activity. The selected papers, written by world class scientists, cover diverse issues ranging from computational models to concrete applications of the methods within the neurosciences. We hope that the readership of CIN could appreciate this special issue as we appreciated it during its composition.

*Laura Astolfi  
Sara Gonzalez Andino  
Fabrizio De Vico Fallani  
Fabio Babiloni*

## Research Article

# A Neural Mass Model to Simulate Different Rhythms in a Cortical Region

**M. Zavaglia, F. Cona, and M. Ursino**

*Department of Electronics, Computer Science, and Systems, University of Bologna, Via Venezia 52, 47023 Cesena, Italy*

Correspondence should be addressed to M. Zavaglia, melissa.zavaglia@unibo.it

Received 12 June 2009; Accepted 16 September 2009

Academic Editor: Laura Astolfi

Copyright © 2010 M. Zavaglia et al. This is an open access article distributed under the Creative Commons Attribution License, which permits unrestricted use, distribution, and reproduction in any medium, provided the original work is properly cited.

An original neural mass model of a cortical region has been used to investigate the origin of EEG rhythms. The model consists of four interconnected neural populations: pyramidal cells, excitatory interneurons and inhibitory interneurons with slow and fast synaptic kinetics,  $GABA_{A,slow}$  and  $GABA_{A,fast}$  respectively. A new aspect, not present in previous versions, consists in the inclusion of a self-loop among  $GABA_{A,fast}$  interneurons. The connectivity parameters among neural populations have been changed in order to reproduce different EEG rhythms. Moreover, two cortical regions have been connected by using different typologies of long range connections. Results show that the model of a single cortical region is able to simulate the occurrence of multiple power spectral density (PSD) peaks; in particular the new inhibitory loop seems to have a critical role in the activation in gamma ( $\gamma$ ) band, in agreement with experimental studies. Moreover the effect of different kinds of connections between two regions has been investigated, suggesting that long range connections toward  $GABA_{A,fast}$  interneurons have a major impact than connections toward pyramidal cells. The model can be of value to gain a deeper insight into mechanisms involved in the generation of  $\gamma$  rhythms and to provide better understanding of cortical EEG spectra.

## 1. Introduction

Neuronal activity in the  $\gamma$  band has been proposed as a physiological indicator of perceptual and higher cognitive processes in the brain, including arousal and attention [1], binding of stimulus features and perception of objects [2], consciousness, and language [3]. Generally,  $\gamma$  rhythms are found in EEG spectra together with other rhythms, such as locally generated activity in the beta ( $\beta$ ) band or thalamocortical activity in the alpha ( $\alpha$ ) band.

In this context, mathematical models can be of the greatest value to gain a deeper insight into the mechanisms involved in the generation of  $\gamma$  rhythms and to provide better understanding of cortical EEG spectra. Models in fact can mimic electrical activity of groups of neurons, taking into account different patterns of connectivity, and simulate brain electrical activity in regions of interest.

In recent years many authors used neural mass models to study the generation of EEG rhythms. In these models the dynamics of entire cortical regions is generally represented with a few state variables, which mimic the interaction

among excitatory and inhibitory populations, arranged in a feedback loop. In particular, neural mass-models of cortical columns, particularly useful to simulate some aspects of EEG signals, were developed by Lopes da Silva et al. [4] and by Freeman [5] in the late seventies, and subsequently improved and extended by Jansen and Rit [6] and Wendling et al. [7].

An intrinsic limitation of these models, however, consists in the way  $\gamma$  rhythms can be generated. Basically, one can obtain a  $\gamma$  rhythm as a consequence of the interaction between pyramidal neurons and fast inhibitory interneurons, provided that small values are used for the synaptic time constants [8]. Conversely, some recent works, both experimental and computational [9, 10], suggest that  $\gamma$  rhythms can be generated by a chain of fast inhibitory interneurons, even without the participation of other types of neurons. A further limitation of previous mass models consists in the difficulty to obtain multiple rhythms within the same cortical region, especially in the  $\beta$  and  $\gamma$  bands. To this end, in previous works at least two regions with different synaptic kinetics have been used to obtain the presence of two peaks in PSD [11].

The present work was devised, within the framework of neural mass models, to overcome the previous limitations. In particular two main objectives have been pursued: (i) to enrich the model of a single cortical region with a new feedback loop, through which fast inhibitory interneurons can produce a  $\gamma$  rhythm per se (i.e., without the participation of the other neural populations), and (ii) to demonstrate that the modified model can easily produce EEGs PSD of a single cortical region characterized by several peaks (i.e., several activities in different bands), using a very parsimonious description of connectivity weights.

The model is first presented in a synthetic form. Then, the role of connectivity between populations of excitatory and inhibitory interneurons internal to the cortical region is studied, with particular attention to the role of GABA<sub>A,fast</sub> interneurons in the generation of  $\gamma$  activity. Subsequently, the effect of connectivity between two cortical regions is simulated. The discussion underlines the main virtues and limitations of the proposed model and points out the main aspects for future research.

## 2. Material and Methods

**2.1. Model of a Single Cortical Region.** The model of a cortical region presented here is a modified version of the model proposed by Wendling et al. [7]. It consists of four neural populations which communicate via excitatory and inhibitory synapses: pyramidal cells, excitatory interneurons, inhibitory interneurons with slow synaptic kinetics (GABA<sub>A,slow</sub>), and inhibitory interneurons with faster synaptic kinetics (GABA<sub>A,fast</sub>). In the following, a quantity which belongs to a neural population will be denoted with the subscripts  $p$  (pyramidal),  $e$  (excitatory interneuron),  $s$  (slow inhibitory interneuron), and  $f$  (fast inhibitory interneuron). Each neural population receives an average postsynaptic membrane potential from the other populations and converts the average membrane potential into an average density of spikes fired by the neurons. Three different kinds of synapses are used to describe the synaptic effect of excitatory neurons (both pyramidal cells and excitatory interneurons), of slow inhibitory interneurons and of fast inhibitory interneurons. Each synapse is simulated by an average gain ( $G_e, G_s, G_f$  for the excitatory, slow inhibitory and fast inhibitory synapses, resp.) and a time constant (in the model, the reciprocal of these time constants is denoted as  $\omega_e, \omega_s$ , and  $\omega_f$ , resp.). The average numbers of synaptic contacts among neural populations are represented by eight variables ( $C_{ij}$ ). The inputs to the model ( $u_p(t)$  and  $u_f(t)$ ) excite pyramidal neurons and fast inhibitory interneurons, respectively, and represent all exogenous contributions, both excitation coming from external sources and the density of action potentials coming from other regions. Inputs to the other two populations have only a scanty effect on model dynamics, and hence have been neglected. The output of the model is represented by the membrane potential of pyramidal cells. Compared with the model described in our previous work [8], the new model exhibits two changes (see Figure 1): (i) fast inhibitory interneurons may receive

an external input (say  $u_f(t)$ ) from pyramidal neurons of other regions; (ii) fast inhibitory interneurons exhibit a negative self-loop; that is, they not only inhibit pyramidal neurons (as in previous model) but also inhibit themselves. This idea agrees with the observation that basket cells in the hippocampus and cortex are highly interconnected and a chain of fast inhibitory interneurons can induce  $\gamma$  activity per se (i.e., even without the participation of other neural populations) thanks to its internal self-inhibitory connections [9].

**2.2. Model of Connectivity among Regions.** In order to study how the cortical regions interact, we then considered a model composed of two cortical regions which are interconnected through long-range excitatory connections. In the following the superscript  $k$  will be used to denote a presynaptic region and the superscript  $h$  to denote the target (post-synaptic) region. To simulate connectivity, we assumed that the average spike density of pyramidal neurons in the pre-synaptic region ( $z_p^k$ ) affects the target region via a weight factor,  $W_j^{hk}$  (where  $j = p$  or  $f$ , depending on whether the synapse targets to pyramidal neurons or fast inhibitory interneurons), and a time delay,  $T$  (assumed equal for all synapses). This is achieved by modifying the input quantities  $u_p^h(t)$  and/or  $u_f^h(t)$  as follows:

$$u_j^h(t) = n_j^h(t) + W_j^{hk} z_p^k(t - T), \quad (1)$$

where  $n_j(t)$  represents a Gaussian white noise (in the present work: mean value  $m_j = 0$  and variance  $\sigma_j^2 = 5$ ).

## 3. Results

**3.1. Sensitivity Analysis on a Single Cortical Region.** The simulations performed in a previous paper [8] demonstrate that a model of a single cortical region, stimulated with input white noise to pyramidal cells ( $u_p(t)$ ), produces just a unimodal spectrum (i.e., a spectrum with a single well defined peak) whose position primarily depends on the synaptic kinetics (i.e.,  $\omega_e, \omega_s, \omega_f$ ) parameters. In order to obtain multiple rhythms in the spectrum, this model needs the contribution of other rhythmic external sources that induce their activity on it.

The most interesting feature presented here is the ability of generating more than one oscillatory rhythm within a single region. Figure 2 shows the membrane potential and the corresponding PSD obtained with the model of a single cortical region simulated with the basal parameters reported in Table 1. It is worth noting that this model produces a bimodal spectrum, with two intrinsic and well-defined peaks, oscillating, respectively, in  $\beta$  and  $\gamma$  ranges. Differently from previous works [7, 8], in these simulations we used a value for the time constant of GABA<sub>A,fast</sub> interneurons of 17 milliseconds, in better agreement with [9].

Figure 3 shows the role of the GABA<sub>A,fast</sub> loop in the generation of a second rhythm in the  $\gamma$  band. Each panel shows how the output of the model, in terms of PSD, changes by incrementing the connection  $C_{pf}$  from

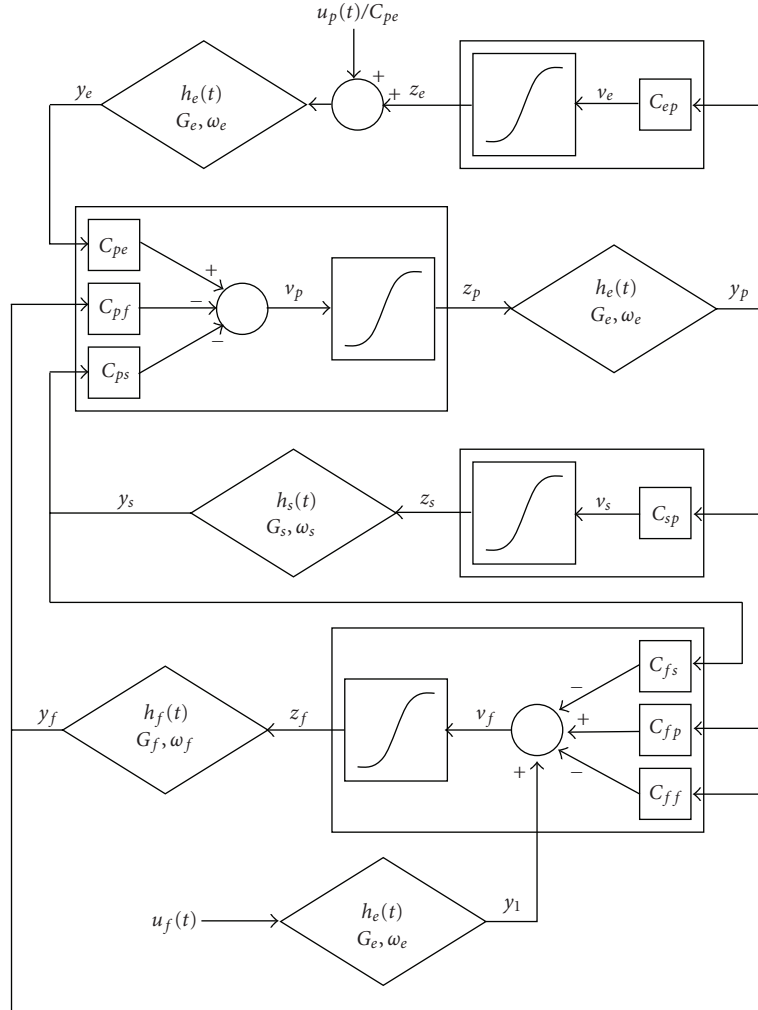


FIGURE 1: Model layout: four neural populations (pyramidal cells, excitatory interneurons, GABA<sub>A,slow</sub> inhibitory interneurons, and GABA<sub>A,fast</sub> inhibitory interneurons) which communicate via excitatory and inhibitory synapses. Worth noting is the presence of a new feedback loop with gain  $C_{ff}$ .

GABA<sub>A,fast</sub> interneurons toward pyramidal cells. With the values reported in Table 1, but setting the value of  $C_{pf}$  to 0, the region exhibits a single rhythm around 5 Hz (first panel). Using small values of  $C_{pf}$  (0.8C and 1.3C) the region exhibits a single rhythm around 30 Hz (second and third panels, resp.). As  $C_{pf}$  increases (from 1.5C to 6C; see Figure 3 caption) the region exhibits two different well-evident rhythms, one in the  $\beta$  band and one in the  $\gamma$  band (fourth to ninth panels).

Figure 4 shows the results of a sensitivity analysis performed on the parameters of the model describing the loops among neural populations. The aim of this analysis is to identify the loops that are essential in order to obtain  $\gamma$  rhythms. In order to do this analysis five crucial connections are cut one at a time. The first panel shows the PSD of the region when all the connections among the neural populations are active (parameters as in Table 1). When connections from pyramidal cells toward excitatory interneurons or from GABA<sub>A,slow</sub> interneurons toward pyramidal cells are set to 0

(second and third panels), the two rhythms persist. In the fourth panel the connection from pyramidal cells toward GABA<sub>A,fast</sub> interneurons is set to 0. Even if two rhythms are not clearly distinguishable, the power band is still fairly broad (0–40 Hz). It is worth noting that the two rhythms collapse in a single one if the connections from GABA<sub>A,slow</sub> interneurons toward GABA<sub>A,fast</sub> interneurons or from GABA<sub>A,fast</sub> interneurons toward themselves are cut (last two panels) suggesting a crucial role for these connections in the generation of a bimodal spectrum, composed of  $\beta$  and  $\gamma$  rhythms. It is worth noting that, in the absence of the loop among fast inhibitory interneurons ( $C_{ff} = 0$ ), the model, with the assigned time constants, produces a rhythm in the alpha band.

3.2. *Connectivity between Two Cortical Regions.* Figure 5 shows the behaviour of a model composed of two interconnected regions. The first line of panels shows the PSD of the two regions when they are not connected to each other. Parameter  $C_{pf}$  is set to 4C in the first region, whereas  $C_{pf}$

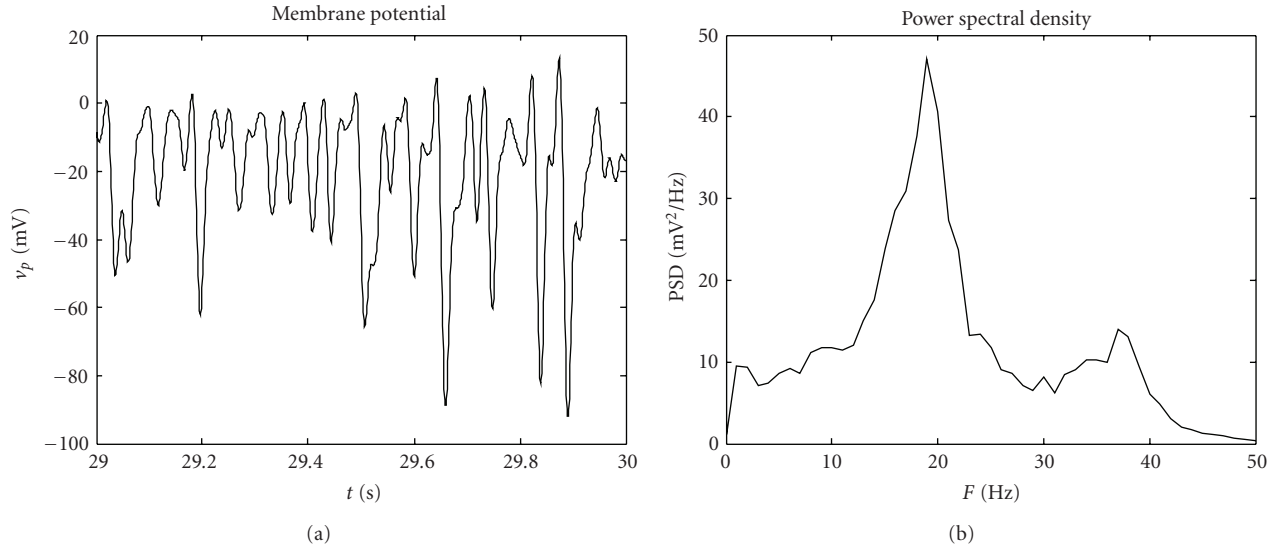


FIGURE 2: Output of the model of a single cortical region in terms of membrane potential (a) and PSD (b), simulated with the basal parameters reported in Table 1.

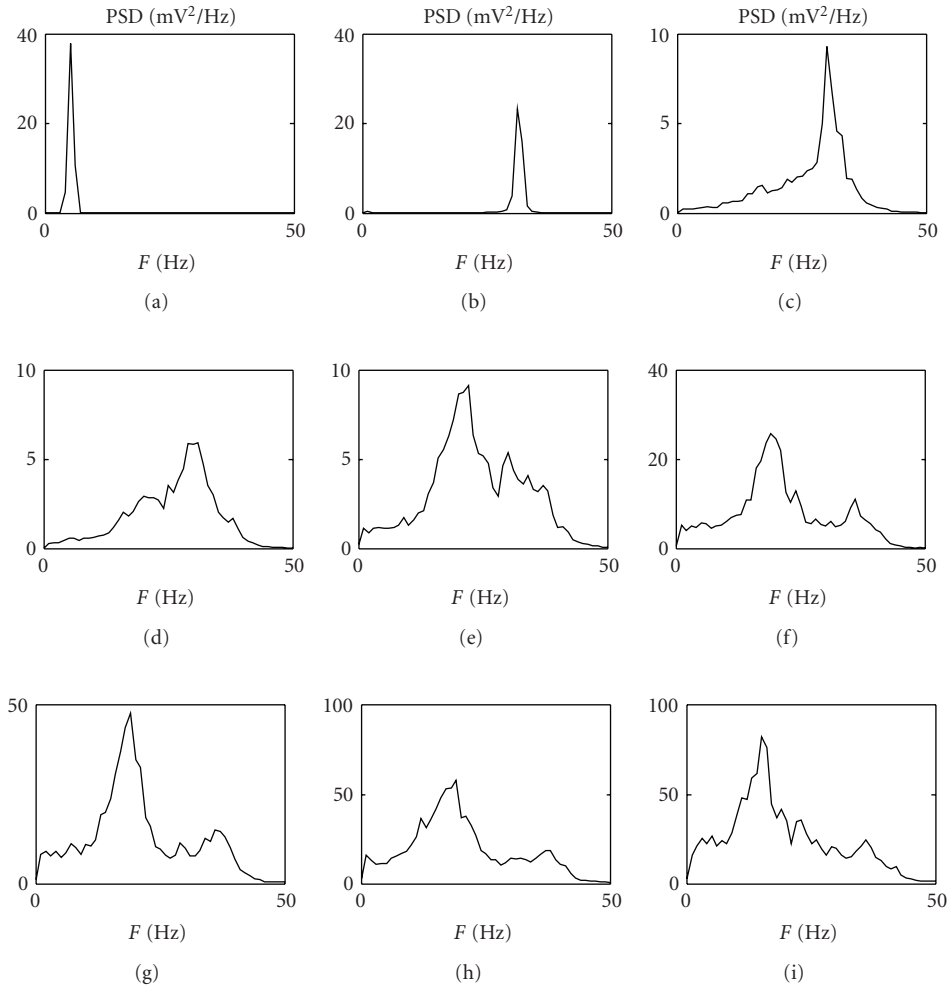


FIGURE 3: PSD of a single region obtained by varying the connection from  $\text{GABA}_{A,\text{fast}}$  interneurons to pyramidal cells (parameter  $C_{pf}$ ). The values of  $C_{pf}$  are 0C, 0.8C, 1.3C, 1.5C, 2C, 3C, 4C, 5C, and 6C.

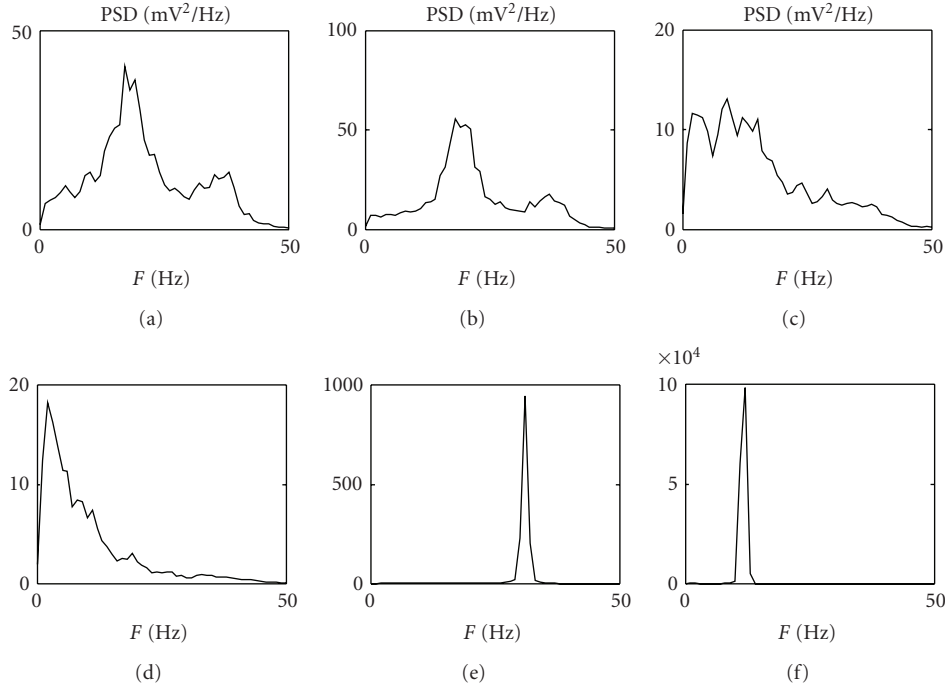


FIGURE 4: PSD of a single cortical region setting off some connections among neural populations. The first panel represents the output of the whole model with parameters as in Table 1. The other five panels represent the power spectra, respectively, when  $C_{ep} = 0$ ,  $C_{sp} = 0$ ,  $C_{fp} = 0$ ,  $C_{fs} = 0$ , and  $C_{ff} = 0$ .

TABLE 1: Model basal parameters.

|                 |                 |                 |                         |                                |
|-----------------|-----------------|-----------------|-------------------------|--------------------------------|
| $C = 135$       | $C_{sp} = 0.4C$ | $C_{fs} = 0.2C$ | $G_e = 5.17 \text{ mV}$ | $\omega_e = 75 \text{ s}^{-1}$ |
| $C_{ep} = 0.4C$ | $C_{ps} = 0.5C$ | $C_{pf} = 4C$   | $G_s = 4.45 \text{ mV}$ | $\omega_s = 30 \text{ s}^{-1}$ |
| $C_{pe} = 0.4C$ | $C_{fp} = 0.4C$ | $C_{ff} = 0.2C$ | $G_f = 57.1 \text{ mV}$ | $\omega_f = 60 \text{ s}^{-1}$ |

is set to  $0.8C$  in the second one. All other parameters have the same values as in Table 1. In this way, the first region exhibits two rhythms, and the second only one rhythm but at a different frequency. The second region can be forced to exhibit the same two rhythms as the first by introducing a connection toward  $\text{GABA}_{A,\text{fast}}$  interneurons (second line). A different spectrum, with a wide activity at high frequencies, is obtained if connectivity is directed toward pyramidal neurons (third line). A small connectivity from the second region towards  $\text{GABA}_{A,\text{fast}}$  cells of the first one makes the first region exhibit three simultaneous rhythms: the two intrinsic rhythms and a third acquired external rhythm (fourth line).

#### 4. Discussion

In this work we used a neural mass model to study the presence of multiple rhythms in the EEG. The model presented here is modified compared with that used in our previous papers [8, 12]. The modifications aim at accentuating the role of the  $\text{GABA}_{A,\text{fast}}$  interneurons in the generation of rhythms in the  $\gamma$  band and obtaining a complex spectrum within a single cortical region. In order to study

these aspects, we modified the model by adding a new input to the  $\text{GABA}_{A,\text{fast}}$  interneurons, and we introduced a feedback loop from the  $\text{GABA}_{A,\text{fast}}$  interneurons toward themselves (parameter  $C_{ff}$ ).

A sensitivity analysis on model parameters representing the internal connectivity among the four neural populations (see Figures 3 and 4) shows that strong short-range connections between  $\text{GABA}_{A,\text{fast}}$  interneurons and pyramidal cells and between  $\text{GABA}_{A,\text{fast}}$  interneurons and  $\text{GABA}_{A,\text{slow}}$  interneurons are fundamental for the generation of multiple rhythms in the EEG, and, above all, for the presence of a peak in the  $\gamma$  band. These results together confirm the findings, obtained in previous studies [9], that networks of fast inhibitory interneurons may be responsible for gamma activity in the brain. Another important result is represented by the use of more biologically plausible values for the time constants. In particular, the simulations performed with the modified model show that, contrarily to previous works [7, 8], one does not need to use very small values (a few ms) for the time constant of  $\text{GABA}_{A,\text{fast}}$  interneurons but more physiological values (13–20 ms) are able to induce oscillations at high frequency [9]. Another remarkable result is that, changing connections weights between populations, the

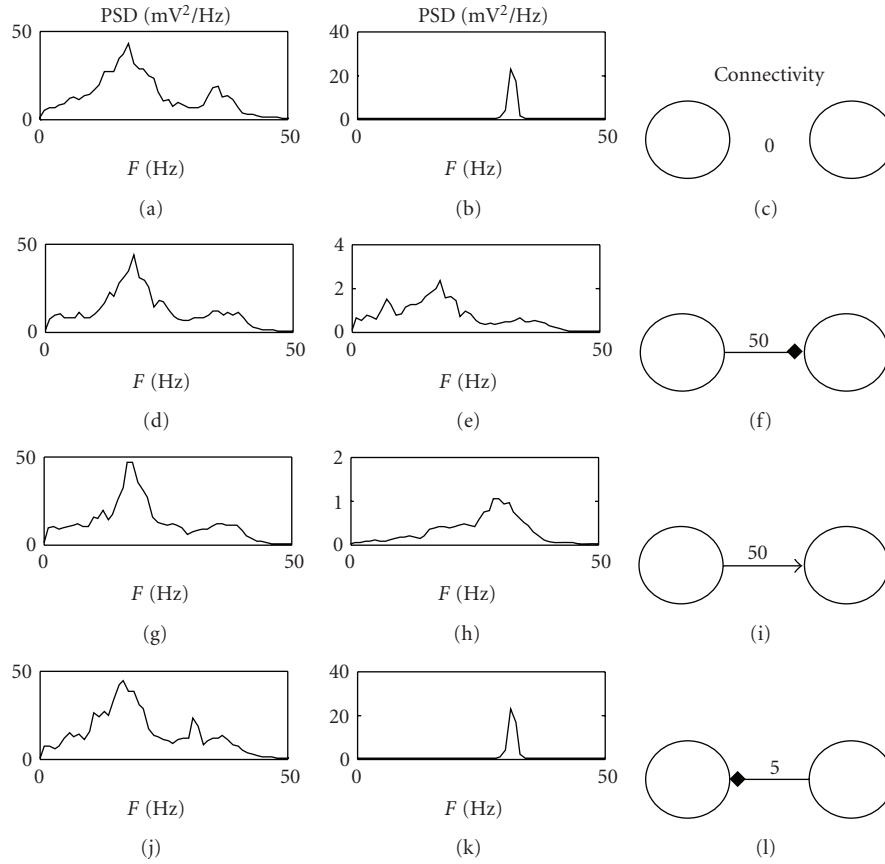


FIGURE 5: PSD of two regions (first region in the first column and second region in the second column) communicating by different connectivity patterns. The connectivity patterns are represented in the third column; the arrow indicates connectivity toward pyramidal cells; the square indicates connectivity toward  $GABA_{A,fast}$  interneurons. The first region is simulated using the parameters reported in Table 1, while the second region is obtained by modifying only  $C_{pf}$  ( $C_{pf} = 0.08C$ ).

rhythmic activity in the model can be easily moved between the alpha, beta, and gamma bands. This is a plausible physiological mechanism, since connectivity strength may be rapidly adjusted *in vivo* by synaptic plasticity. Hence, one does not need to hypothesize a less justifiable modulation of synaptic time constants to mimic the variety of rhythms encountered *in vivo* during motor and cognitive tasks.

Finally, we studied the effect of the long range connections between two neural regions (see Figure 5). The simulations show that, using identical connection strengths (second and third line), the effect on the PSD is completely different, depending on the target population ( $GABA_{A,fast}$  interneurons or pyramidal cells). This original result emphasizes the predominant role of  $GABA_{A,fast}$  interneurons compared to pyramidal cells not only in generating multiple rhythms but also in rhythm transmission from one region to another.

An important possible application of the present model consists in the estimation of effective connectivity between ROIs, starting from real EEG or MEG data. Actually, connectivity in the neurophysiological literature is commonly estimated using signal-based approaches (i.e., empirical black-box models). A major advantage in the use of interpretative models, instead of black-box models, lies in the physiological

meaning of estimated parameters. Each parameter in an interpretative model possesses a clear physiological meaning and summarizes a specific mechanism involved in rhythm generation. Furthermore, interpretative models may permit a fusion between different techniques (e.g., EEG/MEG data and metabolic neuroimaging (fMRI or PET) data), since they allow different quantities (electrical and metabolic) to be simulated. Finally, the present model includes nonlinearities (in particular sigmoidal relationships to describe neuron response) which are known to play a pivotal role in neural signal generation. By contrast, signal-based approaches generally assume the existence on linear relationships among signals.

An actual problem in the use of neural mass models to estimate effective connectivity may be found in the excessive number of estimated parameters, especially when a large number of populations are simultaneously interacting. Estimation of many parameters may demand excessive computational resources and, above all, may lead to the problem of “overfitting” (i.e., good reproducibility of data but with little or none prediction capacity). Two considerations, however, may be followed to limit the number of estimated parameters in a neural mass model. First, not all the

parameters in an ROI require estimation, but only a subset of them. In particular, we have shown that estimation of a single parameter for each region ( $C_{pf}$ ) may allow different rhythms to be produced and controlled quite finely. Second, parameters may be constrained by a priori knowledge (e.g., neuroanatomical data can be used to limit attention only to a few connectivity parameters, and knowledge on synaptic dynamic can be used to provide physiological values for time constants). Nevertheless, the problem of connectivity estimation using neural mass models is still at an initial stage and requires further theoretical and computational active research.

In conclusion, the results underline the performance of the model in the generation of multiple rhythms by using a simple connectivity circuit and may open new perspectives for the study of complex neural oscillations induced by the connection and synchronization among cortical regions. To our knowledge this is a first attempt to use a single neural mass model to reproduce a complex spectrum and investigate the role of fast inhibitory interneurons systematically. In perspective the model could be used as a simulator of the activity in brain regions involved in different cognitive tasks, and for testing the consequences of different connectivity patterns on EEG.

## Appendix

The final model displayed in Figure 1 corresponds to the following set of differential equations:

Pyramidal neurons are

$$\begin{aligned}\frac{dy_p(t)}{dt} &= x_p(t), \\ \frac{dx_p(t)}{dt} &= G_e \omega_e z_p(t) - 2\omega_e x_p(t) - \omega_e^2 y_p(t), \\ z_p(t) &= \frac{2e_0}{1 + e^{-rv_p}} - e_0, \\ v_p(t) &= C_{pe} y_e(t) - C_{ps} y_s(t) - C_{pf} y_f(t).\end{aligned}\tag{A.1}$$

Excitatory interneurons are

$$\begin{aligned}\frac{dy_e(t)}{dt} &= x_e(t), \\ \frac{dx_e(t)}{dt} &= G_e \omega_e \left( z_e(t) + \frac{u_p(t)}{C_{pe}} \right) - 2\omega_e x_e(t) - \omega_e^2 y_e(t), \\ z_e(t) &= \frac{2e_0}{1 + e^{-rv_e}} - e_0, \\ v_e(t) &= C_{ep} y_p(t).\end{aligned}\tag{A.2}$$

Slow inhibitory interneurons are

$$\begin{aligned}\frac{dy_s(t)}{dt} &= x_s(t), \\ \frac{dx_s(t)}{dt} &= G_s \omega_s z_s(t) - 2\omega_s x_s(t) - \omega_s^2 y_s(t), \\ z_s(t) &= \frac{2e_0}{1 + e^{-rv_s}} - e_0, \\ v_s(t) &= C_{sp} y_p(t).\end{aligned}\tag{A.3}$$

Fast inhibitory interneurons are

$$\begin{aligned}\frac{dy_f(t)}{dt} &= x_f(t), \\ \frac{dx_f(t)}{dt} &= G_f \omega_f z_f(t) - 2\omega_f x_f(t) - \omega_f^2 y_f(t), \\ \frac{dy_l(t)}{dt} &= x_l(t), \\ \frac{dx_l(t)}{dt} &= G_e \omega_e u_f(t) - 2\omega_e x_l(t) - \omega_e^2 y_l(t), \\ z_f(t) &= \frac{2e_0}{1 + e^{-rv_f}} - e_0, \\ v_f(t) &= C_{fp} y_p(t) - C_{fs} y_s(t) - C_{ff} y_f(t) + y_l(t),\end{aligned}\tag{A.4}$$

where the sigmoid saturation is  $e_0 = 2.5 \text{ s}^{-1}$  and the sigmoid steepness is  $r = 0.56 \text{ mV}^{-1}$ . It is worth noting that we used a sigmoidal function centered in zero, which corresponds to the assumption that neurons normally work in the linear region.

## References

- [1] M. Steriade, D. A. McCormick, and T. J. Sejnowski, "Thalamo-cortical oscillations in the sleeping and aroused brain," *Science*, vol. 262, no. 5134, pp. 679–685, 1993.
- [2] R. Eckhorn, R. Bauer, W. Jordan, et al., "Coherent oscillations: a mechanism of feature linking in the visual cortex? Multiple electrode and correlation analyses in the cat," *Biological Cybernetics*, vol. 60, no. 2, pp. 121–130, 1988.
- [3] F. Pulvermüller, H. Preissl, W. Lutzenberger, and N. Birbaumer, "Brain rhythms of language: nouns versus verbs," *European Journal of Neuroscience*, vol. 8, no. 5, pp. 937–941, 1996.
- [4] F. H. Lopes da Silva, A. van Rotterdam, P. Barts, E. van Heusden, and W. Bunn, "Models of neuronal populations: the basic mechanisms of rhythmicity," *Progress in Brain Research*, vol. 45, pp. 281–308, 1976.
- [5] W. J. Freeman, "Models of the dynamics of neural populations," *Electroencephalography and Clinical Neurophysiology*, no. 34, pp. 9–18, 1978.
- [6] B. H. Jansen and V. G. Rit, "Electroencephalogram and visual evoked potential generation in a mathematical model of coupled cortical columns," *Biological Cybernetics*, vol. 73, no. 4, pp. 357–366, 1995.

- [7] F. Wendling, F. Bartolomei, J. J. Bellanger, and P. Chauvel, "Epileptic fast activity can be explained by a model of impaired GABAergic dendritic inhibition," *European Journal of Neuroscience*, vol. 15, no. 9, pp. 1499–1508, 2002.
- [8] M. Zavaglia, L. Astolfi, F. Babiloni, and M. Ursino, "A neural mass model for the simulation of cortical activity estimated from high resolution EEG during cognitive or motor tasks," *Journal of Neuroscience Methods*, vol. 157, no. 2, pp. 317–329, 2006.
- [9] J. A. White, M. I. Banks, R. A. Pearce, and N. J. Kopell, "Networks of interneurons with fast and slow gamma-aminobutyric acid type A (GABA(A)) kinetics provide substrate for mixed gamma-theta rhythm," *Proceedings of the National Academy of Sciences of the United States of America*, vol. 97, no. 14, pp. 8128–8133, 2000.
- [10] M. A. Whittington, R. D. Traub, and J. G. R. Jefferys, "Synchronized oscillation in interneuron networks driven by metabotropic glutamate receptor activation," *Nature*, vol. 373, no. 6515, pp. 612–615, 1995.
- [11] M. Zavaglia, L. Astolfi, F. Babiloni, and M. Ursino, "The effect of connectivity on EEG rhythms, power spectral density and coherence among coupled neural populations: analysis with a neural mass model," *IEEE Transactions on Biomedical Engineering*, vol. 55, no. 1, pp. 69–77, 2008.
- [12] M. Ursino, M. Zavaglia, L. Astolfi, and F. Babiloni, "Use of a neural mass model for the analysis of effective connectivity among cortical regions based on high resolution EEG recordings," *Biological Cybernetics*, vol. 96, no. 3, pp. 351–365, 2007.

## Research Article

# A Semantic Model to Study Neural Organization of Language in Bilingualism

**M. Ursino, C. Cuppini, and E. Magosso**

*Department of Electronics, Computer Science and Systems, University of Bologna, Viale Risorgimento 2, I40136 Bologna, Italy*

Correspondence should be addressed to M. Ursino, mauro.ursino@unibo.it

Received 18 June 2009; Accepted 1 December 2009

Academic Editor: Fabio Babiloni

Copyright © 2010 M. Ursino et al. This is an open access article distributed under the Creative Commons Attribution License, which permits unrestricted use, distribution, and reproduction in any medium, provided the original work is properly cited.

A neural network model of object semantic representation is used to simulate learning of new words from a foreign language. The network consists of feature areas, devoted to description of object properties, and a lexical area, devoted to words representation. Neurons in the feature areas are implemented as Wilson-Cowan oscillators, to allow segmentation of different simultaneous objects via gamma-band synchronization. Excitatory synapses among neurons in the feature and lexical areas are learned, during a training phase, via a Hebbian rule. In this work, we first assume that some words in the first language (L1) and the corresponding object representations are initially learned during a preliminary training phase. Subsequently, second-language (L2) words are learned by simultaneously presenting the new word together with the L1 one. A competitive mechanism between the two words is also implemented by the use of inhibitory interneurons. Simulations show that, after a weak training, the L2 word allows retrieval of the object properties but requires engagement of the first language. Conversely, after a prolonged training, the L2 word becomes able to retrieve object per se. In this case, a conflict between words can occur, requiring a higher-level decision mechanism.

## 1. Introduction

The term semantic memory is commonly used to denote a kind of declarative memory which is independent of the context as well as culturally shared and involves words and concepts. Several theories of semantic memory have been developed in the past decades, with the aim of understanding how words are linked with object representation, and how this link is altered in pathological subjects with neurological deficits. In most of these theories, semantic memory is considered a distributed process, which involves many different cortical areas and adopts a multimodal (sensory-motor) representation of objects [1–4]. More specifically, in these theories an object is usually represented as a collection of features spreading across different sensory and motor modalities, which must be linked together and with the corresponding words. Hence, retrieval of objects from memory requires that all these distributed representations, and the corresponding words, be activated all together starting from sensory or lexical cues, and integrated to form a single coherent percept. Synchronization in the gamma band is nowadays assumed to play an essential role in high-

level cognitive processes. Recent results suggest that gamma rhythms are involved in high-level object memorization and retrieval [5], and in linking words with senses [6].

Although the previous ideas are largely debated in the present neurocognitive literature, just a few mathematical models have been presented until now. Recently, we developed a mathematical model of object representation, in which abstract objects are described as a collection of features. In the model, features of the same object are linked together, and separated from those of different objects, via synchronization of neural oscillators in the gamma band. The network was able to recognize objects, and separate them from other objects simultaneously present, even in case of partial or corrupted information, and when objects share some common features [7, 8]. In a more recent version of the same model, this object representation, spreading across different feature areas, is linked with a lexical area devoted to word representation, so that correct object retrieval can evoke the corresponding word, and vice versa. Some simple “semantic” relationships between words which share common features were also realized with this network [9].

In the present work, the same “semantic” network is used to illustrate, with a simple exemplum, how the model can be used to describe the process of word learning in a second language. To this end, we assume that the network, previously trained with a few words in a first language (L1) (so that words are associated with object representation), learns a second-language (L2) word. The L2 word is associated with a previous L1 word via a Hebbian learning procedure. A competitive mechanism between words representing the same object is also implemented. After a prolonged training, the L2 word becomes able to retrieve the same object representation as the original word. The results are commented from the viewpoint of present hypotheses on second-language representation and control.

## 2. Method

The model consists of two different layers: the first (named “feature network”) is devoted to a description of objects represented as a collection of sensory-motor features. The second (named “lexical network”) is devoted to the representation of words, from an upstream process of phonemes. The two networks communicate via trained synapses. Moreover, the lexical network also receives a signal from a “decision network”, which recognizes whether a correct object information is present in the feature network and avoids that a misleading representation can evoke a word. A more complete description of the model, with equations and parameter values, can be found in previous works [8, 9].

In order to simulate learning of a second language, in the present model we included an additional mechanism not used before: two words, which represent the same object (the first, named L1 word, in the original language and the second, named L2 word, in the new language), interact via a competitive mechanism. This competition is realized by means of inhibitory interneurons. The synapses which originate from these interneurons are also subject to Hebbian learning

A schematic description of model structure is presented in Figure 1.

**2.1. The Feature Network.** Each area in the feature network is devoted to the representation of a specific attribute or feature of the object, according to a topological organization. Hence, one object is represented as the collection of  $F$  features (one feature per each area). In this work we used  $F = 4$ . We assume that each attribute has been extracted from a previous processing in the neocortex, which elaborates sensory-motor information. Each unit in the feature areas consists of Wilson-Cowan oscillators [10, 11]. Oscillators in the same area are connected via lateral excitatory and inhibitory synapses, according to a classical “Mexican hat” disposition, which implements a “similarity principle”; this means that elements which signal similar attributes are located in proximal positions in the network; hence, they tend to be reciprocally connected and activate together. Neural oscillators belonging to different areas can be connected via excitatory synapses after training. These synapses are

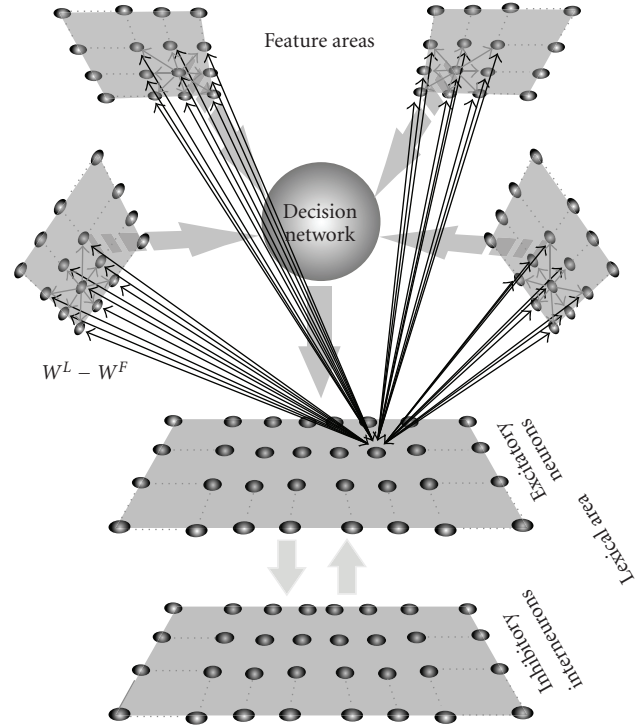


FIGURE 1: Schematic diagram describing the general structure of the network. The upper shadow squares represent distinct Feature Areas and are organized in a topological way. Each area embodies  $20 \times 20$  elements (black circles), represented by means of Wilson-Cowan oscillators, devoted to the representation of a specific feature of an object. The lower squares represent the two populations of neurons in the Lexical Area: excitatory neurons, responsible for the representation of words, and inhibitory interneurons, involved in tasks like problem solving. Each of these areas is made of  $40 \times 40$  elements (black circles), which are represented by a first-order dynamic and a sigmoidal relationship. Between the Feature and the Lexical Areas there is a decision network, which un-inhibits the lexical area, in case of correctly segmented objects. The model includes intra-area (excitatory and inhibitory) synapses among elements belonging to the same Feature Area, long-range excitatory interarea synapses between oscillators in different Feature Areas, and long-range excitatory synapses between elements in the Feature Network and in the Lexical Areas ( $W^F - W^L$ ).

initially set to zero, but may assume a positive value through a learning phase, to memorize “prior knowledge” on attributes occurring together during the presentation of objects. Lateral synapses are not subjected to a training phase. All equations can be found in [7–9].

**2.2. Lexical Area.** Each unit represents a specific “word”. It can receive an input from a preprocessing stage which detects words from phonemes but it can also be stimulated through long-range synapses coming from the feature network; in this way, a “word” is linked with elements in feature areas representing specific properties of a stored object. All together, a “word” and its specific attributes are combined to embody the semantic meaning of that concept and the integrated network can indifferently be activated by language or sensory-motor information of an object.

In the present model we assume that the lexical network can be activated by the elements of the feature areas only if a “decision network” is in the ON state. This is realized sending sufficient inhibition to all elements of the lexical area. This inhibition is withdrawn by the decision network, as soon as an object is recognized.

This network is located downstream of the Feature Network. It receives input from all the elements of the Feature Areas and verifies that (1) there is an “activation bubble” in any area. (2) Any area produces just a single activation bubble at a given instant. (3) The conditions (1) and (2) are verified all along a certain time interval to ensure the continuity of object perception. If all these conditions are verified, then the Decision Network un-inhibit the Lexical Area and allows its activation by object representation in the Feature Network. An accurate description of this decision network can be found in [8].

In the following each element of the lexical area will be denoted with the subscripts  $ij$  or  $hk(i, h = 1, 2, \dots, M_1; j, k = 1, 2, \dots, M_2)$  and with the superscript  $L$ . In the present study we adopted  $M_1 = M_2 = 40$ . Each single element exhibits a sigmoidal relationship (with lower threshold and upper saturation) and a first-order dynamic (with a given time constant). This is described via the following differential equation:

$$\tau^L \cdot \frac{d}{dt} x_{ij}^L(t) = -x_{ij}^L(t) + H^L(u_{ij}^L(t)), \quad (1)$$

where  $\tau^L$  is the time constant, which determines the speed of the answer to the stimulus, and  $H^L(u^L(t))$  is a sigmoidal function. The latter is described by the following equation:

$$H^L(u^L(t)) = \frac{1}{1 + e^{-(u^L(t) - \vartheta^L) \cdot p^L}}, \quad (2)$$

where  $\vartheta^L$  defines the input value at which neuron activity is half the maximum (central point) and  $p^L$  sets the slope at the central point. Equation (2) conventionally sets the maximal neuron activity at 1 (i.e., all neuron activities are normalized to the maximum).

According to the previous description, the overall input,  $u_{ij}^L(t)$ , to a lexical neuron in the  $ij$  position can be computed as follows:

$$u_{ij}^L(t) = I_{ij}^L(t) + V_{ij}^F - G^L \cdot (1 - z^L(t)) - C_{ij}^L - I_{ij}^{\text{Bias}}, \quad (3)$$

where  $I_{ij}^L(t)$  is the input produced by an external linguistic stimulation.  $V_{ij}^F$  represents the intensity of the input due to synaptic connections from the feature network; this synaptic input is computed as follows:

$$V_{ij}^F = \sum_h \sum_k W_{ij,hk}^F \cdot x_{hk}, \quad (4)$$

where  $x_{hk}$  represents the activity of the neuron  $hk$  in the Feature Areas and  $W_{ij,hk}^F$  the strength of synapses from the

feature areas to the lexical area. The term  $G^L \cdot (1 - z^L(t))$  accounts for the inhibition sent to the lexical area, withdrawn by the decision network. In particular,  $z^L(t)$  is a binary variable representing the output of the decision network (1 in case of correct detection, 0 in case of incorrect detection—see [8]); hence, the strength of the inhibition sent to the Lexical Area is  $G^L$  when the decision network is in the OFF state and becomes 0 when the decision network shifts to the ON state. It is worth noting that the external linguistic input  $I_{ij}^L(t)$ , when present, is set sufficiently high to overcome the inhibition entering into the lexical area. The term  $C_{ij}^L$  (not included in the previous model versions) represents the competitive inhibition that the neuron at position  $ij$  in the lexical area receives from other words in the lexical area. This competition is triggered only in case of words representing the same object (as in bilingualism) and is computed as follows:

$$C_{ij}^L = \sum_h \sum_k W_{ij,hk}^I \cdot x_{hk}^I, \quad (5)$$

where  $x_{hk}^I$  is the output of the inhibitory interneuron at position  $hk$ , and  $W_{ij,hk}^I$  are the inhibitory synapses from a presynaptic inhibitory interneuron at position  $hk$  to the postsynaptic neuron at position  $ij$  in the lexical area.

Finally, the term  $I_{ij}^{\text{Bias}}$  in (3) represents an external inhibitory input, coming from high-level top-down influences, which try to inhibit a nontarget word. This input is normally set to zero but may assume a high value in problems like language selection or language switching (see discussion).

The inhibitory interneuron output is computed with equations similar to those of (1) and (2), with an analogous meaning of symbols, that is,

$$\tau^I \cdot \frac{d}{dt} x_{ij}^I(t) = -x_{ij}^I(t) + H^I(x_{ij}^I(t)), \quad (6)$$

with

$$H^I(x_{ij}^I(t)) = \frac{1}{1 + e^{-(x_{ij}^I(t) - \vartheta^I) \cdot p^I}}. \quad (7)$$

It is worth noting, in (6) and (7), that the inhibitory interneuron receives excitation only from the excitatory neuron in the lexical area at the same position  $ij$ .

**2.3. Synapse Training.** Training has been subdivided in three different phases: (i) learning of objects, (ii) learning of L1 words, and (iii) learning of L2 words. The first two phases have been already described in a previous paper; hence, only some general ideas are given here. Phase (iii) is new and described in greater detail.

During the first phase, objects are individually given to the network with all their four features, and the synapses linking the feature areas are trained via a time varying Hebbian mechanism. This is described in detail in [8]. At the end of this phase, objects can be recognized even in the presence of incomplete or moderately altered inputs [8].

During the second phase, an object (already learned in phase (i)) is given to the network together with the corresponding word. Synapses linking the word and the object features (in both directions) are then learned with a Hebbian mechanism. This is described in [9]. At the end of this phase, objects can evoke the corresponding words and words can evoke the sensory-motor object representation in the feature areas. Moreover, several words and their objects representation can coexist by oscillating in time division in the gamma range.

The third phase consists in learning words of a second language. To this end, we assumed that a word in the first language (named L1 word), previously learned in phase (ii), is given to the subject together with a new word (L2 word) representing the same object in a second language. Of course the L1 word activates the object representation in the feature areas, and the synapses linking the feature areas to the L2 word (i.e., synapses  $W_{ij,hk}^F$  in (4)) are learned with a Hebbian mechanism (similar to that used in phase (ii)). Moreover, the inhibitory synapses linking the inhibitory interneurons to the lexical area (i.e., synapses  $W_{ij,hk}^I$  in (5)) are also learned with a Hebbian mechanism. In fact, during this phase, the L1 and the L2 words are active, and so, also the corresponding interneurons are active. The equations for synapse learning are

$$\begin{aligned} W_{ij,hk}^F(t + T_S) &= W_{ij,hk}^F(t) + \beta_{ij,hk}^F \cdot x_{ij}^L(t) \cdot x_{hk}(t), \\ W_{ij,lm}^I(t + T_S) &= W_{ij,lm}^I(t) + \beta_{ij,hk}^I \cdot x_{ij}^L(t) \cdot x_{lm}^I(t), \end{aligned} \quad (8)$$

where  $x_{ij}^L(t)$ ,  $x_{hk}(t)$ , and  $x_{lm}^I(t)$  represent the activity of the excitatory neuron at position  $ij$  in the lexical area, the Wilson-Cowan oscillator at position  $hk$  in the feature area, and of the inhibitory interneuron at position  $lm$ , respectively, and  $\beta$  represent the learning rates. Finally, we assumed that synapses cannot overcome a maximum saturation value. This is realized assuming that the learning rates are progressively reduced to zero when synapses approach saturation.

### 3. Results

Simulations have been performed at three different moments of the second-language learning process: (i) at the beginning of training, when the second language word has never been perceived before, (ii) during an intermediate learning moment, when synapses linking the object with the L2 word are still weak, that is, much smaller than the synapses linking the same object with the L1 word, and (iii) after a long training period, when the synapses linking the object to the L2 word are almost as strong as the synapses from the same object to the L1 word.

Three exemplary cases are presented for each training phase, characterized by different inputs to the model: L2 word as input to the model, L1 word as input to the model, and the object features as input to the model.

Figure 2 shows the model response in the feature areas (upper panels) and in the lexical area (bottom panels) at a particular instant of the simulation, when the L2 word is used as input. In each simulation, the external input activates the corresponding neuron in the lexical area. At the beginning of training (Figure 2(a)) this word cannot evoke any object representation in the feature areas. After moderate training (Figure 2(b)) the L2 word can evoke the representation of the object in the feature areas (with the appearance of four activation bubbles, which represent the four features of the object). However, it is remarkable that also the L1 word representation is activated in the lexical area. This signifies that an L2 word is able to evoke the correct representation of the corresponding object, but it still requires some participation of the L1 word. In other terms, at this stage of training the second language still takes advantage of the first language, and both words (the L2 word and the L1 word) participate synergistically to the object representation. Conversely, after a strong training (Figure 2(c)) the L2 word can evoke the object representation with just a negligible activation of L1. This means that L2 has become almost completely independent of any L1 support.

The temporal patterns of neuron activities are given in Figure 3, when the network is stimulated with the L2 word as input. In case of weak training, L2 word can evoke the object representation (with the four features which oscillate in phase in the gamma band, at about 40 Hz, Figure 3(a)). However, it is noticeable the activation of the L1 word in the lexical area, which oscillates with the same phase as the object representation, Figure 3(c). After a prolonged training, the L2 word is able to almost entirely suppress activity of the L1 word, thanks to the presence of a strong competitive mechanism. The subject can use L2 without evoking L1, Figures 3(b) and 3(d).

Figure 4 shows snapshots of neuron activation in the different areas of the model, when model is stimulated with the L1 word as input. Independently of the training length, the L1 word can evoke a correct object representation in the feature areas without any significant participation of L2. This signifies that, at any stage of learning, L1 is independent of the new language and, even after a prolonged second-language training, it is able to recover an object by totally inhibiting the corresponding L2 word.

The third case (Figure 5) shows model behavior when the network is stimulated with the entire object representation (i.e., all four features are given to the network as an external input). Of course, at the beginning of training the object evokes only the L1 word. Similarly, after a moderate training, when the second language is just poorly known, the object evokes the L1 word only, and the L2 word is almost completely inhibited. However, after a prolonged training, the object representation evokes both the L1 word and the L2 word, which coexist despite the presence of a reciprocal competitive inhibition.

The previous simulations show that, if a subject has a low-proficiency L2, an external object automatically activates L1, while L2 is inhibited. Conversely, for a high-proficiency L2 subject, word production caused by an external object

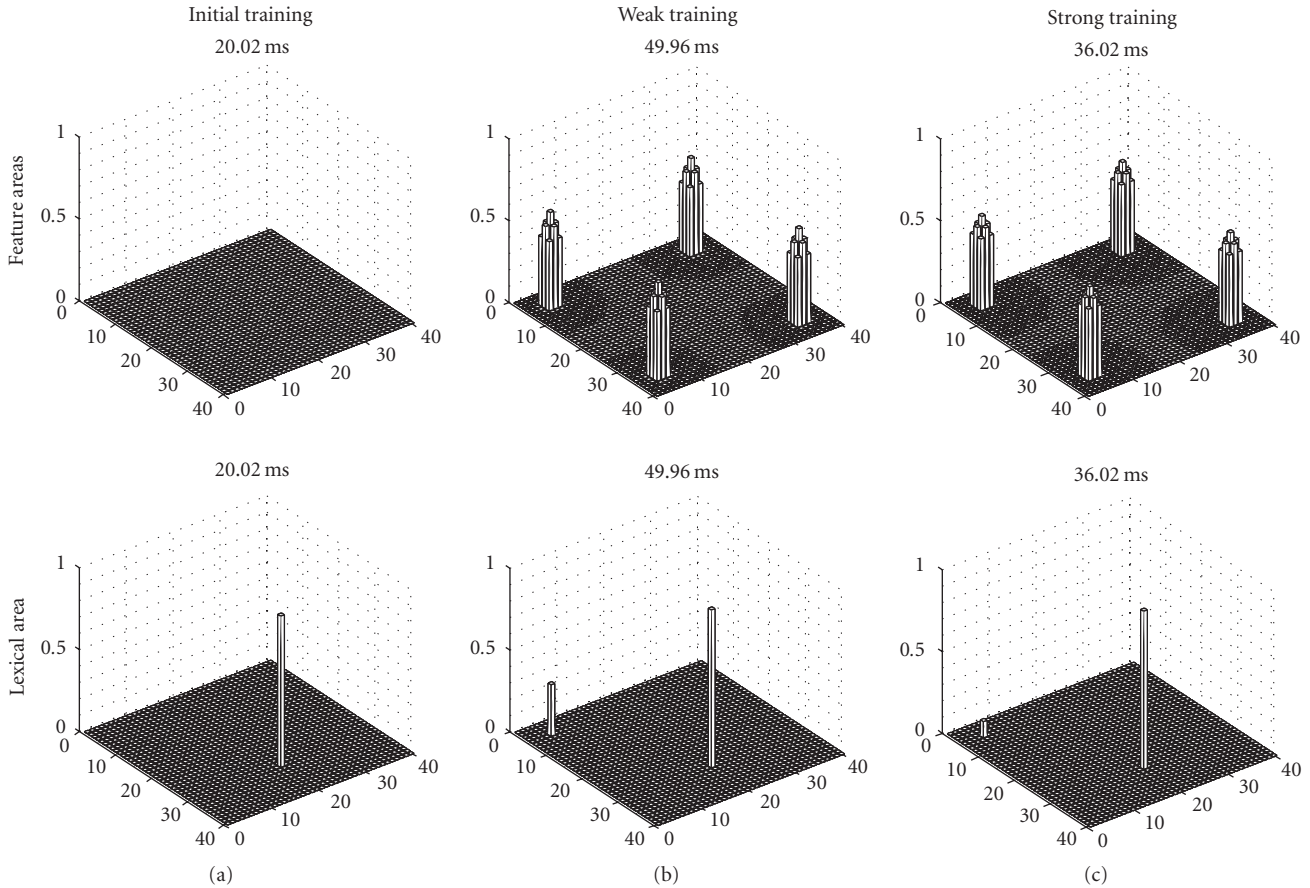


FIGURE 2: Some snapshots of the model response at some instant of the simulations, performed when the L2 word is given as input to the network. The upper panels describe activity in the feature areas, while the bottom panels represent the activity in the lexical area. The L2 word is represented by neuron activity in position 20, 30 of the lexical area, while the corresponding L1 word is represented by activity in position 5, 5. Results of three simulations are given, characterized by a different proficiency of the second language: beginning of L2 training (a), after a weak L2 training (b), and after a prolonged L2 training (c). It is worth noting that, after weak training, the L2 word can evoke the correct object representation in the feature areas (represented by simultaneous activation of four features), but it still requires activation of the L1 word. After prolonged training the L2 word becomes almost completely autonomous from L1.

causes a conflict between L1 and L2 words. Some problems, thus, arise. How can a low-proficiency L2 subject produce a correct L2 word (for instance, when he/she is forced to use L2 in a foreign context or a classroom)? And how can the conflict between L1 and L2 words be solved in high-proficiency L2 subjects? To answer these questions, model must assume the presence of a further top-down inhibitory input (i.e., the term  $I_{ij}^{\text{Bias}}$  in (3)) probably coming from higher cognitive centers, which is directed to the nontarget language. As an example, in Figure 6 we repeated the same simulations as in Figure 5 (object as input to the network, i.e., the word production paradigm) assuming that all L1 words are receiving an inhibitory input from an external source. Results show that, in this condition, the presentation of the object engages activation of the L2 word, less active in the low-proficiency case (Figure 6(b)) and more active in the high-proficiency case (Figure 6(c)), but without any interference from L1.

#### 4. Discussion

The term “bilinguals” means people who can use two languages in their life, a first or native language usually denoted as L1 and a second language named L2. Bilingualism, of course, entails several complex problems, which are still debated in the psycholinguistic literature. A first problem is whether the second language (or L2) makes use of the same neural structures as L1 or whether different structures and different mechanisms underlie the acquisition of L2. A second fundamental aspect of bilingualism is the necessity of some control mechanisms to establish which language should be used at a given moment and in a given context and which language should be inhibited, for both what concerns word production and word comprehension.

Most studies on bilingualism appeared in recent years (some of them summarized by Abutalebi [12]) making use of functional neuroimaging techniques (such as PET or fMRI) to detect which brain regions are involved or activated

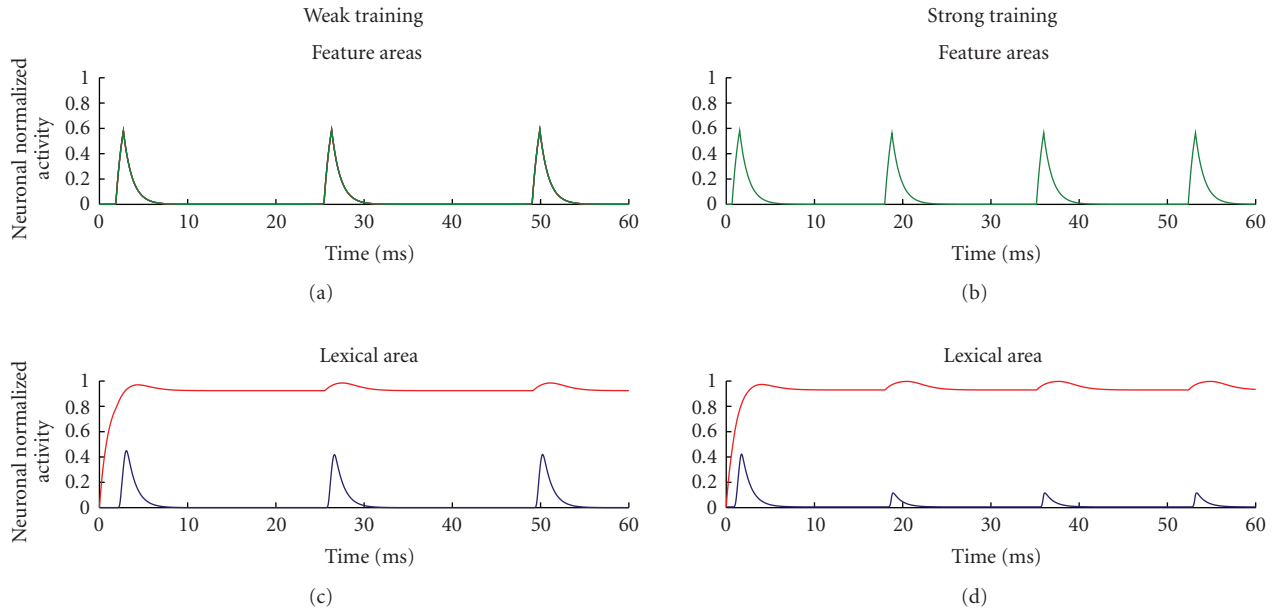


FIGURE 3: Temporal pattern of neuron activity in the feature areas representing the object (a) and (b) and in the lexical area (c) and (d) in the same simulations as in Figure 2, in case of weak training (a) and (c) and in case of strong training (b) and (d). All object features oscillate in synchronism in the gamma band (about 40 Hz). The L2 word, stimulated from an external input, exhibits quite a constant activity close to maximal saturation (red line) while the L1 word, triggered by the object representation, exhibits a significant activity in the gamma band (blue line).

during a specific psycholinguistic test. Although these studies provide important information on brain organization in bilingualism, they do not explore the neural mechanisms involved. Moreover, language is a typical characteristic of humans; hence, animal experiments cannot be used to deepen our knowledge of the problem.

In this situation, mathematical models and computer simulations, although drastically simplified compared with the reality, may provide important contributions to clarify the possible mechanisms involved in language processing (at least for what concerns basic aspects as word recognition and word production) and to convert current hypotheses into rigorous quantitative theories. Indeed, several current theories on language frequently use expressions like “competition”, “inhibition”, “neural activity”, and “control” and can be regarded as “qualitative models”, which may certainly benefit of a more accurate quantitative formalization.

The model presented in this work wishes to represent a first step in that direction. However, it aspires to describe only the lexical-semantic aspects of language, without any inclusion of grammatical issues: in particular, attention is focused on *word recognition* (i.e., the process through which a word is converted into a coherent object representation) and *word production* (the process through which the representation of an object is converted into a word).

The main assumption of the model is that neurons labeling words, and neurons describing their semantic object representation over different areas, are linked together via excitatory synapses. It is remarkable that the model, for the sake of simplicity, does not incorporate the two “external”

aspects of this processing stream, namely, how phonemes are converted to lemmas (and words) and how the sensory-motor information coming from senses is generalized to arrive at an abstract representation of objects.

A second fundamental aspect of the model is that the synaptic links between object representation and words are learned during a training phase, in which the object and the corresponding word are presented together. This particularly of the model allows learning of L2 words with the same basic mechanism as that of L1, supposing a training phase in which the L2 word is presented together with a previously learned L1 word.

The latter assumption, which is fundamental in our work, received several confirms from recent neuroimaging studies (some of them summarized by Perani and Abutalebi [13] and Abutalebi [12]). Indeed, a traditional viewpoint in the neurolinguistic literature, which dominated for more than one century, was that the first and second languages depend on different cerebral structures and on different neural mechanisms [14]. Following this line of thinking, a recent qualitative model (named the Ullman declarative/procedural model [15]) assumes that processing of L2, acquired late on life, depends upon different cognitive mechanisms and different cerebral structures than L1. Several recent results, however, using functional neuroimaging data [16, 17], contradict this hypothesis for what concerns the lexical-semantic aspects of L2 (although structural differences between L1 and L2 may effectively occur for what concerns the grammatical aspects). As summarized in the review paper by Abutalebi [12] “The emerging picture from studies investigating the

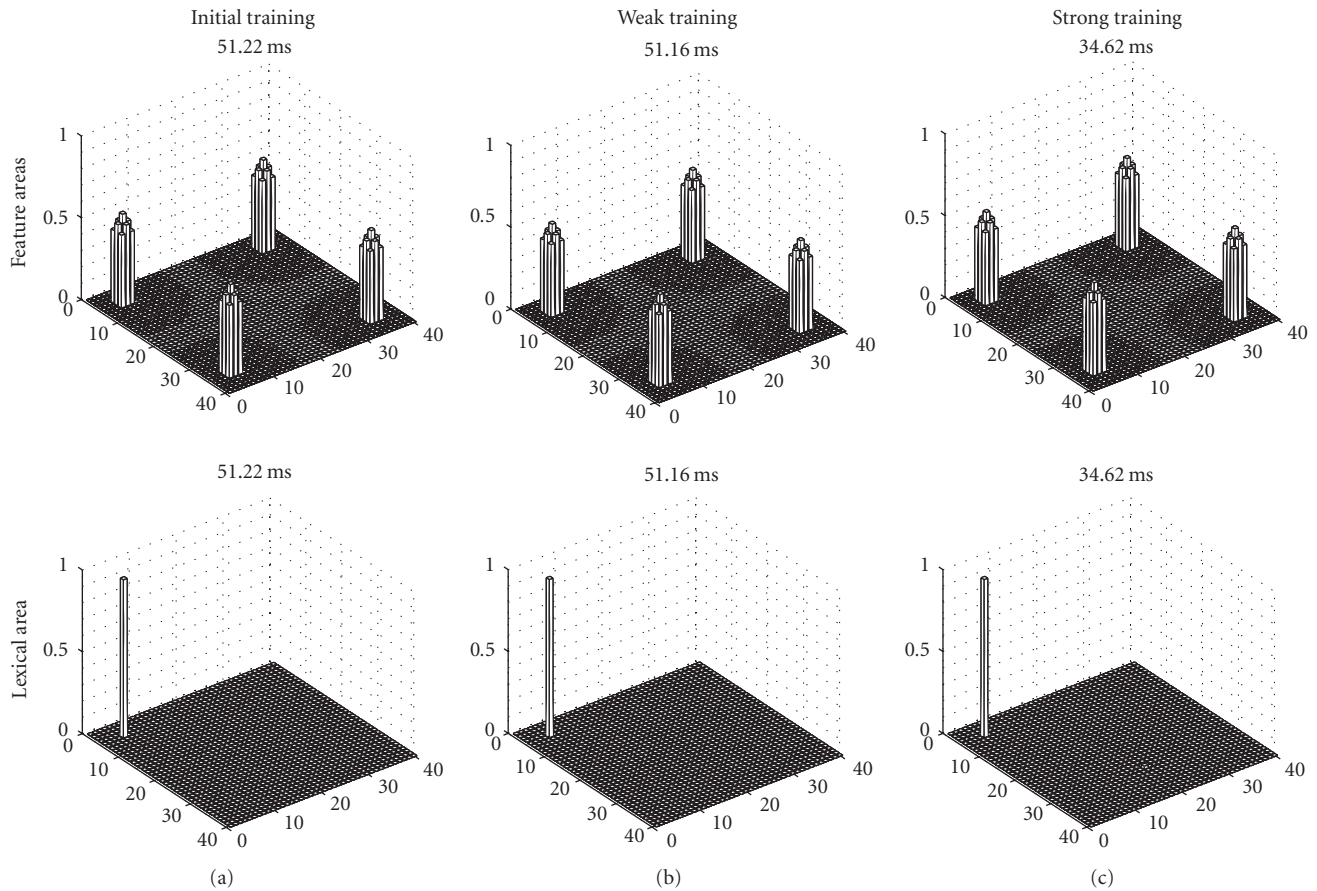


FIGURE 4: Some snapshots of the model response at some instant of the simulations, performed when the L1 word is given as input to the network. The upper panels describe activity in the feature areas, while the bottom panels represent the activity in the lexical area. The L1 word is represented by neuron activity in position 5, 5 of the lexical area, while the corresponding L2 word is represented by activity in position 20, 30. Results of three simulations are given, characterized by a different proficiency of the second language: beginning of L2 training (a), after a weak L2 training (b), and after a prolonged L2 training (c). It is worth noting that, at any training level, the L1 word can evoke the correct object representation in the feature areas (represented by simultaneous activation of four features), without any significant participation of the L2 word.

lexical-semantic domain is that L2 is essentially processed through the same neural networks underlying L1 processing.”

Assuming that the lexical-semantic aspects of L2 are acquired through the same neural structures and the same plasticity rules as L1, the present model makes some testable predictions, at different stages of the learning process, which can be compared with present functional neuroimaging data and with present theories on bilingualism. In the following, these predictions will be separately discussed for what concerns the neural representation of L2 (i.e., the neural substrates of words and concepts) and the control mechanisms implicated in bilingualism.

*The neural representation of L2*—An interesting result of our simulations is that, at a low proficiency level, when L2 is just poorly learned, the recognition of an object from an L2 word implicates the participation of L1. This is evident in Figures 2 and 3 by the activation of the L1 word in the lexical area. These simulation results agree with some psycholinguistic theories. For instance, Kroll and Stewart [18] state

that, during the early stages of L2 acquisition, L2 depends on L1 to access meaning for its lexical items. A consequence of this idea is that, at low proficiency level, the use of an L2 word causes a greater neural activation in the lexical and in the inhibitory areas, compared with the use of L1 words. Let us consider the situation depicted in Figure 2(b), and in Figures 3(a) and 3(c): here one can observe two zones of the lexical area which are simultaneously active; of course, the inhibitory interneurons are also active in same zones (since they receive their input directly from the lexical area). This signifies that a greater activation is recruited when the low-proficiency subject is trying to use an L2 word. This result is supported by neuroimaging data, although it is quite difficult to force this parallelism beyond a very qualitative level. Studies investigating the lexical-semantic domain show that bilinguals with low-proficiency L2 entail additional brain activity compared with the L1 word or compared with monolingual subjects: the increased activity is especially observed in the left inferior frontal gyrus and in prefrontal areas [16, 19].

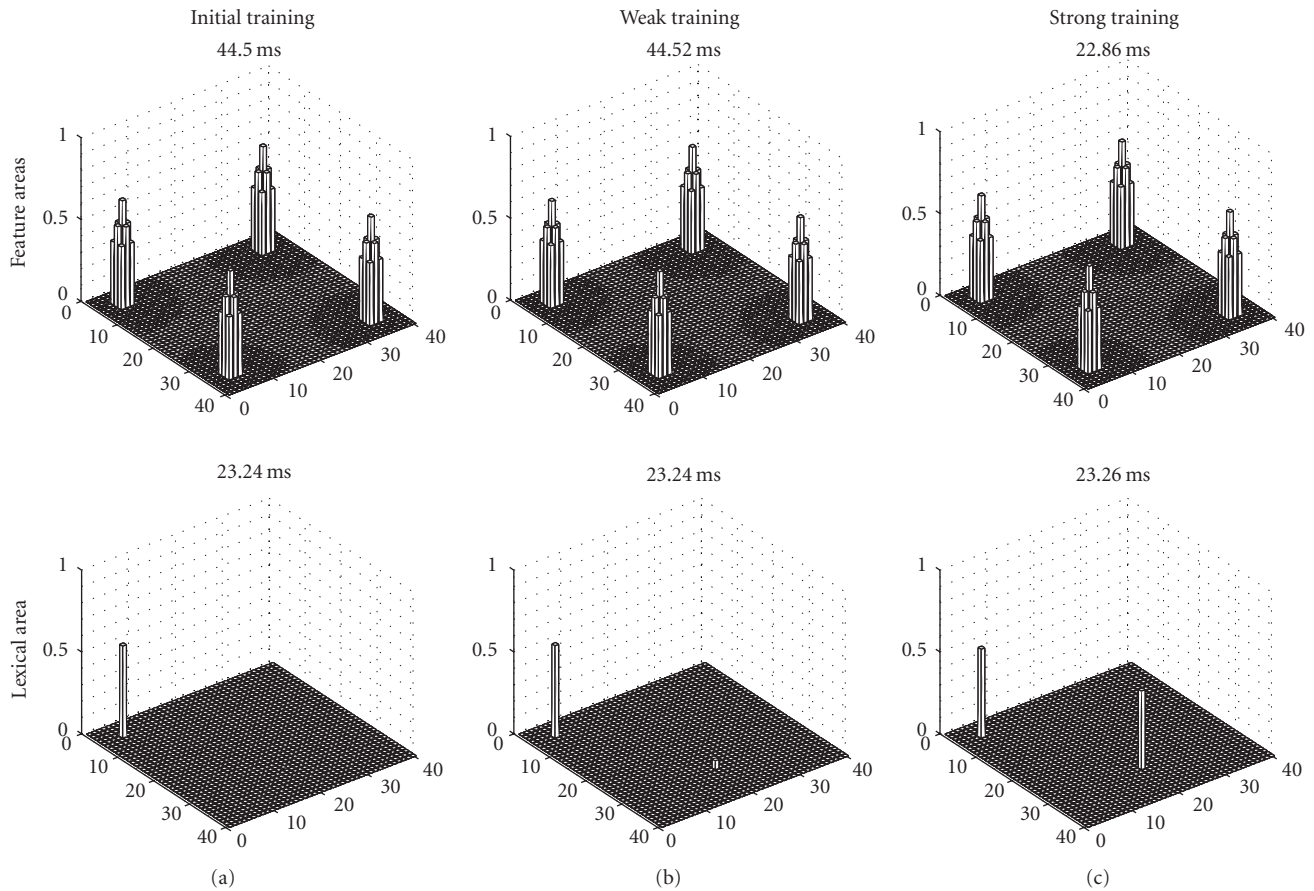


FIGURE 5: Some snapshots of the model response at some instant of the simulations, performed when the object (i.e., its four features) is given as input to the network. The upper panels describe activity in the feature areas, while the bottom panels represent the activity in the lexical area. The L2 word is represented by neuron activity in position 20, 30 of the lexical area, while the corresponding L1 word is represented by activity in position 5, 5. Results of three simulations are given, characterized by a different proficiency of the second language: beginning of L2 training (a), after a weak L2 training (b), and after a prolonged L2 training (c). It is worth noting that, at the beginning of training and after a weak training, the external object can evoke only the L1 word without any significant activity of the L2 word. Conversely, after prolonged training, the external object simultaneously evokes both the L1 word and the L2 word, despite the presence of a competitive mechanism. This requires the participation of a higher-level mechanism (perhaps inhibitory) to resolve the conflict.

In addition, model predicts that, with an increase in L2 proficiency, the neural activity engaged by L2 words is reduced and becomes progressively comparable with that engaged by L1 words. This model predictions reflect the so-called Green’s convergence hypothesis [20], according to which higher levels of proficiency in L2 produce a lexical-semantic representation which more closely resembles that produced by L1. Indeed, neuroimaging studies have reported similar activations in the left frontal and tempo-parietal brain areas when a subject performs a word production task, in case of L1 and high-proficiency L2 [21, 22]. This signifies that highly proficient bilinguals do not need to recruit additional resources when using L2 to achieve similar results as L1.

*Control mechanisms*—The model stresses the need of some control mechanisms, which must be put into action to solve several conflicts involved in bilingualism: which language must be used at a given moment and in a given context? How can a low-proficiency subject use L2 words

avoiding any interference from the stronger L1? A common hypothesis in the neurolinguistic literature assumes that control entails a sort of competition between the two languages and that this competition is solved by inhibiting the nontarget language [23]. Of course, competition can occur both at the level of phonemes (for instance, the English word “dog” competes with the English word “dot”), and at a semantic level (the English word “dog” competes with the French word “chien”). Since the first aspect, linking phonemes to words, is not considered in this model, only the second kind of competition will be considered below.

According to a former assumption by Rodriguez-Fornells et al. [24], model suggests the presence of two distinct but interrelated control mechanisms, which work through inhibition.

A local bottom-up inhibitory mechanism aims to inhibit the weaker language without the participation of higher control centers. This mechanism is directly implemented

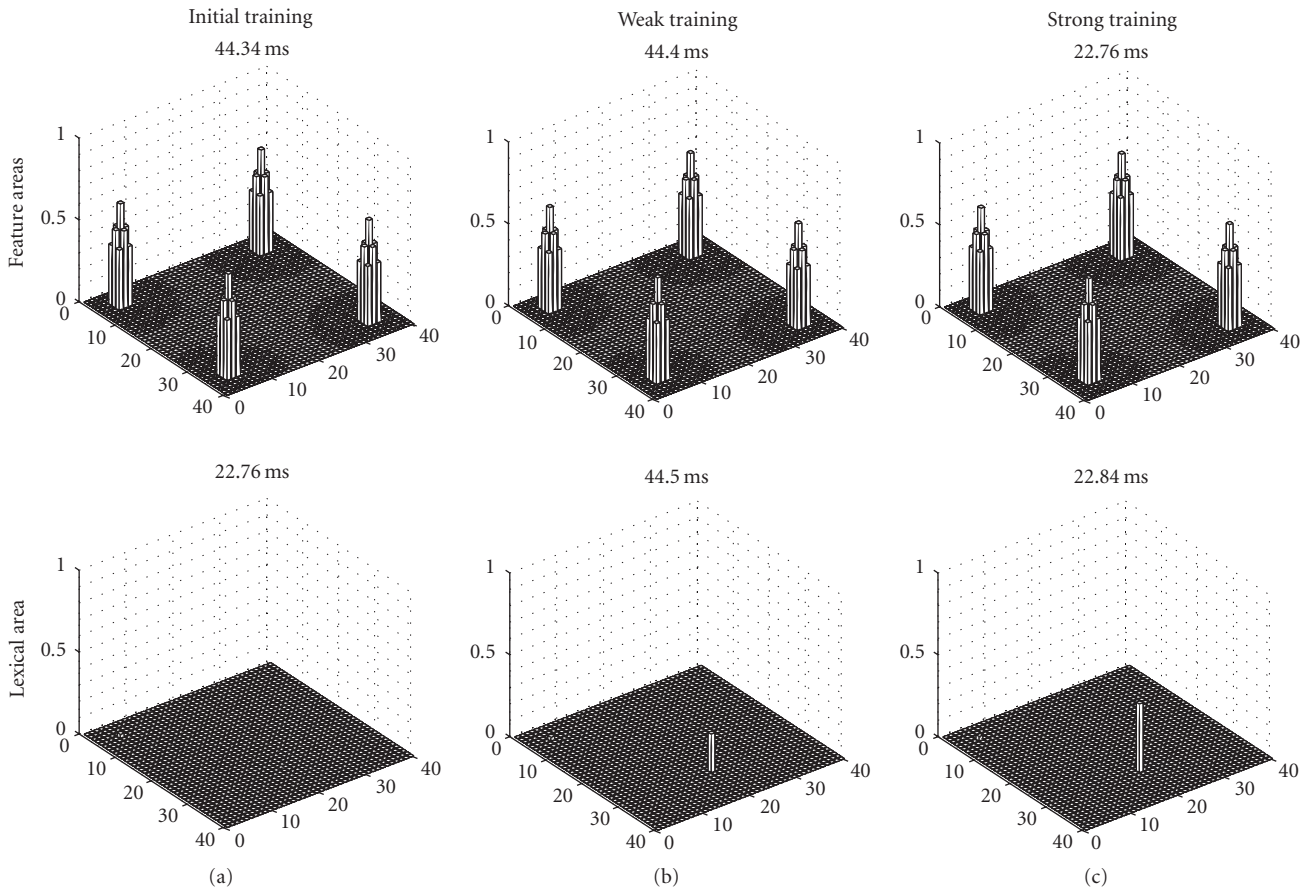


FIGURE 6: Some snapshots of the model response at some instant of the simulations, performed when the object (i.e., its four features) is given as input to the network. Simulations are the same as in Figure 5, with the same meaning of figures, but in this case we assumed that a strong top-down inhibitory input (from a higher control center) targets all L1 words. It is noticeable that, in this situation, the object representation can evoke the L2 word, but with a different level of activation depending on the proficiency level.

within the model via inhibitory interneurons and is trained with the same Hebbian rule used to link words and objects. In the present simulations, this mechanism operates when L2 proficiency is lower than L1 proficiency and the subject perceives an object and must produce the corresponding word. In this condition, word production in response to an object spontaneously engages L1 without any activation of the L2 word (L2 is inhibited by the internal competition; see Figure 5 central column).

Results in Figures 5 and 6 stress the need for a second top-down control system, which can be considered an external input to the model and inhibits one language to favor the other. This situation may involve paradigms like language switching, language translation, or language selection. In our simulations this external input may become necessary when two languages have a similar proficiency level (compare Figures 5(c) and 6(c)) or when the subject is forced to use a low-proficiency language despite the interference from the high-proficiency one (compare Figures 5(b) and 6(b)). A classic point of view is that these conflicts are solved by a dynamical inhibitory input to the nontarget language, and this may originate from

various brain areas classically related to cognitive control, such as the caudate nucleus, the prefrontal cortex, and the anterior cingulate cortex [25–27]. An interesting question is whether this top-down control system is specifically dedicated to language or represents a more general structure, devoted to conflict resolution independently of its explicit domain. Inclusion of such an external mechanism may be the subject of future improvement of the present model.

In conclusion, the present work represents a first attempt to study lexical-semantic aspects of language, such as word production and word comprehension, using neural networks and computer simulations. Assuming that the same neural structures and the same learning mechanisms operate for L1 and L2, the model makes several predictions which agree with some psycholinguistic theories and recent neuroimaging data. Further aspects which require model extension are especially concerned with language control via top-down inhibitory mechanisms. Introduction of this mechanism may allow more complex paradigms to be simulated, such as language selection, language switching, or language translation.

## References

- [1] E. K. Warrington and T. Shallice, "Category specific semantic impairments," *Brain*, vol. 107, no. 3, pp. 829–853, 1984.
- [2] A. Caramazza and J. R. Shelton, "Domain-specific knowledge systems in the brain: the animate-inanimate distinction," *Journal of Cognitive Neuroscience*, vol. 10, no. 1, pp. 1–34, 1998.
- [3] G. W. Humphreys and E. M. E. Forde, "Hierarchies, similarity, and interactivity in object recognition: "Category-specific" neuropsychological deficits," *Behavioral and Brain Sciences*, vol. 24, no. 3, pp. 453–509, 2001.
- [4] M. A. Kraut, S. Kremen, J. B. Segal, V. Calhoun, L. R. Moo, and J. Hart Jr., "Object activation from features in the semantic system," *Journal of Cognitive Neuroscience*, vol. 14, no. 1, pp. 24–36, 2002.
- [5] C. Tallon-Baudry and O. Bertrand, "Oscillatory gamma activity in humans and its role in object representation," *Trends in Cognitive Sciences*, vol. 3, no. 4, pp. 151–162, 1999.
- [6] J. González, A. Barros-Loscertales, F. Pulvermüller, et al., "Reading cinnamon activates olfactory brain regions," *NeuroImage*, vol. 32, no. 2, pp. 906–912, 2006.
- [7] M. Ursino, E. Magosso, G.-E. La Cara, and C. Cuppini, "Object segmentation and recovery via neural oscillators implementing the similarity and prior knowledge gestalt rules," *BioSystems*, vol. 85, no. 3, pp. 201–218, 2006.
- [8] M. Ursino, E. Magosso, and C. Cuppini, "Recognition of abstract objects via neural oscillators: interaction among topological organization, associative memory and gamma band synchronization," *IEEE Transactions on Neural Networks*, vol. 20, no. 2, pp. 316–335, 2009.
- [9] C. Cuppini, E. Magosso, and M. Ursino, "A neural network model of semantic memory linking feature-based object representation and words," *BioSystems*, vol. 96, no. 3, pp. 195–205, 2009.
- [10] H. R. Wilson and J. D. Cowan, "Excitatory and inhibitory interactions in localized populations of model neurons," *Biophysical Journal*, vol. 12, no. 1, pp. 1–24, 1972.
- [11] S. Campbell and D. Wang, "Synchronization and desynchronization in a network of locally coupled Wilson-Cowan oscillators," *IEEE Transactions on Neural Networks*, vol. 7, no. 3, pp. 541–554, 1996.
- [12] J. Abutalebi, "Neural aspects of second language representation and language control," *Acta Psychologica*, vol. 128, no. 3, pp. 466–478, 2008.
- [13] D. Perani and J. Abutalebi, "The neural basis of first and second language processing," *Current Opinion in Neurobiology*, vol. 15, no. 2, pp. 202–206, 2005.
- [14] R. Scoresby-Jackson, "Case of aphasia with right hemiplegia," *Edinburgh Medical Journal*, vol. 12, pp. 696–706, 1867.
- [15] M. T. Ullman, "A neurocognitive perspective on language: the declarative/procedural model," *Nature Reviews Neuroscience*, vol. 2, no. 10, pp. 717–726, 2001.
- [16] R. S. Briellmann, M. M. Saling, A. B. Connell, A. B. Waites, D. F. Abbott, and G. D. Jackson, "A high-field functional MRI study of quadri-lingual subjects," *Brain and Language*, vol. 89, no. 3, pp. 531–542, 2004.
- [17] K. L. Sakai, K. Miura, N. Narafu, and Y. Muraishi, "Correlated functional changes of the prefrontal cortex in twins induced by classroom education of second language," *Cerebral Cortex*, vol. 14, no. 11, pp. 1233–1239, 2004.
- [18] J. F. Kroll and E. Stewart, "Category interference in translation and picture naming: evidence for asymmetric connections between bilingual memory representations," *Journal of Memory and Language*, vol. 33, no. 2, pp. 149–174, 1994.
- [19] R. De Bleser, P. Dupont, J. Postler, et al., "The organisation of the bilingual lexicon: a PET study," *Journal of Neurolinguistics*, vol. 16, no. 4-5, pp. 439–456, 2003.
- [20] D. W. Green, "The neural basis of the lexicon and the grammar in L2 acquisition," in *The Interface between Syntax and the Lexicon in Second Language Acquisition*, R. van Hout, A. Hulk, F. Kuiken, and R. Towell, Eds., John Benjamins, Amsterdam, The Netherlands, 2003.
- [21] D. Klein, B. Milner, R. J. Zatorre, V. Zhao, and J. Nikelski, "Cerebral organization in bilinguals: a PET study of Chinese-English verb generation," *NeuroReport*, vol. 10, no. 13, pp. 2841–2846, 1999.
- [22] D. Perani, J. Abutalebi, E. Paulesu, et al., "The role of age of acquisition and language usage in early, high-proficient bilinguals: a fMRI study during verbal fluency," *Human Brain Mapping*, vol. 19, no. 3, pp. 170–182, 2003.
- [23] D. W. Green, "Mental control of the bilingual lexico-semantic system," *Bilingualism: Language and Cognition*, vol. 1, pp. 67–81, 1998.
- [24] A. Rodriguez-Fornells, A. van der Lugt, M. Rotte, B. Britti, H.-J. Heinze, and T. F. Münte, "Second language interferes with word production in fluent bilinguals: brain potential and functional imaging evidence," *Journal of Cognitive Neuroscience*, vol. 17, no. 3, pp. 422–433, 2005.
- [25] J. Abutalebi and D. Green, "Bilingual language production: the neurocognition of language representation and control," *Journal of Neurolinguistics*, vol. 20, no. 3, pp. 242–275, 2007.
- [26] Y. Wang, G. Xue, C. Chen, F. Xue, and Q. Dong, "Neural bases of asymmetric language switching in second-language learners: an ER-fMRI study," *NeuroImage*, vol. 35, no. 2, pp. 862–870, 2007.
- [27] C. J. Price, D. W. Green, and R. von Studnitz, "A functional imaging study of translation and language switching," *Brain*, vol. 122, no. 12, pp. 2221–2235, 1999.

## Research Article

# Crossmodal Links between Vision and Touch in Spatial Attention: A Computational Modelling Study

Elisa Magosso,<sup>1</sup> Andrea Serino,<sup>2,3</sup> Giuseppe di Pellegrino,<sup>2,3</sup> and Mauro Ursino<sup>1</sup>

<sup>1</sup>Department of Electronics, Computer Science and Systems, University of Bologna, 40136 Bologna, 47023 Cesena, Italy

<sup>2</sup>Department of Psychology, University of Bologna, 40127 Bologna, Italy

<sup>3</sup>Centro Studi e Ricerche in Neuroscienze Cognitive, 47023 Cesena, Italy

Correspondence should be addressed to Elisa Magosso, elisa.magosso@unibo.it

Received 18 June 2009; Accepted 28 July 2009

Academic Editor: Fabrizio De Vico Fallani

Copyright © 2010 Elisa Magosso et al. This is an open access article distributed under the Creative Commons Attribution License, which permits unrestricted use, distribution, and reproduction in any medium, provided the original work is properly cited.

Many studies have revealed that attention operates across different sensory modalities, to facilitate the selection of relevant information in the multimodal situations of every-day life. Cross-modal links have been observed either when attention is directed voluntarily (endogenous) or involuntarily (exogenous). The neural basis of cross-modal attention presents a significant challenge to cognitive neuroscience. Here, we used a neural network model to elucidate the neural correlates of visual-tactile interactions in exogenous and endogenous attention. The model includes two unimodal (visual and tactile) areas connected with a bimodal area in each hemisphere and a competition between the two hemispheres. The model is able to explain cross-modal facilitation both in exogenous and endogenous attention, ascribing it to an advantaged activation of the bimodal area on the attended side (via a top-down or bottom-up biasing), with concomitant inhibition towards the opposite side. The model suggests that a competitive/cooperative interaction with biased competition may mediate both forms of cross-modal attention.

## 1. Introduction

Our environment constantly provides us a large amount of information. An important goal for the brain is to filter out irrelevant information and to select only relevant events in order to guide behaviour. A basic mechanism for selecting information is to process stimuli from a limited portion of space; this function is mediated by *spatial attention*. Most research on spatial attention has been focused on purely unimodal situations [1–5]. Most studies show that responses to stimuli presented at the attended locations increased in comparison to those at the unattended locations, both at behavioural and electrophysiological level. Moreover, extensive theoretical and experimental work on the visual system [1, 3, 6–9] has suggested an influential hypothesis about the neural mechanisms underlying visuospatial attention, known as the *biased competition hypothesis*. The basic idea is that attention biases the competition between multiple stimuli in the visual field in favour of one stimulus, so that

neurons encoding the attended stimulus win the competition and suppress the activity of the cells representing unattended stimuli. The competition among concurrent stimuli can be biased both voluntarily, when the subject dedicates more attentional resources to a given spatial position (endogenous or top-down spatial orienting), or reflexively, when an external stimulus cue suddenly appears at a given spatial location (exogenous or bottom-up spatial orienting) [10, 11].

Recently, the issue of spatial attention has been addressed from a cross-modal perspective. Indeed, an external event typically produces multimodal signals, stimulating different senses simultaneously (as when a visible object moves to touch the body, e.g.). Hence, attention needs to be coordinated across different sensory modalities, in order to select visual, auditory, and tactile information originating from the same object or event, meaning the same spatial location. Behavioural studies showed several cross-modal interactions in spatial attention, that involve different combinations of

modalities (e.g., visual-acoustic, visual-tactile). Both *exogenous* and *endogenous* spatial orienting have been studied *crossmodally* [12–15]. In exogenous attention paradigms, the appearance of a single target is preceded by an abrupt “cue,” which is task-irrelevant and spatially nonpredictive (i.e., the cue location does not predict where the subsequent target stimulus will appear). Responses have been found to be faster and more accurate for targets that appear shortly afterwards on the same side as the cue than on the opposite side, even when the cue and target modalities are different; this suggests that attention is automatically captured towards the cue location not only within the cued modality but also in other modalities. Cross-modal links also exist in the more active, endogenous, form of attentional orienting. When subjective expectations about the appearance of a target in one sensory modality direct attention towards a given side of space, responses are facilitated on that side compared to the opposite side, not only for targets in the attended modality but also for targets in a secondary modality.

A number of studies have investigated the neural correlates of crossmodal attentional interactions using event related potentials (ERP) [13, 16, 17] and hemodynamic measures [18, 19]. Some results support the idea that cross-modal links in spatial attention may reflect the activity of a supramodal system that controls attentional orienting in different modalities. Such account accords with recent neurophysiological findings of multimodal neurons, especially in the parietal and premotor cortex, that respond to multiple modalities in approximate spatial register [20–22]. However, the neural circuits and mechanisms implicated in cross-modal attentional links are not clearly identified yet, and important issues are still open. Among the others, it is not yet clear whether the conceptual framework of the biased competition hypothesis, which successfully accounts for different aspects of visual attention, may apply also for cross-modal attentional effects, and whether the two forms of attention (endogenous and exogenous) are mediated by the same or different neural mechanisms.

Recently, we have developed a neural network model that simulates visual-tactile integration in parietal and frontal regions, involved in the perception of the space near the body (peripersonal space) [23]. In particular, the network mimics the visuotactile representation of the peripersonal space around both hands and is able to account for several results both in healthy subjects and in neuropsychological patients. Moreover, the model has been used to investigate the resizing of perihand space following tool use [24].

The aim of this study is to use an adapted version of our network to investigate the neural bases of visual-tactile interactions in endogenous and exogenous spatial attention.

## 2. Model Description

*2.1. Qualitative Model Description.* The present paper aspires to simulate and interpret—by using an appropriate neural network model—experimental results of visual-tactile links

in attention. All experimental data, which the model aspires to reproduce and to which simulation results are compared, are taken from previous studies in literature performed by other researchers (in particular, Spence et al. [13, 15]); that is, the present study is entirely a theoretical study, not including any experimental design and participants. In particular, the proposed model aims at reproducing only results of *covert orienting* of exogenous [13] or endogenous attention [15]; covert orienting of attention involves purely internal attentional shifts, without any receptor shift (absence of eyes, head or hands movements). In the above quoted studies, participants (healthy subjects) adopted a fixed “default” posture, with eyes and head facing forward (participants were required to fixate a central point), and the hands resting symmetrically each in its own hemispace; tactile and visual stimuli were applied only on the hands. The tactile stimuli were delivered via tactile stimulators attached to or in contact with the hands; visual stimuli were delivered via led positioned in close proximity to the tactile stimulators; a central led served as fixation point [13, 15]. Tactile and visual targets had a duration of several tens of milliseconds (200 milliseconds); in exogenous attention paradigm [13], the cue preceding the target had a shorter duration (few tens of milliseconds).

The model has been conceived to reproduce and interpret the above described experimental studies of covert attention [13, 15]. Accordingly, the model includes two subnetworks, one per hemisphere, each referred to the contralateral hand; moreover, owing to the assumption of fixed postural conditions, we did not include any postural signal in the model and the only external inputs are tactile and visual stimuli (see Figure 1). We hypothesized—with reasonable approximation—that the hand of an adult subject is 10 cm wide and 20 cm length, thus roughly covering a surface of 10 cm × 20 cm.

The single subnetwork embodies three areas of neurons, which communicate via synaptic connections. The two upstream areas are bidimensional matrices of unimodal neurons: neurons in one area respond to tactile stimuli on the contralateral hand (*tactile area*); neurons in the other area respond to visual stimulation on the same hand (*visual area*). Each unimodal neuron has its own *receptive field* (RF), reproduced by means of a Gaussian function, through which receives external stimulation. In both areas, the RFs are in hand-centered coordinates and are arranged according to a topological organization, so that each area maps the external (visual or tactile) space in an orderly manner (proximal neurons respond to stimuli coming from proximal positions in the space). In particular, we assumed that the RFs in both unimodal areas are arranged at a distance of 0.5 cm along both the  $x$  and  $y$  directions; this choice is arbitrary and has been made to represent the hand surface of 10 cm × 20 cm by using a limited number of neurons (20 × 40), in order to maintain model computational weight within acceptable limits. However, each neuron in the model should not be considered representative of a single cell, but rather as a pool of cells with the RF approximately located in the same position. It is worth noting that in the present model, the visual area embodies the same number of neurons

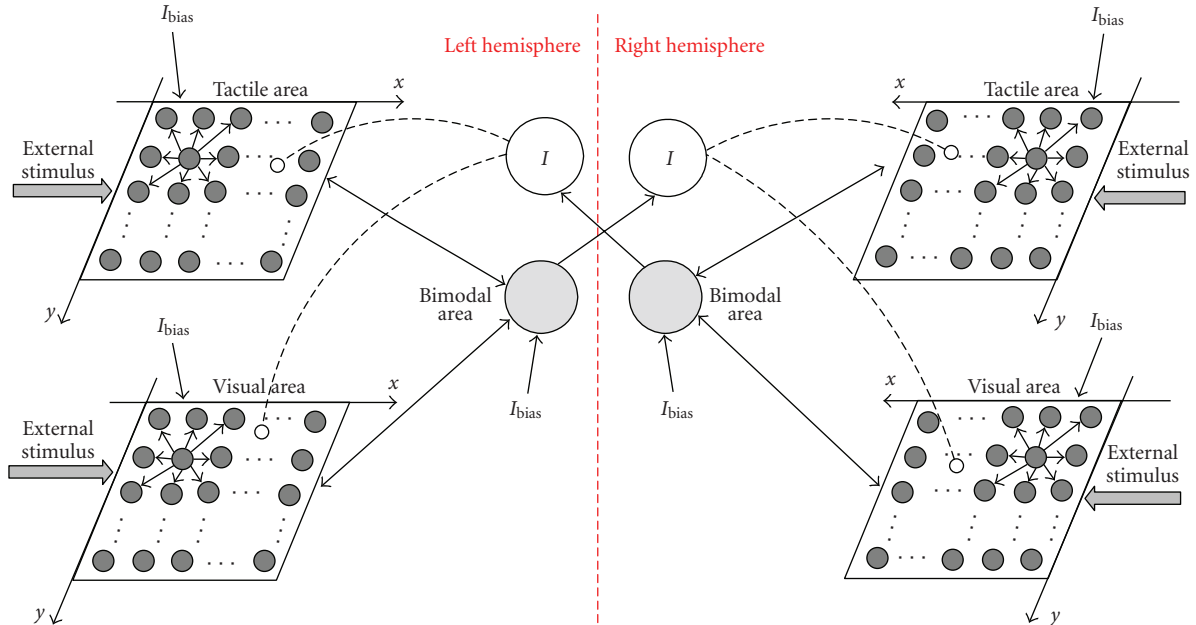


FIGURE 1: Schematic diagram describing the network. Continuous lines represent excitatory connections (lines with arrows in both direction denotes the presence of both feedback and feedforward connections); dashed lines represent inhibitory connections.  $I$  denotes inhibitory interneurons.  $I_{bias}$  is a top-down bias input mimicking endogenous attention conditions; its value may be selectively modified in each of the six areas.

as the tactile one ( $20 \times 40$  neurons), exactly coding the visual space on the hand ( $10 \text{ cm} \times 20 \text{ cm}$ ); indeed, in this study we consider only visual stimuli applied on the hand surface. Neurons within each unimodal area interact via *lateral synapses* with a Mexican hat arrangement (i.e., short range excitation and long range inhibition).

The unimodal tactile and visual neurons in each sub-network send *feedforward synapses* to a third downstream multimodal area devoted to visual-tactile integration. For the sake of simplicity, we consider a single visual-tactile neuron, covering the entire hand. The feedforward synapses linking the unimodal (either visual or tactile) neurons to the downstream bimodal neuron have a uniform distribution; that is, their value is independent of the position of the unimodal neuron in the area.

The bimodal visual-tactile neuron within one hemisphere sends feedback excitatory synapses to the upstream unimodal areas within the same hemisphere. The feedback synapses have a uniform distribution, too.

The two subnetworks are reciprocally interconnected via inhibitory interneurons, realizing a competitive mechanism. The inhibitory interneuron in one hemisphere receives information from the bimodal neuron in the other hemisphere, through a synaptic connection characterized by a *pure delay*, to account for the interhemispheric transit time via the corpus callosum; then, the interneuron sends inhibition to the local unimodal areas. In the model, the inhibitory synapses from the interneuron to tactile and visual neurons have a uniform distribution.

Finally, unimodal and bimodal neurons within each hemisphere may receive a top-down bias input ( $I_{bias}$ )

mimicking attention conditions (see Section 2.3). We assumed  $I_{bias} = 0$  in basal conditions.

The input-output relationship of each neuron (both unimodal, bimodal and inhibitory) includes a first-order dynamics and a static sigmoidal relationship with a lower threshold and an upper saturation. Each neuron in the network is normally in a silent state and can be activated if stimulated by a sufficiently high excitatory input.

**2.2. Model Equations.** In the following, the main equations of the model are presented. Since the overall network has a symmetrical structure, only equations for one hemisphere (the left one) will be reported. The superscripts  $t$ ,  $v$ , and  $m$  will denote quantities referring to tactile, visual, and multimodal (i.e., bimodal) neurons, respectively; the superscript  $g$  will indicate quantities referring to the inhibitory interneuron; the superscripts  $L$  and  $R$  will distinguish the left and right hemisphere; the subscripts  $ij$  or  $hk$  will represent the spatial position of individual neurons.

**2.2.1. The Unimodal Neurons.** The unimodal areas are composed of  $N^s \times M^s$  neurons ( $s = t, v$ ), with  $N^s = 20$ ,  $M^s = 40$ . In both areas, the RFs of neurons are arranged at a distance of 0.5 cm along both the  $x$  and  $y$  directions.

By considering a reference frame rigidly connected with the hand (see Figure 1), the coordinates of the RF centre of a generic neuron  $ij$  are given by

$$\begin{aligned} x_i^s &= i \cdot 0.5 \text{ cm} \quad (i = 1, 2, \dots, N^s), \\ y_j^s &= j \cdot 0.5 \text{ cm}, \quad (j = 1, 2, \dots, M^s), \end{aligned} \quad s = t, v. \quad (1)$$

The receptive field of the unisensory neurons is described via a Gaussian function. For a generic neuron  $ij$ , the following equation holds:

$$\Phi_{ij}^{s,L}(x, y) = \Phi_0^{s,L} \cdot \exp\left(-\frac{(x_i^{s,L} - x)^2 + (y_j^{s,L} - y)^2}{2 \cdot (\sigma_\Phi^{s,L})^2}\right), \quad s = t, v, \quad (2)$$

where  $x_i$  and  $y_j$  are the centre of the RF,  $x$  and  $y$  are the spatial coordinates, and  $\Phi_0^{s,L}$  and  $\sigma_\Phi^{s,L}$  represent the amplitude and standard deviation of the Gaussian function. According to this equation, a punctual external stimulus applied at the position  $x, y$  excites not only the neuron centred in that point but also the proximal neurons whose receptive fields cover that position.

The total input received by a generic neuron  $ij$  in the unimodal area  $s = t, v$  is given by five different contributions.

(a) The first contribution is due to the external stimulus, computed as the inner product of the stimulus and the receptive field:

$$\begin{aligned} \varphi_{ij}^{s,L}(t) &= \int_x \int_y \Phi_{ij}^{s,L}(x, y) \cdot I^{s,L}(x, y, t) dx dy \\ &\cong \sum_x \sum_y \Phi_{ij}^{s,L}(x, y) \cdot I^{s,L}(x, y, t) \Delta x \Delta y, \quad s = t, v, \end{aligned} \quad (3)$$

where  $I^{s,L}(x, y, t)$  is the external stimulus (tactile or visual) applied on the righthand (processed by the left hemisphere) at the coordinates  $x, y$  and at time  $t$ . The right-hand member of (3) means that the integral is computed with the histogram rule (with  $\Delta x = \Delta y = 0.2$  cm).

(b) The second contribution is due to the lateral synapses linking the neuron with the other elements in the same area. This contribution is defined as

$$\lambda_{ij}^{s,L}(t) = \sum_{h=1}^{N^s} \sum_{k=1}^{M^s} \Lambda_{ij,hk}^{s,L} \cdot z_{hk}^{s,L}(t), \quad s = t, v. \quad (4)$$

$z_{hk}^{s,L}(t)$  represents the activity of the  $hk$  neuron in the area  $s$  ( $s = t, v$ ) of the left hemisphere.  $\Lambda_{ij,hk}^{s,L}$  indicates the strength of the synaptic connection from the presynaptic neuron at the position  $hk$  to the postsynaptic neuron at the position  $ij$ . These synapses are symmetrical and are arranged according to a ‘‘Mexican hat’’ function.

(c) The third contribution is due to the feedback excitatory projections from the bimodal neuron, computed as

$$\beta_{ij}^{s,L}(t) = B_{ij}^{s,L} \cdot z^{m,L}(t), \quad s = t, v. \quad (5)$$

$z^{m,L}(t)$  represents the activity of the bimodal neuron.  $B_{ij}^{s,L}$  indicates the strength of the synaptic connection from the presynaptic bimodal neuron to the postsynaptic unimodal neuron  $ij$ ; in the model the feedback synapses have a uniform distribution (i.e.,  $B_{ij}^{s,L} = B_0^{s,L}$ , for all  $i, j$ ).

(d) The fourth contribution is due to the synapses from the inhibitory interneuron, given by

$$\gamma_{ij}^{s,L}(t) = \Gamma_{ij}^{s,L} \cdot z^{g,L}(t), \quad s = t, v. \quad (6)$$

$z^{g,L}(t)$  represents the activity of the inhibitory interneuron, which depends on the visual-tactile information at the other hemisphere (see below).  $\Gamma_{ij}^{s,L}$  is the strength of the synaptic connection from the interneuron to unimodal neuron  $ij$ ; the inhibitory synapses have a uniform distribution, too ( $\Gamma_{ij}^{s,L} = \Gamma_0^{s,L}$ , for all  $i, j$ ).

(e) The fifth contribution is due to the attentional top-down bias input. We assumed that the attentional bias to one unimodal area acts as a constant input ( $I_{\text{bias}}^{s,L}$ ) and affects all the neurons within the area. In basal conditions, the attentional bias input is set equal to zero in both unimodal areas of each hemisphere.

The total input is obtained by summing the four excitatory contributions (a), (b), (c), and (e) and subtracting the inhibitory contribution (d). Then, neuron activity ( $z_{ij}^{s,L}(t)$ ) is computed from the total input through a first-order dynamics and a static sigmoidal relationship.

**2.2.2. The Bimodal Neuron.** The overall input to a bimodal neuron in one hemisphere is the sum of two contributions.

(a) The first contribution is due to the inputs from neurons in the two unimodal areas via feedforward synapses, computed as

$$\eta^{m,L}(t) = \sum_{i=1}^{N^t} \sum_{j=1}^{M^t} W_{ij}^{t,L} \cdot z_{ij}^{t,L}(t) + \sum_{i=1}^{N^v} \sum_{j=1}^{M^v} W_{ij}^{v,L} \cdot z_{ij}^{v,L}(t). \quad (7)$$

$z_{ij}^{s,L}(t)$  ( $s = t, v$ ) represents the activity of the unimodal neuron  $ij$  in tactile or visual area.  $W_{ij}^{s,L}$  denotes the feedforward synapses from the unisensory neuron  $ij$  to the bimodal neuron; their strength is independent of the position of the unimodal neuron ( $W_{ij}^{s,L} = W_0^{s,L}$ , for all  $i, j$ ).

(b) The second contribution is due to the attentional top-down bias input reproduced as a constant input ( $I_{\text{bias}}^{m,L}$ ). In basal conditions, the attentional bias to the bimodal neuron is set equal to zero in both hemispheres.

The activity of the bimodal neuron ( $z^{m,L}(t)$ ) is obtained from its overall input via a first order dynamics and a static sigmoidal characteristic.

**2.2.3. The Inhibitory Interneuron.** The inhibitory interneuron in one hemisphere receives synapses from the bimodal neuron in the other hemisphere. Hence, the input to the interneuron in the left hemisphere is

$$u^{g,L}(t) = X^R \cdot z^{m,R}(t - D), \quad (8)$$

where  $z^{m,R}(t)$  is the activity of the bimodal neuron in the right hemisphere and  $D$  is a pure delay, simulating the interhemispheric transit time.  $X^R$  represents the strength of the cross-connection.

Starting from this input, a lowpass dynamics and a sigmoidal static function are used to compute the activity of the interneuron ( $z^{g,L}(t)$ ).

Basal values for all model parameters were assigned on the basis of neurophysiological [21, 25, 26], psychophysical [27, 28], and behavioural literature [29–31] (a detailed

parameter assignment can be found in our previous papers [23, 24]). The two hemispheres have the same parameter values. Moreover, unimodal tactile and visual areas in each hemisphere are characterized by the same parameter values (static and dynamic neuron characteristics, lateral synapses).

**2.3. Simulation Trials Description.** To investigate the neural correlates of exogenous/endogenous attention, we simulated the delivery of target stimuli (of both modality and on any side of space) to the hypothetical subject, under four different conditions: the first represents a “neutral”, that is, *unbiased*, condition whereas the other three aim at resembling different conditions of *attentional orienting* towards one side of space. Specifically, we considered the following cases:

- (A) “neutral” condition (*unbiased*): the network works in basal condition, without any unbalance between the two hemispheric subnetworks,
- (B) voluntary (*endogenous*) allocation of attention towards one side of space, *irrespective of the modality*: application of a nonzero top-down bias input to the bimodal area in one hemisphere contralateral to the attended side,
- (C) voluntary (*endogenous*) allocation of attention towards one side of space, *in a particular modality*, for example, tactile: application of a nonzero top-down bias input to the tactile area and the bimodal area (but not to the visual area) in one hemisphere contralateral to the attended side,
- (D) involuntary (*exogenous*) capture of attention towards one side of space: application of a short tactile cue on a specific side (corresponding to the cued side), before any target stimulus; in this condition, the top-down bias input is maintained at zero in both hemispheres.

Both tactile and visual targets are reproduced via a two-dimensional Gaussian function of  $x$  and  $y$  coordinates, with small standard deviation to reproduce punctual stimuli as those used in *in vivo* studies. The amplitude of the target stimulus is affected by a Gaussian random noise to create variability in the network response (as it occurs in real conditions). Tactile cue in the exogenous attention condition was simulated as a brief (30 milliseconds) stimulus.

For each condition (A, B, C, D), we performed four blocks of simulations, each block being characterized by the target modality (visual or tactile) and the side of target application (left or right). Ten simulations were performed in each block (40 simulations per condition). Each simulation lasted until the network transient response to the target stimulus was exhausted (see result figures). Network performance in response to each target stimulus was assessed by computing the 98% settling time ( $T_s$ ) of the bimodal neuron on the same side as the target.

### 3. Results

All results describe network response to application of a target stimulus on one side of space (i.e., in each simulation,

a single target stimulus on either side is delivered to the network). Each simulation is continued as long as the network reaches a new steady state in response to the target (target application is maintained until the end of the stimulation). Targets are applied while the network operates in one of the four different conditions described above (A, B, C, D).

Table 1 reports the bimodal neuron settling time (mean  $\pm$  std) as a function of target modality and target side in all examined conditions. Data are analysed via two-tailed paired  $t$ -tests.

Condition A corresponds to the absence of any specific spatial allocation of attention (“neutral” condition). Simulations in this condition show network basal functioning and provide reference values for network settling time.

Figure 2 displays the neural activity in response to a visual target on one side, in unbiased, neutral condition. Panel (a) shows the steady-state response of the overall network after the transient has exhausted. The visual stimulus induces the activation of a group of neurons in the visual unimodal area; the occurrence of an “activation bubble” is due to the partial superimposition of the RFs of adjacent neurons and to the lateral excitation within the unimodal area which produces reciprocal reinforcement of neighbouring neurons activity. The bimodal neuron in the same hemisphere is activated thanks to the large input from the stimulated visual area. The bimodal neuron, in turn, elicits activation of the inhibitory interneuron in the opposite hemisphere via the interhemispheric synapse. All other neurons in the network are silent. Panel (b) shows the temporal pattern of the activated neurons (precisely, the visual neuron on which the stimulus was centred, the bimodal neuron in the same hemisphere, and the inhibitory interneuron in the opposite hemisphere). The blue dashed vertical line denotes the onset of target application. The visual neuron exhibits a fast response (left plot); whereas the bimodal neuron takes some milliseconds to reach its new steady-state activity following target application (central plot). The inhibitory interneuron follows the same temporal pattern of the contralateral bimodal neuron with few milliseconds delay (right plot), due to the delay in the interhemispheric connection.

Performances of the network in this unbiased condition (see Table 1 Section A) do not differ across sides and modalities (the two hemispheres are perfectly symmetrical, and no difference exists between the tactile and visual areas within each hemisphere).

Figure 3 displays the exemplary temporal pattern of neural activity in response to a *visual* target in condition B. In condition B, a top down bias input ( $I_{bias} = 10$ ) is tonically applied to the bimodal neuron in one hemisphere (contralateral to the “attended” side of space). This aims at resembling conditions of voluntary allocation of attention towards one side of space in a supramodal fashion, as it might be necessary when target modality is uncertain. The visual target was applied first on the attended side (panel (a)) and then on the unattended side (panel (b)); that is, the target was present on a single side at a time. In both panels, we displayed the temporal patterns of the unimodal neuron on

TABLE 1: Settling time ( $T_s$ ) of the bimodal neuron (mean  $\pm$  std) in response to tactile and visual targets on both sides, in the four examined conditions, and results of two-tailed paired  $t$ -tests on tactile-minus-visual differences and unattended/uncued side-minus-attended/cued side differences (ns: nonsignificant; \* $P < .05$ ; \*\* $P < .01$ ; \*\*\* $P < .01$ ).

| Condition A |                                 |                                 |                                 |
|-------------|---------------------------------|---------------------------------|---------------------------------|
|             | One side                        | Other side                      | Difference                      |
| Tactile     | $T_s = 41.9 \pm 1.7$ ms         | $T_s = 41.5 \pm 3.9$ ms         | $\Delta = -0.44 \pm 3.7$ ms(ns) |
| Visual      | $T_s = 39.8 \pm 3.3$ ms         | $T_s = 40.3 \pm 4.0$ ms         | $\Delta = 0.48 \pm 4.7$ ms (ns) |
| Difference  | $\Delta = 2.12 \pm 3.4$ ms (ns) | $\Delta = 1.2 \pm 4.86$ ms (ns) |                                 |
| Condition B |                                 |                                 |                                 |
|             | Attended side                   | Unattended side                 | Difference                      |
| Tactile     | $T_s = 24.1 \pm 1.1$ ms         | $T_s = 52.5 \pm 11$ ms          | $\Delta = 28.36 \pm 11$ ms***   |
| Visual      | $T_s = 25.4 \pm 3.8$ ms         | $T_s = 54.8 \pm 13$ ms          | $\Delta = 29.44 \pm 12.5$ ms*** |
| Difference  | $\Delta = -1.32 \pm 3.7$ ms(ns) | $\Delta = -2.4 \pm 18.5$ ms(ns) |                                 |
| Condition C |                                 |                                 |                                 |
|             | Attended side                   | Unattended side                 | Difference                      |
| Tactile     | $T_s = 10.6 \pm 0.7$ ms         | $T_s = 56.4 \pm 8$ ms           | $\Delta = 45.8 \pm 8.6$ ms***   |
| Visual      | $T_s = 26.7 \pm 1.6$ ms         | $T_s = 53 \pm 11$ ms            | $\Delta = 26.3 \pm 11.6$ ms***  |
| Difference  | $\Delta = -16.2 \pm 2.11$ ms*** | $\Delta = 3.4 \pm 13.4$ ms (ns) |                                 |
| Condition D |                                 |                                 |                                 |
|             | Cued side                       | Uncued side                     | Difference                      |
| Tactile     | $T_s = 32.9 \pm 1.7$ ms         | $T_s = 58.5 \pm 6.9$ ms         | $\Delta = 25.6 \pm 8.1$ ms***   |
| Visual      | $T_s = 34.1 \pm 1.2$ ms         | $T_s = 56.1 \pm 9.3$ ms         | $\Delta = 22 \pm 10.3$ ms***    |
| Difference  | $\Delta = -1.2 \pm 2.16$ ms(ns) | $\Delta = 2.4 \pm 12.5$ ms(ns)  |                                 |

which the target is centred and of the bimodal neuron and inhibitory interneuron at the same side as the target. The dashed blue vertical line in each plot denotes the time onset of target application. It is worth noticing that the bias input is applied throughout the entire simulation (i.e., even before the target application). The bias input produces a sustained baseline activation of the bimodal neuron in the attended side (up to 20% of its maximum activity) and a consequent tonic activity of the inhibitory interneuron in the opposite hemisphere (corresponding to the unattended side); these effects can be observed, respectively, in Figure 3(a) central panel before target application and in Figure 3(b) right panel. A target applied on the “attended” side produces faster responses of the bimodal neuron thanks to its baseline excitation (compare the response of the bimodal neuron to the target in Figure 3(a) central panel, with respect to unbiased condition in Figure 2(b) central panel). Conversely, a target applied on the “unattended” side is disadvantaged because of the nonnull activity of the inhibitory interneuron (Figure 3(b) right panel) activated by the bias input to the bimodal neuron in the other hemisphere; the inhibitory interneuron slows down the response of the unimodal neurons (Figure 3(b) left panel) and—as a consequence—of the bimodal neuron too (Figure 3(b) central panel). Network performances within each side (attended/unattended) did not differ across modalities (see Table 1); on the contrary, an extremely significant effect of side (attended versus unattended) was found for targets in both modalities (Table 1).

Results of these simulations are consistent with *in vivo* data obtained from subjects who voluntarily allocate their

attention towards a specific side of space irrespective of the modality [15]. In that study, participants were informed about the likely side for the upcoming target (towards which they oriented their attention), whereas target modality was uncertain (tactile or visual in every trial): speeded discrimination responses were significantly faster on the expected side than on the other side for targets in both modalities, and the amount of facilitation was similar for visual and tactile targets.

In condition C, a top-down bias input ( $I_{\text{bias}} = 10$ ) is applied to both tactile and bimodal neurons in one hemisphere (corresponding to the attended side). Figure 4 displays typical network responses to a target applied on the attended side (panel (a)) or on the unattended side (panel (b)) in this condition. In this figure too, each panel shows the temporal response of the unimodal neuron on which the stimulus was centred and of the bimodal neuron and inhibitory interneuron at the same side as the target. In this case, the bias input is applied also to the tactile unimodal area; hence some differences in network response may occur between tactile and visual targets delivered to the attended side. For this reason, in panel (a) we reported neuron responses to both a tactile and a visual target. The dashed blue vertical line in each plot denotes the time onset of target application. The bias input to tactile and bimodal areas in the attended side is applied throughout the entire simulation (even before the target application). As in condition B, the bias input applied to the bimodal neuron produces a tonic activity in the bimodal neuron (see Figure 4(a) central panel, before target application) as well

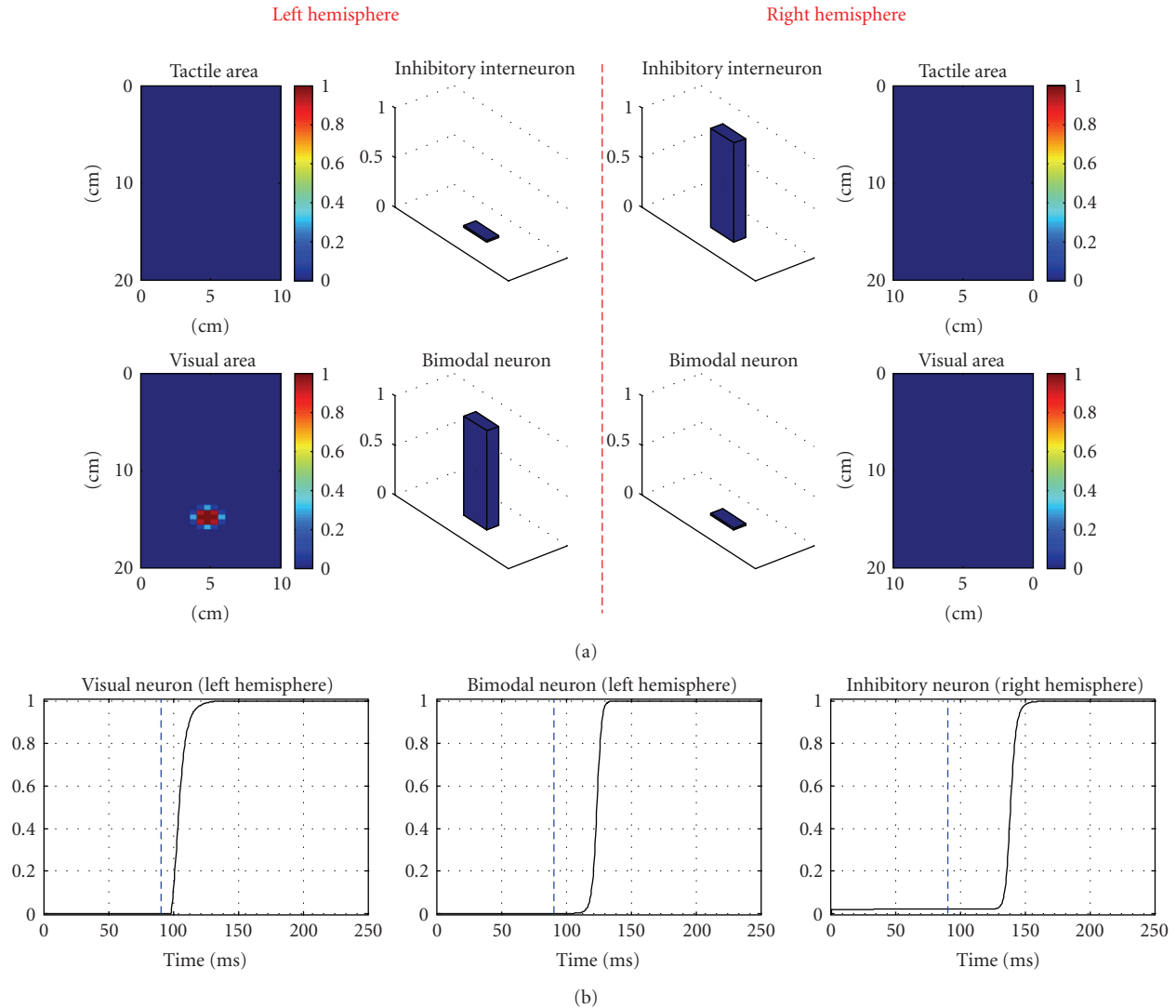


FIGURE 2: Exemplary network response to a visual target on one hand (the right hand) in basal conditions. Only the response to a visual target on one side is shown, since in condition A the network behaves in a similar way for targets on any side and modality. The target stimulus is maintained, from the onset time of application, throughout the entire simulation. *Panel (a)* shows network activity in steady-state conditions, that is, after the transient response to the stimulus has exhausted. The  $x$  and  $y$  axes of the unimodal areas represent the spatial coordinates of neurons RF center; the colour denotes the level of activation of the neurons. *Panel (b)* shows the temporal pattern of the activated neurons; the blue vertical dashed line indicates the onset time of the target stimulus. The left panel displays only the response of the visual neuron on which the stimulus is centred.

as in the inhibitory interneuron in the opposite hemisphere (see Figure 4(b) right panel). On the contrary, the bias input applied to the tactile neurons is not sufficient to activate them (tactile neurons are silent before target application; see green dashed line in Figure 4(a) left panel); anyway, the bias input leads tactile neurons closer to their excitation threshold. Therefore, when a target is applied on the attended side, the bimodal neuron responds faster because of its baseline excitation due to the bias input. Moreover, since the tactile unimodal neurons are closer to their excitation threshold (thanks to the bias input), their response is more rapidly. Consequently, response performances for tactile targets on the attended side are significantly better than those for visual

targets on the same side (see Figure 4(a) left and central panels, and Table 1). Similarly to condition B, responses to targets on unattended side are slowed down because of the tonic activity of the inhibitory interneuron (produced by the bias input to the contralateral bimodal neuron, Figure 4(b)). Significant effects of side application were present for targets in both modalities, although the effect was larger for targets in the tactile modality, because of their higher advantage on the attended side (Table 1).

Network performances in this condition agree with *in vivo* data obtained from subjects who intentionally direct attention in a specific modality towards one side of space [15]. In such experiments, subjects were instructed to direct

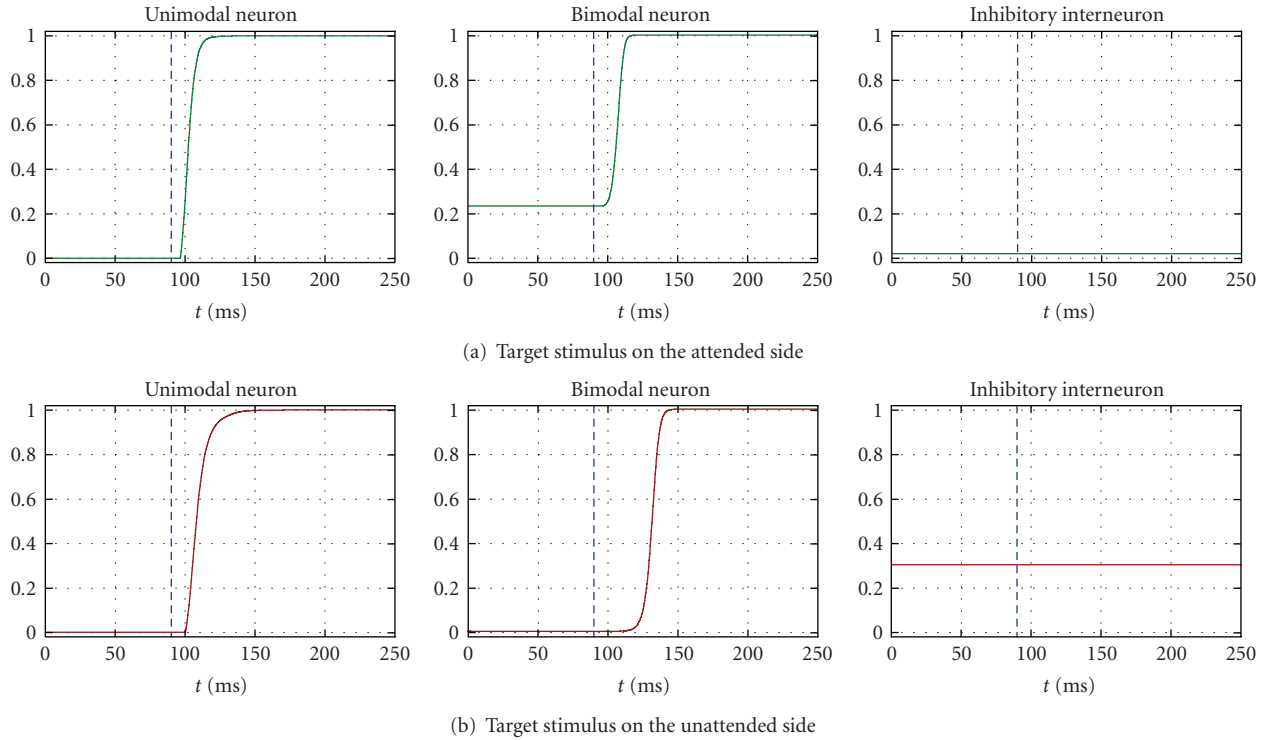


FIGURE 3: Exemplary temporal patterns of neuron responses to a visual target delivered either on one side or on the other side in condition B (application of the top-down bias input = 10 to the bimodal neuron in one hemisphere contralateral to the attended side). Only the responses to a visual target are shown since in condition B responses on each side do not differ significantly across modalities. *Panel (a)* displays the response of neurons in the attended side to a visual target on that side. *Panel (b)* displays the response of neurons in the unattended side to a visual target on that side. In each panel, the displayed curves are the time response of the unimodal neuron on which the target stimulus is centred, the time response of the bimodal neuron, and the time response of the inhibitory neuron. The blue vertical dashed line denotes the onset time of the target stimulus, maintained throughout the rest of the simulation.

their attention to one side in just one modality (e.g., tactile, primary modality), without any specific allocation of attention for the secondary modality (e.g., visual). Subjects showed faster discriminations on the side that was attended in the primary modality not only for targets in that modality but also for targets in the secondary modality. Spatial effects were significant for both modalities, although larger for the targets in the primary modality: indeed, on the attended side, targets in the primary modality were more facilitated than targets in the secondary modality [15].

In condition D, a 30-millisecond tactile cue is delivered to one side (“cued” side), before the application of any target stimulus (stimulus onset asynchrony = 90 milliseconds). The top-down input is set to zero in both hemispheres. Exemplary responses to a visual target on the cued (panel (a)) or uncued (panel (b)) side are shown in Figure 5. Each panel shows the temporal response of the unimodal neuron on which the stimulus was centred and of the bimodal neuron and inhibitory interneuron at the same side as the target. The blue dashed vertical line in each plot denotes the onset of target application. The transient response of the bimodal neuron in the cued side before target onset (see Figure 5(a) central plot) is elicited by the tactile cue. Analogously, the transient response of the inhibitory interneuron in the uncued side (Figure 5(b) right plot) is due

to the application of the tactile cue on the cued side, via the interhemispheric synapse. Responses were faster for targets (both modalities) on the same side as the cue (see Table 1): indeed, at the time of target application, the bimodal neuron on the cued side has not completely recovered its baseline condition (Figure 5(a) central panel) and it is closer to the threshold level. Conversely, the response to a target on the uncued side is hindered by the inhibitory action of the interneuron, transiently activated by the cue on the opposite side. In particular, because of the interhemispheric delay, the inhibitory interneuron on the uncued side is still active at the target time presentation (Figure 5(b), right panel), slowing down the response of the unimodal neurons and, consequently, of the bimodal neuron (Figure 5(b), left and central panels). On the overall, network responds significantly more rapidly on the cued side than on the uncued side, for targets in both modalities, not only in the cue modality.

Network performances are in agreement with results of exogenous attention studies [13]. In the study by Kennett et al. [13], single visual stimuli presented on the left or right hand were preceded by a spatially nonpredictive tactile cue; responses to visual targets were faster and more accurate when these were presented on the cued versus the uncued side.

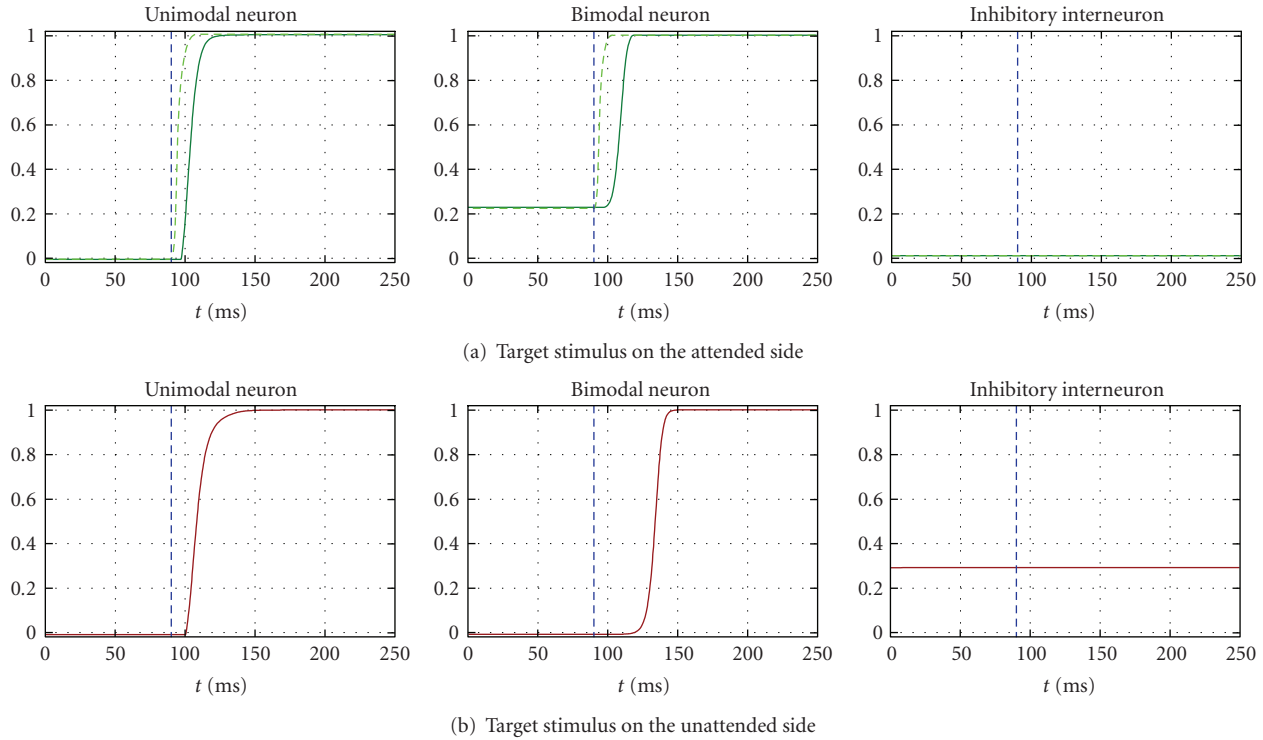


FIGURE 4: Exemplary temporal patterns of neuron responses to a target delivered either on one side or on the other side in condition C (application of the top-down bias input = 10 to the tactile area and to the bimodal neuron in one hemisphere contralateral to the attended side). *Panel (a)* displays the response of neurons in the attended side to both a tactile target (dashed light green line) and a visual target (continuous dark green line) on that side. On the attended side, network responses to tactile targets are faster than those to visual targets. *Panel (b)* displays the response of neurons in the unattended side to a visual target on that side. In each panel, the displayed curves are the time response of the unimodal neuron on which the target stimulus is centred, the time response of the bimodal neuron, and the time response of the inhibitory neuron. The blue vertical dashed line denotes the onset time of the target stimulus, maintained throughout the rest of the simulation.

#### 4. Discussion

Many behavioral and neuroimaging studies have revealed that attention operates across different sensory modalities [12, 13, 15, 16, 19]. Despite considerable experimental research, understanding the neural basis of cross-modal links in spatial attention still remains a significant challenge to cognitive neuroscience. In this work, we used a neural network model to elucidate the mechanisms and possible neural correlates of multisensory integration in spatial attention.

Neurocomputational models have been proposed in literature to explain mechanisms of unimodal attention. Most of these models aimed at investigating different aspects of visual attention [6, 9, 32, 33]; recently, artificial neural networks have been applied also to study attentional effects in other modalities too (e.g., somatosensory) [34]. At present, we are not aware of any work that exploits a computational modelling approach in order to shed light on the neural mechanisms underlying multimodal spatial attention.

We implemented a simple neural network with limited complexity, which includes two unimodal areas and a bimodal area connected via excitatory feedforward and feedback synapses within each hemisphere and a competitive

interaction via inhibitory interneurons between the two hemispheres.

Such model architecture has several physiological counterparts. The bimodal neurons in the model may represent cells in the parietal and frontal cortex that have been found to respond to tactile stimuli on a specific body part (e.g., the hand) and to visual stimuli near the same body part [20–22]. The visual and tactile receptive fields of such neurons are in close spatial register and can be very large, even encompassing the entire hand [21, 22]. Some studies [13, 35] suggested that such bimodal neurons may be involved in generating the visual-tactile links in spatial attention. The two upstream unimodal layers in the model account for primary and secondary somatosensory and visual areas, which project into the multisensory areas through different pathways [20–22]. The presence of back-projections from the bimodal neuron into the upstream unimodal areas is supported by neuroimaging data according to which activity in the tactile area due to a tactile stimulus is amplified by a concurrent visual stimulus on the same hand, and vice versa [36, 37]. However, in the simulations performed in the present study, feedback connections do not play any role, since we applied only one unimodal stimulus at a time on each hand.

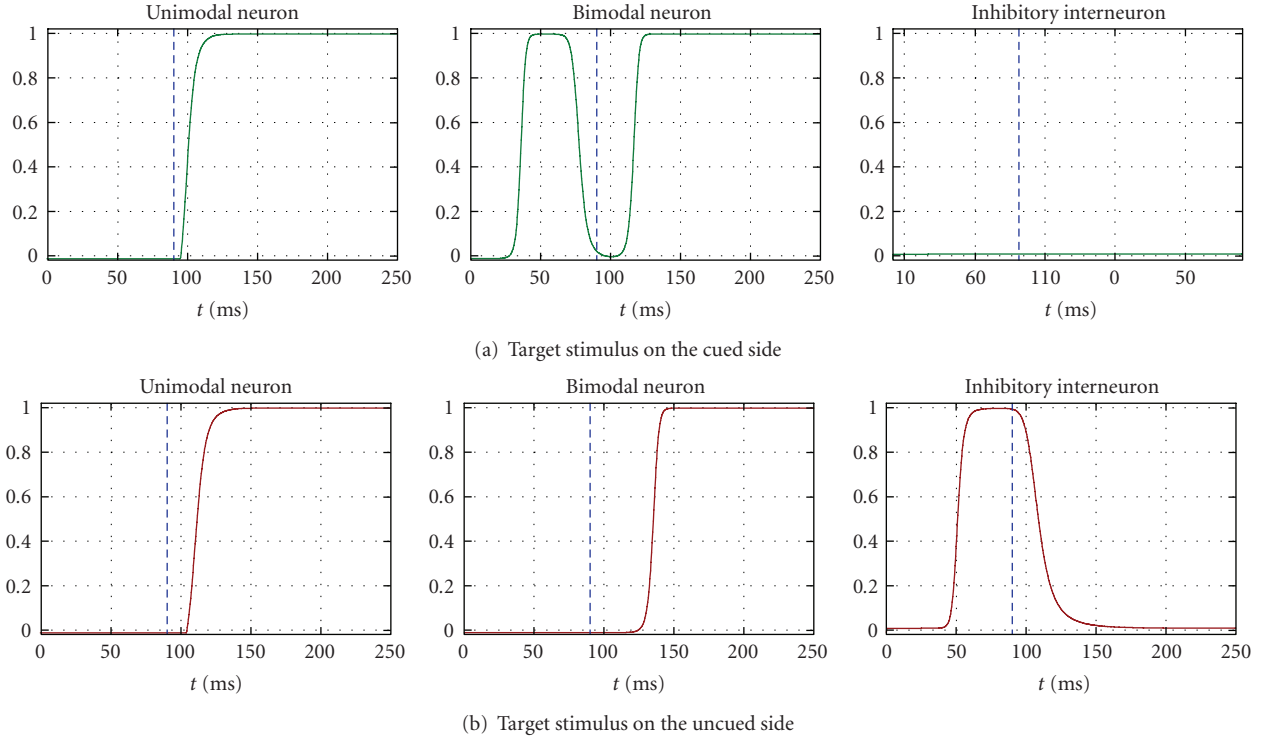


FIGURE 5: Exemplary temporal patterns of neuron responses to a visual target delivered either on one side or on the other side in condition D (a tactile cue of 30 milliseconds preceded any target stimulus; stimulus onset asynchrony = 90 milliseconds). Only the responses to a visual target are shown since, in condition D, responses on each side do not differ significantly across modalities. *Panel (a)* displays the response of neurons in the cued side to a visual target on that side. *Panel (b)* displays the response of neurons in the uncued side to a visual target on that side. In each panel, the displayed curves are the time response of the unimodal neuron on which the target stimulus is centred, the time response of the bimodal neuron, and the time response of the inhibitory neuron. The blue vertical dashed line denotes the onset time of the target stimulus, maintained throughout the rest of the simulation.

Several researches (see [38] for a review) suggest that the functional interaction between the two hemispheres may be inhibitory at times and excitatory at other times, depending on the task. In some instances, it may be more efficient for the hemispheres to compete, so that the dominant hemisphere takes the control of the processing; in other instances, inter-hemispheric cooperation might be necessary to complete the task. In particular, the existence of an interhemispheric competition for accessing limited attentional resources has received several neurophysiological and behavioural evidence [1, 31]. The most striking evidence of attentional competition between the hemispheres is provided by right brain damaged patients, suffering from sensory extinction. They are able to detect stimuli presented to either side of space but fail to detect the stimulus on the contralesional side when both sides are stimulated simultaneously, even under two different sensory modalities (e.g., one stimulus is visual and the other tactile [39]). An attention-capturing event on the ipsilesional intact side competes with—and may completely extinguish—the stimulus on the contralesional affected side.

Thanks to this network structure, we are able to reproduce several phenomena of cross-modal interactions in both endogenous (voluntary or top-down) and exogenous

(reflexive or bottom-up) attention. It is worth noticing that to relate model results with behavioural responses (i.e., reaction times), network performances have been evaluated in terms of bimodal neuron settling time, rather than unimodal neurons response. Indeed, recent studies [40, 41] suggest that activation of early sensory cortices is not sufficient to produce perceptual awareness; rather, the conscious perception of sensory stimuli depends on the activation of higher level multimodal areas (in a parietal-frontal network), which make conscious information available for further processes such as memorization, action, and verbal report [42].

In order to simulate endogenous allocation of attention, we introduced an external top-down bias, that is, an excitatory input to pools of neurons in the hemisphere contralateral to the attended side of space. Indeed, it has been argued [43, 44] that the direction of covert spatial attention depends on the relative level of activation between the two cerebral hemispheres, so that higher left hemisphere activation tends to direct attention rightwards and viceversa. Moreover, experimental and theoretical studies on visual system indicate that attention may act as an excitatory input boosting the activity of neurons encoding the attended stimuli [6, 32, 45]. Crucially, our model analysis shows

that boosting activity in appropriate brain areas via top-down bias input may explain various—and for some aspects controversial—results of endogenous attention.

By applying the top-down bias input to just the bimodal neuron in one hemisphere, the model predicts an improvement in the perception of contralateral stimuli (in the attended side) and shows that such improvement generalizes with the same extent for stimuli in both modalities. Such results are in agreement with *in vivo* data obtained when only target location is known in advance and target modality is unpredictable [15]. In this case, since the target modality is uncertain, attentional boosting of only a supramodal system would have both functional and parsimonious significance.

By applying the top-down bias input to the bimodal neuron and to a pool of unimodal neurons (e.g., tactile) in the same hemisphere, the network predicts that performance improvement on the attended side for targets in the biased modality (tactile) is larger than for targets in the unbiased modality (visual), as observed experimentally when attending to a spatial location in a specific modality [15]. Hence, attentional boosting of both a supramodal system and a modality-specific system can explain how endogenous attention in a primary modality can spread into other modalities, but only in an attenuated fashion. Conversely, if the biased input was applied only to one area of unimodal (e.g., tactile) neurons, the model would not be able to reproduce the spreading of attention into the other modality (unshown simulations). Model postulations are supported by recent neuroimaging studies showing that sustained spatial attention within one modality modulates the activity of both modality-specific and multimodal areas (e.g., in the intraparietal sulcus) [18].

Hence, model analysis suggests that endogenous attention may operate entirely at a supramodal level or at both modality-specific and supramodal levels, depending on whether subject's expectancy concerns only stimuli location or also stimuli modality.

By setting the top-down bias input at zero and presenting a cue before any target, the model is able to reproduce results of exogenous attention [13]. In the model, capture of attention both in the cue modality and in the other modality is due to the involvement of the bimodal neuron, which receives advantage activation thanks to the cue stimulus.

An important aspect of simulation results is that both in endogenous and in exogenous attention, the network reproduces not only response benefits at the attended/cued side but also response detriments at the unattended/uncued location [46] (see also [47], for a review). Detrimental responses at the unattended/uncued side arise from the competitive interaction between the two hemispheres, so that the increased activity in the attended side hemisphere (due to the bias input or to the cue) inhibits activity in the opposite hemisphere.

To sum up, differences in network performances between the two sides (attended versus unattended or cued versus uncued) are mediated by the same mechanisms in both endogenous and exogenous attention. (1) The shift of the working point of the bimodal neuron above or near the threshold of its activation function, induced by the top-down

bias or by the cue application, speeds up the responses to targets on the attended/cued side. This facilitation may be further improved in one modality, by adding a further bias to a unimodal area. (2) The tonic/phasic activation of the inhibitory interneuron on the unattended/uncued side (due, resp., to the contralateral top-down bias or cue application), slows down the responses to targets on that side.

Hence, our study shows that the unimodal and cross-modal effects of orienting attention to one hemisphere both exogenously and endogenously can be explained via a model of cooperative and competitive interactions among unimodal and bimodal areas in the two hemispheres: inter-hemispheric interactions can be biased both by a stimulus-driven or by a top-down mechanism. According to our results, the Biased Competition Hypothesis, proposed in the context of the visual system and successfully explaining several aspects of visual attention, applies also to crossmodal attention, suggesting that a basic mechanism of attention may be replicated at different levels and across multiple areas and multiple sensory modalities in the brain. The novel insight coming from the present results is that spatial attentional orienting acting both at a unimodal level and at a multimodal level seems to necessarily tap onto associative, multisensory brain areas, probably located in the parietal cortex.

The proposed model may be of value to help interpretation of behavioural results on spatial attention and to drive experiments on attention and cross-modal construction of space. Future studies may be devoted to investigate further aspects not considered in the present work, such as the “inhibition of return” effect [48].

## References

- [1] R. Desimone and J. Duncan, “Neural mechanisms of selective visual attention,” *Annual Review of Neuroscience*, vol. 18, pp. 193–222, 1995.
- [2] H. Johansen-Berg and D. M. Lloyd, “The physiology and psychology of selective attention to touch,” *Frontiers in Bioscience*, vol. 5, pp. D894–D904, 2000.
- [3] S. J. Luck, L. Chelazzi, S. A. Hillyard, and R. Desimone, “Neural mechanisms of spatial selective attention in areas V1, V2, and V4 of macaque visual cortex,” *Journal of Neurophysiology*, vol. 77, no. 1, pp. 24–42, 1997.
- [4] H. Pashler, *The Psychology of Attention*, MIT Press, Cambridge, Mass, USA, 1998.
- [5] C. Spence and J. Driver, “Covert spatial orienting in audition: exogenous and endogenous mechanisms,” *Journal of Experimental Psychology*, vol. 20, no. 3, pp. 555–574, 1994.
- [6] G. Deco and E. T. Rolls, “Neurodynamics of biased competition and cooperation for attention: a model with spiking neurons,” *Journal of Neurophysiology*, vol. 94, no. 1, pp. 295–313, 2005.
- [7] J. Duncan, “Coordinated brain systems in selective perception and action,” in *Attention and Performance*, T. Inui and J. L. McClelland, Eds., pp. 549–578, MIT Press, Cambridge, Mass, USA, 1996.
- [8] J. Reynolds, L. Chelazzi, and R. Desimone, “Competitive mechanisms subserve attention in macaque areas V2 and V4,” *The Journal of Neuroscience*, vol. 19, no. 5, pp. 1736–1753, 1999.

- [9] M. Szabo, R. Almeida, G. Deco, and M. Stetter, "Cooperation and biased competition model can explain attentional filtering in the prefrontal cortex," *European Journal of Neuroscience*, vol. 19, no. 7, pp. 1969–1977, 2004.
- [10] J. Theeuwes, "Exogenous and endogenous control of attention: the effects of visual onsets and offsets," *Perception & Psychophysics*, vol. 49, no. 1, pp. 83–90, 1991.
- [11] C. B. Warner, J. F. Juola, and H. Koshino, "Voluntary allocation versus automatic capture of visual attention," *Perception & Psychophysics*, vol. 48, no. 3, pp. 243–251, 1990.
- [12] J. Driver and C. Spence, "Cross-modal links in spatial attention," *Philosophical Transactions of the Royal Society B*, vol. 353, no. 1373, pp. 1319–1331, 1998.
- [13] S. Kennett, M. Eimer, C. Spence, and J. Driver, "Tactile-visual links in exogenous spatial attention under different postures: convergent evidence from psychophysics and ERPs," *Journal of Cognitive Neuroscience*, vol. 13, no. 4, pp. 462–478, 2001.
- [14] J. J. McDonald, W. A. Teder-Sälejärvi, and L. M. Ward, "Multisensory integration and crossmodal attention effects in the human brain," *Science*, vol. 292, no. 5523, p. 1791, 2001.
- [15] C. Spence, J. Driver, and F. Pavani, "Crossmodal links between vision and touch in covert endogenous spatial attention," *Journal of Experimental Psychology*, vol. 26, no. 4, pp. 1298–1319, 2000.
- [16] M. Eimer and J. Driver, "Crossmodal links in endogenous and exogenous spatial attention: evidence from event-related brain potential studies," *Neuroscience and Biobehavioral Reviews*, vol. 25, no. 6, pp. 497–511, 2001.
- [17] M. Eimer and J. van Velzen, "Crossmodal links in spatial attention are mediated by supramodal control processes: evidence from event-related potentials," *Psychophysiology*, vol. 39, no. 4, pp. 437–449, 2002.
- [18] E. Macaluso, C. D. Frith, and J. Driver, "Selective spatial attention in vision and touch: unimodal and multimodal mechanisms revealed by PET," *Journal of Neurophysiology*, vol. 83, no. 5, pp. 3062–3075, 2000.
- [19] E. Macaluso, C. D. Frith, and J. Driver, "Directing attention to locations and to sensory modalities: multiple levels of selective processing revealed with PET," *Cerebral Cortex*, vol. 12, no. 4, pp. 357–368, 2002.
- [20] J.-R. Duhamel, C. L. Colby, and M. E. Goldberg, "Ventral intraparietal area of the macaque: congruent visual and somatic response properties," *Journal of Neurophysiology*, vol. 79, no. 1, pp. 126–136, 1998.
- [21] M. S. Graziano, X. T. Hu, and C. G. Gross, "Visuospatial properties of ventral premotor cortex," *Journal of Neurophysiology*, vol. 77, no. 5, pp. 2268–2292, 1997.
- [22] G. Rizzolatti, C. Scandolara, M. Matelli, and M. Gentilucci, "Afferent properties of periarculate neurons in macaque monkeys. II. Visual responses," *Behavioural Brain Research*, vol. 2, no. 2, pp. 147–163, 1981.
- [23] E. Magosso, M. Zavaglia, A. Serino, G. di Pellegrino, and M. Ursino, "Visuotactile representation of peripersonal space: a neural network study," *Neural Computation*.
- [24] E. Magosso, M. Ursino, G. di Pellegrino, M. Làdavas, and A. Serino, "Neural bases of peri-hand space plasticity through tool-use: insights from a combined computational-experimental approach," *Neuropsychologia*, in press.
- [25] P. Dayan and L. F. Abbott, "Model neurons I: neuroelectronics," in *Theoretical Neuroscience*, pp. 153–194, MIT Press, Cambridge, Mass, USA, 2001.
- [26] E. R. Kandel, J. H. Schwartz, and T. M. Jessell, "The bodily senses," in *Principles of Neural Science*, pp. 430–450, McGraw-Hill, New York, NY, USA, 4th edition, 2000.
- [27] N. Dambeck, R. Sparing, I. G. Meister, et al., "Interhemispheric imbalance during visuospatial attention investigated by unilateral and bilateral TMS over human parietal cortices," *Brain Research*, vol. 1072, no. 1, pp. 194–199, 2006.
- [28] R. Fendrich, J. J. Hutsler, and M. S. Gazzaniga, "Visual and tactile interhemispheric transfer compared with the method of Poffenberger," *Experimental Brain Research*, vol. 158, no. 1, pp. 67–74, 2004.
- [29] L. Battelli, G. A. Alvarez, T. M. Carlson, and A. Pascual-Leone, "The role of the parietal lobe in visual extinction studied with transcranial magnetic stimulation," *Journal of Cognitive Neuroscience*, vol. 21, no. 10, pp. 1946–1955, 2008.
- [30] A. E. Hillis, S. Chang, J. Heidler-Gary, et al., "Neural correlates of modality-specific spatial extinction," *Journal of Cognitive Neuroscience*, vol. 18, no. 11, pp. 1889–1898, 2006.
- [31] J. B. Mattingley, J. Driver, N. Beschin, and I. H. Robertson, "Attentional competition between modalities: extinction between touch and vision after right hemisphere damage," *Neuropsychologia*, vol. 35, no. 6, pp. 867–880, 1997.
- [32] A. Buehlmann and G. Deco, "The neuronal basis of attention: rate versus synchronization modulation," *The Journal of Neuroscience*, vol. 28, no. 30, pp. 7679–7686, 2008.
- [33] G. Deco and E. T. Rolls, "Attention and working memory: a dynamical model of neuronal activity in the prefrontal cortex," *European Journal of Neuroscience*, vol. 18, no. 8, pp. 2374–2390, 2003.
- [34] R. Dowman and D. Ben-Avraham, "An artificial neural network model of orienting attention toward threatening somatosensory stimuli," *Psychophysiology*, vol. 45, no. 2, pp. 229–239, 2008.
- [35] E. Macaluso, C. D. Frith, and J. Driver, "Supramodal effects of covert spatial orienting triggered by visual or tactile events," *Journal of Cognitive Neuroscience*, vol. 14, no. 3, pp. 389–401, 2002.
- [36] E. Macaluso, C. D. Frith, and J. Driver, "Modulation of human visual cortex by crossmodal spatial attention," *Science*, vol. 289, no. 5482, pp. 1206–1208, 2000.
- [37] E. Macaluso and J. Driver, "Multisensory spatial interactions: a window onto functional integration in the human brain," *Trends in Neurosciences*, vol. 28, no. 5, pp. 264–271, 2005.
- [38] J. S. Bloom and G. W. Hynd, "The role of the corpus callosum in interhemispheric transfer of information: excitation or inhibition?" *Neuropsychology Review*, vol. 15, no. 2, pp. 59–71, 2005.
- [39] G. di Pellegrino, E. Làdavas, and A. Farnè, "Seeing where your hands are," *Nature*, vol. 388, no. 6644, p. 730, 1997.
- [40] M. Eimer, A. Maravita, J. van Velzen, M. Husain, and J. Driver, "The electrophysiology of tactile extinction: ERP correlates of unconscious somatosensory processing," *Neuropsychologia*, vol. 40, no. 13, pp. 2438–2447, 2002.
- [41] M. Sarri, F. Blankenburg, and J. Driver, "Neural correlates of crossmodal visual-tactile extinction and of tactile awareness revealed by fMRI in a right-hemisphere stroke patient," *Neuropsychologia*, vol. 44, no. 12, pp. 2398–2410, 2006.
- [42] S. Dehaene and L. Naccache, "Towards a cognitive neuroscience of consciousness: basic evidence and a workspace framework," *Cognition*, vol. 79, no. 1–2, pp. 1–37, 2001.
- [43] M. Kinsbourne, "The mechanism of hemispheric control of the lateral gradient of attention," in *Attention and Performance, Vol. 5*, P. M. A. Rabbit and S. Dornic, Eds., pp. 81–97, Academic Press, London, UK, 1975.
- [44] M. Kinsbourne, "Orientational bias model of unilateral neglect: evidence from attentional gradients within hemispace," in *Unilateral Neglect: Clinical and Experimental Studies*,

- I. H. Robertson and J. C. Marshall, Eds., pp. 63–86, Erlbaum, Hillsdale, NJ, USA, 1993.
- [45] S. Kastner, M. A. Pinsk, P. de Weerd, R. Desimone, and L. G. Ungerleider, “Increased activity in human visual cortex during directed attention in the absence of visual stimulation,” *Neuron*, vol. 22, no. 4, pp. 751–761, 1999.
- [46] C. C. Hilgetag, H. Théoret, and A. Pascual-Leone, “Enhanced visual spatial attention ipsilateral to rTMS-induced ‘virtual lesions’ of human parietal cortex,” *Nature Neuroscience*, vol. 4, no. 9, pp. 953–957, 2001.
- [47] C. Spence, F. Pavani, A. Maravita, and N. Holmes, “Multisensory interactions,” in *Haptic Rendering: Foundations, Algorithms, and Applications*, M. C. Lin and M. A. Otaduy, Eds., pp. 21–25, AK Peters, Wellesley, Mass, USA, 2008.
- [48] C. Spence, D. Lloyd, F. McGlone, M. Nicholls, and J. Driver, “Inhibition of return is supramodal: a demonstration between all possible pairings of vision, touch, and audition,” *Experimental Brain Research*, vol. 134, no. 1, pp. 42–48, 2000.

## Research Article

# Realistic and Spherical Head Modeling for EEG Forward Problem Solution: A Comparative Cortex-Based Analysis

Federica Vatta,<sup>1</sup> Fabio Meneghini,<sup>1</sup> Fabrizio Esposito,<sup>2,3</sup>  
Stefano Mininel,<sup>1</sup> and Francesco Di Salle<sup>3</sup>

<sup>1</sup>DEEI, University of Trieste, Via A. Valerio 10, 34127 Trieste, Italy

<sup>2</sup>Department of Neurological Sciences, University of Naples Federico II, II Policlinico Padiglione 17, Via S. Pansini 5, 80131 Naples, Italy

<sup>3</sup>Department of Cognitive Neuroscience, Maastricht University, P.O. Box 616, 6200 MD Maastricht, The Netherlands

Correspondence should be addressed to Federica Vatta, federica.vatta@deei.units.it

Received 24 June 2009; Revised 20 August 2009; Accepted 9 November 2009

Academic Editor: Fabio Babiloni

Copyright © 2010 Federica Vatta et al. This is an open access article distributed under the Creative Commons Attribution License, which permits unrestricted use, distribution, and reproduction in any medium, provided the original work is properly cited.

The accuracy of forward models for electroencephalography (EEG) partly depends on head tissues geometry and strongly affects the reliability of the source reconstruction process, but it is not yet clear which brain regions are more sensitive to the choice of different model geometry. In this paper we compare different spherical and realistic head modeling techniques in estimating EEG forward solutions from current dipole sources distributed on a standard cortical space reconstructed from Montreal Neurological Institute (MNI) MRI data. Computer simulations are presented for three different four-shell head models, two with realistic geometry, either surface-based (BEM) or volume-based (FDM), and the corresponding sensor-fitted spherical-shaped model. Point Spread Function (PSF) and Lead Field (LF) cross-correlation analyses were performed for 26 symmetric dipole sources to quantitatively assess models' accuracy in EEG source reconstruction. Realistic geometry turns out to be a relevant factor of improvement, particularly important when considering sources placed in the temporal or in the occipital cortex.

## 1. Introduction

Localization of neural brain sources is important in several areas of research of basic neuroscience, such as cortical organization and integration [1], and in some areas of clinical neuroscience such as preoperative planning [2] and epilepsy [3]. Localization of neural brain sources based on electroencephalography (EEG) uses scalp potential data to infer the location of underlying neural activity [1]. This procedure entails with (i) modeling the brain electrical activity, (ii) modeling the head volume conduction process for linking the neural electrical activity to EEG recordings, and (iii) reconstructing the brain electrical activity from recorded EEG data (measured scalp potentials). The first two modeling steps serve to solve the so-called EEG forward problem, which describes the distribution of electric potentials for given source locations, orientations, and signals; the following step is the inverse of the previous ones, thereby it is commonly referred to as the EEG inverse problem solution.

A model of brain electrical activity (in short “source model”) is composed of bioelectric units distributed within the entire brain volume or over specific brain surfaces or confined to a few brain locations. A single source unit is often modeled as a current dipole, which well approximates the synchronized synaptic currents at a columnar level [4]. When confined to the cerebral cortex, the orientation of the current dipoles can be either free or constrained to be perpendicular to the cortical surface [5].

Linking the source model to the physical electromagnetic signals measurable at the sensor locations on the scalp (forward model) requires constructing a volume conductor model that explains the propagation of the currents throughout the human head in terms of geometry and conductivity of this medium. Modeling errors produced by the differences between the actual head and the volume conductor model affect the accuracy of the EEG forward and hence of the inverse problem solution, as the observed scalp potentials are determined not only by the location and strength of

the neural generators but also by the geometry and the conductive properties of the head. Modeling errors include differences in actual head and model shape, skull thickness, and electrical conductivities of the head tissues. This study focuses on the effect of head model geometry on EEG forward solution. Historically, the volume conductor head model assumes that the head consists of a set of three or four concentric homogeneous spherical shells, respectively, representing brain (white and gray matter), cerebrospinal fluid (CSF), skull, and scalp [6]. Sphere-shaped head models are computationally efficient in forward problem formulation and estimation, since they allow using analytical solutions. Of course, they seriously lack in geometrical adherence of the assumed shape with respect to a real human head. The “sensor-fitted sphere” approach fits a multilayer sphere individually to each sensor and has shown to produce some improvement over standard spherical models [7]. More accurate forward solutions become possible by using numerical algorithms, such as the boundary element method (BEM) [8], finite-element method (FEM) [9] and finite difference method (FDM) [10] algorithms. These numerical models allow incorporating the realistic geometry of the head and brain after reconstruction of the anatomical structure from individual or standardized magnetic resonance imaging (MRI) data sets. Previous studies [6–12] have found that a more realistic head model performs better than a less complex, for example, spherical, head model in EEG simulations, since volume currents are more precisely taken into account. More specifically, the BEM approach is able to improve the source reconstruction in comparison with spherical models, particularly in basal brain areas, including the temporal lobe [13], because it gathers a more realistic shape of brain compartments of isotropic and homogeneous conductivities by using closed triangle meshes [14]. The FDM and the FEM allow better accuracy than the BEM because they allow a better representation of the cortical structures, such as sulci and gyri in the brain, in a three-dimensional head model [15].

The effect of head model geometry on the EEG forward solution has been considered in several previous studies [12]. These studies analyzed the differences in EEG forward and inverse problem solution due to different spherical or realistic model geometry [16–18], evaluated the effects of variations in the skull thickness [19–21] or due to different model complexity [11, 15], presenting results for particular cases of head models. In [22] the effect of few millimeters random variations in the realistic head shape on the EEG forward and inverse problems was studied. The localization error when solving the inverse problem with head models from several different individuals was studied by [23, 24]. The effect of the head shape variations on the EEG forward and inverse problems was studied in [25] building a random head model based on a set of 30 deterministic models from adults in comparison with a standard average head model. For a dipolar source model, the effect of the head shape variations on the EEG inverse problem due to the random head model resulted slightly larger than the effect of the electronic noise present in the sensors. With the aim of defining a brain that is more representative of the population, the Montreal Neurological Institute (MNI) defined

a standard brain by using a large series of MRI scans on normal controls. The current standard MNI template is the ICBM152, which is based on the average of 152 normal MRI scans, thus reflecting average neuroanatomy. In this paper we readdress the effect of realistic geometry in head modeling by adopting the MNI standard anatomy as the most typical real geometry, seeking for more general results also extensible to other application studies in this field, given the above specified characteristics of the MNI template. A realistic highly heterogeneous FDM model of the head based on the MNI anatomy has been developed for these purposes, since an FDM captures complex head geometry and accurately describes the boundary conditions of different tissues with unique conductivity values, including skull orifices [11]. The aim of the presented study is to investigate the accuracy in terms of EEG source modeling that can be achieved adopting realistic, either surface-based (BEM) or volume-based (FDM), or spherical geometries in standard head modeling. We present here a detailed computer simulation study in which the performances in terms of accuracy of three different four-shell head models are compared, the realistic MNI-based BEM and FDM and the sensor-fitted spherical-shaped model. As figures of merit for the comparative analysis, the point spread function (PSF) maps and the lead field (LF) correlation coefficients are used. The models used in the present work are noise-free. Although noise modeling is also important in source localization [2], the purpose of the present study is the punctual evaluation of differences that arise from specific anatomically relevant geometrical modeling of the human brain.

## 2. Material and Methods

A realistic-shaped FDM volume conductor model of the head was derived from an averaged T1-weighted MRI dataset, available from the Montreal Neurologic Institute (<http://www.mni.mcgill.ca/>). Segmentation by BrainSuite analysis tool (<http://brainsuite.usc.edu/>) was used to identify the following five tissue types in the head: scalp, skull, cerebrospinal fluid (CSF), gray matter, and white matter (see Figure 1). For the purpose of this comparative study, only four compartments have been set in the model, corresponding to scalp, skull, CSF, and brain (see Figure 1(d)), unifying gray and white matter tissues. In addition to the standard three compartments of scalp, skull, and brain, the CSF layer has been considered as it plays an important role in modifying the scalp potentials and can also influence the inverse source localizations [11]. 62 electrodes positions have been defined evenly spaced over the scalp surface of the realistic head model (see Figure 2). For the comparative study, using the same segmentation results, a four-shell BEM head model has been built [7] with the *BrainStorm* toolkit (<http://neuroimage.usc.edu/brainstorm/>), after resampling each surface mesh from the original tessellation to 1500 vertices. Finally, a spherical head model has been developed, composed of four concentric spheres representing scalp, skull, CSF, and brain (see Figure 3) with the proportions for the radii of the layers of 1:0.95:0.87:0.84. The “sensor-fitted

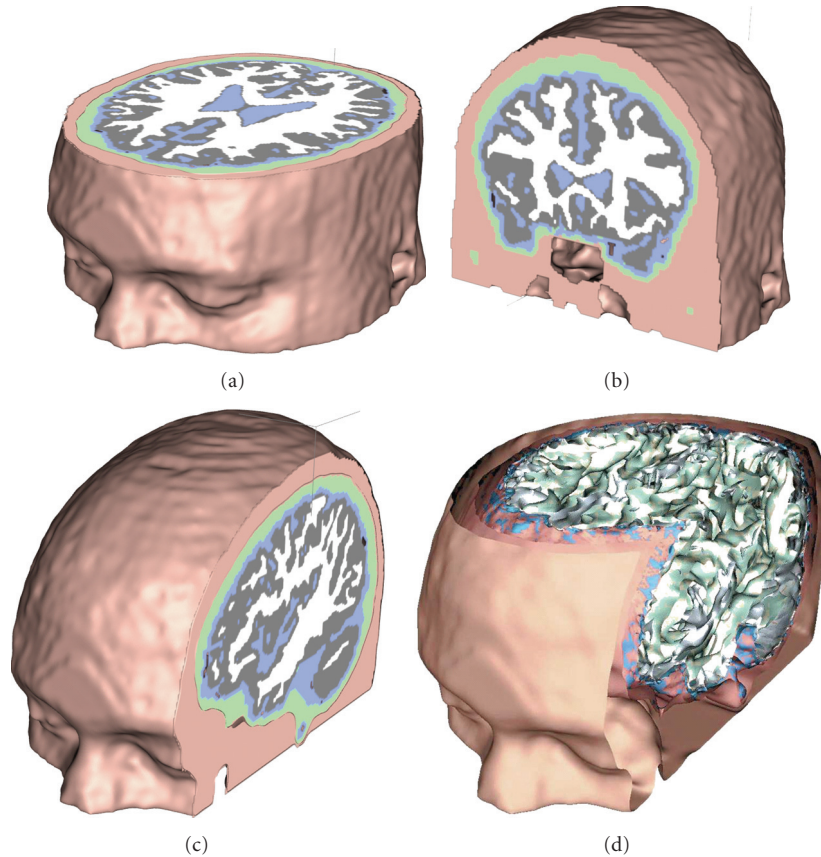


FIGURE 1: (a), (b), and (c): Realistic FDM model based on the MNI anatomy composed by four compartments representing scalp (pink), skull (green), CSF (blue), and brain, given by fusion of grey matter and white matter. (d): The complete 3D model, with rendered surfaces.

sphere” approach has been followed [7], according to which the multilayer sphere is fitted individually to each sensor. The conductivity values assigned to the compartments of all the analyzed models were 0.33 S/m for the scalp, 0.0042 S/m for the skull, 1.79 S/m for the CSF, and 0.33 S/m for the brain [26]. The brain cortex mesh was reconstructed from gray matter segmentation and used as space for placing the sources (see Figure 2). The head surface mesh was reconstructed from the unsegmented MNI images and used for placing the 62 EEG electrodes.

The sources used for the simulation study are shown in Figure 4. In detail, 5000 evenly spaced points on the brain cortex mesh were initially considered as possible source positions while 26 “true” source positions have been placed in specific vertices of this mesh. The 26 source positions have been selected in order to achieve a rather uniform spatial sampling of the source space, with the aim of investigating the main differences that can be observed in terms of source reconstruction for the various cortical regions in the spherically approximated and in the two different superficial- and volume-based realistic models. For each source position, three single dipole sources have been placed, oriented parallel to the  $x$ ,  $y$ , or  $z$  orthogonal Cartesian axes according to the “Talairach” coordinate system, since a source with generic orientation can be always decomposed in its components

along the coordinate axes [6]. The study was performed using the numerical FDM for EEG forward problem solution presented in [10], the Galerkin BEM with linear basis algorithm described in [7] for BEM, and analytic calculations for the spherical model [7].

The lead fields of dipoles at the 5000 positions on the cortex mesh were computed and stored for the 62 electrode scalp positions. This procedure has been repeated for each source orientation ( $x$ ,  $y$ , and  $z$ ) for the same source position, for the realistic BEM and FDM models, and for the sensor-fitted spherical model. Hence, nine leadfield matrices of  $62 \times 5000$  elements were obtained [14], in which each column vector gives the leadfield potentials at the 62 electrodes for each of the 5000 sources in the cortex mesh. Due to the linearity of both the forward and inverse problems, a measure of the estimation error can be obtained by means of the “point spread function” (PSF) [27–29]. The PSF can be calculated, for each source location and orientation, by computing the sensitivity of the estimate at a location  $j$  to activity at location  $i$ , after estimating the correlation coefficient between the corresponding column vectors of the leadfield matrices. This procedure, when repeated for each of the 5000 points of the source space in the cortical mesh, leads to the definition of a PSF map for each active source and each orientation; thus, we obtained 78 PSF maps for each model.

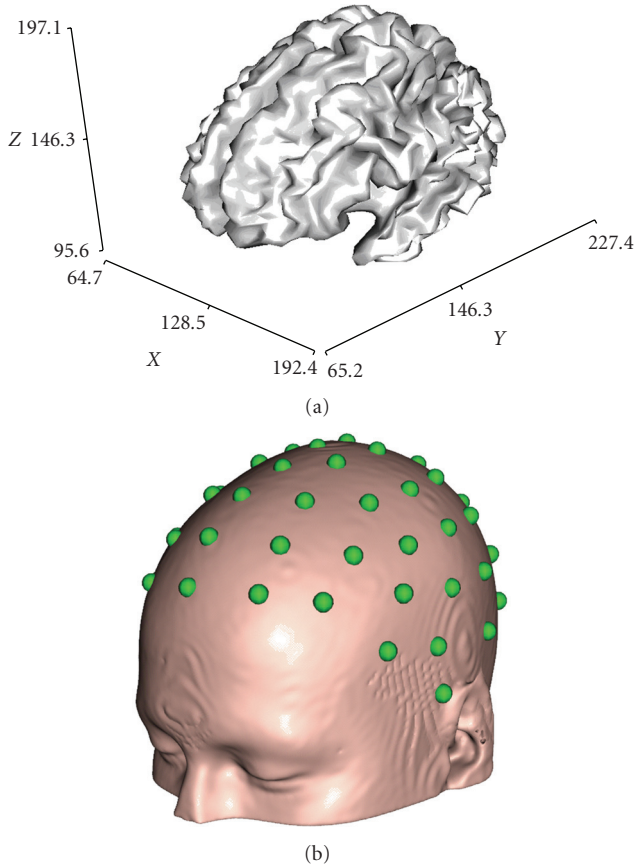


FIGURE 2: (a): Brain cortex mesh, representing the source space and (b): Scalp surface with spheres indicating the electrodes positions on scalp.

Given its definition, the PSF function specifies a measure of the spatial blurring of the true activity at any given source position. Therefore, a location with lower PSF is expected to have a smaller spatial extent and higher estimation accuracy. A root mean squared (RMS) superimposition of the effects given by the three source orientations has then been computed, in order to gather a broader vision of the PSF behavior. In order to quantify the differences for the head models considered for each specified source, a measure of the full width at half maximum (FWHM) for the PSF function has also been estimated for each source for both the realistic and the spherical models.

### 3. Results

The PSF maps on the cortex mesh have been computed for each source location and orientation for a total of 78 PSF maps for the realistic and the spherical head models. The visual inspection of the PSF maps allowed a qualitative evaluation of the spatial blurring of the true activity at the considered source position for the specific head model. The obtained results showed in many cases marked differences between the realistic and the sensor-fitted spherical models when applied to the same source space (cortex) and generally

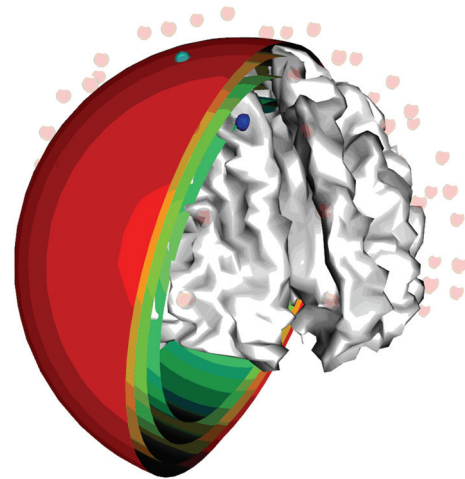


FIGURE 3: Sensor-fitted 4-shells concentric-spheres model; blue dot: active cortical source; green dot: sensor to which the model is fitted.

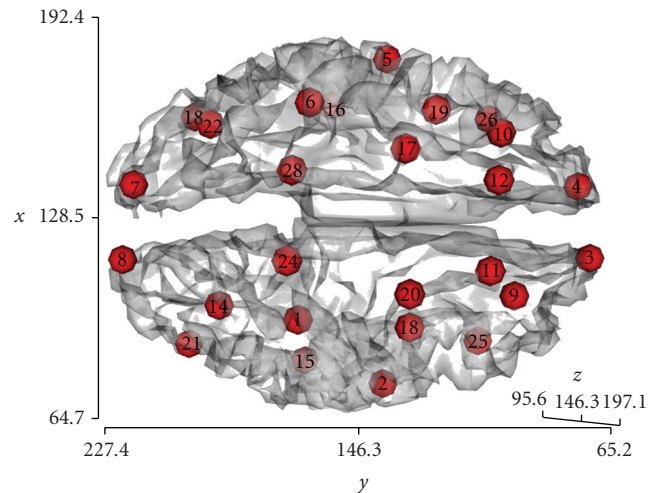


FIGURE 4: The simulated 26 cortical sources in the Talairach coordinate system.

indicated the presence of a more pronounced spatial blurring for the latter model, as evidenced by a broader extent of higher PSF values, with respect to the same source in the realistic BEM and FDM models. Figure 5 shows an example of the results obtained for source 2, placed in the temporal region and  $x$ -oriented. The PSF maps in the three models indicate the presence of a more pronounced spatial blurring for the sensor-fitted spherical model, evidenced by a broader extent of higher PSF values in the figure, with respect to the same source in the realistic BEM and in the FDM models.

To quantitatively compare, for the different head models, the spatial characteristics of the PSF maps at any given source position, and hence their power of discrimination for the EEG source reconstruction, the mean and minimum values of the obtained PSFs have been reported and compared for all the 78 analyzed dipole sources, being 1 the maximum PSF value in each condition, for the realistic BEM and FDM and the sensor-fitted spherical models. Tables 1 and 2 summarize

the quantitative results of the performed analysis on the PSF maps. A closer inspection of the PSF values presented in Tables 1 and 2 indicates that the reported mean PSF values are larger in the realistic BEM than in the FDM model in 79% of the total tested conditions (62 cases over 78), and specifically in 50%, 88%, and 100% of the analyzed situations for the  $x$ -,  $y$ -, and  $z$ -oriented sources, respectively (i.e., 13, 23, and 26 cases over 26, resp.), rising up to 100% for the RMS superimposition of the effects given by the three source orientations. The minimum PSF values result larger in the BEM with respect to the FDM model in 27% of the tested conditions (21 cases over 78), in the 0%, 4%, and 77% of cases for the  $x$ -,  $y$ -, and  $z$ -oriented sources, respectively, rising up to 85% for the RMS data. The spherical head model (SPH) presents larger mean PSF values with respect to both the realistic BEM, and FDM models, for 60% (BEM) and 92% (FDM) of the total tested conditions (47 and 72 cases over 78, resp.), with minimum PSF values larger in 97% and 85% of the total conditions (76 and 66 cases over 78, resp.). The analysis of the RMS superimposition of the effects given by the three source orientations indicates that the spherical model shows larger mean PSF values in 85% of the tested conditions with respect to the BEM model, rising up to 96% for the FDM; the minimum PSF values result larger in 96% of the tested conditions for the BEM model and in 54% for the FDM. For  $x$ -oriented sources the spherical model shows larger mean and minimum PSF values in 96% and 100% of the tested conditions, respectively, for both the BEM and the FDM models. The  $y$ -oriented sources show a similar behavior with larger mean and minimum PSF values for the spherical model in 85% and 100% of the tested conditions with respect to BEM, and in 92% and 54% with respect to FDM. For  $z$ -oriented sources, the minimum PSF values result larger for the spherical model in 92% (BEM) and 100% (FDM) of the tested conditions. Conversely, the  $z$ -oriented sources present smaller mean PSF values for the spherical model in comparison with the BEM in all the 26 tested conditions, while for the FDM this situation shows up only for 3 cases out of 26, thus giving larger mean PSF values for the spherical model with respect to FDM in 88% of the tested conditions. The evaluation of the mean  $\pm$  SD values of the reported mean PSF values for the three models analyzed, listed in Table 1, confirmed these trends for the three source orientations and for the RMS data. The data from all the analyzed samples (FDM, BEM and SPH) resulted normally distributed and nine two-tailed paired  $t$ -tests have been performed to investigate differences between the spherical and the realistic models, that is, FDM versus BEM, FDM versus SPH and BEM versus SPH for the three source orientations. Statistically significant differences have been found in the mean PSF values in 7 cases out of the total 9: for all source orientations for both BEM versus SPH ( $x: p = 6.43 \times 10^{-7}$ ;  $y: p = 1.90 \times 10^{-5}$ ;  $z: p = 9.45 \times 10^{-8}$ ) and FDM versus SPH ( $x: p = 1.25 \times 10^{-10}$ ;  $y: p = 6.74 \times 10^{-8}$ ;  $z: p = 3.13 \times 10^{-4}$ ) and for the  $z$ -oriented sources ( $p = 3.23 \times 10^{-13}$ ) in FDM versus BEM. No statistically significant differences have been found in 2 cases, that is, for the  $x$ -oriented ( $p = 0.70$ ) and for the  $y$ -oriented sources ( $p = 0.28$ ) in FDM versus BEM.

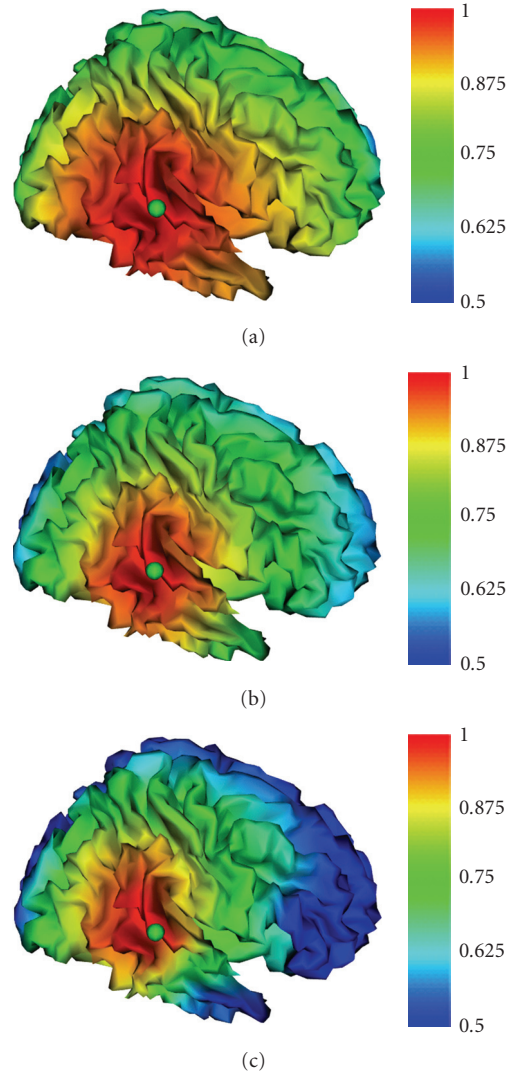


FIGURE 5: PSF maps obtained for source 2 placed in the temporal region, for the  $x$ -oriented source, in the Talairach coordinate system: (a) sensor-fitted spherical model; (b) BEM model; (c) FDM model.

The analysis on the minimum PSF data led to similar results, with 7 cases of significant differences out of the total 9: for all source orientations in BEM versus SPH ( $x: p = 1.43 \times 10^{-13}$ ;  $y: p = 9.55 \times 10^{-11}$ ;  $z: p = 2.17 \times 10^{-8}$ ), for the  $x$ -oriented ( $p = 2.35 \times 10^{-6}$ ) and the  $z$ -oriented sources ( $p = 2.02 \times 10^{-9}$ ) in FDM versus SPH ( $y$ -oriented sources:  $p = 0.29$ ), and for the  $x$ -oriented ( $p = 1.49 \times 10^{-12}$ ) and the  $y$ -oriented sources ( $p = 3.49 \times 10^{-9}$ ) in FDM versus BEM ( $z$ -oriented sources:  $p = 0.08$ ). The RMS data showed significant differences in both FDM versus BEM and FDM versus SPH for either the mean (FDM versus BEM:  $p = 1.90 \times 10^{-10}$ ; FDM versus SPH:  $p = 1.90 \times 10^{-11}$ ) and the minimum PSF values (FDM versus BEM:  $p = 8.34 \times 10^{-5}$ ; FDM versus SPH:  $p = 4.71 \times 10^{-7}$ ).

Following spatial smoothing, the quantitative evaluation of the PSF maps has been conducted by plotting, for each of the 78 analyzed sources, the obtained PSF values as function

TABLE 1: Summary of the mean PSF values for the realistic (BEM and FDM) and the sensor-fitted spherical (SPH) models, for sources 1÷26 parallel to  $x$ ,  $y$ , and  $z$  orientations and for the RMS maps.

|      | Mean PSF |        |        |        |        |        |        |        |        |        |        |        |
|------|----------|--------|--------|--------|--------|--------|--------|--------|--------|--------|--------|--------|
|      | $x$      |        |        | $y$    |        |        | $z$    |        |        | RMS    |        |        |
|      | FDM      | BEM    | SPH    | FDM    | BEM    | SPH    | FDM    | BEM    | SPH    | FDM    | BEM    | SPH    |
| 1    | 0.76     | 0.74   | 0.82   | 0.74   | 0.76   | 0.83   | 0.65   | 0.75   | 0.71   | 0.71   | 0.75   | 0.79   |
| 2    | 0.66     | 0.67   | 0.75   | 0.61   | 0.64   | 0.78   | 0.52   | 0.77   | 0.65   | 0.58   | 0.70   | 0.73   |
| 3    | 0.57     | 0.66   | 0.69   | 0.55   | 0.57   | 0.46   | 0.46   | 0.80   | 0.49   | 0.48   | 0.69   | 0.56   |
| 4    | 0.51     | 0.61   | 0.46   | 0.55   | 0.56   | 0.44   | 0.52   | 0.78   | 0.35   | 0.47   | 0.66   | 0.42   |
| 5    | 0.67     | 0.71   | 0.77   | 0.64   | 0.71   | 0.8    | 0.55   | 0.80   | 0.65   | 0.60   | 0.74   | 0.74   |
| 6    | 0.75     | 0.74   | 0.8    | 0.74   | 0.74   | 0.82   | 0.64   | 0.77   | 0.7    | 0.70   | 0.75   | 0.78   |
| 7    | 0.6      | 0.57   | 0.66   | 0.58   | 0.63   | 0.62   | 0.52   | 0.69   | 0.44   | 0.56   | 0.64   | 0.58   |
| 8    | 0.61     | 0.56   | 0.74   | 0.55   | 0.62   | 0.68   | 0.56   | 0.70   | 0.53   | 0.57   | 0.63   | 0.66   |
| 9    | 0.7      | 0.73   | 0.8    | 0.65   | 0.65   | 0.81   | 0.61   | 0.78   | 0.68   | 0.64   | 0.72   | 0.77   |
| 10   | 0.72     | 0.71   | 0.81   | 0.66   | 0.69   | 0.81   | 0.59   | 0.81   | 0.7    | 0.64   | 0.74   | 0.78   |
| 11   | 0.77     | 0.75   | 0.8    | 0.75   | 0.76   | 0.83   | 0.65   | 0.79   | 0.69   | 0.71   | 0.77   | 0.78   |
| 12   | 0.76     | 0.73   | 0.79   | 0.72   | 0.74   | 0.81   | 0.6    | 0.81   | 0.66   | 0.70   | 0.76   | 0.76   |
| 13   | 0.74     | 0.72   | 0.83   | 0.69   | 0.72   | 0.83   | 0.66   | 0.81   | 0.73   | 0.69   | 0.75   | 0.80   |
| 14   | 0.75     | 0.69   | 0.83   | 0.7    | 0.72   | 0.83   | 0.66   | 0.78   | 0.73   | 0.69   | 0.74   | 0.80   |
| 15   | 0.76     | 0.72   | 0.82   | 0.73   | 0.74   | 0.84   | 0.66   | 0.78   | 0.72   | 0.70   | 0.75   | 0.80   |
| 16   | 0.76     | 0.76   | 0.83   | 0.74   | 0.77   | 0.85   | 0.66   | 0.83   | 0.73   | 0.70   | 0.79   | 0.81   |
| 17   | 0.63     | 0.72   | 0.77   | 0.7    | 0.54   | 0.83   | 0.47   | 0.81   | 0.63   | 0.58   | 0.70   | 0.75   |
| 18   | 0.68     | 0.74   | 0.78   | 0.7    | 0.57   | 0.83   | 0.53   | 0.81   | 0.67   | 0.62   | 0.72   | 0.76   |
| 19   | 0.74     | 0.74   | 0.82   | 0.73   | 0.75   | 0.83   | 0.66   | 0.82   | 0.71   | 0.70   | 0.77   | 0.79   |
| 20   | 0.74     | 0.75   | 0.8    | 0.72   | 0.71   | 0.82   | 0.64   | 0.74   | 0.68   | 0.69   | 0.73   | 0.77   |
| 21   | 0.72     | 0.68   | 0.8    | 0.65   | 0.70   | 0.82   | 0.63   | 0.80   | 0.68   | 0.65   | 0.73   | 0.77   |
| 22   | 0.72     | 0.72   | 0.82   | 0.68   | 0.70   | 0.83   | 0.63   | 0.80   | 0.69   | 0.66   | 0.75   | 0.79   |
| 23   | 0.75     | 0.72   | 0.83   | 0.71   | 0.74   | 0.84   | 0.65   | 0.79   | 0.74   | 0.68   | 0.76   | 0.80   |
| 24   | 0.73     | 0.66   | 0.82   | 0.73   | 0.74   | 0.83   | 0.63   | 0.77   | 0.73   | 0.68   | 0.73   | 0.80   |
| 25   | 0.64     | 0.70   | 0.77   | 0.64   | 0.64   | 0.76   | 0.57   | 0.70   | 0.62   | 0.59   | 0.68   | 0.73   |
| 26   | 0.6      | 0.64   | 0.72   | 0.59   | 0.65   | 0.64   | 0.52   | 0.77   | 0.55   | 0.55   | 0.69   | 0.64   |
| Mean | 0.69     | 0.70   | 0.77   | 0.67   | 0.68   | 0.77   | 0.59   | 0.78   | 0.65   | 0.64   | 0.72   | 0.74   |
| ± SD | ± 0.07   | ± 0.05 | ± 0.08 | ± 0.07 | ± 0.07 | ± 0.11 | ± 0.06 | ± 0.04 | ± 0.10 | ± 0.07 | ± 0.04 | ± 0.09 |

of the distance from the source position and fitting the map values with the corresponding best-fitting Gaussian-like function (biexponential Gaussian), as shown in Figure 6. The spatial extent of the PSF function, measured in mm, has been quantified by means of its full width at half maximum (FWHM) measure. The obtained PSF FWHMs have been reported and compared for all the 26 analyzed dipole sources for each source orientation, for the realistic BEM and FDM and the sensor-fitted spherical models. Table 3 summarizes the quantitative results of the performed analysis on the PSF maps. Basing upon a closer inspection of the PSF FWHM results presented in Table 3, it can be observed that the realistic FDM model presents an improvement over BEM in 68% of the total tested conditions (53 cases over 78), and specifically in 54% of the  $x$ -oriented sources (14 cases over 26), in 81% and 69% for the  $y$ - and  $z$ -oriented sources,

respectively (21 and 18 cases over 26, resp.), and in 38% of the RMS (10 over 26). The realistic BEM presents an improvement over the spherical model in 62% of the total tested conditions (48 cases over 78), in 77%, 73%, 35%, and 77% of the situations for the  $x$ -,  $y$ -, and  $z$ -oriented sources and RMS, respectively. The improvement of FDM over the spherical model shows up in 88% of the analyzed situations for all the three source orientations, and in the 66% for the RMS. These trends are also confirmed by the mean  $\pm$  SD values of the reported PSF FWHM results for the three models, shown in Table 3. Nine two-tailed paired  $t$ -tests have been performed to investigate differences between the spherical and the realistic models (pairs FDM versus BEM, FDM versus SPH, and BEM versus SPH) for the three source orientations. Statistically significant differences have been found in 7 out of the total 9 cases analyzed: for all

TABLE 2: Summary of the minimum PSF values for the realistic (BEM and FDM) and the sensor-fitted spherical (SPH) models, for sources 1÷26 parallel to  $x$ ,  $y$  and  $z$  orientations and for the RMS maps.

|      | Min PSF |        |        |        |        |        |        |        |        |        |        |        |
|------|---------|--------|--------|--------|--------|--------|--------|--------|--------|--------|--------|--------|
|      | $x$     |        |        | $y$    |        |        | $z$    |        |        | RMS    |        |        |
|      | FDM     | BEM    | SPH    | FDM    | BEM    | SPH    | FDM    | BEM    | SPH    | FDM    | BEM    | SPH    |
| 1    | 0.4     | 0.12   | 0.42   | 0.38   | 0.13   | 0.28   | -0.16  | 0.10   | 0.2    | 0.34   | 0.38   | 0.32   |
| 2    | 0.26    | 0.06   | 0.3    | 0.23   | -0.03  | 0.29   | 0      | 0.06   | 0.17   | 0.25   | 0.33   | 0.27   |
| 3    | 0.23    | -0.03  | 0.31   | 0.11   | -0.33  | 0.06   | -0.24  | -0.22  | -0.07  | 0.15   | 0.37   | 0.18   |
| 4    | 0.21    | 0.10   | 0.23   | 0.11   | -0.17  | 0.08   | -0.26  | -0.38  | -0.11  | 0.16   | 0.37   | 0.16   |
| 5    | 0.27    | -0.24  | 0.3    | 0.23   | 0.11   | 0.16   | -0.26  | -0.21  | 0.14   | 0.27   | 0.44   | 0.27   |
| 6    | 0.37    | 0.09   | 0.39   | 0.37   | 0.06   | 0.24   | -0.28  | -0.03  | 0.18   | 0.36   | 0.33   | 0.30   |
| 7    | 0.23    | -0.08  | 0.24   | 0.17   | -0.21  | -0.02  | -0.12  | -0.10  | -0.11  | 0.21   | 0.25   | 0.15   |
| 8    | 0.23    | 0.08   | 0.28   | 0.14   | -0.15  | 0.06   | -0.14  | -0.06  | -0.07  | 0.23   | 0.22   | 0.17   |
| 9    | 0.32    | -0.06  | 0.42   | 0.09   | -0.21  | 0.38   | 0.02   | -0.09  | 0.09   | 0.28   | 0.38   | 0.33   |
| 10   | 0.36    | 0.16   | 0.43   | 0.11   | 0.10   | 0.38   | -0.22  | -0.20  | 0.13   | 0.25   | 0.40   | 0.34   |
| 11   | 0.38    | 0.08   | 0.46   | 0.32   | 0.08   | 0.39   | -0.09  | 0.07   | 0.14   | 0.31   | 0.43   | 0.37   |
| 12   | 0.44    | 0.12   | 0.44   | 0.26   | 0.14   | 0.38   | -0.32  | -0.06  | 0.13   | 0.28   | 0.37   | 0.35   |
| 13   | 0.31    | -0.09  | 0.37   | 0.23   | -0.15  | 0.22   | -0.16  | -0.10  | 0.13   | 0.29   | 0.32   | 0.27   |
| 14   | 0.33    | 0.12   | 0.38   | 0.23   | -0.05  | 0.23   | -0.06  | 0.05   | 0.15   | 0.31   | 0.30   | 0.27   |
| 15   | 0.35    | 0.12   | 0.39   | 0.31   | 0.10   | 0.26   | -0.01  | 0.10   | 0.19   | 0.34   | 0.37   | 0.30   |
| 16   | 0.38    | -0.03  | 0.38   | 0.33   | 0.00   | 0.26   | -0.4   | -0.11  | 0.19   | 0.36   | 0.37   | 0.31   |
| 17   | 0.31    | 0.06   | 0.32   | 0.27   | -0.14  | 0.28   | -0.11  | -0.31  | 0.18   | 0.31   | 0.42   | 0.29   |
| 18   | 0.32    | -0.08  | 0.34   | 0.33   | -0.32  | 0.3    | -0.02  | -0.03  | 0.22   | 0.28   | 0.41   | 0.30   |
| 19   | 0.4     | 0.11   | 0.39   | 0.31   | 0.17   | 0.36   | -0.28  | -0.11  | 0.18   | 0.33   | 0.39   | 0.34   |
| 20   | 0.34    | 0.02   | 0.4    | 0.29   | -0.03  | 0.36   | 0.02   | 0.11   | 0.14   | 0.32   | 0.37   | 0.35   |
| 21   | 0.29    | 0.14   | 0.34   | 0.08   | -0.09  | 0.28   | -0.06  | -0.05  | 0.13   | 0.29   | 0.28   | 0.27   |
| 22   | 0.3     | -0.23  | 0.35   | 0.15   | -0.26  | 0.19   | -0.08  | -0.21  | 0.12   | 0.28   | 0.37   | 0.28   |
| 23   | 0.39    | 0.06   | 0.39   | 0.23   | -0.07  | 0.22   | -0.26  | -0.04  | 0.16   | 0.34   | 0.29   | 0.27   |
| 24   | 0.34    | 0.20   | 0.39   | 0.32   | -0.02  | 0.18   | -0.17  | 0.04   | 0.15   | 0.33   | 0.25   | 0.26   |
| 25   | 0.24    | -0.12  | 0.39   | 0.11   | -0.18  | 0.34   | -0.01  | -0.40  | 0.05   | 0.25   | 0.35   | 0.30   |
| 26   | 0.27    | 0.17   | 0.35   | -0.05  | 0.14   | 0.23   | -0.33  | -0.31  | 0      | 0.21   | 0.37   | 0.24   |
| Mean | 0.32    | 0.03   | 0.36   | 0.22   | -0.05  | 0.25   | -0.15  | -0.10  | 0.11   | 0.28   | 0.35   | 0.28   |
| ± SD | ± 0.06  | ± 0.12 | ± 0.06 | ± 0.11 | ± 0.15 | ± 0.11 | ± 0.12 | ± 0.15 | ± 0.10 | ± 0.06 | ± 0.06 | ± 0.06 |

source orientations in FDM versus SPH ( $x: p = 2.03 \times 10^{-6}$ ;  $y: p = 1.98 \times 10^{-4}$ ;  $z: p = 1.93 \times 10^{-3}$ ), for the  $y$ - and  $z$ -oriented sources in FDM versus BEM ( $y: p = 1.69 \times 10^{-3}$ ;  $z: p = 3.66 \times 10^{-4}$ ), and for the  $x$ - and  $y$ -oriented sources in BEM versus SPH ( $x: p = 1.67 \times 10^{-2}$ ;  $y: p = 2.83 \times 10^{-2}$ ). The two-tailed paired  $t$ -tests performed on the RMS results showed significant differences in the FDM versus SPH pair ( $p = 1.36 \times 10^{-2}$ ) and nonsignificant differences in the FDM versus BEM ( $p = 0.91$ ) and in the BEM versus SPH ( $p = 5.63 \times 10^{-2}$ ). In order to gather a broader evaluation of the PSF behavior on the overall brain cortex, we extended the evaluation of the FWHM PSF to all the 5000 points of the cortex surface. Figure 7 shows the differences between the FWHM RMS PSF maps between couples of different head models, to investigate the principal benefits or pitfalls given by the adoption of the different head models.

#### 4. Discussion

The dissimilarities between the forward fields simulated for the spherically approximated and the two different superficial- and volume-based realistic models have been investigated on a standard real cortex geometry by means of analysis of the lead fields. The Point Spread Function (PSF) has then been used to quantify the amount of spatial blurring of simulated cortical activity effects. The reported PSF values generally indicate a smaller extent, and hence a clear improvement, for the FDM realistic model in comparison with the BEM, and of the BEM model in comparison with the sensor-fitted spherical model (see Figures 5 and 7 and Tables 1–3). This can be better observed analyzing the mean  $\pm$  SD values of the reported PSF FWHM results for the three models, for which a clear trend in this sense can be

TABLE 3: Summary of the FWHM PSF values for the realistic (BEM and FDM) and the sensor-fitted spherical (SPH) models, for sources 1÷26 parallel to x, y and z orientations and for the RMS maps.

|      | FWHM  |        |        |       |        |        |        |        |       |       |        |        |
|------|-------|--------|--------|-------|--------|--------|--------|--------|-------|-------|--------|--------|
|      | x     |        |        | y     |        |        | z      |        |       | RMS   |        |        |
|      | FDM   | BEM    | SPH    | FDM   | BEM    | SPH    | FDM    | BEM    | SPH   | FDM   | BEM    | SPH    |
| 1    | 66.3  | 57.7   | 75.7   | 55    | 73.7   | 80     | 73.1   | 61.8   | 71.6  | 72.23 | 61.38  | 68.81  |
| 2    | 68.2  | 54.1   | 81.1   | 59    | 76.8   | 82.4   | 61.2   | 81.1   | 80.2  | 62.20 | 54.62  | 80.19  |
| 3    | 65    | 97.6   | 97.6   | 77.2  | 70.3   | 54.8   | 92.5   | 114.4  | 73.9  | 69.90 | 100.41 | 66.67  |
| 4    | 60.1  | 87.5   | 41.9   | 81.5  | 72.1   | 40.4   | 105.7  | 109.3  | 54.5  | 72.49 | 78.09  | 46.02  |
| 5    | 63    | 77.5   | 78.4   | 58.7  | 77.6   | 79.4   | 57.3   | 83.0   | 73.8  | 57.89 | 78.81  | 77.27  |
| 6    | 70.4  | 59.9   | 70.3   | 59.5  | 78.7   | 69.9   | 61.6   | 54.1   | 73.3  | 65.92 | 62.26  | 67.84  |
| 7    | 67.4  | 57.4   | 71.3   | 75.4  | 91.5   | 79.6   | 60.3   | 63.6   | 63.4  | 69.29 | 65.59  | 68.98  |
| 8    | 68.5  | 61.9   | 95.3   | 68.8  | 90.5   | 85.8   | 66.7   | 60.0   | 86.2  | 84.33 | 63.71  | 77.90  |
| 9    | 71.8  | 89.0   | 77.7   | 83.2  | 85.3   | 99.6   | 64.1   | 76.8   | 87.2  | 85.64 | 71.69  | 80.72  |
| 10   | 68.3  | 86.6   | 80.7   | 72.5  | 84.0   | 96.1   | 67.5   | 90.3   | 80.1  | 83.16 | 73.22  | 82.23  |
| 11   | 70.5  | 71.4   | 64.5   | 75.2  | 78.5   | 88.5   | 66.9   | 82.4   | 75.7  | 77.09 | 69.65  | 69.81  |
| 12   | 65    | 79.6   | 68.6   | 75.3  | 79.3   | 91.3   | 61.8   | 60.9   | 76.8  | 77.88 | 71.24  | 66.83  |
| 13   | 72.2  | 49.6   | 90.6   | 66.9  | 76.0   | 100.4  | 63.2   | 90.3   | 86.9  | 68.47 | 86.60  | 94.13  |
| 14   | 74.1  | 58.9   | 89.5   | 66.1  | 83.2   | 99.0   | 68.3   | 59.4   | 85.6  | 81.90 | 61.44  | 91.65  |
| 15   | 72.1  | 58.4   | 82.5   | 63    | 78.3   | 87.1   | 70.5   | 63.1   | 77.8  | 78.16 | 61.56  | 81.94  |
| 16   | 67.8  | 62.0   | 76.5   | 60.2  | 78.4   | 77.5   | 58.1   | 77.6   | 73.2  | 75.18 | 63.60  | 76.06  |
| 17   | 50.9  | 89.3   | 78.9   | 62.7  | 33.7   | 68.5   | 63     | 84.0   | 74.2  | 51.55 | 82.72  | 67.74  |
| 18   | 60.2  | 74.4   | 75.1   | 58.4  | 70.1   | 79.3   | 58.2   | 77.6   | 73.7  | 56.99 | 74.41  | 75.06  |
| 19   | 58.3  | 67.2   | 79.4   | 70.3  | 75.9   | 82.1   | 60.4   | 78.8   | 74.3  | 63.52 | 77.17  | 78.88  |
| 20   | 64.6  | 78.8   | 80     | 71.2  | 77.1   | 81.6   | 65.8   | 78.5   | 76.2  | 76.17 | 72.64  | 79.15  |
| 21   | 73.7  | 64.0   | 89.7   | 64.1  | 86.2   | 98.7   | 68.7   | 89.9   | 83.4  | 68.56 | 60.98  | 88.92  |
| 22   | 71.8  | 52.5   | 87.6   | 66.8  | 85.6   | 95.2   | 58.4   | 87.7   | 82    | 67.03 | 85.39  | 87.55  |
| 23   | 71.1  | 58.8   | 85.6   | 65.9  | 80.1   | 95.6   | 69.6   | 86.1   | 84    | 79.21 | 63.48  | 89.28  |
| 24   | 69.2  | 79.1   | 88.2   | 71.4  | 81.9   | 98.3   | 66.1   | 58.2   | 84.6  | 69.02 | 63.07  | 88.12  |
| 25   | 69.1  | 92.1   | 96.3   | 79.5  | 66.8   | 81.5   | 71.2   | 69.4   | 81    | 69.41 | 73.55  | 93.01  |
| 26   | 62.0  | 79.0   | 89.3   | 68.1  | 66.1   | 63.7   | 60.4   | 97.2   | 76.5  | 61.55 | 76.10  | 73.57  |
| Mean | 67.0  | 70.9   | 80.5   | 68.3  | 76.8   | 82.9   | 66.9   | 78.3   | 77.3  | 71.0  | 71.3   | 77.6   |
| ± SD | ± 5.4 | ± 14.0 | ± 11.7 | ± 7.7 | ± 10.9 | ± 14.6 | ± 10.6 | ± 15.6 | ± 7.4 | ± 8.8 | ± 10.3 | ± 10.8 |

observed for the  $x$ - and  $y$ -oriented sources, a slight worsening can be observed for the  $z$ -oriented sources in BEM versus SPH accompanied by an improvement in both FDM versus BEM and FDM versus SPH, and a slight improvement in FDM versus BEM for the RMS data, accompanied by an improvement of both FDM and BEM versus SPH. This trend in FDM versus BEM is reported also by the mean PSF values that are larger in the realistic BEM than in the FDM model in most of the total tested conditions for the separate source orientations, rising up to totality for the RMS superimposition of the effects given by the three source orientations. This situation is accompanied by generally lower minimum PSF values for the BEM with the three separate source orientations but not for the RMS data, leading in general to smaller PSF FWHMs for FDM versus BEM with the separate source orientations, inferring a lower

spatial blurring effect for FDM with respect to BEM; for the RMS superimposition of the effects given by the three source orientations the PSF FWHMs result rather similar, as indicated also by the presence of statistical significant differences in FDM versus BEM for the only  $y$ - and  $z$ -oriented sources. The resulting trend in SPH versus BEM and versus FDM is also confirmed by the larger mean and minimum PSF values presented by the spherical head model with respect to both the realistic BEM and FDM in most of the total tested conditions for the separate three source orientations and for the RMS superimposition of the effects, with the exception of smaller mean PSF values for the spherical model than for the BEM for the  $z$ -oriented sources. The exception behavior observed for the  $z$ -oriented sources is reflected also by their PSF FWHMs, with an improvement of the realistic BEM over the spherical model in only 35%

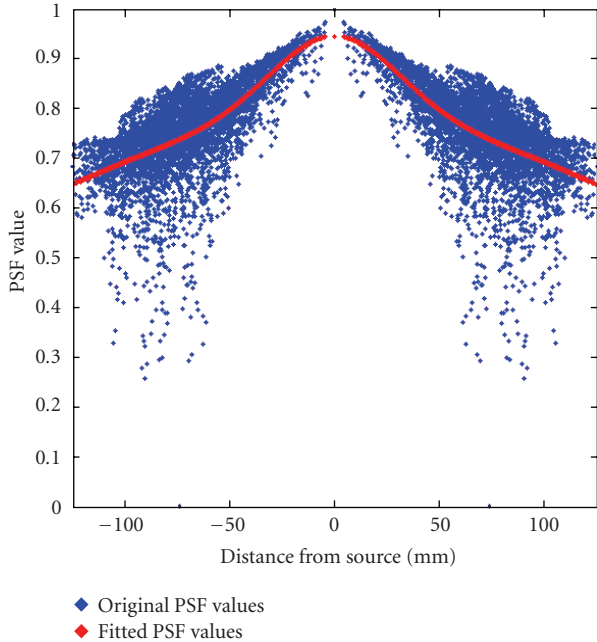


FIGURE 6: Example of PSF values distribution versus distance from source, and fitting with biexponential Gaussian curve.

of the tested situations and by the presence of statistical significant differences for all source orientations and for the RMS values in the pair FDM versus SPH and for only the  $x$ - and  $y$ -oriented sources in the pair BEM versus SPH. It should be however observed that the improvement of one of the models with respect to the other one might be evaluated not only in terms of the sole mean PSF or of the PSF FWHM value but also in terms of the combined information which can be gathered basing upon these data. The relationship between the PSF FWHM and the standard deviation  $\sigma$  of the PSF can be in fact expressed as  $\text{FWHM} = 2\sqrt{2 \ln 2} \sigma \approx 2.35482\sigma$ . Considering that the signal-to-noise ratio (SNR) of the PSF can be expressed as the reciprocal of the coefficient of variation (CV) of the PSF distribution, which can be in turn expressed as the ratio of the standard deviation  $\sigma$  and the mean PSF, the SNRs of the PSF distributions for the BEM and the SPH models can be computed based upon the mean PSFs and the standard deviations obtained by the PSF FWHM values reported in Tables 1 and 3. The evaluation of the SNRs of the  $z$ -oriented sources for the BEM and the SPH models indicates that there is a general increase (22.7% mean) in the SNR for the BEM model with respect to the spherical one for all the  $z$ -oriented tested sources.

A worsening of both the realistic models versus the spherical can be observed for sources in the frontal lobe (Figures 7(c)–7(e), sources 3–4 in Figure 4), positioned in proximity of the frontal sinus. This might be due to the vicinity of the paranasal sinuses, which are actually filled with humid air but are nonetheless modeled as compact bone in our realistic models, in order not to introduce a fifth compartment. To test this hypothesis, sources 9–10 and 25–26 (see Figure 4) have been selected on the cortex mesh, placed

laterally to sources 3 and 4 and to the paranasal sinuses, with the positive effect of improvement in terms of spatial blurring given by the realistic model (see Figures 7(c)–7(e)).

Results for sources placed in the temporal cortex (namely 2–5, 15–16, 17–18, and 19–20 in Figure 4) indicate that the realistic model generally leads to an improvement in terms of spatial blurring with respect to spherical model. The same trend is presented by realistic FDM with respect to BEM. These results are in agreement with previous studies that showed that a 3-compartment realistic BEM model of the head outperformed a 3-shell spherical model, particularly in the temporal lobe [13]. This trend is also confirmed for sources which are positioned in the occipital cortex, namely, 7–8, 13–14, 21–22, and 23–24, again demonstrating that the adoption of a realistic model instead of a spherical one can lead to benefits in terms of power of discrimination for the reconstruction of these sources. The spherical model results in fact to perform best in the more spherical upper parts of the brain (see Figures 7(c)–7(f)), but fails in the temporal and occipital lobe areas, which cannot be well represented by the spherical shells. These findings confirm earlier studies that showed similar behavior [24]. Moreover, for sources located in parieto-occipital areas (see Table 3 for sources n. 13–17 and 21–24 and see Figures 7(b), 7(d), 7(e)), PSF parameters exhibit smaller FWHM for the realistic model, compared to the spherical one, with slightly smaller FWHM for BEM with respect to FDM that might be due to the smoothing of sulci presented by BEM.

The computational performances of the spherically approximated and of the two different BEM and FDM realistic models analyzed can provide also useful elements in order to assess cost-benefit of the specific model adopted. Computational performance was determined for the spherical and the BEM models with a standard PC (AMD64 3.00 GHz/3 GB RAM, 2 MB cache 2L) and for the FDM model with a Linux cluster PC composed by 8 elements of the same type (i.e., the above described unit as the front-end node plus 7 AMD64 3.00 GHz / 2 GB RAM elements), as the FDM EEG forward problem solution was set up on a parallel computing implementation, given the higher computational load presented by the volume-based realistic models (FDM and FEM) [12]. When measuring the wall-clock time, it should be distinguished between the setup-computation that only has to be carried out once per head model for the building of the lead field matrix and the forward computations that have to be carried out hundreds or hundreds of thousands of times depending on the inverse problem solution procedure [30]. During the setup, the computation of the leadfield matrix by means of the FDM solver took about 5.7 hours, that is, about 330 seconds per sensor. The resulting linear system matrix for the computation of each column vector of the lead field matrix had a size of about 14 GB, while the final lead field matrix had a size of about 8 MB for all the three models considered. The computation of the leadfield matrix by means of the BEM solver took about 4.1 hours, being this the total time needed for the transfer matrix setup and decomposition with additional 12 s for the computation of the columns of the leadfield matrix for all the sensors. The computation of the leadfield matrix

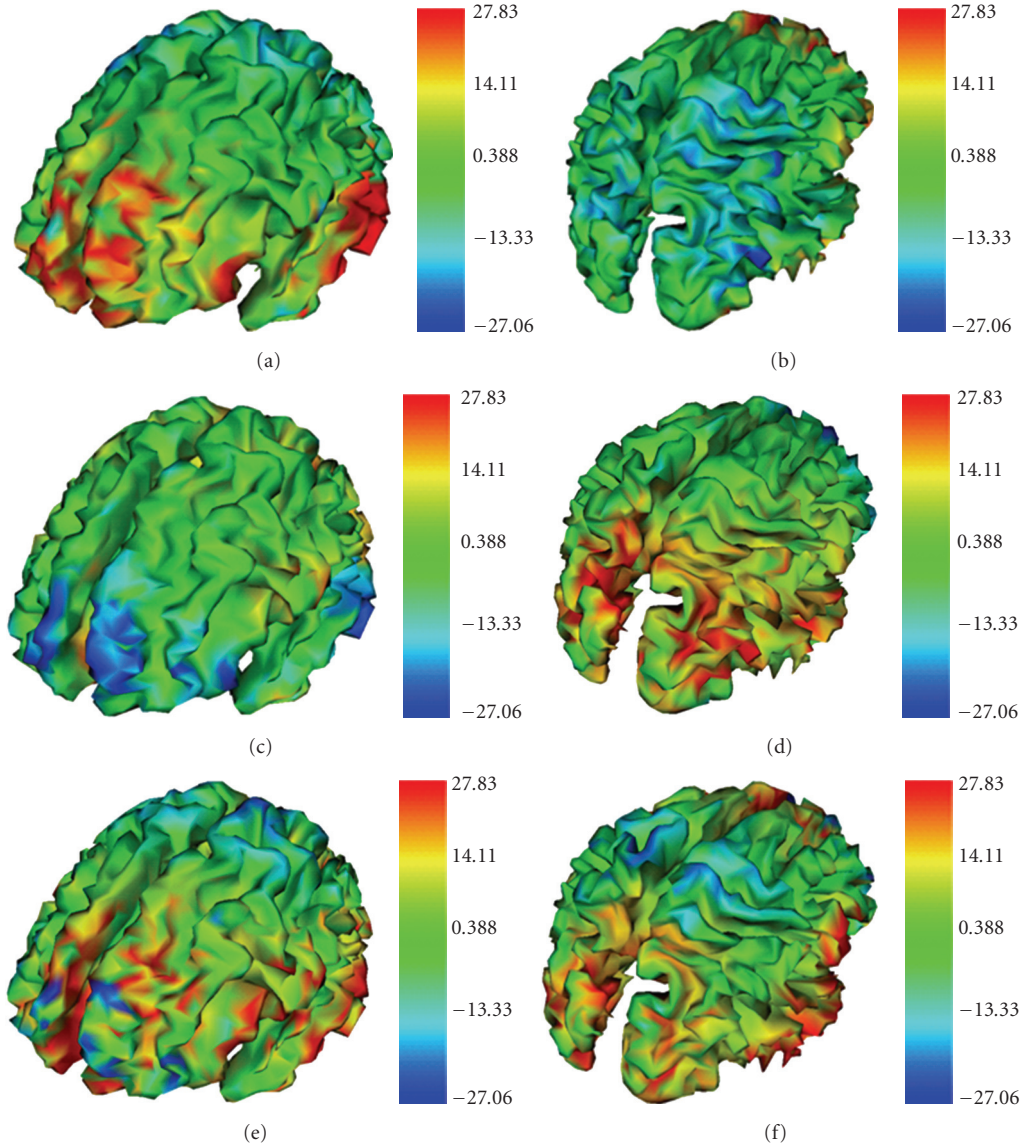


FIGURE 7: Differences between the FWHM values of the RMS PSF maps for the three couples of analyzed head models, computed as the difference between values of  $\text{FWHM}_{\text{Model1}}$  and  $\text{FWHM}_{\text{Model2}}$  over the cortex mesh ( $\text{FWHM}_{\text{Model1}} - \text{FWHM}_{\text{Model2}}$ ). (A, B)  $\text{FWHM}_{\text{BEM}} - \text{FWHM}_{\text{FDM}}$ ; (C, D)  $\text{FWHM}_{\text{SPH}} - \text{FWHM}_{\text{BEM}}$ ; (E, F)  $\text{FWHM}_{\text{SPH}} - \text{FWHM}_{\text{FDM}}$ . Positive values in the computed  $\text{FWHM}_{\text{Model1}} - \text{FWHM}_{\text{Model2}}$  differences are represented in red; negative values are represented in blue. Red zones correspond to a smaller spatial extent and hence to a better capacity in terms of spatial discrimination of neural sources of Model 2 with respect to Model 1 for the different model pairs.

by means of the adopted sensor-fitted spherical approach needed a time of 0.82 hours (2960 seconds). It should finally be underlined that the cost-benefit of having selected one or the other of the analyzed models should consider only the initial setup time for computing and storing the leadfield matrixes for the different models [30]. The choice of adopting one specific head model has then to be made in terms of costs basing on the one-time initial setup time, and taking into consideration for the benefits the factors of improvement that are gathered by the different models which have been here evaluated in terms of the specific PSF maps.

In conclusion, the obtained results demonstrate that realistic geometry can provide a factor of improvement

which is particularly important when considering sources placed in the temporal or in the occipital cortex. In these situations, using a realistic head model will allow a better spatial discrimination of neural sources in comparison with the spherical model, as it can be appreciated by the analysis of the PSF maps presented in this paper. It is also worth stressing that the results presented in this paper, thanks to the adoption of the MNI-based models, based on a large series of MRI scans on normal controls and thus reflecting average neuroanatomy more representative of the population, can be an enrichment with respect to other studies for the possibility of gathering more general information also extensible to other application studies in this field.

## References

- [1] B. He, Ed., *Neural Engineering Norwell*, Kluwer Academic Publishers, Boston, Mass, USA, 2005.
- [2] F. Vatta, P. Bruno, and P. Inchingolo, "Improving lesion conductivity estimate by means of EEG source localization sensitivity to model parameter," *Journal of Clinical Neurophysiology*, vol. 19, no. 1, pp. 1–15, 2002.
- [3] J. S. Ebersole and S. Hawes-Ebersole, "Clinical application of dipole models in the localization of epileptiform activity," *Journal of Clinical Neurophysiology*, vol. 24, no. 2, pp. 120–129, 2007.
- [4] P. L. Nunez and R. Srinivasan, *Electrical Fields of the Brain: The Neurophysics of EEG*, Oxford University Press, New York, NY, USA, 2005.
- [5] A. M. Dale and M. I. Sereno, "Improved localization of cortical activity by combining EEG and MEG with MRI cortical surface reconstruction: a linear approach," *Journal of Cognitive Neuroscience*, vol. 5, no. 2, pp. 162–176, 1993.
- [6] F. Vatta, P. Bruno, and P. Inchingolo, "Multiregion bicentric-spheres models of the head for the simulation of bioelectric phenomena," *IEEE Transactions on Biomedical Engineering*, vol. 52, no. 3, pp. 384–389, 2005.
- [7] J. J. Ermer, J. C. Mosher, S. Baillet, and R. M. Leahy, "Rapidly recomputable EEG forward models for realistic head shapes," *Physics in Medicine and Biology*, vol. 46, no. 4, pp. 1265–1281, 2001.
- [8] M. Fuchs, R. Drenckhahn, H.-A. Wischmann, and M. Wagner, "An improved boundary element method for realistic volume-conductor modeling," *IEEE Transactions on Biomedical Engineering*, vol. 45, no. 8, pp. 980–997, 1998.
- [9] Y. Zhang, L. Ding, W. van Drongelen, K. Hecox, D. M. Frim, and B. He, "A cortical potential imaging study from simultaneous extra- and intracranial electrical recordings by means of the finite element method," *Neuroimage*, vol. 31, no. 4, pp. 1513–1524, 2006.
- [10] B. Vanrumste, G. van Hoey, R. van de Walle, M. R. P. D'Havé, I. A. Lemahieu, and P. A. Boon, "The validation of the finite difference method and reciprocity for solving the inverse problem in EEG dipole source analysis," *Brain Topography*, vol. 14, no. 2, pp. 83–92, 2001.
- [11] C. Ramon, P. H. Schimpf, and J. Haueisen, "Influence of head models on EEG simulations and inverse source localizations," *BioMedical Engineering Online*, vol. 5, article 10, 2006.
- [12] H. Hallez, B. Vanrumste, R. Grech, et al., "Review on solving the forward problem in EEG source analysis," *Journal of NeuroEngineering and Rehabilitation*, vol. 4, article 46, 2007.
- [13] M. Fuchs, M. Wagner, and J. Kastner, "Boundary element method volume conductor models for EEG source reconstruction," *Clinical Neurophysiology*, vol. 112, no. 8, pp. 1400–1407, 2001.
- [14] M. Fuchs, M. Wagner, and J. Kastner, "Development of volume conductor and source models to localize epileptic foci," *Journal of Clinical Neurophysiology*, vol. 24, no. 2, pp. 101–119, 2007.
- [15] C. Ramon, J. Haueisen, and P. H. Schimpf, "Influence of head models on neuromagnetic fields and inverse source localizations," *BioMedical Engineering Online*, vol. 5, article 55, 2006.
- [16] B. N. Cuffin, "Effects of head shape on EEG's and MEG's," *IEEE Transactions on Biomedical Engineering*, vol. 37, no. 1, pp. 44–52, 1990.
- [17] B. Roth, A. Gorbach, and S. Sato, "How well does a three-shell model predict positions of dipoles in a realistically shaped head?" *Electroencephalography and Clinical Neurophysiology*, vol. 87, pp. 175–184, 1993.
- [18] B. Yvert, O. Bertrand, M. Thévenet, J. F. Echallier, and J. Pernier, "A systematic evaluation of the spherical model accuracy in EEG dipole localization," *Electroencephalography and Clinical Neurophysiology*, vol. 102, no. 5, pp. 452–459, 1997.
- [19] J. P. Ary, S. A. Klein, and D. H. Fender, "Location of sources of evoked scalp potentials: corrections for skull and scalp thicknesses," *IEEE Transactions on Biomedical Engineering*, vol. 28, no. 6, pp. 447–452, 1981.
- [20] B. N. Cuffin, "Effects of local variations in skull and scalp thickness on EEG's and MEG's," *IEEE Transactions on Biomedical Engineering*, vol. 40, no. 1, pp. 42–48, 1993.
- [21] G. Huiskamp, M. Vroeijsstijn, R. van Dijk, G. Wieneke, and A. C. van Huffelen, "The need for correct realistic geometry in the inverse EEG problem," *IEEE Transactions on Biomedical Engineering*, vol. 46, no. 11, pp. 1281–1287, 1999.
- [22] N. von Ellenrieder, C. H. Muravchik, and A. Nehorai, "Effects of geometric head model perturbations on the EEG forward and inverse problems," *IEEE Transactions on Biomedical Engineering*, vol. 53, no. 3, pp. 421–429, 2006.
- [23] D. Van't Ent, J. C. de Munck, and A. L. Kaas, "A fast method to derive realistic BEM models for E/MEG source reconstruction," *IEEE Transactions on Biomedical Engineering*, vol. 48, no. 12, pp. 1434–1443, 2001.
- [24] M. Fuchs, J. Kastner, M. Wagner, S. Hawes, and J. S. Ebersole, "A standardized boundary element method volume conductor model," *Clinical Neurophysiology*, vol. 113, no. 5, pp. 702–712, 2002.
- [25] N. von Ellenrieder, C. H. Muravchik, M. Wagner, and A. Nehorai, "Effect of head shape variations among individuals on the EEG/MEG forward and inverse problems," *IEEE Transactions on Biomedical Engineering*, vol. 56, no. 3, pp. 587–597, 2009.
- [26] K. A. Awada, D. R. Jackson, S. B. Baumann, et al., "Effect of conductivity uncertainties and modeling errors on eeg source localization using a 2-D model," *IEEE Transactions on Biomedical Engineering*, vol. 45, no. 9, pp. 1135–1145, 1998.
- [27] A. M. Dale, A. K. Liu, B. R. Fischl, et al., "Dynamic statistical parametric mapping: combining fMRI and MEG for high-resolution imaging of cortical activity," *Neuron*, vol. 26, no. 1, pp. 55–67, 2000.
- [28] A. K. Liu, A. M. Dale, and J. W. Belliveau, "Monte Carlo simulation studies of EEG and MEG localization accuracy," *Human Brain Mapping*, vol. 16, no. 1, pp. 47–62, 2002.
- [29] R. D. Pascual-Marqui, "Review of methods for solving the EEG inverse problem," *International Journal of Bioelectromagnetism*, vol. 1, no. 1, pp. 75–86, 1999.
- [30] D. Weinstein, L. Zhukov, and C. Johnson, "Lead-field bases for electroencephalography source imaging," *Annals of Biomedical Engineering*, vol. 28, no. 9, pp. 1059–1065, 2000.

## Research Article

# The Influence of Age and Skull Conductivity on Surface and Subdermal Bipolar EEG Leads

**Katrina Wendel,<sup>1</sup> Juho Väisänen,<sup>1</sup> Gunnar Seemann,<sup>2</sup> Jari Hyttinen,<sup>1</sup> and Jaakko Malmivuo<sup>1</sup>**

<sup>1</sup>Department of Biomedical Engineering, Tampere University of Technology, Korkeakoulunkatu 3, P.O. Box 692, 33101 Tampere, Finland

<sup>2</sup>Institute of Biomedical Engineering, Karlsruhe Institute of Technology, 76131 Karlsruhe, Germany

Correspondence should be addressed to Katrina Wendel, katrina.wendel@tut.fi

Received 1 July 2009; Accepted 8 October 2009

Academic Editor: Fabrizio De Vico Fallani

Copyright © 2010 Katrina Wendel et al. This is an open access article distributed under the Creative Commons Attribution License, which permits unrestricted use, distribution, and reproduction in any medium, provided the original work is properly cited.

Bioelectric source measurements are influenced by the measurement location as well as the conductive properties of the tissues. Volume conductor effects such as the poorly conducting bones or the moderately conducting skin are known to affect the measurement precision and accuracy of the surface electroencephalography (EEG) measurements. This paper investigates the influence of age via skull conductivity upon surface and subdermal bipolar EEG measurement sensitivity conducted on two realistic head models from the Visible Human Project. Subdermal electrodes (a.k.a. subcutaneous electrodes) are implanted on the skull beneath the skin, fat, and muscles. We studied the effect of age upon these two electrode types according to the scalp-to-skull conductivity ratios of 5, 8, 15, and 30 : 1. The effects on the measurement sensitivity were studied by means of the half-sensitivity volume (HSV) and the region of interest sensitivity ratio (ROISR). The results indicate that the subdermal implantation notably enhances the precision and accuracy of EEG measurements by a factor of eight compared to the scalp surface measurements. In summary, the evidence indicates that both surface and subdermal EEG measurements benefit better recordings in terms of precision and accuracy on younger patients.

## 1. Introduction

Clinical electroencephalography (EEG) and evoked potential (EP) recordings such as the visually evoked potentials (VEPs) demand high signal-to-noise ratios (SNRs), minimization of skin artifacts, and high accuracy, to name a few important criteria. Subdermal needle electrodes (a.k.a. subcutaneous needle electrodes) are commonly used in clinical electromyography (EMG), which are inserted into the muscles of interest. It is less commonly known that these subdermal needle electrodes also record continuous EEGs and EPs in intensive care units (ICU) [1–4]. The measurement setup is achieved by inserting the needle nearly tangentially to the skin so that it is stabilized and the recording tip touches the skull. Furthermore, these recordings offer higher SNRs with lower proclivity of standard measurement artifacts when compared with traditional surface measurements and are more suitable for long-term EEG monitoring in the ICU.

Higher SNR requires less averaging, thus yielding faster and more accurate diagnostic measurements. We believe that clinical EEGs and EPs such as the VEP could adopt the subdermal measurement setup, thus placing the lead on the skull bypassing the artifact-prone skin.

Previously, we correlated skull conductivity with age (Figure 1) [6]. In that former study, we analyzed the reported skull conductivities of living skull fragments temporarily excised during epilepsy surgery with the age of the patient [5]. We reported a decreasing trend that stabilized in early adulthood. According to medical texts, physiologists explain that the calvarial bone completes the ossification process between the ages of 18 and 20 [7]; therefore, the skull conductivity should nearly approach steady state after adolescence. From the study of Hoekema et al. [5], we extrapolate that the scalp-to-skull conductivity ratio of 5 represents children and a small percentage of adolescents, the ratio of 8 represents adolescents and some adults, the

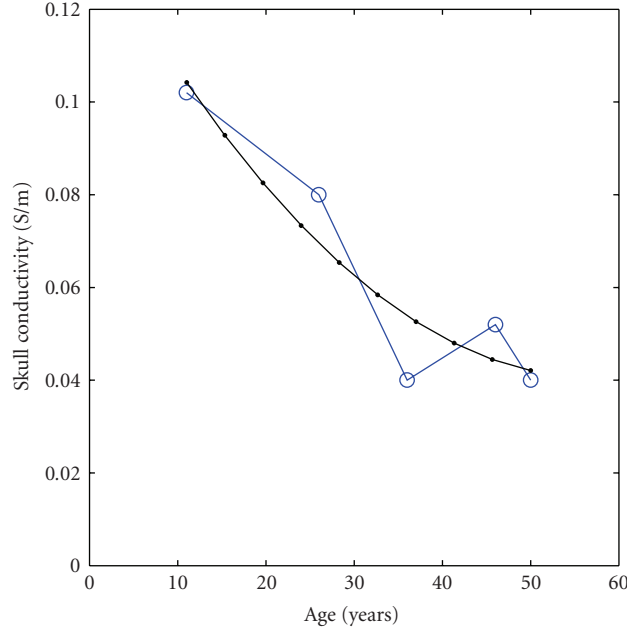


FIGURE 1: Reported conductivity values of live skull samples temporarily removed during epileptic surgery plotted against patient age [5]. The thick blue trend with circles graphs raw data and the thin gray trend with dots graphs the least squares fit. Reproduced from [6].

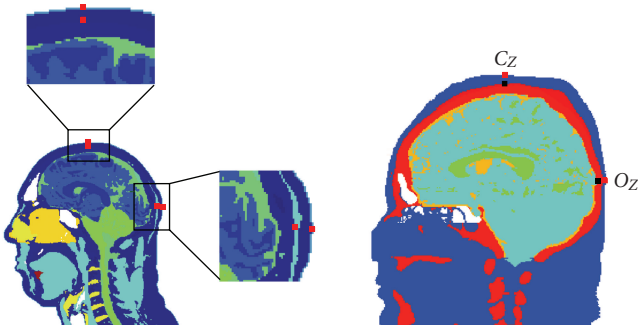


FIGURE 2: The midsagittal views show the bipolar electrode locations of the surface and subdermal (i.e., on the skull) measurement locations at the apex  $C_z$  and the occipital cortex  $O_z$ . The EEG electrode dimensions are  $1\text{ mm} \times 1\text{ mm} \times 1\text{ mm}$ . (a) The sagittal slice of the *Visible Human Man* displays all four locations. (b) The sagittal slice of the *Visible Human Woman* also shows the surface and subdermal locations.

ratio of 15 represents most adults, and lastly the ratio of 30 represents cadavers suffering from postcellular death. Ages that overlap scalp-to-skull conductivity ratios accommodate inter- and intrasubject variability [1, 8]. Taking standard skin conductivity values [9, 10] divided by the adult skull conductivity values yields a ratio of 8.5, and then scaled by the living to postmortem factor [6, 11, 12] yields approximately 20 to 26. These ratios fit accordingly with [13], which reported a ratio of 15 for post mortem skulls beyond cellular death.

In the present study we apply the concepts of the half-sensitivity volume (HSV) [14] and region of interest sensitivity ratio (ROISR) [15]. We use these metrics to analyze the

effects of EEG electrode implantation on the measurement sensitivity distribution within the brain. Specifically, we aim to compare the sensitivity distributions of the bipolar subdermal EEG measurement with the well-documented surface electrode according to a patient's age [6, 14, 16–19].

## 2. Methods

**2.1. Sensitivity Distribution.** The sensitivity distributions of measurement leads in an inhomogeneous volume conductor can be illustrated with lead current fields as defined by [20–22]. The lead vectors define the relationship between the measured signal in the lead and the current sources in the volume conductor such that

$$V_{LE}(\mathbf{x}) = \int_{\nu} \frac{1}{\sigma} \mathbf{J}_{LE} \cdot \mathbf{J}^i dv, \quad (1)$$

where  $V_{LE}(\mathbf{x})$  is the voltage, for example, measured EEG voltage, in the volume conductor  $\nu$ . The reciprocal current field  $\mathbf{J}_{LE}$  is the lead field,  $\mathbf{J}^i$  ( $\text{A}/\text{cm}^2$ ) is the impressed current density vector in the volume conductor, and  $\sigma$  is the conductivity ( $\text{S}/\text{m}$ ) [17].

The sensitivity distribution in the volume conductor can be established by applying the reciprocity theorem of Helmholtz with Poisson' equation (2) applied to describe quasistatic bioelectric source-field problems [23, 24]. A source distribution,  $\mathbf{J}^i$ , containing only reciprocal source currents at the measurement electrodes raises a gradient potential distribution,  $\nabla\Phi$ , that is, measurement sensitivity, according to the linear Poisson equation

$$\nabla \cdot (\sigma \nabla \Phi) = \nabla \cdot \mathbf{J}^i \quad (\text{in } \Omega), \quad (2)$$

setting the Neumann boundary conditions equal to zero on the scalp

$$\boldsymbol{\sigma}(\nabla\Phi) \cdot \mathbf{n} = 0 \quad (\text{on } \Gamma_\Omega), \quad (3)$$

where  $\boldsymbol{\sigma}$  is the electrical conductivity tensor,  $\Phi$  is the electrical potential,  $\mathbf{J}^i$  is the current source density,  $\mathbf{n}$  is a vector normal to the surface,  $\Omega$  is the volume of the head, and  $\Gamma_\Omega$  is the surface of the head [25].

**2.2. The Half-Sensitivity Volume.** In Malmivuo et al. [14], the concept of the half-sensitivity volume (HSV) was applied to define the volume in which the sensitivity of the measurement lead is concentrated. The HSV is the size of the volume within the source region of the volume conductor, where the magnitude of the sensitivity is at least half of its maximum value. The size of the HSV reflects how focused the region is from which the lead measures bioelectric activity, that is, smaller volumes have a higher measurement resolution and, conversely, larger volumes have a lower measurement resolution. The half-sensitivity volume is thus applied to evaluate the ability of the lead to concentrate the measurement sensitivity.

**2.3. The Region of Interest Sensitivity Ratio.** Väisänen et al. [15] introduced the concept of the region of interest sensitivity ratio (ROISR), which provides a parameter to analyze the specificity of a measurement system. Equation (4) defines ROISR as a ratio between the average sensitivity of a predefined region-of-interest (ROI) volume  $v_{\text{ROI}}$  (5) and the average sensitivity in the rest of the source volume, hereafter called a nonROI volume. The ratio is formulated such that

$$\text{ROISR} = \frac{(1/|v_{\text{ROI}}|) \int_{v_{\text{ROI}}} \nabla\Phi_{\text{LE}}(\mathbf{y}, \mathbf{x}) d\mathbf{y}}{(1/|v_{\text{nonROI}}|) \int_{v_{\text{nonROI}}} \nabla\Phi_{\text{LE}}(\mathbf{y}, \mathbf{x}) d\mathbf{y}}, \quad (4)$$

where  $v_{\text{ROI}}$  is the ROI source volume ( $\text{cm}^3$ ) and  $v_{\text{nonROI}}$  is the nonROI source volume ( $\text{cm}^3$ ).

In the case of EEG, the nonROI volume consists of the entire brain source volume excluding the ROI volume. ROISR thus defines how well the measurement sensitivity is concentrated within the selected ROI, that is, how specific the measurement is to the signals generated within the ROI. We define the ROI volume as

$$v_{\text{ROI}} = v_B \cap v_S, \quad (5)$$

where  $v_B$  is the brain source volume containing the gray and white matters, and  $v_S$  is a sphere with a 20 mm radius from the cortical electrode located on the occipital cortex surface (10/20 location,  $O_Z$ , Figure 2). Consequently, our ROI contains both gray and white matters. We selected this location due to its relevance in visually evoked studies by Sörnmo and Laguna [26].

**2.4. Model and Computations.** We calculate the sensitivity distributions in a realistically shaped male and female heads model based on the U.S. National Library of Medicine's

Visible Human Project digital male and female anatomical dataset [27–29], VHP. Calculation of the sensitivity distributions is based on the principle of reciprocity and the numerical finite difference method (FDM) solution of EEG electrode sensitivity. In the FDM model, the segmented head data from a magnetic resonance image (MRI) data set is divided into cubic elements forming a resistive network [30]. The conductivities, of the elements correspond to the tissue conductivities and the dimensions of the elements correspond to the resolution of the dataset. The FDM is based on Poisson's equation that can be used to describe the bioelectric quasistatic source field problems [24]. A potential distribution within the model for a specific source configuration is solved with linear equations and iterative methods [31, 32].

EEG source localization and head model simulations significantly depend on the conductivities used in the models. In literature many studies apply a brain-to-skull conductivity ratio between 15 and 80 [33]; however, these two parameters vary widely in their conductivity values. The brain tissue conductivity value ranges from 0.12 S/m to 0.48 S/m [1, 8, 34–40], whereas the skull conductivity value ranges from 0.0042 S/m to 0.3 S/m [5, 8, 11, 13, 34–36, 41]. The scalp (skin) conductivity value varies less in literature from 0.33 S/m to 0.45 S/m [8, 9, 34, 35, 42]. Therefore, in the present study we apply the scalp-to-skull conductivity ratios of 5, 8, 15, and 30 : 1 [1, 6, 13, 38–40, 43]. The tissues and their corresponding conductivity values that we used in this study are listed in Table 1 [10].

We calculate the sensitivity distributions of the brain for each bipolar electrode pair located on the scalp and the skull. The surface electrodes (a.k.a. scalp electrodes) and the subdermal electrodes measure  $1 \text{ mm} \times 1 \text{ mm} \times 1 \text{ mm}$ , which reflects the size of one pixel. These dimensions represent one type of subdermal recording electrodes that are insulated up to the tip. Our bipolar leads reflect a visually evoked measurement over the occipital cortex (10/20 location  $O_Z$ ) referenced against an apex electrode (10/20 location  $C_Z$ ). The sagittal views of the models (Figure 2) show the two bipolar EEG locations: surface electrode on the scalp and the subdermal electrode on the skull.

### 3. Results

Figures 3 and 4 present the sensitivity distributions of both the scalp and subdermal leads solved with different conductivity ratios. Clearly, the conductivity ratio has a significant impact on the sensitivity distribution when we consider only one type of electrodes. However, the comparison of both types of electrodes diminishes the influence of the conductivity correlated with age, thus indicating the improved measurement resolution of the needle electrodes irrespective of the patient's age.

Optimally placed subdermal electrodes nearly outperform surface electrodes at every age. The smearing effect of the scalp disappears with the subdermal leads because the recording locations are closer to the target region, thus bypassing the skin (Figures 3 and 4). Tables 2 and 3 show that

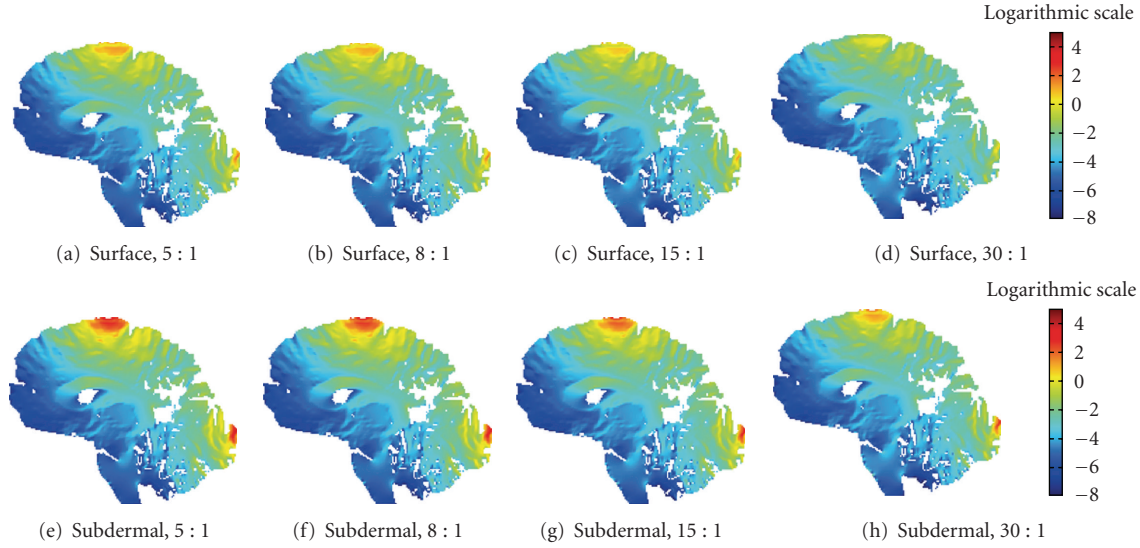


FIGURE 3: Measurement sensitivity distributions of the *Visible Human Man* mapped in the logarithmic scale: ((a)–(d)) surface electrodes placed on the scalp solved according to the scalp-to-skull conductivity ratio mentioned in the subcaption and ((e)–(h)) subdermal insulated needle electrodes inserted through the skin placing the measuring tip on the skull surface solved according to the scalp-to-skull conductivity ratio mentioned in the subcaption. Scalp-to-skull conductivity ratios are specified in each subcaption: ((a), (e)) 5 : 1, ((b), (f)) 8 : 1, ((c), (g)) 15 : 1, and ((d), (h)) 30 : 1.

TABLE 1: Tissues and conductivities (S/m) included in our realistic head models [10].

| Tissue              | Conductivity (S/m)         | Tissue  | Conductivity (S/m) |
|---------------------|----------------------------|---------|--------------------|
| Bone marrow         | 0.046                      | Scalp   | 0.43               |
| Fat                 | 0.040                      | Eye     | 0.51               |
| Skull/Bones         | 0.087, 0.054, 0.029, 0.014 | Muscles | 0.11               |
| White matter        | 0.14                       | Blood   | 1.0                |
| Gray matter         | 0.33                       | CSF     | 1.54               |
| Other neural tissue | 0.16                       |         |                    |

the subdermal lead’s HSV decreases to nearly one-seventh, one-ninth, one-eighth, and one-fourth the size of the scalp lead’s HSV. Similarly, we find a 35% to 37% improvement in the subdermal lead’s ROISR over the surface lead’s ROISR. Figures 3 and 4 illustrate that the subdermal measurement distributions visibly concentrate the measurement sensitivity more efficiently to the target region on the cortex of the younger patient’s skull (i.e., lower conductivity values). Moreover, the smearing effect of the skull is reduced with the subdermal leads, and nearly the entire scalp and skull smearing is eliminated when the patient is the youngest (i.e., the skull conducting value is at its peak). Conversely, the older the patient, namely, the higher the scalp-to-skull conductivity ratio, the more the skull conductivity smears the lead field formation. Precisely, the subdermal leads measure neuroelectric activity on or near the gyral cortical surface rather than sulcal or deep sources.

#### 4. Discussion

The present study compares two variables influencing EEG source localization studies: age and electrode location. This

study shows that the ratio between the scalp and subdermal measurements regarding the HSV is smallest with the lowest skull conductivity ratio. The correlation between the HSV ratios indicates that measurements will be more localized, that is, increased sensitivity, with higher specificity (ROISR). The subdermal measurement distributions visibly concentrate the measurement sensitivity more efficiently to the target region on the cortex as the skull conductivity increases. The smearing effect of the scalp is reduced with the subdermal leads, and nearly the entire scalp and skull smearing is eliminated when the skull has its highest conducting value [8]. Precisely, the subdermal leads measure neuroelectric activity on or near the gyral cortical surface rather than sulcal or deep sources.

Tissue conductivities such as skin, cortical bone, and brain conductivities change with age [41, 44–50]. Their results indicate a decrease in conductivity between 40.7% and 75.4% from newborn to maturity stages. Furthermore, their results show that the aging process slows during childhood before adolescence after the rapid growth phases of the body have been completed. This is due to the reduction of water content in tissue as a function of age [47, 50]. We believe that the conductivity of the skin changes

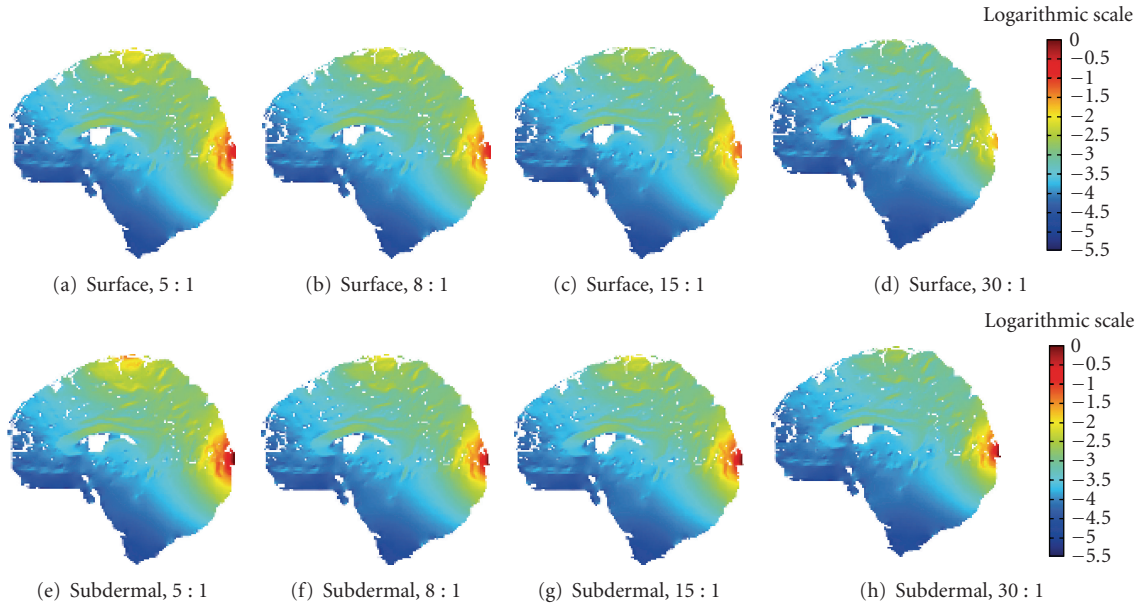


FIGURE 4: Measurement sensitivity distributions of the *Visible Human Woman* mapped in the logarithmic scale: (a)–(d) surface electrodes placed on the scalp solved according to the scalp-to-skull conductivity ratio mentioned in the subcaption and (e)–(h) subdermal insulated needle electrodes inserted through the skin placing the measuring tip on the skull surface solved according to the scalp-to-skull conductivity ratio mentioned in the subcaption. Scalp-to-skull conductivity ratios are specified in each subcaption: (a), (e) 5 : 1, (b), (f) 8 : 1, (c), (g) 15 : 1, and (d), (h) 30 : 1.

TABLE 2: Results of the visually evoked bipolar measurement for the surface and subdermal leads of the *Visible Human Man* dataset. All parameters are calculated from the brain region containing both the gray and white matters.

| Leads     | Conductivity Ratio | Maximum Sensitivity ( $A/cm^3$ ) | HSV ( $mm^3$ ) | ROISR |
|-----------|--------------------|----------------------------------|----------------|-------|
| Surface   | 5 : 1              | 0.420                            | 4999           | 2.43  |
| Surface   | 8 : 1              | 0.405                            | 5239           | 2.31  |
| Surface   | 15 : 1             | 0.387                            | 4002           | 2.09  |
| Surface   | 30 : 1             | 0.336                            | 2446           | 1.81  |
| Subdermal | 5 : 1              | 0.85                             | 706            | 3.17  |
| Subdermal | 8 : 1              | 0.83                             | 586            | 3.00  |
| Subdermal | 15 : 1             | 0.72                             | 516            | 2.72  |
| Subdermal | 30 : 1             | 0.54                             | 610            | 2.39  |

again in late adulthood, that is, the elderly, particularly decreasing in conductivity. Therefore, the skin conductivity from adolescence onwards should minimally affect this study.

We selected our scalp-to-skull conductivity ratios to span from early childhood through adulthood. Our skull values reflect an 83.9% decrease in the human skull conductivity value compared with the 75.4% change in rats, whereas we kept a fixed conductivity for the brain and skin. When we compare similar sets of measurements such as the surface measurements we obtain an improvement in measurement resolution between 10.4% and 51.1% for the HSV and an improvement in the measurement accuracy between 25.5% and 38.2% for the ROISR. When we include the subdermal needle measurements, we yield improvements between 75% and 89% in the measurement resolution over the surface electrodes. If we had factored in growth from youth through adolescence to adulthood, then the change in HSV and

ROISR would have increased the variation in the results. The additional variables would have plausibly enhanced the measurement precision in children due to the high water content of their tissues [47].

## 5. Conclusion

The implantation of EEG electrode on the skull notably increases the measurement sensitivity and accuracy over traditional surface electrodes. These measurements known as subdermal or subcutaneous measurements bypass the artifact prone skin to obtain relatively artifact-free, high-resolution EEG recordings. The measurement sensitivity of the needle electrodes concentrates the subdermal EEG measurements. Consequently, the subdermal electrode reduces the need for the extremely invasive electrocorticogram (ECoG) and minimizes the influence of age on EEG source

TABLE 3: Results of the visually evoked bipolar measurement for the surface and subdermal leads of the *Visible Human Woman* dataset. All parameters are calculated from the brain region containing both the gray and white matters.

| Leads     | Conductivity Ratio | Maximum Sensitivity (A/cm <sup>3</sup> ) | HSV (mm <sup>3</sup> ) | ROI SR |
|-----------|--------------------|--|------------------------|--------|
| Surface   | 5 : 1              | 0.900                                    | 221                    | 5.95   |
| Surface   | 8 : 1              | 0.775                                    | 199                    | 5.41   |
| Surface   | 15 : 1             | 0.515                                    | 190                    | 4.58   |
| Surface   | 30 : 1             | 0.379                                    | 198                    | 3.68   |
| Subdermal | 5 : 1              | 1.689                                    | 44                     | 6.88   |
| Subdermal | 8 : 1              | 1.671                                    | 36                     | 6.60   |
| Subdermal | 15 : 1             | 1.595                                    | 27                     | 6.20   |
| Subdermal | 30 : 1             | 1.491                                    | 25                     | 5.92   |

localization. We found that the scalp-to-skull conductivity ratio influenced the subdermal EEG measurement less than the surface EEG measurements. From our correlative study we can definitively claim that children, specifically preadolescent children, would benefit the most from the increased resolution of the subdermal electrodes.

The age plays an important role in the surface electrode measurements, but the change in measurement location to subdermal electrodes irrefutably improves the measurement sensitivity distributions. Succinctly, the subdermal electrodes outperform surface electrodes because they minimize the effect due to the intersubject variability in the scalp-to-skull conductivity ratio associated with the change in age.

## References

- [1] J. Latikka, T. Kuurne, and H. Eskola, "Conductivity of living intracranial tissues," *Physics in Medicine and Biology*, vol. 46, no. 6, pp. 1611–1616, 2001.
- [2] J. R. Ives, "New chronic EEG electrode for critical/intensive care unit monitoring," *Journal of Clinical Neurophysiology*, vol. 22, no. 2, pp. 119–123, 2005.
- [3] S. Fossi, A. Amantini, A. Grippo, et al., "Continuous EEG-SEP monitoring of severely brain injured patients in NICU: methods and feasibility," *Neurophysiologie Clinique*, vol. 36, no. 4, pp. 195–205, 2006.
- [4] G. Bryan Young, J. R. Ives, M. G. Chapman, and S. M. Mirsattari, "A comparison of subdermal wire electrodes with collodion-applied disk electrodes in long-term EEG recordings in ICU," *Clinical Neurophysiology*, vol. 117, no. 6, pp. 1376–1379, 2006.
- [5] R. Hoekema, G. H. Wieneke, F. S. S. Leijten, et al., "Measurement of the conductivity of skull, temporarily removed during epilepsy surgery," *Brain Topography*, vol. 16, no. 1, pp. 29–38, 2003.
- [6] K. Wendel and J. Malmivuo, "Correlation between live and post mortem skull conductivity measurements," in *Proceedings of the 28th Annual International Conference of the IEEE Engineering in Medicine and Biology Society*, pp. 4285–4288, August 2006.
- [7] K. L. Moore and A. F. Dalley, *Clinically Oriented Anatomy*, Lippincott Williams & Wilkins, Philadelphia, Pa, USA, 5th edition, 2005.
- [8] C. H. Wolters, A. Anwander, X. Tricoche, D. Weinstein, M. A. Koch, and R. S. MacLeod, "Influence of tissue conductivity anisotropy on EEG/MEG field and return current computation in a realistic head model: a simulation and visualization study using high-resolution finite element modeling," *NeuroImage*, vol. 30, no. 3, pp. 813–826, 2006.
- [9] T. C. Ferree, K. J. Eriksen, and D. M. Tucker, "Regional head tissue conductivity estimation for improved EEG analysis," *IEEE Transactions on Biomedical Engineering*, vol. 47, no. 12, pp. 1584–1592, 2000.
- [10] C. Ramon, P. H. Schimpf, and J. Haueisen, "Influence of head models on EEG simulations and inverse source localizations," *BioMedical Engineering Online*, vol. 5, article 10, 2006.
- [11] J. D. Kosterich, K. R. Foster, and S. R. Pollack, "Dielectric permittivity and electrical conductivity of fluid saturated bone," *IEEE Transactions on Biomedical Engineering*, vol. 30, no. 2, pp. 81–86, 1983.
- [12] J. D. Kosterich, K. R. Foster, and S. R. Pollack, "Dielectric properties of fluid-saturated bone—the effect of variation in conductivity of immersion fluid," *IEEE Transactions on Biomedical Engineering*, vol. 31, no. 4, pp. 369–374, 1984.
- [13] T. F. Oostendorp, J. Delbeke, and D. F. Stegeman, "The conductivity of the human skull: results of in vivo and in vitro measurements," *IEEE Transactions on Biomedical Engineering*, vol. 47, no. 11, pp. 1487–1492, 2000.
- [14] J. Malmivuo, V. Suihko, and H. Eskola, "Sensitivity distributions of EEG and MEG measurements," *IEEE Transactions on Biomedical Engineering*, vol. 44, no. 3, pp. 196–208, 1997.
- [15] J. Väisänen, O. Väisänen, J. Malmivuo, and J. Hyttinen, "New method for analysing sensitivity distributions of electroencephalography measurements," *Medical and Biological Engineering and Computing*, vol. 46, no. 2, pp. 101–108, 2008.
- [16] M. F. Suesserman, F. A. Spelman, and J. T. Rubinstein, "In vitro measurement and characterization of current density profiles produced by nonrecessed, simple recessed, and radially varying recessed stimulating electrodes," *IEEE Transactions on Biomedical Engineering*, vol. 38, no. 5, pp. 401–408, 1991.
- [17] J. Malmivuo and R. Plonsey, *Bioelectromagnetism: Principles and Applications of Bioelectric and Biomagnetic Fields*, Oxford University Press, New York, NY, USA, 1995.
- [18] S. Grimnes and O. G. Martinsen, *Bioimpedance and Bioelectricity Basics*, Academic Press, San Diego, Calif, USA, 2000.
- [19] J. O. Ollikainen, M. Vauhkonen, P. A. Karjalainen, and J. P. Kaipio, "Effects of electrode properties on EEG measurements and a related inverse problem," *Medical Engineering and Physics*, vol. 22, no. 8, pp. 535–545, 2000.
- [20] R. McFee and F. D. Johnston, "Electrocardiographic leads: I. Introduction," *Circulation*, vol. 8, no. 10, pp. 554–568, 1953.
- [21] R. McFee and F. D. Johnston, "Electrocardiographic leads: II. Analysis," *Circulation*, vol. 9, no. 2, pp. 255–266, 1954.
- [22] R. McFee and F. D. Johnston, "Electrocardiographic leads: III. Synthesis," *Circulation*, vol. 9, no. 6, pp. 868–880, 1954.

- [23] H. L. F. Helmholtz, "Über einige Gesetze der Vertheilung elektrischer Ströme in körperlichen Leitern mit Anwendung auf die thierisch-elektrischen Versuche," *Annalen der Physik und Chemie*, vol. 89, pp. 211–233, 354–377, 1853.
- [24] J. Sarvas, "Basic mathematical and electromagnetic concepts of the biomagnetic inverse problem," *Physics in Medicine and Biology*, vol. 32, no. 1, pp. 11–22, 1987.
- [25] C. Johnson, M. Mohr, U. Rude, A. Samsonov, and K. Zyp, "Multilevel methods for inverse bioelectric field problems," in *Multiscale and Multiresolution Methods in Computational Science and Engineering*, Springer, Berlin, Germany, 2003.
- [26] L. Sörnmo and P. Laguna, *Bioelectrical Signal Processing in Cardiac and Neurological Applications*, Academic Press, San Diego, Calif, USA, 2005.
- [27] M. J. Ackerman, "The visible human project," *The Journal of Biocommunication*, vol. 18, no. 2, p. 14, 1991.
- [28] National Institutes of Health, "Visible human project," U.S. National Library of Medicine, [http://www.nlm.nih.gov/research/visible/visible\\_human.html](http://www.nlm.nih.gov/research/visible/visible_human.html).
- [29] F. B. Sachse, C. D. Werner, K. Meyer-Waarden, and O. Dössel, "Applications of the visible man dataset in electrocardiology: calculation and visualization of body surface potential maps of a complete heart cycle," in *Proceedings of the 2nd Users Conference of the National Library of Medicine's Visible Human Project*, pp. 47–48, 1998.
- [30] X. Franceries, B. Doyon, N. Chauveau, B. Rigaud, P. Celsis, and J.-P. Morucci, "Solution of Poisson's equation in a volume conductor using resistor mesh models: application to event related potential imaging," *Journal of Applied Physics*, vol. 93, no. 6, pp. 3578–3588, 2003.
- [31] C. R. Johnson, "Computational and numerical methods for bioelectric field problems," *Critical Reviews in Biomedical Engineering*, vol. 25, no. 1, pp. 1–81, 1997.
- [32] P. Kauppinen, J. Hyttinen, P. Laarne, and J. Malmivuo, "A software implementation for detailed volume conductor modelling in electrophysiology using finite difference method," *Computer Methods and Programs in Biomedicine*, vol. 58, no. 2, pp. 191–203, 1999.
- [33] S. Rush and D. A. Driscoll, "EEG electrode sensitivity—an application of reciprocity," *IEEE Transactions on Biomedical Engineering*, vol. 16, no. 1, pp. 15–22, 1969.
- [34] C. Gabriel, S. Gabriel, and E. Corthout, "The dielectric properties of biological tissues: I. Literature survey," *Physics in Medicine and Biology*, vol. 41, no. 11, pp. 2231–2249, 1996.
- [35] S. Gabriel, R. W. Lau, and C. Gabriel, "The dielectric properties of biological tissues: II. Measurements in the frequency range 10 Hz to 20 GHz," *Physics in Medicine and Biology*, vol. 41, no. 11, pp. 2251–2269, 1996.
- [36] S. Gabriel, R. W. Lau, and C. Gabriel, "The dielectric properties of biological tissues: III. Parametric models for the dielectric spectrum of tissues," *Physics in Medicine and Biology*, vol. 41, no. 11, pp. 2271–2293, 1996.
- [37] J. A. Latikka, J. A. Hyttinen, T. A. Kuurne, H. J. Eskola, and J. A. Malmivuo, "The conductivity of brain tissues: comparison of results in vivo and in vitro measurements," in *Proceedings of the 23rd Annual International Conference of the IEEE Engineering in Medicine and Biology Society*, vol. 1, pp. 910–912, Istanbul, Turkey, October 2001.
- [38] S. Goncalves, J. de Munck, J. P. A. Verbunt, F. Bijma, R. M. Heethaar, and F. H. Lopes da Silva, "In vivo measurement of the brain and skull resistivities using an EIT-based method and realistic models for the head," *IEEE Transactions on Biomedical Engineering*, vol. 50, pp. 754–767, 2003.
- [39] S. Goncalves, J. de Munck, J. P. A. Verbunt, R. M. Heethaar, and F. H. Lopes da Silva, "In vivo measurement of the brain and skull resistivities using an EIT-based method and the combined analysis of SEF/SEP data," *IEEE Transactions on Biomedical Engineering*, vol. 50, no. 9, pp. 1124–1128, 2003.
- [40] Y. Lai, W. van Drongelen, L. Ding, et al., "Estimation of in vivo human brain-to-skull conductivity ratio from simultaneous extra- and intra-cranial electrical potential recordings," *Clinical Neurophysiology*, vol. 116, no. 2, pp. 456–465, 2005.
- [41] C. Gabriel, A. Peyman, and E. H. Grant, "Electrical conductivity of tissue at frequencies below 1 MHz," *Physics in Medicine and Biology*, vol. 54, no. 16, pp. 4863–4878, 2009.
- [42] V. Raicu, N. Kitagawa, and A. Irimajiri, "A quantitative approach to the dielectric properties of the skin," *Physics in Medicine and Biology*, vol. 45, no. 2, pp. L1–L4, 2000.
- [43] T. C. Ferree and D. M. Tucker, "Development of high-resolution EEG devices," *International Journal of Bioelectromagnetism*, vol. 1, pp. 4–10, 1999.
- [44] A. Peyman, A. A. Rezazadeh, and C. Gabriel, "Changes in the dielectric properties of rat tissue as a function of age at microwave frequencies," *Physics in Medicine and Biology*, vol. 46, pp. 1617–1629, 2001.
- [45] A. Peyman, A. A. Rezazadeh, and C. Gabriel, "Erratum: changes in the dielectric properties of rat tissue as a function of age at microwave frequencies," *Physics in Medicine and Biology*, vol. 47, no. 12, pp. 2187–2188, 2002.
- [46] C. Gabriel, "Dielectric properties of biological tissue: variation with age," *Bioelectromagnetics*, vol. 26, supplement 7, pp. S12–S18, 2005.
- [47] J. Keshvari, R. Keshvari, and S. Lang, "The effect of increase in dielectric values on specific absorption rate (SAR) in eye and head tissues following 900, 1800 and 2450 MHz radio frequency (RF) exposure," *Physics in Medicine and Biology*, vol. 51, no. 6, pp. 1463–1477, 2006.
- [48] A. Peyman, S. J. Holden, S. Watts, R. Perrott, and C. Gabriel, "Dielectric properties of porcine cerebrospinal tissues at microwave frequencies: in vivo, in vitro and systematic variation with age," *Physics in Medicine and Biology*, vol. 52, no. 8, pp. 2229–2245, 2007.
- [49] J. Wiart, A. Hadjem, M. F. Wong, and I. Bloch, "Analysis of RF exposure in the head tissues of children and adults," *Physics in Medicine and Biology*, vol. 53, no. 13, pp. 3681–3695, 2008.
- [50] A. Peyman, C. Gabriel, E. H. Grant, G. Vermeeren, and L. Martens, "Variation of the dielectric properties of tissues with age: the effect on the values of SAR in children when exposed to walkie-talkie devices," *Physics in Medicine and Biology*, vol. 54, no. 2, pp. 227–241, 2009.

## Research Article

# Determination of Neural Fiber Connections Based on Data Structure Algorithm

**Dilek Göksel Duru and Mehmed Özkan**

*Institute of Biomedical Engineering, Bogazici University, 34684 Istanbul, Turkey*

Correspondence should be addressed to Dilek Göksel Duru, gokseld@boun.edu.tr

Received 10 July 2009; Revised 27 August 2009; Accepted 28 September 2009

Academic Editor: Fabio Babiloni

Copyright © 2010 D. Göksel Duru and M. Özkan. This is an open access article distributed under the Creative Commons Attribution License, which permits unrestricted use, distribution, and reproduction in any medium, provided the original work is properly cited.

The brain activity during perception or cognition is mostly examined by functional magnetic resonance imaging (fMRI). However, the cause of the detected activity relies on the anatomy. Diffusion tensor magnetic resonance imaging (DTMRI) as a noninvasive modality providing in vivo anatomical information allows determining neural fiber connections which leads to brain mapping. Still a complete map of fiber paths representing the human brain is missing in literature. One of the main drawbacks of reliable fiber mapping is the correct detection of the orientation of multiple fibers within a single imaging voxel. In this study a method based on linear data structures is proposed to define the fiber paths regarding their diffusivity. Another advantage of the proposed method is that the analysis is applied on entire brain diffusion tensor data. The implementation results are promising, so that the method will be developed as a rapid fiber tractography algorithm for the clinical use as future study.

## 1. Introduction

Functional magnetic resonance imaging (fMRI) serves to determine the brain activity during perception or cognition. BOLD contrast for fMRI is remarkable in cognitive neuroscience, surgical treatment planning, and preclinical studies in examining the main parameters such as the blood flow, blood volume, resting state connectivity, and anatomical connectivity within the brain [1]. To define the cause of the detected activity, the anatomy of the underlying tissue must be analyzed. The functional properties of the region of interests (ROIs) in the brain can be investigated by combination of different modalities such as diffusion tensor magnetic resonance imaging (DTMRI or DTI), ADC fMRI, and BOLD fMRI [2]. As a noninvasive imaging modality DTMRI helps identification and visualization of the fiber connections in the anatomy [3–5]. DTMRI is unique in its ability providing in-vivo anatomical information noninvasively. The potential of DTI is to make the determination of anatomical connectivity in the investigated brain regions by mapping the axonal pathways in white matter noninvasively [6].

The lack of a complete neural fiber map in literature makes the postprocessing of the data very important. Methods and updates are to be researched to define the fiber trajectories in the uncertainty regions where multiple fiber orientations cross within a single imaging voxel [7, 8]. Our proposed technique aims to track the white matter fibers according to data structure algorithm noniteratively and depending on the structural information of the underlying tissue. The proposed algorithm is based on two major processes. One is decision making and the other one is storing process. Decision making process is basically an operation based on comparison between the orientations of diffusivities of adjacent voxel pairs. In other words, it is the determination of the path to be traced for computing the neural pathways. The decision making involves setting a similarity measure having a constant scalar value for a subject. The voxels which succeeded to pass the threshold is stored in a data structure. This process is performed for all the adjacent voxel pairs in the examined brain MR images. So the study applies the method to the entire human brain DT images to construct maps of neural fibers in uncertainty regions.

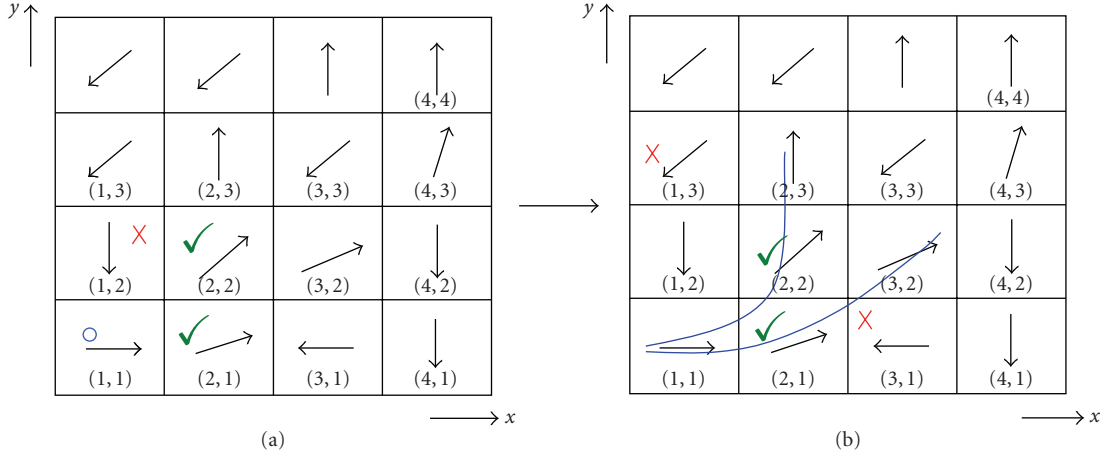


FIGURE 1: Sample synthetic eigenvector pattern. (a) (1, 1) is the starting node, where green checks represent the neighbors within the similarity measure.

## 2. Material and Methods

**2.1. Principles of Diffusion Tensor Analysis.** The Stejskal-Tanner imaging sequence is used to measure diffusion weighted images [3, 4, 9]. The diffusion tensor  $D$  is calculated from this raw data source at each point in the tissue formulated by the Stejskal-Tanner equation as [10, 11]

$$S_i = S_0 e^{-b \hat{g}_i^T D \hat{g}_i}, \quad (1)$$

where  $S_i$  is the signal received with diffusion gradient pulses,  $S_0$  is the RF signal received for a measurement without diffusion gradient pulses,  $b$  is the diffusion weighting factor, and  $|g|$  is the strength of the diffusion gradient pulses.

The diffusion tensor  $D$  is a real, symmetric second-order tensor, represented in matrix form as a real, symmetric  $3 \times 3$  matrix [3, 4]. The six unique elements of the diffusion tensor  $D$  are calculated according to the three-dimensional Gaussian Stejskal-Tanner model as (2) by acquiring at least six diffusion-weighted measurements in noncollinear measurement directions  $g$  along with a nondiffusion-weighted measurement  $S_0$  [3, 4, 7, 12, 13]. On regular DTMR scans more than six diffusion-weighted measurements are taken which creates an over constrained system of equations solved using least square methods [9, 12, 14, 15]:

$$\begin{bmatrix} x_1^2 & y_1^2 & z_1^2 & 2x_1y_1 & 2y_1z_1 & 2x_1z_1 \\ x_2^2 & y_2^2 & z_2^2 & 2x_2y_2 & 2y_2z_2 & 2x_2z_2 \\ \vdots & \vdots & \vdots & \vdots & \vdots & \vdots \\ x_n^2 & y_n^2 & z_n^2 & 2x_ny_n & 2y_nz_n & 2x_nz_n \end{bmatrix} \begin{bmatrix} D_{xx} \\ D_{yy} \\ D_{zz} \\ D_{xy} \\ D_{xz} \\ D_{yz} \end{bmatrix} = \begin{bmatrix} -\frac{1}{b} \ln \frac{S_1}{S_0} \\ -\frac{1}{b} \ln \frac{S_2}{S_0} \\ \vdots \\ -\frac{1}{b} \ln \frac{S_n}{S_0} \end{bmatrix}. \quad (2)$$

Equation (2) equals a vector containing natural logarithmic scaled RF signal loss resulting from the Brownian motion of spins, and  $x_i, y_i, z_i$  denote the  $n$  gradient measurement directions. An orthogonal basis is the eigensystem of the

symmetric matrix  $D$  by finding its eigenvalues and eigenvectors are calculated [16]. Principal component analysis (PCA) is used to perform the diffusion tensor analysis and compression. The diagonalization of the diffusion tensor as (3) results in a set of three eigenvalues  $\lambda_1 > \lambda_2 > \lambda_3$  representing the principal diffusion orientation in an investigated pixel [5, 8]. The eigensystem is defined by the eigenvectors  $e_i$  and the corresponding eigenvalues  $\lambda_i$  (4). The eigenvectors  $e_i$  represent the principal diffusion directions:

$$D_x \vec{e}_i = \lambda_i \vec{e}_i \quad (i = 1, 2, 3), \quad (3)$$

$$|D_x - \lambda I| = 0. \quad (4)$$

Examining the raw data for every pixel, the eigensystem of  $D$  is calculated in each pixel. The eigensystem calculation for analyzed image data provides information about the diffusion distribution throughout the investigated image data. The first principal component  $\lambda_1$  shows the dominant diffusivity direction. The second and third principal components  $\lambda_2$  and  $\lambda_3$  provide information of the intermediate and the smallest principal diffusivity, respectively [17].

**2.2. List Data Structure Implementation.** The linear data structure used here helps to create a list of investigated region of interest eigenvectors where data item insertions and retrievals/deletions are made at one end, namely, the top of the list. A data item insertion is called pushing and removing is called popping the list. The created list can be called a linked list in which all insertions and deletions are performed at the list head (top) [18]. For each data item push, the previous top data item and all lower data items move farther down. When the time arrives to pop a data item from the list, the top data item is retrieved and deleted from the list. To clarify the implementation routine, application steps are explained on the synthetic data as in Figure 1.

The starting point is selected as  $x = 1$  and  $y = 1$  as shown in Figure 1(a). This selected coordinate having the eigenvector  $[1, 0]$  is the bottom of the linked list. The predefined similarity measure is a set of angular thresholds

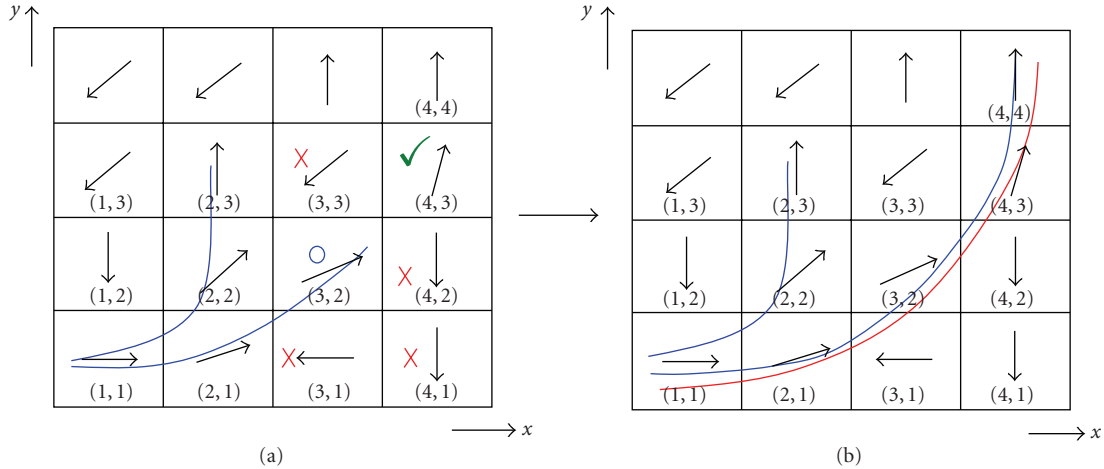


FIGURE 2: Listed data structure analysis results shown on sample pattern with its principal eigenvectors. Two possible resulting fiber paths are represented.

$\pi/j$  ( $j = 4, 6, 12, 18, 20$ ). Pixel (1, 2) is not within the limits of similarity measure  $\pi/4$  (see Figure 1(a)). Pixel (2, 1) is stored in the stack on the top again in compliance with similarity. Top is now assigned to the new node. Next, pixel (2, 2) fulfilling the selected similarity measure is stored on the top of the list. The eigenvector  $[0.7 \ 0.7]$  with its neighboring pixels' eigenvectors is being compared for similarity. As a result, neighbors with coordinates (1, 3) and (3, 3) with both having the eigenvector  $[-0.7 \ -0.7]$  are eliminated (see Figure 1(b)). The implementation follows by pushing the coordinates (2, 3) and (3, 2) to the list. Pixel (3, 2) is popped. Then its neighbors are examined as in Figure 2(a). The routine follows by determining pixels matching with the predefined similarity rule  $\pi/4$ . The synthetic fiber path (represented in blue) is defined as a result as in Figure 2(b).

Selecting the similarity measure as  $\pi/4$  allows the pixel (2, 2) to be on the list as described above. But examining the pattern by a different try for a varying angular threshold such as  $\pi/6$  or  $\pi/12$ , this pixel is not being assigned for the neighboring pixel list. As a result the track represented in red on Figure 2(b) is the outcome of the computational routine. The decision making here about to select a track follows regarding to the underlying tissue's structural information.

The proposed approach relies on the assumption of the unique path description of an axon. Each element in the implementation represents a voxel in the ROI, and each voxel is related with its neighboring voxels. Regarding the neighboring voxel knowledge, the computation sorts the elements in the list for tracking, where the elements which do not fulfill the criteria are kept in a secondary matrix. While examining the investigated pattern pixelwise, the elements in the secondary matrix come up as potential neighboring pixels in question. The repeated check for if they are within the similarity criteria and if they belong to the fiber track gives the chance of a double check in the system. By that way, the neighboring is updated and a more secure resulting track is being defined and followed. The routine updates itself so that for the one selected starting node the first and second neighboring pixels are investigated and the computational

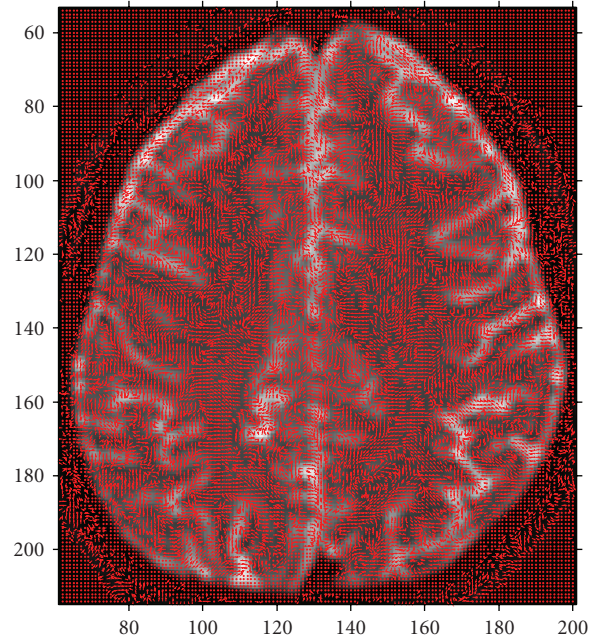


FIGURE 3: Calculated principal eigenvectors of the entire slice superimposed on axial brain MR image.

routine is stretched to a wide range via this increased neighborhood.

### 3. Results

The proposed method is implemented on simulated fiber eigensystem to determine the predefined synthetic trajectories in Section 2.2. The output of the algorithm is in agreement with the visual inspection results as shown in Figure 2. Variation of the similarity measure causes major differences in the calculated neural path as seen in Figure 2(b). Small values of the similarity measure decreases the number of voxels in the solution which are defined by

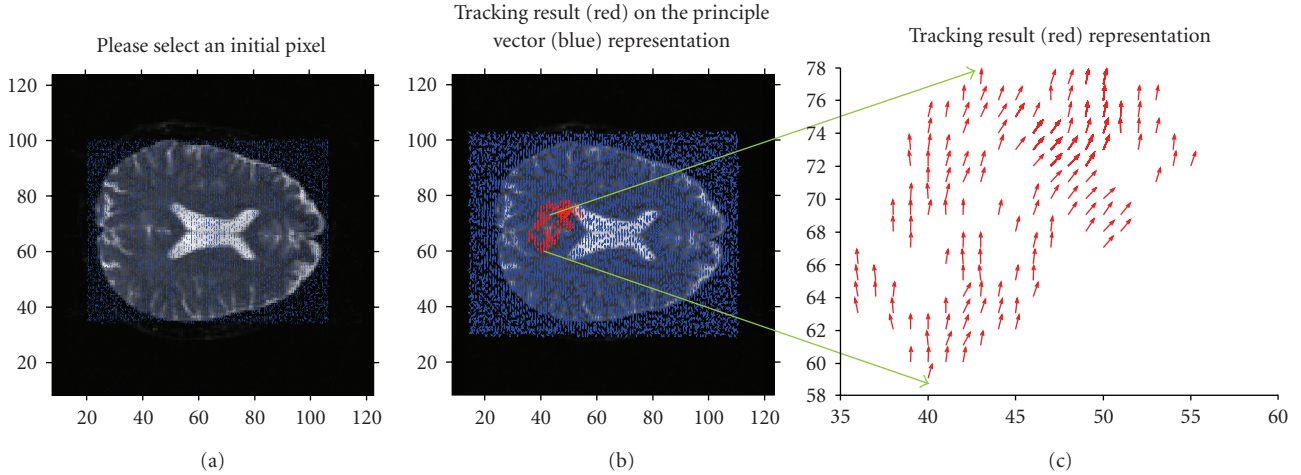


FIGURE 4: Fiber tracking results traced on axial slice with a similarity measure of  $\pi/20$ . (a) Starting point at  $[44, 70]$ . (b) Calculated neighboring pixels with related diffusivity mapped on entire eigenvector map. (c) Zoomed region of interest.

the decision making as neighboring voxels while increased similarity measure selections generate more well-defined and close results to the underlying tissue structure.

Following the promising results of the synthetic data implementations, the method is applied on real DT brain images. As explained in detail in Section 2.1 ((3) and (4)), the eigensystem of  $D$  is determined by PCA [19] and interpreted graphically as seen in Figure 3.

It is obvious that visual detection of any fiber path on the 2D axial MR image representing the eigenvectors is pretty hard unlike the simulated case. Therefore the developed linear list data structure algorithm is applied to the entire brain for neural fiber mapping. The search process of the pattern in the selected limits is completed in examining the eigenvectors of each pixel based on the predefined similarity measure. This examined data set sample might be a whole image data or a single ROI as in Figure 4.

The selection of the investigated brain region's size is directly related with the elapsed time of the computation. To be able to visualize the results of the algorithm, not the whole brain volume but only a selected and easily recognized region is computed. The results of such an example are represented in Figures 5 and 6 from different view angles in 3D.

#### 4. Discussion

Some modalities such as PET and fMRI makes it possible to map the brain functions noninvasively. A parallel fMRI experiment with DTI is promising for understanding the brain function in both neuroimaging and neuroanatomical techniques' sense [2]. The knowledge derived from the DTI make it possible to map the in vivo information of the human neural fiber pathways noninvasively. This is an important motivation in diffusion tensor analysis research. The postprocessing of DTI analyzing tools plays great role in determination of the anatomical structural maps of fiber tracts. To follow a fiber tract and to build a neural map, each

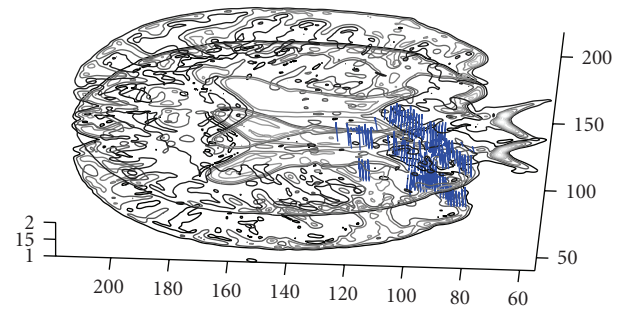


FIGURE 5: Tracking results of the implementation are represented on 2 consecutive slices.

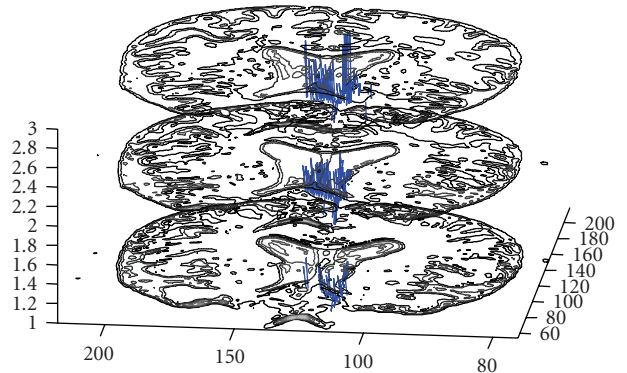


FIGURE 6: Fiber tracking results of the ROI close to inferior frontal lobe registered with the anatomic MR images.

voxel's trajectory is approximated by a set of computed lines in each voxel regarding their major diffusivity. Each resulting tract defines a curvature representing a small bundle of axons in the pathway.

In the existence of fiber crossings and branches in an investigated ROI, the accuracy of the computed neural paths by DTI analyzing tools is unclear. One of the main limitations of diffusion tensor analysis relies on providing a solution for identification of the orientations of the brain fibers in uncertainty regions which is of great importance [3, 4, 8]. Therefore this problem arising in these so-called uncertainty regions is tried to be eliminated by different research groups [12, 20–23].

The aim of this study is to propose a rapid and reliable tracking algorithm which may eliminate the uncertainty region problem in DTI analysis. As seen in results, the synthetic fiber tracking implementation succeeded for predefined neural pathways. This motivated us to implement the algorithm on real diffusion tensor brain images. The computed tracts are found in agreement with the spatial visual inspection. Detailed anatomic information can be gathered via the computed tractography based on the Talairach atlas to become a gold standard, which is still missing.

Future work relies on eliminating the tracking problems in the uncertainty areas by upgrading the proposed method so that the calculation will be implemented on neural system basis and physiological background. The results will provide the base to reliable brain mapping.

## 5. Conclusion

This work aims to develop a promising approach which may eliminate the uncertainties in DT-MRI fiber tractography reconstructions and enhance a neural mapping. The degree of uncertainty in fiber orientation is subject to change by the selection made for similarity measure to detect neighboring voxel pairs. The fiber tracking tools are limited to trajectory-based representations. Therefore the detection of the anatomical connectivity and reliable computation of the neural map should be applied carefully being aware of any mistaken result.

It has been shown that linear list data structure gives promising analysis results in diffusion tensor fiber tract estimation. The identifying similarity measure varies in a range which is accepted in the means of anatomical fiber structure knowledge. Comparing the resulting tracts in synthetic eigenvector pattern with the known predefined pathways, the algorithm gives promising results and works well for the tracking purposes. The computed neural pathways varying with the change of the similarity measure cause to decrease or increase the number of the neighboring voxels for a selected starting voxel. The differing resulting pathways can be thought as an error of the method where it might be also in some cases the possible orientation of a fiber bundle in a wide range, which may be determined by an anatomical brain atlas, that is, Talairach atlas.

Besides the existing algorithms the proposed technique provides the possibility to compute the whole eigensystem of the investigated brain volume. The neighboring voxel pair calculation compares the investigated node in every step of the algorithm within the entire image volume. Each voxel is checked for more than one trial in the total analysis. In

that way the decision making of the algorithm becomes more precise.

## Acknowledgment

This work was supported in part by Bogazici University Scientific Research Project 07HX104D.

## References

- [1] D. G. Norris, "Principles of magnetic resonance assessment of brain function," *Journal of Magnetic Resonance Imaging*, vol. 23, no. 6, pp. 794–807, 2006.
- [2] S. A. Huettel, A. W. Song, and G. McCarthy, *Functional Magnetic Resonance Imaging*, Sinauer Associates, Sunderland, Mass, USA, 2004.
- [3] P. J. Basser, J. Mattiello, and D. LeBihan, "MR diffusion tensor spectroscopy and imaging," *Biophysical Journal*, vol. 66, no. 1, pp. 259–267, 1994.
- [4] P. J. Basser, J. Mattiello, and D. LeBihan, "Estimation of the effective self-diffusion tensor from the NMR spin echo," *Journal of Magnetic Resonance*, vol. 103, no. 3, pp. 247–254, 1994.
- [5] P. J. Basser, S. Pajevic, C. Pierpaoli, J. Duda, and A. Aldroubi, "In vivo fiber tractography using DT-MRI data," *Magnetic Resonance in Medicine*, vol. 44, no. 4, pp. 625–632, 2000.
- [6] S. Mori, B. J. Crain, V. P. Chacko, and P. C. M. Van Zijl, "Three-dimensional tracking of axonal projections in the brain by magnetic resonance imaging," *Annals of Neurology*, vol. 45, no. 2, pp. 265–269, 1999.
- [7] P. J. Basser and D. K. Jones, "Diffusion-tensor MRI: theory, experimental design and data analysis—a technical review," *NMR in Biomedicine*, vol. 15, no. 7-8, pp. 456–467, 2002.
- [8] D. Le Bihan, C. Poupon, A. Amadon, and F. Lethimonnier, "Artifacts and pitfalls in diffusion MRI," *Journal of Magnetic Resonance Imaging*, vol. 24, no. 3, pp. 478–488, 2006.
- [9] P. J. Basser, "Inferring microstructural features and the physiological state of tissues from diffusion-weighted images," *NMR in Biomedicine*, vol. 8, no. 7-8, pp. 333–344, 1995.
- [10] E. O. Stejskal, "Use of spin echoes in a pulsed magnetic-field gradient to study anisotropic, restricted diffusion and flow," *The Journal of Chemical Physics*, vol. 43, no. 10, pp. 3597–3603, 1965.
- [11] E. O. Stejskal and J. E. Tanner, "Spin diffusion measurements: spin echoes in the presence of a time-dependent field gradient," *The Journal of Chemical Physics*, vol. 42, no. 1, pp. 288–292, 1965.
- [12] C. F. Westin, S. E. Maier, H. Mamata, A. Nabavi, F. A. Jolesz, and R. Kikinis, "Processing and visualization for diffusion tensor MRI," *Medical Image Analysis*, vol. 6, no. 2, pp. 93–108, 2002.
- [13] P. B. Kingsley, "Introduction to diffusion tensor imaging mathematics—part I. Tensors, rotations, and eigenvectors," *Concepts in Magnetic Resonance*, vol. 28, no. 2, pp. 101–122, 2006.
- [14] S. Pajevic and C. Pierpaoli, "Color schemes to represent the orientation of anisotropic tissues from diffusion tensor data: application to white matter fiber tract mapping in the human brain," *Magnetic Resonance in Medicine*, vol. 42, no. 3, pp. 526–540, 1999.
- [15] C. H. Sotak, "The role of diffusion tensor imaging in the evaluation of ischemic brain injury—a review," *NMR in Biomedicine*, vol. 15, no. 7-8, pp. 561–569, 2002.

- [16] A. I. Borisenko and I. E. Tarapov, *Vector and Tensor Analysis with Applications*, Dover, New York, NY, USA, 1979.
- [17] C. Pierpaoli, A. Barnett, S. Pajevic, et al., "Water diffusion changes in wallerian degeneration and their dependence on white matter architecture," *NeuroImage*, vol. 13, no. 6, pp. 1174–1185, 2001.
- [18] N. Wirth, *Algorithms and Data Structures*, Prentice-Hall, Englewood Cliffs, NJ, USA, 1986.
- [19] D. Goksel and M. Ozkan, "Towards rapid analysis of diffusion tensor MR imaging," *ESR Supplements*, vol. 16, no. 1, p. 286, 2006.
- [20] S. Pajevic and P. J. Basser, "Parametric and non-parametric statistical analysis of DT-MRI data," *Journal of Magnetic Resonance*, vol. 161, no. 1, pp. 1–14, 2003.
- [21] D. K. Jones, "Determining and visualizing uncertainty in estimates of fiber orientation from diffusion tensor MRI," *Magnetic Resonance in Medicine*, vol. 49, no. 1, pp. 7–12, 2003.
- [22] D. K. Jones and C. Pierpaoli, "Towards a marriage of deterministic and probabilistic tractography methods: bootstrap analysis of fiber trajectories in the human brain," in *Proceedings of the 12th International Society for Magnetic Resonance in Medicine (ISMRM '04)*, p. 1276, Kyoto, Japan, May 2004.
- [23] D. K. Jones, A. R. Travis, G. Eden, C. Pierpaoli, and P. J. Basser, "PASTA: pointwise assessment of streamline tractography attributes," *Magnetic Resonance in Medicine*, vol. 53, no. 6, pp. 1462–1467, 2005.

## Research Article

# Simultaneous EEG-fMRI in Patients with Unverricht-Lundborg Disease: Event-Related Desynchronization/Synchronization and Hemodynamic Response Analysis

Elisa Visani,<sup>1</sup> Ludovico Minati,<sup>2,3</sup> Laura Canafoglia,<sup>1</sup> Isabella Gilioli,<sup>1</sup> Lucia Salvatoni,<sup>1</sup> Giulia Varotto,<sup>1</sup> Patrik Fazio,<sup>1</sup> Domenico Aquino,<sup>2</sup> Maria Grazia Bruzzone,<sup>2</sup> Silvana Franceschetti,<sup>1</sup> and Ferruccio Panzica<sup>1</sup>

<sup>1</sup> Department of Neurophysiopathology, "Carlo Besta" IRCCS Neurological Institute, 20133 Milan, Italy

<sup>2</sup> Department of Neuroradiology, "Carlo Besta" IRCCS Neurological Institute, 20133 Milan, Italy

<sup>3</sup> Scientific Department, "Carlo Besta" IRCCS Neurological Institute, 20133 Milan, Italy

Correspondence should be addressed to Elisa Visani, visani.e@istituto-besta.it

Received 12 June 2009; Revised 3 September 2009; Accepted 14 October 2009

Academic Editor: Fabio Babiloni

Copyright © 2010 Elisa Visani et al. This is an open access article distributed under the Creative Commons Attribution License, which permits unrestricted use, distribution, and reproduction in any medium, provided the original work is properly cited.

We performed simultaneous acquisition of EEG-fMRI in seven patients with Unverricht-Lundborg disease (ULD) and in six healthy controls using self-paced finger extension as a motor task. The event-related desynchronization/synchronization (ERD/ERS) analysis showed a greater and more diffuse alpha desynchronization in central regions and a strongly reduced post-movement beta-ERS in patients compared with controls, suggesting a significant dysfunction of the mechanisms regulating active movement and movement end. The event-related hemodynamic response obtained from fMRI showed delayed BOLD peak latency in the contralateral primary motor area suggesting a less efficient activity of the neuronal populations driving fine movements, which are specifically impaired in ULD.

## 1. Introduction

The analysis of the EEG recorded during motor performance (self-paced movement) provides information about the movement-related changes in oscillatory cortical activity. In normal subjects, an amplitude attenuation of specific frequency components (event-related desynchronization, ERD) in the  $\alpha$ - and  $\beta$ -bands precedes a voluntary movement and reflects cortical activation concurring with movement planning. At the end of the movement, event-related synchronization (ERS) in the  $\beta$ -band replaces ERD [1]. Simultaneous EEG-fMRI acquisition during performance of a motor task enables the identification of changes of brain activity in motor areas and provides information on the source of the event generator.

In Unverricht-Lundborg disease (ULD) patients, voluntary movements are selectively impaired by the presence of action myoclonus [2]. In these patients, ERD/ERS changes highlight increased and diffuse activation of the motor cortex during movement planning and severely

reduced postexcitatory inhibition of the motor cortex [3].

We simultaneously acquired EEG and fMRI in order to study the spatiotemporal pattern of ERD/ERS resulting from self-paced extension of the index finger in ULD patients and to explore the correlation with hemodynamic changes.

## 2. Material and Methods

We enrolled 7 right-handed patients (mean age:  $29.1 \pm 10$  years; four women) with ULD, whose main clinical features are reported in Table 1 and 6 right-handed healthy controls (mean age:  $29.1 \pm 6.7$  years; five women). In all patients, the diagnosis of ULD was established on the basis of the typical electroclinical presentation and of the genetic finding of dodecamer expansion at *cstb* gene [4].

**2.1. Motor Task.** Inside the bore of the scanner, subjects laid supine with their arms relaxed; their head was stabilized

TABLE 1: Patient data.

| Subject, Age [yrs], Sex | Disease duration [yrs] | AED                 | Simplified myoclonus rating |
|-------------------------|------------------------|---------------------|-----------------------------|
| 1, 22, f                | 12                     | VPA, TPM, CLZ       | 2                           |
| 2, 26, f                | 16                     | VPA, CZP            | 2                           |
| 3, 36, m                | 22                     | VPA, LVT, PB        | 2                           |
| 4, 25, m                | 14                     | VPA, CZP, piracetam | 3                           |
| 5, 49, m                | 34                     | VPA, TPM            | 2                           |
| 6, 22, f                | 11                     | VPA, LVT, TPM       | 2                           |
| 7, 24, f                | 12                     | VPA                 | 3                           |

AED: antiepileptic drugs; VPA: valproate; TPM: topiramate; CLZ: clobazam; CZP: clonazepam LVT: levetiracetam; PB: phenobarbital. Simplified myoclonous rating [5]: 2: mild myoclonous, interference with fine movements and/or speech, no interference with walking; 3: moderate myoclonous, patient still able to walk without support.

with adjustable padded restraints on both sides. They were instructed to remain as still as possible throughout the experiment, to keep their eyes open and avoid blinking during the task. Subjects were asked to perform brisk (i.e., lasting less than one second) self-paced extensions of the right index, with a time interval between the end of a movement and the onset of the following one of about 10 seconds. Each subject was trained for several minutes before the experiment. The movement was monitored by electromyography (EMG) and visual observation.

**2.2. EEG-fMRI Acquisition.** EEG was acquired using an MR compatible EEG amplifier (SD MRI 32, Micromed, Treviso, Italy) and a cap providing 30 Ag/AgCl electrodes positioned according to the 10/20 system. Impedance was kept below 5 k $\Omega$ . Electrocardiogram (ECG) and EMG were simultaneously recorded. The EMG activity was recorded from pairs of Ag/AgCl surface electrodes placed bilaterally 2–3 cm apart over the right index flexor muscles. EEG data were acquired at the rate of 1024 Hz using the software package provided by the manufacturer.

Imaging was performed on a 1.5 T MR scanner (Magnetom Avanto, Siemens AG, Erlangen, Germany). Functional images were acquired with an axial gradient-echo echoplanar sequence (21 slices, TR = 2000 ms, TE = 50 ms, 2  $\times$  2 mm<sup>2</sup> in-plane voxel size, 5 mm slice thickness, no gap). A T<sub>1</sub>-weighted anatomical scan (160 slices, TR = 1640 ms, TE = 2 ms; 1 mm<sup>3</sup> isotropic voxels) was also acquired.

The scanner provided a trigger signal corresponding to the excitation of the first slice of each volume, which was recorded by the EEG system enabling real-time artefact removal, making possible to monitor the EEG signal as well as task performance through EMG.

**2.3. Data Analysis.** The imaging gradient artefact and the ballistocardiogram were digitally removed from the EEG using an adaptive filter [6], implemented on software provided by the manufacturer.

Movement onset was determined by the beginning of the burst of EMG activity. EEG data were epoched four seconds before and three seconds after movement onset. Epochs with artefacts, incomplete muscle relaxation between movements, and intertrial interval shorter than 8 seconds were excluded

from the analysis. A reference period at rest, from 3500 to 2500 ms before movement onset, was considered. Each trial was digitally band-pass filtered from 1 Hz below to 1 Hz above the individual frequencies of the most movement-sensitive power peaks in  $\alpha$ - and  $\beta$ -bands. The filtered EEG data were then squared and averaged over all trials and over time (one value every 125 ms). The ERD or ERS values were calculated according to the following formula:

$$\text{ERD/S}(k) = \frac{A(k) - R}{R} \times 100, \quad (1)$$

where  $A(k)$  is the power at sample  $k$  and  $R$  represents the mean power of the reference period (negative values correspond to ERD, positive values to ERS).

The statistical significance of the differences between the mean power observed during the reference period and that measured during the subsequent 125-millisecond intervals was expressed as a probability value using Wilcoxon's signed rank test. The power changes were considered significant when the  $P$  value was less than .05. ERD/ERS data analysis was performed using software developed in Matlab (Mathworks Inc., Natick, MA, USA). For statistical analysis, we divided the time course of ERD/ERS in five epochs of 1 second each ( $t_1$ : -2.5 to -1.5 s,  $t_2$ : -1.5 to -0.5 s,  $t_3$ : -0.5 to 0.5 s,  $t_4$ : 0.5 to 1.5 s,  $t_5$ : 1.5 to 2.5 s) and we compared the values measured on F4, C4, P4, F3, C3, P3, Fz, Cz, and Pz electrodes.

The fMRI data were analyzed by means of the SPM5 software (Wellcome Neuroimaging Dept., Institute of Neurology, London, UK). Preprocessing included three-dimensional motion correction, slice-timing correction, Gaussian smoothing, and normalization into MNI (Montreal Neurological Institute) space. First-level analysis was performed by general linear model (GLM), using the event function from EMG, convolved with the canonical hemodynamic response function, as regressor. Three-dimensional regions of interest (ROIs) were manually drawn for each subject by an experienced operator on the contralateral and ipsilateral primary motor areas as well as on the contralateral supplementary motor area. The average signal time-course was obtained, and the amplitude and latency of the peak of the fitted hemodynamic response were measured.

For statistical analysis, the Mann-Whitney  $U$  test was applied.

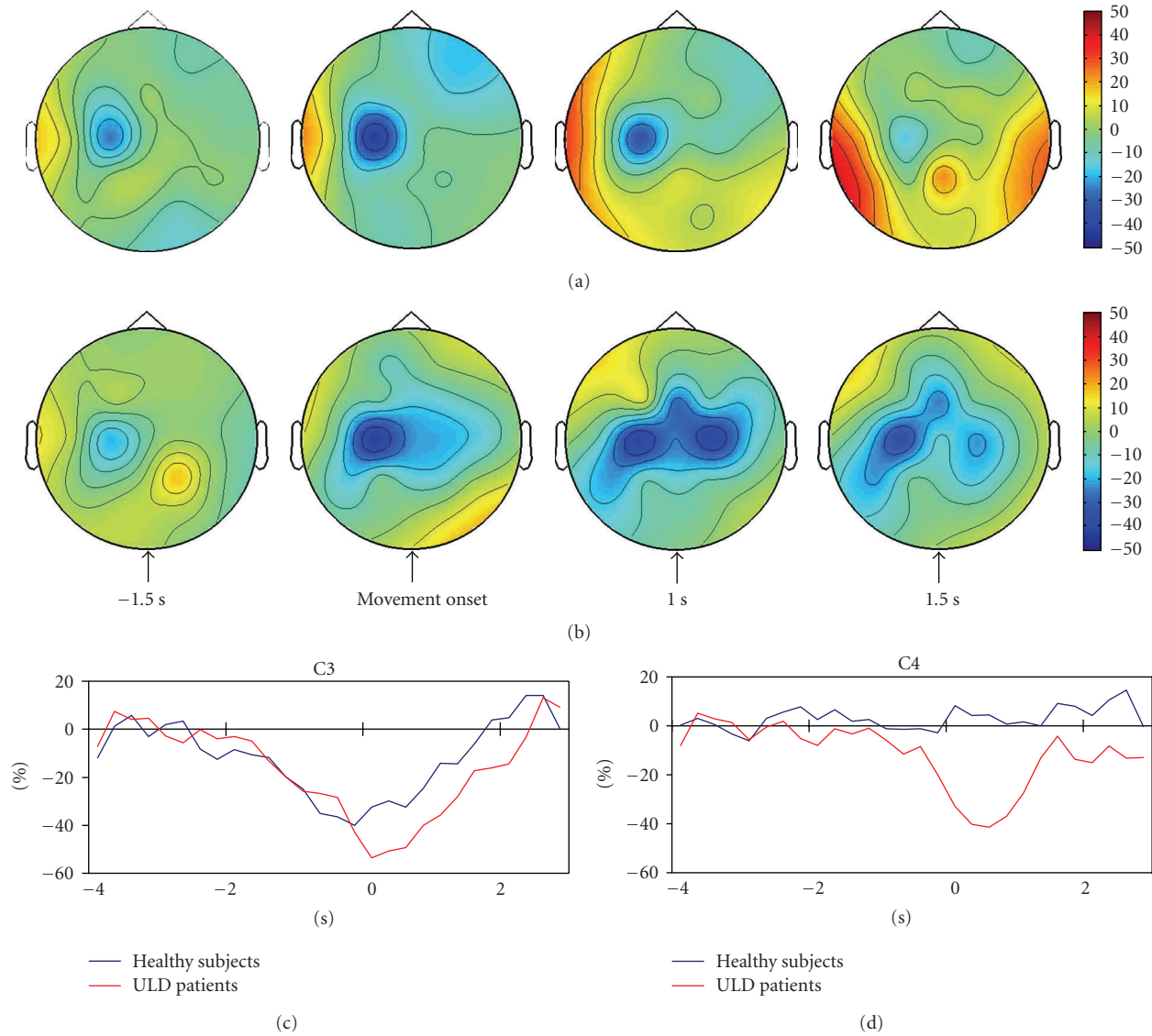


FIGURE 1: Color maps showing the grand average of  $\alpha$ -ERD in control subjects (a) and in patients (b). Color scale: maximum ERD and ERS are coded in blue and red. The lower panels show the grand average of  $\alpha$ -ERD time series recorded from contralateral (c) and ipsilateral (d) central derivations in patients and controls.

### 3. Results

All subjects performed the motor task well: the mean movement duration was on average longer in the patients group ( $535.8 \pm 110.3$  versus  $728.6 \pm 195.5$  ms;  $P = .062$ ). The  $\alpha$ - and  $\beta$ -band peak frequencies, selected as movement reactive EEG frequency, were lower in the patient group with respect to controls and in  $\alpha$ -band this difference reached statistical significance ( $\alpha$ :  $11.3 \pm 0.8$  versus  $9.1 \pm 1.6$  Hz,  $P = .02$ ;  $\beta$ :  $22 \pm 5.6$  versus  $18.6 \pm 1.5$  Hz).

**3.1. ERD/ERS Analysis.** In all subjects  $\alpha$ - and  $\beta$ -ERD were observed (Figure 1). The time course of the  $\alpha$ - and  $\beta$ -desynchronization was similar for the two groups, but in patients the desynchronization in the  $\alpha$ -band was significantly greater in the contralateral central derivation

( $-48.5 \pm 13$  versus  $-58.4 \pm 9.6$ ;  $P = .032$ , for controls and patients, Figure 1(c)) and also involved the midline and the ipsilateral central derivations (Table 2 and Figures 1(b) and 1(d)).

The expected postmovement  $\beta$ -ERS was observed in all controls; it was undetectable in two patients, whereas in the remaining patients it was significantly smaller with respect to that measured in controls ( $107.5 \pm 86.9$  versus  $31.3 \pm 8.8$ ;  $P = .025$ , for controls and patients, Table 2 and Figure 2).

**3.2. fMRI Analysis.** The peak amplitude of the hemodynamic response was comparable in controls and patients in the contralateral ( $0.56 \pm 0.18\%$  versus  $0.63 \pm 0.30\%$ ,  $P = .6$ ) and ipsilateral ( $0.17 \pm 0.15\%$  versus  $0.15 \pm 0.14\%$ ,  $P = .8$ ) motor areas as well as in the contralateral supplementary

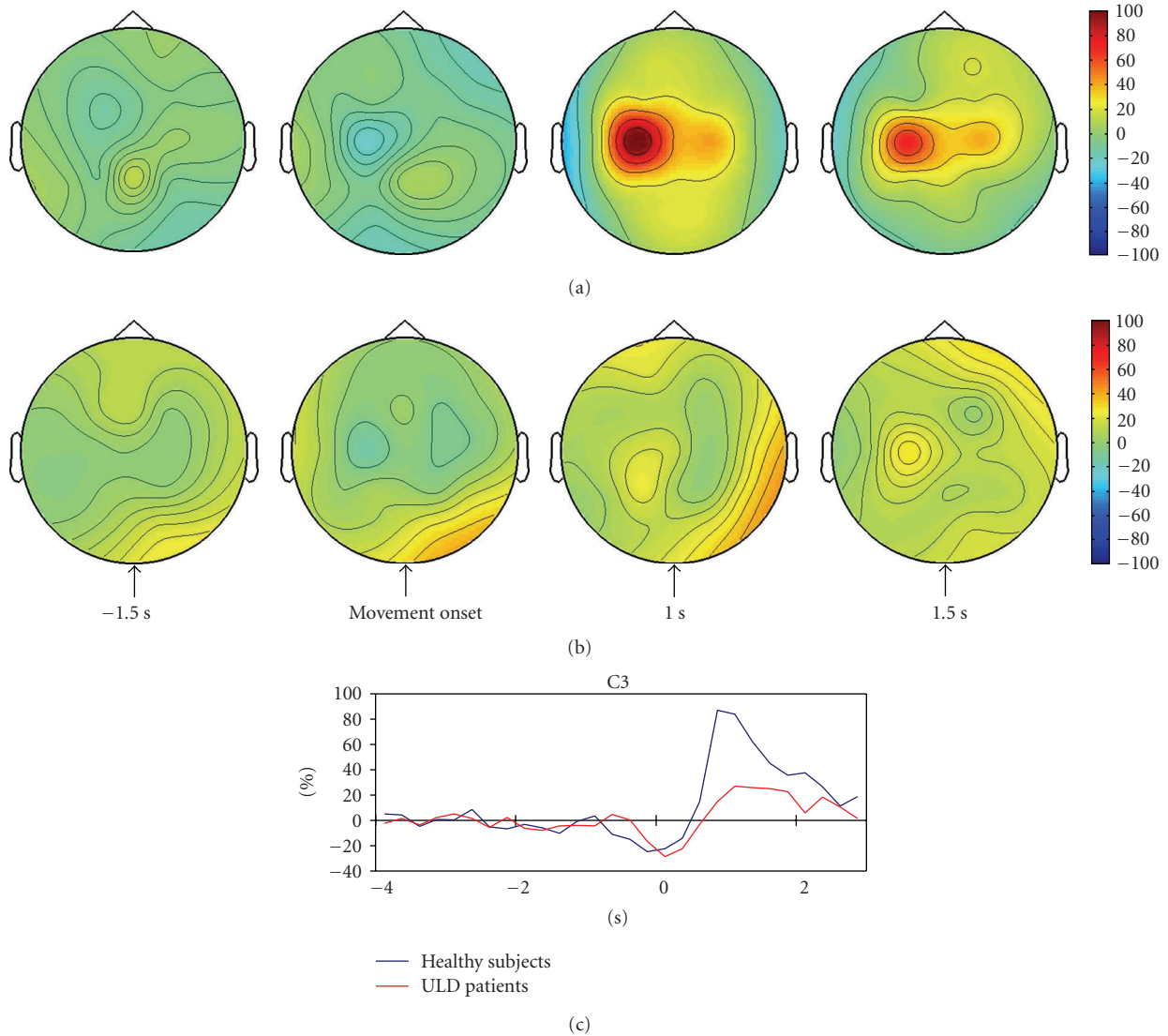


FIGURE 2: Color maps showing the grand average of  $\beta$ -ERD/ERS in control subjects (a) and patients (b). Color scale: maximum ERD and ERS are coded in blue and red. The lower panel (c) shows the grand average of  $\beta$ -ERD/ERS time series recorded from the contralateral central derivation in patients and controls.

motor area ( $0.58 \pm 0.15\%$  versus  $0.60 \pm 0.17\%$ ,  $P = .8$ ). There was, however, a trend towards longer response latency in patients, which reached statistical significance in the contralateral motor area ( $3.1 \pm 0.4$  s versus  $3.6 \pm 0.5$  s,  $P = .011$ ) and approached statistical significance in the contralateral supplementary motor area ( $3.1 \pm 0.4$  s versus  $3.4 \pm 0.2$  s,  $P = .08$ ); the effect was not found in the ipsilateral motor area ( $2.7 \pm 0.2$  s versus  $3.3 \pm 0.8$  s,  $P = .1$ ) (Figure 3).

#### 4. Discussion and Conclusions

The changes found in ERD/ERS pattern of ULD subjects suggest an increased activation of motor cortex during movement planning and a significant reduction of post-excitatory inhibition. These data overlap those obtained in our previous study [3] on EEG signal recorded in

standard laboratory and demonstrate the applicability of the event-related protocol during simultaneous EEG/fMRI.

Differently from ERD/ERS, fMRI did not highlight any clear difference in the amplitude of cortical activation in ULD patient with respect to controls. The hemodynamic response analysis allowed detecting subtle but significant effects on the time course of activation that showed a delayed peak in ULD patients. This finding, together with the slightly longer duration of individual movements in patients with respect to controls, may agree with a less efficient performance of the motor cortex in this disorder, characterized by a prominent motor dysfunction resulting in action activated myoclonic jerks. Based on the present data, the ERD/ERS changes detectable on EEG appear to be more reliable with respect to fMRI in detecting the cortical dysfunction characterizing ULD patients, being

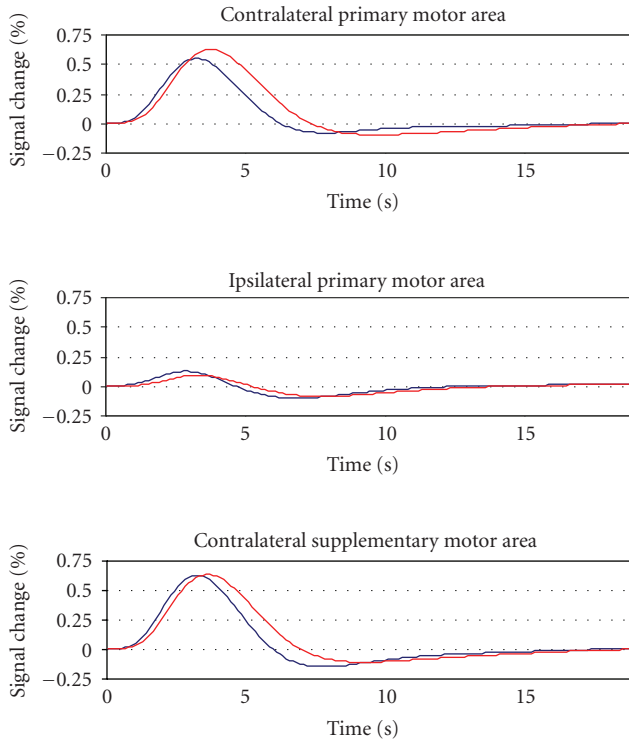


FIGURE 3: Time-courses of the hemodynamic response for controls (blue) and patients (red).

TABLE 2: Statistical analysis of ERD/ERS values assessed in subsequent epochs.

| Alpha ERD     | F4    | C4    | P4    | F3 | C3    | P3    | Fz    | Cz    | Pz    |
|---------------|-------|-------|-------|----|-------|-------|-------|-------|-------|
| $t_1$         | —     | 0.015 | —     | —  | —     | —     | —     | 0.032 | —     |
| $t_2$         | —     | 0.010 | —     | —  | —     | 0.042 | —     | —     | —     |
| $t_3$         | —     | 0.003 | —     | —  | —     | —     | —     | 0.003 | —     |
| $t_4$         | 0.045 | 0.010 | —     | —  | 0.015 | 0.004 | 0.007 | 0.003 | 0.032 |
| $t_5$         | —     | —     | —     | —  | —     | —     | —     | 0.007 | —     |
| Beta ERD/ERS* | F4    | C4    | P4    | F3 | C3    | P3    | Fz    | Cz    | Pz    |
| $t_1$         | —     | —     | —     | —  | —     | —     | —     | —     | —     |
| $t_2$         | —     | —     | —     | —  | —     | —     | —     | —     | —     |
| $t_3$         | —     | —     | —     | —  | —     | —     | —     | —     | —     |
| $t_4$         | 0.032 | —     | 0.007 | —  | 0.032 | —     | 0.015 | —     | —     |
| $t_5$         | —     | 0.032 | 0.022 | —  | 0.012 | —     | —     | 0.010 | —     |

Results of  $U$ -Mann Whitney test between patients and controls group. —= not significant. \* $t_1$ -  $t_3$  correspond to beta ERD and  $t_4$ - $t_5$  to beta ERS.

able to detect and quantify the functional changes of the neuronal pools impaired by the disease. A final conclusion cannot however be reached because of the small number of observation that limited the statistical power; moreover, further analyses exploring the functional connectivity during motor performance may allow to better detect subtle changes in the BOLD signals [7].

## Acknowledgment

The research leading to these results has received funding from the European Community’s Seventh Framework Programme (FP7/2007–2013) under Grant agreement no. HEALTH-F5-2008-201076.

## References

- [1] G. Pfurtscheller and F. H. Lopes da Silva, “Event-related EEG/MEG synchronization and desynchronization: basic principles,” *Clinical Neurophysiology*, vol. 110, no. 11, pp. 1842–1857, 1999.
- [2] M. Koskineemi, E. Toivakka, and M. Donner, “Progressive myoclonus epilepsy. Electroencephalographical findings,” *Acta Neurologica Scandinavica*, vol. 50, pp. 333–359, 1974.
- [3] E. Visani, P. Agazzi, L. Canafoglia, et al., “Movement-related desynchronization-synchronization (ERD/ERS) in patients with Unverricht-Lundborg disease,” *NeuroImage*, vol. 33, no. 1, pp. 161–168, 2006.
- [4] K. Virtaneva, E. D’Amato, J. Miao, et al., “Unstable minisatellite expansion causing recessively inherited myoclonus epilepsy, EPM1,” *Nature Genetics*, vol. 15, no. 4, pp. 393–396, 1997.
- [5] A. Magauda, P. Gelisse, and P. Genton, “Antimyoclonic effect of levetiracetam in 13 patients with Unverricht-Lundborg disease: clinical observations,” *Epilepsia*, vol. 45, no. 6, pp. 678–681, 2004.
- [6] H. Laufs, J. Daunizeau, D. W. Carmichael, and A. Kleinschmidt, “Recent advances in recording electrophysiological data simultaneously with magnetic resonance imaging,” *NeuroImage*, vol. 40, no. 2, pp. 515–528, 2008.
- [7] K. Li, L. Guo, J. Nie, G. Li, and T. Liu, “Review of methods for functional brain connectivity detection using fMRI,” *Computerized Medical Imaging and Graphics*, vol. 33, no. 2, pp. 131–139, 2009.

## Research Article

# Cross-Correlation of Motor Activity Signals from dc-Magnetoencephalography, Near-Infrared Spectroscopy, and Electromyography

Tilmann H. Sander,<sup>1</sup> Stefanie Leistner,<sup>2</sup> Heidrun Wabnitz,<sup>1</sup> Bruno-Marcel Mackert,<sup>2,3</sup> Rainer Macdonald,<sup>1</sup> and Lutz Trahms<sup>1</sup>

<sup>1</sup> Division of Medical Physics, Physikalisch-Technische Bundesanstalt, Abbestraße 2-12, 10587 Berlin, Germany

<sup>2</sup> Department of Neurology, Charité Campus Benjamin Franklin, 12200 Berlin, Germany

<sup>3</sup> Department of Neurology, Vivantes Auguste Viktoria Klinikum, 12157 Berlin, Germany

Correspondence should be addressed to Tilmann H. Sander, [tilmann.sander-thoemmes@ptb.de](mailto:tilmann.sander-thoemmes@ptb.de)

Received 16 June 2009; Accepted 26 October 2009

Academic Editor: Laura Astolfi

Copyright © 2010 Tilmann H. Sander et al. This is an open access article distributed under the Creative Commons Attribution License, which permits unrestricted use, distribution, and reproduction in any medium, provided the original work is properly cited.

Neuronal and vascular responses due to finger movements were synchronously measured using dc-magnetoencephalography (dcMEG) and time-resolved near-infrared spectroscopy (trNIRS). The finger movements were monitored with electromyography (EMG). Cortical responses related to the finger movement sequence were extracted by independent component analysis from both the dcMEG and the trNIRS data. The temporal relations between EMG rate, dcMEG, and trNIRS responses were assessed pairwise using the cross-correlation function (CCF), which does not require epoch averaging. A positive lag on a scale of seconds was found for the maximum of the CCF between dcMEG and trNIRS. A zero lag is observed for the CCF between dcMEG and EMG. Additionally this CCF exhibits oscillations at the frequency of individual finger movements. These findings show that the dcMEG with a bandwidth up to 8 Hz records both slow and faster neuronal responses, whereas the vascular response is confirmed to change on a scale of seconds.

## 1. Introduction

The methodologies to characterize neurovascular coupling in humans [1] can be separated at least into two categories. The first relies on two sequential measurements of the same subject and infers coupling parameters, the second performs multimodal synchronous measurements of neuronal and vascular effects, and the coupling is observed directly. The second methodology is technically more complicated, but the effect of a subject's performance changing between two measurements is eliminated. Furthermore it allows to study the coupling on continuous time series, that is, without relying on epoch averages removing the variability between individual epochs. Results from these approaches complement the detailed findings for neurovascular coupling obtained from invasive studies in animals [2].

One possibility to study neurovascular coupling by synchronous measurements was described in [3–5] combining dc-magnetoencephalography (dcMEG) with time-resolved near-infrared spectroscopy (trNIRS) during intermittent finger movements. These synchronous measurements were so far limited to a bandwidth from DC to 0.4 Hz due to the modulation technique used for the dcMEG [4]. With the possibility to obtain unmodulated dcMEG in a magnetically extremely shielded room [6, 7] the bandwidth of the synchronous measurements is considerably increased; that is, slow signal changes close to DC and standard neuronal responses above 1 Hz can be recorded at the same time. To keep in line with earlier literature the term dcMEG is maintained, but it denotes here a bandwidth of the signal from 0.01 Hz to about 8 Hz. Oscillatory signals at higher frequencies such as the  $\gamma$ -rhythm will not be considered here.

An alternative method [8] used trains of somatosensory MEG responses at latencies between 20 and 100 milliseconds and the related NIRS responses. These fast MEG responses can be measured in standard shielded rooms, where the lower MEG bandwidth limit is 0.1 Hz. The fast neuronal responses are well suited to investigate the linearity of neurovascular coupling, but to study temporal characteristics of the coupling the dcMEG and related stimulation paradigms seem more appropriate. Often neurovascular coupling is studied through the combination of electroencephalography (EEG) and functional magnetic resonance imaging (fMRI) [9]. This combination again allows to record only fast neuronal responses and the EEG contains strong fMRI induced artifacts.

An intermittent finger movement of 30-second duration was chosen as the paradigm to induce neurovascular responses here. The finger movement was monitored by recording the lower arm muscle EMG. This allows to employ the well-known coupling between EEG or MEG signals of the motor cortex and peripheral muscle activity [10] as a control parameter. Using independent component analysis (ICA) single unaveraged time series related to the finger movements were extracted from the multichannel dcMEG and trNIRS data. The frequently applied coherence cannot be estimated here in a meaningful way as 30 event repetitions in a 30-minute measurement session are not sufficient to obtain reliable spectral statistics. Therefore the coupling between the dcMEG, trNIRS, and EMG time series was analyzed using the cross-correlation function (CCF). The suitability of this approach for our experimental setting is assessed.

## 2. Material and Methods

**2.1. Measurement Technique and Preprocessing.** The measurement setup is similar to the setup combining modulated dcMEG with trNIRS as described in [4]. The trNIRS instrument operates at the wavelengths 690 nm, 803 nm, and 826 nm and is equipped with one source and four detector optodes. The detector optodes are arranged in a cross with the source in the center and a source-detector separation of 3 cm. In the present study, the logarithm of the relative count rate, that is, the change in attenuation at each wavelength with respect to a baseline interval, is used as NIRS parameter for the analysis. This allows the application of ICA at the wavelength level, which is not possible anymore after estimation of oxy- and deoxy-hemoglobin changes from the attenuation. With respect to the dcMEG, the present setup is improved employing the stationary, unmodulated dcMEG technique [3] with a sampling rate of 500 Hz. Both, dcMEG and trNIRS sensors, were approximately centered above the motor cortex contralateral to the finger movements. To control the subjects performance, the peripheral signals EMG, heartbeat, and respiration were measured in simultaneous recording tracks. The data set presented here is a representative example from a group study of six subjects.

A highly structured finger movement pattern of the right hand was used as the stimulation paradigm. This movement

pattern requires some practice before the measurement and ensures the attention of the subject during the experiment. The paradigm consists of a continuous sequence of finger contractions of the right hand: 2 \* thumb, 2 \* ring finger, 2 \* index finger, 2 \* middle finger, and 2 \* little finger. The two contractions of each finger should be performed within a second and the full sequence lasted typically 5 seconds. Naturally the individual speed was variable. Following an auditory cue, which was the prerecorded word “fast” chosen for its brevity and motivating appeal, the subjects had to start this structured finger movement. After 30 seconds of continuous movement another cue (“stop”) indicated the start of the 30 seconds rest period. This cycle was repeated 30 times resulting in a measurement duration of 30 minutes. The first and last two epochs (trials) from a measurement session were discarded, in order to eliminate edge effects due to highpass filtering of the raw dcMEG data at a frequency of 0.01 Hz, so that 26 of the 30 epochs remain (see Figure 1). In the following both the on/off cycles, that is, the intermittent finger movement and the rhythm of the finger movement within each 30 seconds period will be important.

To obtain the response due to the intermittent finger movement paradigm ICA was applied separately to dcMEG and trNIRS as demonstrated before in [7]. The ICA algorithm chosen was SOBI/TDSEP [11, 12], which is well suited to extract signals with a clear spectral structure as expected here due to the repetitive block design paradigm with 30 seconds of movement followed by 30 seconds of rest. The actual calculation is performed in the time domain as cross-covariances for a given delay  $\tau_k$  between signal channels  $x_i$ :  $C_{ij}(\tau_k) = \sum x_i(t)x_j(t + \tau_k)$ . A group of matrices  $\{C(\tau_k)\}$  is then diagonalised and the approximate diagonalising operator yields the independent components.

The groups of component time series resulting from the ICA for the magnetic field  $B(t)$  and the attenuation  $\Delta A(t)$  are searched each for a single time series with the highest correlation to the stimulation. These  $B(\text{dcMEG-ICA})$  and  $\Delta A(\text{trNIRS-ICA})$  time series and its associated component maps are then taken as the neuronal and vascular response to the finger movement. Only a single component was selected as all other components had a weak correlation with the stimulation sequence. Clearly it cannot be decided whether the single ICA component accounts for the whole motor response, but individual data sets with a good signal-to-noise ratio indicate this through the similarity between the ICA component and the standard average. At present the search is not automated, but the epoch averages of the ICA component time series are inspected manually. Although the ICA calculation is performed on nonaveraged raw data, the averaged ICA time series will be shown below.

Two parameter options have to be chosen for the SOBI/TDSEP algorithm: the first is the bandwidth of the signals and the second is the set of delays  $\{\tau_k\}$ . Both parameters have to be chosen heuristically due to the lack of a theoretical foundation. In the MEG strong cortical background signals can be found in the  $\alpha$ - and  $\beta$ -band starting around 8 Hz. It was found that ICA extracts a better movement-related response if the signal bandwidth is limited to 0.01–8 Hz excluding the background signals. The upper

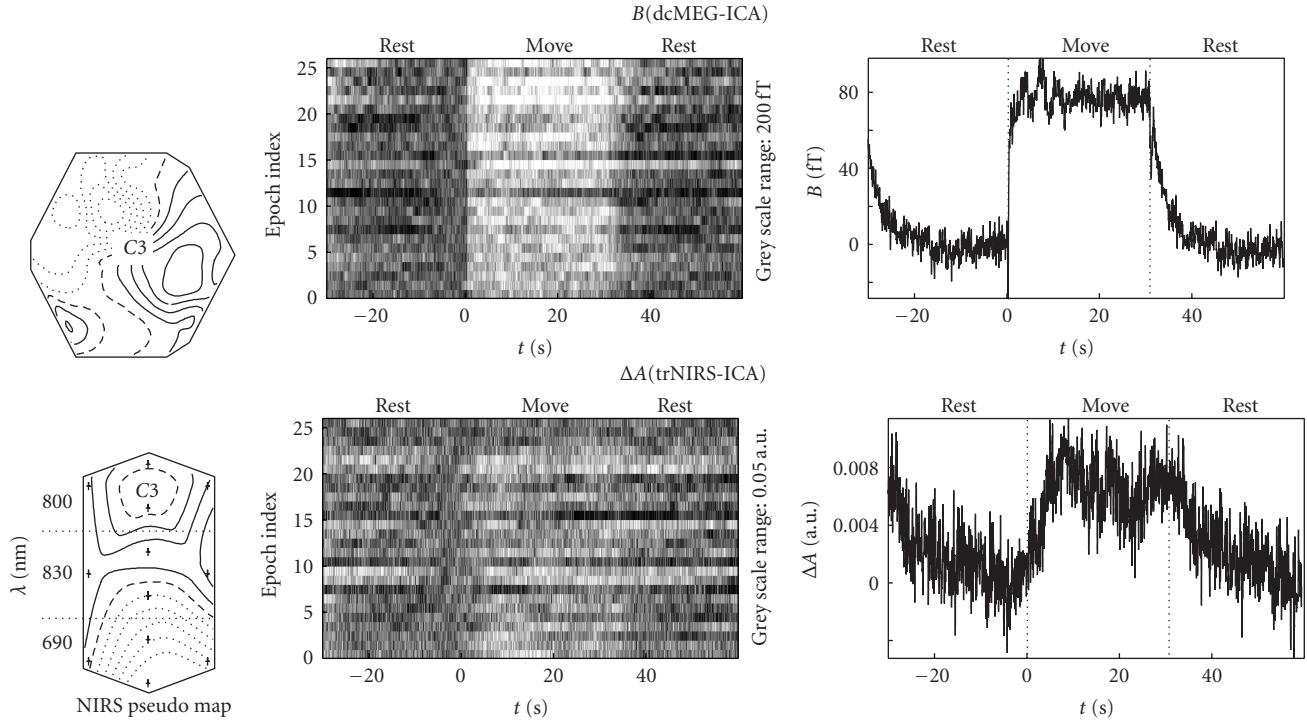


FIGURE 1: ICA components for  $B$  (dcMEG) and  $\Delta A$  (trNIRS) due to finger movement. The component and its time series are characterized by the ICA map (left, see text for details of trNIRS map), the ST plot of the time series (middle), and the epoch average of the time series (right). In the averages the signal change between rest and move is clearly visible; in the ST plot it is more pronounced for  $B$ . The slower onset of  $\Delta A$  compared to  $B$  at the beginning of the move window is obvious.

limit of 8 Hz has the additional advantage that then dcMEG and trNIRS have a similar upper band limit as the trNIRS is sampled at 20 Hz. The lower limit of 0.01 Hz is chosen to exclude monotonous signal drifts during the 30-minute measurement. Such monotonous signals are nonstationary and violate the ICA assumptions. Filtering as preprocessing is often performed implicitly by analog filters in the signal conditioning chain if ICA is applied to MEG data with a bandwidth of, for example, 1 to 100 Hz.

The set of delays  $\{\tau_k\}$  was optimized in a heuristic search using all data sets from the group study; that is, for a new set of delays SOBI/TDSEP was recalculated for all data sets in the group. This search was possible through a parallel implementation of the ICA algorithm running on a PC cluster (<http://www.rocksclusters.org/>) using a parallel computation interface (<http://www.open-mpi.org/>) and optimized linear algebra routines (<http://math-atlas.sourceforge.net/>). The final set of delays chosen for SOBI/TDSEP was  $\{\tau_k\} = \{0.2, 0.4, 0.6, \dots, 60.0, 60.012, 60.024, \dots, 120.0\}$  seconds. This set does not consist of evenly spaced delays, but it has a higher number of cross-covariance matrices at delays  $\tau_k$  in the range of the 60 seconds stimulus repetition rate. This turned out to extract a better movement-related response.

From the measured EMG a rate (EMGR) was calculated by a process called amplitude demodulation. The full bandwidth EMG (sampling frequency 500 Hz, lowpass 250 Hz) was rectified and then input into a modified Paynter filter (readily available in <http://sourceforge.net/projects/biosig/>)

with an 8 Hz lowpass characteristics. The resulting signal is the envelope of the oscillatory EMG signal. With respect to the subsequent cross-correlation analysis it was important that all signals had the same bandwidth. Therefore the heart rate derived from the ECG was filtered with the 8 Hz lowpass too.

**2.2. Cross-Correlation Analysis.** The CCF (e.g., [13]) is a tool to detect common periodicities between two time series, if the length of the time series is large compared to the oscillation period of interest. Given two time series  $u_t$  and  $v_t$  with  $n$  points their cross-correlation as a function of lag  $\tau$  is given by

$$\text{CCF}_{uv}(\tau) = \frac{1}{n\sqrt{\text{VAR}(u_t)\text{VAR}(v_{t+\tau})}} \sum_{t=t_0}^{t_n} (u_t - \bar{u}_t)(v_{t+\tau} - \bar{v}_{t+\tau}), \quad (1)$$

where  $\tau = 0, 1, \dots, (m-1)$  up to a maximum lag  $m \ll n$  and  $\text{VAR}(x)$  is the sample variance. Due to the shifting of  $v_t$  by the lag  $\tau$  the absolute positions of the cross-correlation maxima are related to phase shifts [13] for signals with similar basic periodicity.

For the time series related to the intermittent finger movements two types of CCFs were investigated. The first was calculated using the complete unaveraged ICA time series of 26 minutes duration covering all rest/move sequences. This CCF probes for the coupling related to the

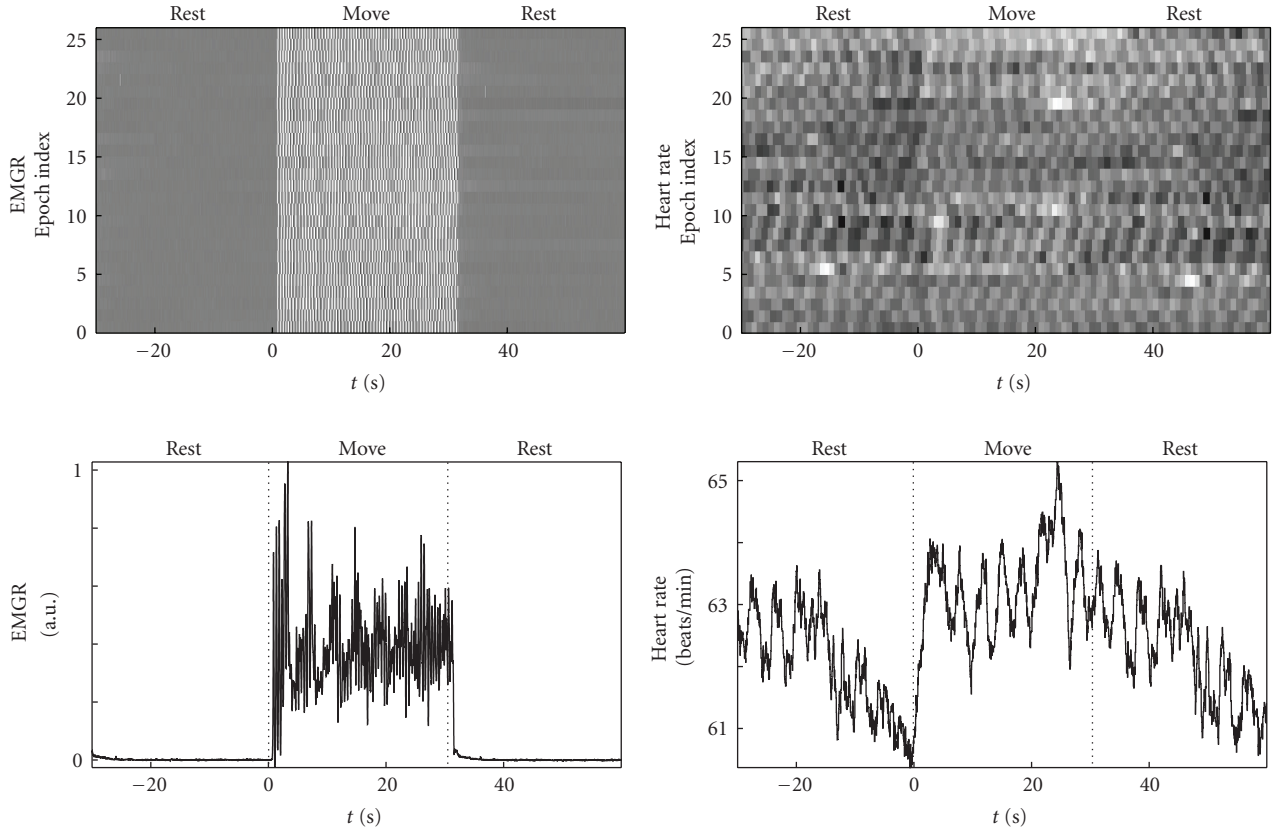


FIGURE 2: ST plots and resulting averages over the epochs of EMGR rate (top) and heart rate (bottom). The ST plots show that the changes observed in the average are not due to outliers in a single epoch.

transition between the two states, that is, fingers moving and at rest. The second was calculated for a new time series created by concatenation of the *move windows* with their mean values subtracted to minimize steps between the windows. This second type of CCF probes the coupling due to the rhythm of the finger movement. CCFs were calculated pairwise for a “signal triangle” consisting of  $B$ ,  $\Delta A$ , and EMGR.

### 3. Results

**3.1. dcMEG, trNIRS, and EMGR Time Series.** The continuous dcMEG and trNIRS time series extracted by ICA,  $B$ (dcMEG-ICA) and  $\Delta A$ (trNIRS-ICA), are presented in Figure 1 using single trial (ST) plots. In an ST plot the continuous data are segmented into identical intervals and aligned at the time of the auditory start instruction. Epochs are presented in a stacked plot, where the amplitude value is coded as a shade of grey. This results in a two-dimensional grey-scale image of the complete continuous time series. A baseline correction is calculated in the 5-second window prior to finger movement onset. In Figures 1 and 2 the zero of the time axis corresponds to the auditory start instruction and the labels “rest” and “move” are added to emphasize the different regions. The dashed vertical lines

in the average indicate the start and end of the “move” window.

ICA-extracted maps, ST plots, and averages of the finger movement-induced responses are shown for  $B$  and  $\Delta A$  in Figure 1. For  $\Delta A$  a pseudomap is used, which has a vertically elongated outline and dotted horizontal lines separating three wavelengths zones. In each zone the geometrical arrangement of the four detector optodes is indicated by the large dots. The interpolation is performed across the map and, therefore, the transitions across a dotted horizontal line have no meaning and each zone should be considered separately. The  $B$ -field map is a conventional field map displaying multichannel (scalar) magnetic field data. The motor cortex for right hand finger movements is typically associated with the EEG position C3 in the international 10–20 system for electrode placement and C3 is shown in the  $B$ -field map and the 800 nm part of the  $\Delta A$  pseudomap in Figure 1. A source close to the center of the dcMEG sensor can be deduced from the dipolar structure of the  $B$ -field map. This is the expected result for position C3 and motor activity. The four-detector trNIRS setup covering roughly an area of 9 cm<sup>2</sup> does not allow an accurate localization of the cortical trNIRS response, but the different sign of  $\Delta A$  at 690 and 830 nm is a typical signature of cortical activity. This confirms that the positioning above the motor cortex was successful.

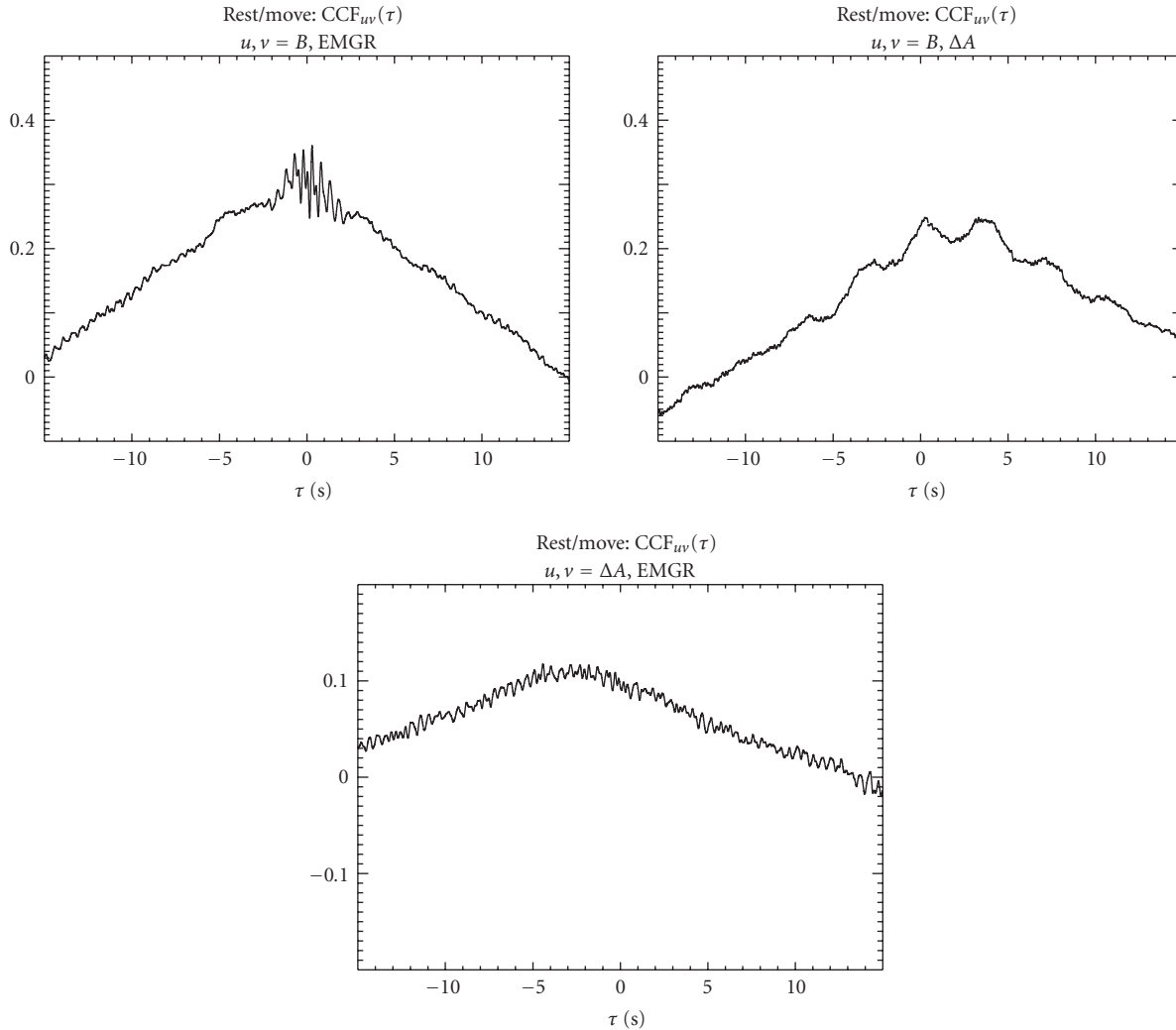


FIGURE 3: Pairwise CCFs of the measured modalities using the continuous time series, that is, including all rest/move cycles, for time lags from  $\tau = -15$  to 15 seconds. Note the different  $y$ -axis of the bottom figure. The highest correlations are reached for  $CCF(B, EMGR)$  and the curve is fairly symmetric with respect to zero lag ( $\tau = 0$  seconds). The correlations are slightly lower for  $CCF(B, \Delta A)$  and the peak of the curve is shifted to positive  $\tau$ . Low correlations result for  $CCF(\Delta A, EMGR)$  and the peak of the curve is shifted to negative  $\tau$ .

For  $B$  almost all epochs show a response during finger movement in the ST plots in Figure 1 and for  $\Delta A$  the same holds despite a larger variability. Note that the grey-scale range in the ST plot for  $\Delta A$  is five times larger than the resulting average value. This is a consequence of the large variability in the  $\Delta A$  single responses, which is most likely due to physiological noise. The overall stable responses in the ST plots show that the time series extracted by ICA are correctly attributed to the intermittent finger movements. Most important is the immediate rise in the  $B$  signal (neuronal response) at finger movement onset contrasting with the much slower rise in the  $\Delta A$  signal (vascular response).

The ST plots and associated epoch averages of the peripheral signals are shown in Figure 2. The sharp rise in the EMGR after  $t = 0$  seconds both in the ST plot and the average shows the immediate start of finger movements. The heart rate shows a rapid increase at the beginning of the finger

movement followed by oscillations around a constant value and a slow decrease after the end of finger movements. In the EMGR and the heart rate oscillations with a periodicity of 3 seconds to 4 seconds are visible in Figure 2. It is beyond the scope of this work to investigate this effect in detail, but preliminary cross-correlation results indicate coupling between heart rate and EMGR.

**3.2. Cross-Correlation.** The pairwise CCFs of the full continuous time series covering all rest/move epochs are shown in Figure 3 for the “signal triangle” consisting of  $B$ (dcMEG-ICA),  $\Delta A$ (trNIRS-ICA), and EMGR. For  $CCF(B, EMGR)$  the maximum correlation is reached around  $\tau = 0$  seconds with superimposed oscillations. For  $CCF(B, \Delta A)$  the peak of the curve is shifted to (positive)  $\tau \sim 2$  seconds, which means that  $\Delta A$  has a phase lag towards  $B$  as the order of the arguments is relevant for  $CCF(t)$  (see equation (1)).

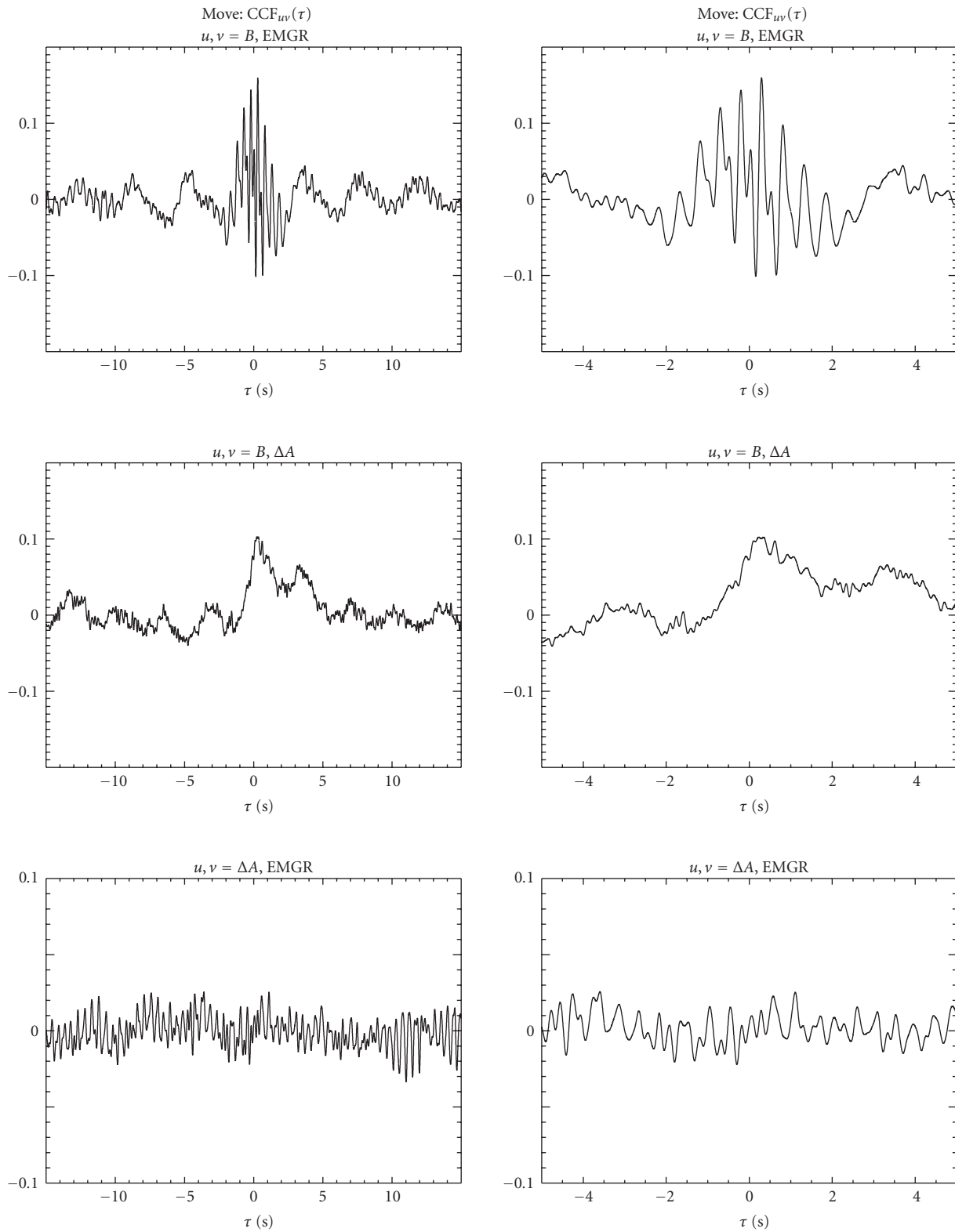


FIGURE 4: Pairwise CCFs for the time series consisting of the concatenated move windows. Two time lag ranges are displayed:  $\tau = -15$  to 15 seconds (left column) and  $\tau = -5$  to 5 seconds (right column). Note the different y-axis of the figures at the bottom. Two separate periodicities are observed only in  $\text{CCF}(B, \text{EMGR})$ .

This phase shift is consistent with the data in Figure 1. The peak of the CCF( $\Delta A$ , EMGR) curve is shifted to negative  $\tau$ , which is consistent with the immediate EMGR increase following finger movement onset as can be seen in Figure 2 and the much slower signal change in  $\Delta A$  in Figure 1. The lower absolute correlation of CCF( $\Delta A$ , EMGR) compared to CCF( $B$ , EMGR) shows that the overall signal shape differs more for CCF( $\Delta A$ , EMGR) again consistent with Figures 1 and 2. The peak shift to positive  $\tau$  in CCF( $B$ ,  $\Delta A$ ) was seen before in a preliminary investigation [7].

In Figure 4 the CCFs of the time series consisting of the concatenated *move windows* are shown for the “signal triangle” for two different  $\tau$  ranges. The CCF( $B$ , EMGR) function in Figure 4 (top) shows rapid oscillations around  $\tau = 0$  seconds and slower oscillations with a period of 4 seconds throughout the  $\tau$  range. Such clear oscillations are observed neither in CCF( $B$ ,  $\Delta A$ ) nor in CCF( $\Delta A$ , EMGR). The detailed plot of CCF( $B$ , EMGR) around  $\tau = 0$  seconds (right column) shows that the rapid oscillations have a periodicity of 0.5 seconds. These rapid oscillations could be attributed to the coupling between neuronal signal and each individual finger contraction. This interpretation is consistent with the disappearance of the fast oscillations with increasing  $\tau$ . The naturally somewhat irregular rhythm of individual finger movements for the duration of the 30-second move windows implies that only short range temporal correlations exist. For larger  $\tau$  possibly the envelope of the finger contraction sequence is reflected in the CCF as the periodicity of 4 seconds is in the expected range. In CCF( $B$ ,  $\Delta A$ ) oscillations similar to the slow oscillations in CCF( $B$ , EMGR) are observed, which could be interpreted as variations in vascular demand related to the envelope of the finger movements. The 4-second periodicity of the slow oscillations is not in contradiction to the time scale of neurovascular coupling [1–3]. The indirect coupling from EMGR to  $B$  and then to  $\Delta A$  is apparently ineffective as CCF( $\Delta A$ , EMGR) is rather small and irregular.

#### 4. Conclusions

The synchronous triple measurement of dcMEG, trNIRS, and EMGR enabled a CCF analysis on continuous time series related to intermittent finger movements. The well-known difference in transition time for vascular and neuronal responses is reflected in a peak shift to positive  $\tau$  for CCF( $B$ (dcMEG-ICA),  $\Delta A$ (trNIRS-ICA)). The value of the peak shift might serve as a parameter [13] to quantify the temporal characteristics of neurovascular coupling. A coupling on the basis of individual finger movements is likely between EMGR and  $B$  as their CCF shows oscillations at the finger movement frequency. This means that the unmodulated dcMEG with the increased bandwidth up to 8 Hz represents both slow and faster neuronal processes. The absence of apparent coupling between  $\Delta A$  and EMGR indicates that the vascular response does not follow the individual finger movements. This is in agreement with the temporal characteristics of neurovascular coupling [1–3], that is, the peak shift in CCF( $B$ ,  $\Delta A$ ) here. The triple

measurement in combination with the signal extraction by ICA and the CCF analysis allows a powerful coupling analysis at several time scales. Future work will try to incorporate spontaneous and induced fluctuations in the finger movement intensity to characterize the temporal behavior and the linearity of the coupling in a single experiment.

#### Acknowledgments

General advice for this work by M. Burghoff and G. Curio is gratefully acknowledged. This work is supported by BMBF Grants 01 GO 0208 and 01 GO 0503, GF GO 01184601, Berlin Neuroimaging Center.

#### References

- [1] O. J. Arthurs and S. Boniface, “How well do we understand the neural origins of the fMRI BOLD signal?” *Trends in Neurosciences*, vol. 25, no. 1, pp. 27–31, 2002.
- [2] N. K. Logothetis, J. Pauls, M. Augath, T. Trinath, and A. Oeltermann, “Neurophysiological investigation of the basis of the fMRI signal,” *Nature*, vol. 412, no. 6843, pp. 150–157, 2001.
- [3] B.-M. Mackert, G. Wübbeler, S. Leistner, et al., “Neurovascular coupling analyzed non-invasively in the human brain,” *NeuroReport*, vol. 15, no. 1, pp. 63–66, 2004.
- [4] T. H. Sander, A. Liebert, B. M. Mackert, et al., “DC-magnetoencephalography and time-resolved near-infrared spectroscopy combined to study neuronal and vascular brain responses,” *Physiological Measurement*, vol. 28, no. 6, pp. 651–664, 2007.
- [5] B.-M. Mackert, S. Leistner, T. Sander, et al., “Dynamics of cortical neurovascular coupling analyzed by simultaneous DC-magnetoencephalography and time-resolved near-infrared spectroscopy,” *NeuroImage*, vol. 39, no. 3, pp. 979–986, 2008.
- [6] M. Burghoff, T. H. Sander, A. Schnabel, et al., “Dc magnetoencephalography: direct measurement in a magnetically extremely-well shielded room,” *Applied Physics Letters*, vol. 85, no. 25, pp. 6278–6280, 2004.
- [7] T. H. Sander, A. Liebert, M. Burghoff, H. Wabnitz, R. Macdonald, and L. Trahms, “Cross-correlation analysis of the correspondence between magnetoencephalographic and near-infrared cortical signals,” *Methods of Information in Medicine*, vol. 46, no. 2, pp. 164–168, 2007.
- [8] W. Ou, I. Nissilä, H. Radhakrishnan, D. A. Boas, M. S. Hämmäläinen, and M. A. Franceschini, “Study of neurovascular coupling in humans via simultaneous magnetoencephalography and diffuse optical imaging acquisition,” *NeuroImage*, vol. 46, no. 3, pp. 624–632, 2009.
- [9] C. S. Herrmann and S. Debener, “Simultaneous recording of EEG and BOLD responses: a historical perspective,” *International Journal of Psychophysiology*, vol. 67, no. 3, pp. 161–168, 2008.
- [10] P. Grosse, M. J. Cassidy, and P. Brown, “EEG-EMG, MEG-EMG and EMG-EMG frequency analysis: physiological principles and clinical applications,” *Clinical Neurophysiology*, vol. 113, no. 10, pp. 1523–1531, 2002.
- [11] A. Belouchrani, K. Abed-Meraim, J.-F. Cardoso, and E. Moulines, “A blind source separation technique using second-order statistics,” *IEEE Transactions on Signal Processing*, vol. 45,

no. 2, pp. 434–444, 1997.

- [12] A. Ziehe and K. R. Müller, “TDSEP—an efficient algorithm for blind separation using time structure,” in *Proceedings of the 8th International Conference on Artificial Neural Networks (ICANN '98)*, L. Niklasson, et al., Ed., pp. 675–680, Skövde, Sweden, September 1998.
- [13] L. Zhang and X. Wu, “On the application of cross correlation function to subsample discrete time delay estimation,” *Digital Signal Processing*, vol. 16, no. 6, pp. 682–694, 2006.

## Research Article

# Improvement of EEG Signal Acquisition: An Electrical Aspect for State of the Art of Front End

**Ali Bulent Usakli**

*Department of Technical Sciences, The NCO Academy, 10100 Balikesir, Turkey*

Correspondence should be addressed to Ali Bulent Usakli, [ausakli@yahoo.com](mailto:ausakli@yahoo.com)

Received 13 June 2009; Revised 4 August 2009; Accepted 2 November 2009

Academic Editor: Fabrizio De Vico Fallani

Copyright © 2010 Ali Bulent Usakli. This is an open access article distributed under the Creative Commons Attribution License, which permits unrestricted use, distribution, and reproduction in any medium, provided the original work is properly cited.

The aim of this study is to present some practical state-of-the-art considerations in acquiring satisfactory signals for electroencephalographic signal acquisition. These considerations are important for users and system designers. Especially choosing correct electrode and design strategy of the initial electronic circuitry front end plays an important role in improving the system's measurement performance. Considering the pitfalls in the design of biopotential measurement system and recording session conditions creates better accuracy. In electroencephalogram (EEG) recording electrodes, system electronics including filtering, amplifying, signal conversion, data storing, and environmental conditions affect the recording performance. In this paper, EEG electrode principles and main points of electronic noise reduction methods in EEG signal acquisition front end are discussed, and some suggestions for improving signal acquisition are presented.

## 1. Introduction

Although basics of the electroencephalogram (EEG) measurement in man have been the same since 1929, it was first made by Hans Berger, the technological developments give the opportunity to build much more sophisticated acquisition systems regarding clinical needs and scientific researches. The human brain generates electrical signals called EEG signals which are related to body functions, and this paper is about their acquiring. These signals are roughly less than  $100\ \mu\text{V}$  and 100 Hz and can be measured with electrodes placed on the scalp, noninvasively. Because of their low amplitude due to the skull's composition, the measurement of EEG is more difficult than the other noninvasive biosignal measurements such as the electrocardiogram, electromyogram, electrooculogram, and so forth. Having expensive bio-signal recording systems cannot guarantee acquiring proper signals. In that sense, some factors to acquire good EEG signals should be considered in new designs and during recording sessions. These major considerations are discussed and some suggestions are presented in this paper.

In bio-signal recordings, electrodes are the initial elements which are used for converting biopotential signals due to biopotential sources into electrical signals. Figure 1 shows

the simplified biopotential measurement. EEG electrodes are usually made of metal and are produced as cup-shaped, disc, needle, or microelectrode to measure intracortex potentials. Silver chloride (AgCl) is preferred for common neurophysiologic applications [1]. Because Ag is a slightly soluble salt, AgCl quickly saturates and comes to equilibrium. Therefore, Ag is a good metal for metallic skin-surface electrodes [2]. Choosing the correct electrode as well as preparation of the skin before recording affects the accuracy of the measurements.

Another major factor is electronic noise which is quite important for the bio-signal measurements. Electronic noise can be caused by internal and external noise sources. The internal noise sources are thermal (due to resistive components), shot (due to semiconductor holes and diffusions), flicker (due to contact pins), and burst (or popcorn, due to impurities in semiconductors) noise [3]. The most important external noise is caused by power-line interference. It is clearly seen in spectral analysis at 50 Hz (or 60 Hz). Between power lines and the subject there are capacitances (parasitic and isolation). To extract biosignals precisely from electronic noise requires efficient noise reduction methods [3, 4]. Efficient analog and/or digital filtering are needed for this purpose.

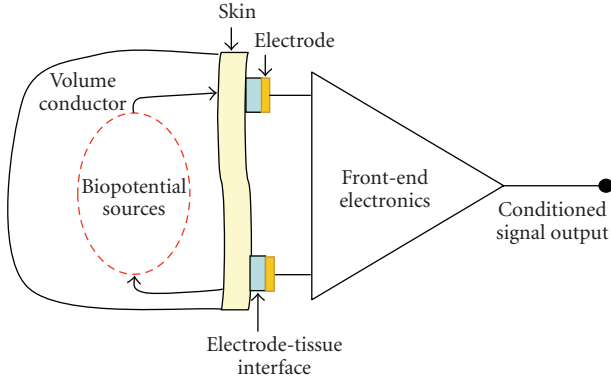


FIGURE 1: Biopotential measurement via electrodes.

In the following sections, EEG electrodes as well as EEG recording and design considerations are presented.

## 2. Materials and Methods

**2.1. EEG Electrodes.** Electrodes may be polarized (nonreversible) or nonpolarized (reversible). Polarization is avoided since the chloride ion is common to both the electrode and the electrolyte. Other metals such as gold or platinum can be used for electrode fabrication but is costly. Polarized electrodes tend to make significant capacitance, and this may interfere with the transmission of underlying bio-signals. These electrodes behave like a low-frequency filter (low-pass filter). Non-polarized electrodes, such as those of AgCl, are preferred for common neurophysiologic applications [1, 2]. Normal Ag/AgCl electrodes need to be chlorinated in time; however, sintered (making electrodes from powder, by heating the material in a sintering furnace below its melting point) Ag/AgCl electrodes do not need to be chlorinated.

The EEG electrodes can be classified as disposable reusable disc and cup shaped (EEG caps), subdermal needles (single-use needles that are placed under the skin), and implanted electrodes (to precisely pinpoint the origin of seizure activity). Needles are available with permanently attached wire leads, where the whole assembly is discarded, or sockets that are attached to lead wires with matching plugs. They are made of stainless steel or platinum. Some of EEG electrodes can be used for special applications. For example, implanted EEG electrodes also can be used to stimulate the brain and map cortical and subcortical neurological functions, such as motor or language function, in preparation for epilepsy surgery. Infection must be considered a major risk of implanted EEG electrodes.

In a noninvasive electrical brain signal measurement, there is an interface material between the electrode and the skin. This material is an electrolyte and can be in EEG gel or paste form. The electrophysiological activity caused by a biopotential source is a current source that causes current flow in the extracellular fluid and other conductive paths through the tissue.

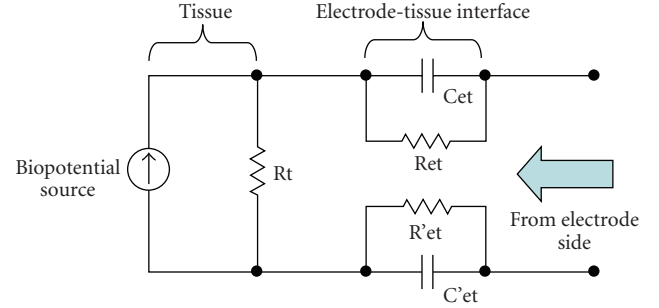


FIGURE 2: Simplified equivalent circuit of biopotential source and electrode-tissue interface from electrode. Biopotential source as a current source and tissue resistance is shown  $R_t$ .  $C_{et}$  and  $R_{et}$  electrode-tissue equivalent elements may change for each electrode contact.

A cup-shaped electrode provides enough volume to contain an electrolyte, including chlorine ions. In these electrodes, the skin never touches the electrode material directly. The electrode-tissue interface has impedance depending on several factors. Some of these factors are the interface layer (such as skin preparation, fat mass, hair, etc.), area of electrode's surface, and temperature of the electrolyte. The electrode-tissue contact can be modeled as in Figure 2. As it is seen from the figure, the electrode-tissue interface not only is resistive but consists of capacitive elements too. This is important for the frequency dependency of the electrode-skin contact.

Because of the interaction between metallic electrode and electrolyte, the ions accumulated as parallel plates. Ion-electron exchange occurs between the electrode and the electrolyte. This exchange results in voltage and it is called the half-cell potential. Because of this potential, in some cases, biopotential amplifiers must tolerate up to  $\pm 300$  mV. This value depends on the electrode and electrolyte materials. This can be explained by the Nernst Equation, simply, as

$$\varepsilon = \varepsilon^0 - \frac{0,05916}{n_e} \log Q. \quad (1)$$

Here, we have  $\varepsilon$ : Half-cell potential (V),  $n_e$ : Transported electron (mol number), and  $Q$ : Rate of inside and outside ions:  $Q = [\text{Ions}_{\text{Inside}}]/[\text{Ions}_{\text{Outside}}]$ .

In clinical EEG recordings, 10/20 Electrode Placement System is a standard and in general, it has been used for many clinical or research applications [5]. Although there are 75 locations in this system, 8 to 32 electrodes may be sufficient for clinical applications. 8 channels can also be sufficient for some Brain Computer Interface (BCI) applications; on the other hand, for Electrical Source Imaging (ESI) more than 100 channels are required. Electrodes are positioned over the frontal, temporal, parietal, and occipital lobes, and odd and even numbers refer to the left and right hemispheres, respectively. Because of the requirements, another placement system is 5% electrode placement and 345 locations are determined [6], but it is not a common standard.

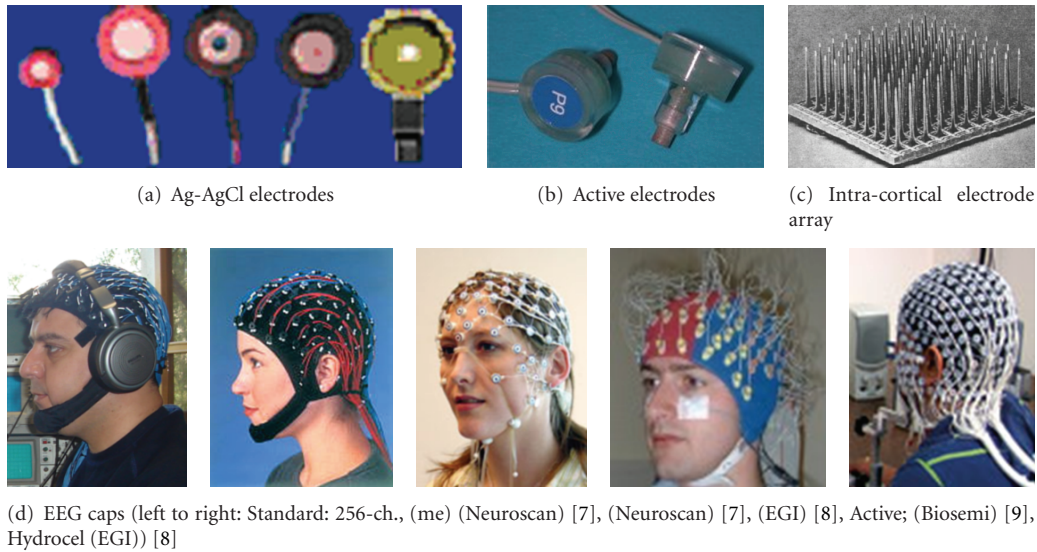


FIGURE 3: Commercially available EEG electrodes and cap samples; (c) is for invasive applications.

**2.2. EEG Recordings.** In the EEG system, as a non-invasive application, the electrodes are placed on the scalp, and a sufficient number of electrodes may be 1 to 256 (or more in near future) placed on EEG cap for easy application. To provide ionic current and to reduce contact impedance between the electrode surface and the scalp, EEG gel or paste must be used together for proper skin preparation. In biopotential measurements, the most important point is preserving the biosignal's originality. The contact impedance should be between  $1\text{ k}\Omega$  to  $10\text{ k}\Omega$  to record an accurate signal. Less than  $1\text{ k}\Omega$  contact impedance indicates a possible shortcut between electrodes; on the other hand, impedance greater than  $10\text{ k}\Omega$  can cause distorting artifacts.

Drying the gel or paste in time, as well as the subject's perspiration and movements (eye blinks, muscle movements, heart beats, etc.), can easily affect the measurement performance negatively. Because of these reasons, recording time is generally limited for several hours. For long periods of time or ambulatory EEG recordings, additional requirements are necessary to make patients more comfortable and to allow for consistent system performance. High-resolution applications such as ESI or wireless data transfer also require a different approach for the design of the novel electrodes. To reduce the skin preparation time and to measure the bio-signals more accurately, several approaches are attempted for electrode fabrication. For example, multiarray thin film electrodes are developed especially for different depth in operational applications [10]; nitride-covered steel is used as an electrode and there is no need for EEG paste to result in successful recordings [11]. In the last few years, active electrode (small or unity gain amplifier close to electrode) research is gaining popularity. With these types of electrodes, without the use of electrode gel and with much more skin preparation, noise reductions are reported [9, 12–14].

In commercial applications, apart from classical cup- or disc-shaped electrodes and active electrodes, another

approach is used to reduce preparation time (by EGI's HydroCel Geodesic Sensor Net). In this approach, scalp preparation and abrasion are not required. Because the soft pedestal design of the chamber creates a sealed environment, it hydrates the skin and creates an interface between the skin and electrode. Application times for the sponge-based HydroCel Geodesic Sensor Net that range between 5 minutes for 32 channels to 15 minutes for 256 channels are reported [8]. In practical consideration, at least 45 minutes are required for the electrode while 15 minutes are reasonable in skin preparations for the 256-channel cup-shaped electrode cap. Figure 3 shows some EEG electrodes and caps commercially available. In this figure several examples as non-invasive electrodes and EEG caps as well as one intracortical electrode array are shown.

Another approach for fabricating EEG electrode is dry electrode (Figure 4). This type of electrode does not need an extensive set-up time, and it is convenient for long-term recordings. These properties are advantageous for BCI and neurofeedback applications. As an example, in order to design dry electrode,  $1.5\text{ mm}$  thick silicone conductive rubber-shaped discs of  $8\text{ mm}$  diameter are used. The active side of the electrode is capacitive and coupled through a layer of insulating silicon rubber with a metal shield wired to the active guard shield. The impedance of the realized electrodes at  $100\text{ Hz}$  is greater than  $20\text{ M}\Omega$  with a parasitic capacitance smaller than  $2\text{ pF}$  [15].

For under cortex applications intra-cortical electrodes are used. One of these types of electrodes (The Utah Intra-cortical Electrode Array) is an array of 100 penetrating silicon microelectrodes designed to electrically focus stimulation or record neurons residing in a single layer up to  $1.5\text{ mm}$  beneath the surface of the cerebral cortex [16]. Each electrode of the intra-cortical array electrode is  $1.5\text{ mm}$  long,  $0.08\text{ mm}$  wide at the base, and  $0.001\text{ mm}$  at the tip.

Each type of electrode should be used with a successful electronic circuit. In Figure 5 EEG electrode and initial signal

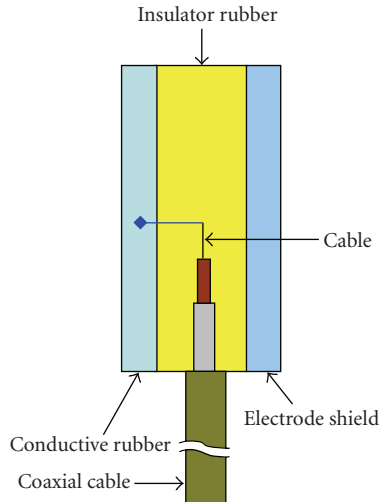


FIGURE 4: A dry electrode principle.

acquisition examples are shown. Recording environment conditions, contact impedance value and its stability, amplification method (ac or dc), and recording time must be considered. In the next subsection design considerations are explained, briefly.

**2.3. The Design Considerations.** In EEG recordings, as the other bio-signal measurements, one of the major problems is the 50 (or 60) Hz noise due to power lines. Between power lines and the subject there are capacitances (parasitic and isolation). Electromagnetic interference (EMI) ways are shown in Figure 6. The environmental factors influence the subject and measurement system. For example, a fluorescent lamp 1-2 m away from the measurement system interferes with the measuring signal as several kHz peaks. The interference signal may be half of the power line noise. In the same way, other electrical or electronic devices may interfere with the bio-signal measurements.

The dc component of the common mode signal is about several thousand, volts and the ac component may be about 1 V. This value may be in mV scale when the subject's body is grounded with earth ground and may be as high as 20 V when power line is held [17]. Electrostatic discharge (ESD) and defibrillator should be considered in electronic design. Protection for these must be provided for patient/subject and also initial active components. To reduce common mode signal effects, the instrumentation amplifiers having higher common mode rejection ratio (CMRR) must be used [18, 19]. Some research studies related to biopotential design report that 80–136 dB CMRRs are obtained [20–23]. To reduce isolation capacitance effects, battery powered operation is efficient [9].

In order to guarantee the subject/patient safety, leakage current should be less than the levels determined by IEC 601-1. According to this regulation, leakage current must be less than  $10\ \mu\text{A}$  in normal conditions, while regarding the connection to the main power supply,  $50\ \mu\text{A}$  is allowable.

Biopotential amplifiers can be dc coupled or ac coupled. In design strategy, dc or ac coupling and filtering (hardware or software) decisions are the initial steps for the biopotential measurement system designer. For ac amplification more than 10 bits digital resolution may be enough. However, for dc amplification, because number of effective bits is decreased, more than 20 bits are necessary for the analog digital converter (ADC). For high digital resolution sigma-delta technology ADC is one of good solutions [22, 23].

The input amplifier circuit is presented in Figure 7. It can be used wired electrodes (classical approach) or close to electrodes (active electrode approach). After the tests, it is observed that the circuit can be used for EEG, EOG or EMG signal measurements. This amplifier's gain is 16, and it does not cause biopotential amplifier saturation, and its CMRR is 102 dB under no shielding conditions or EMI protection.

### 3. Discussions

Acquiring EEG signal properly means mainly safety, bio-signal measurement with higher Signal to Noise Ratio (SNR) and no data loss. The major points that the author briefly proposed for the entire recording process are the following.

(i) *Subject/Patient Safety.* Because of the leakage current from system electronics and defibrillator (if used), subject/patient safety should be provided. Subject/patient and front-end circuitry and earth grounds should be separated (i.e., analog and digital grounds). Increasing the isolation mode rejection ratio of the amplifier reduces the influence of isolation mode voltage.

(ii) *EMI Protection.* Operation of electrical or electronic devices and especially fluorescent lamps near the recording set-up is prohibited. Otherwise acquired EEG signals are distorted and the signal corrupted with noise. Using instrumentation amplifier can help getting rid of this problem.

(iii) *No Subject/Patient Muscular Movements.* Muscular movements (i.e., EMG-related contamination) such as eye blinks, clenching teeth, movement of shoulders or legs, and so forth affect EEG signal acquisition, badly. These cases may cause wrong comments on the signals and signal processing error.

(iv) *ESD Protection.* Active electronic components must have greater than 2000 V ESD protection. No ESD protection may cause damage of active electronic components and may cause serious problem for subject/patient.

(v) *Efficient Grounding.* Metal cases must be connected to metal plate/rod buried under ground. Proper grounding technique helps to reduce noise therefore increasing SNR.

(vi) *Electrodes.* Choosing correct electrode and montage should be decided regarding clinical or research application purposes. In addition to availability of commercial standard or active types, electrodes can be made such as capacitive coupling or dry electrode. Number of electrodes and their placement is also important for the application.

(vii) *Electrode Contact Impedance.* Contact impedance value must be between 1 k $\Omega$  and 10 k $\Omega$  for classical electrodes. Less than 1 k $\Omega$  contact impedance indicates probable shortcut between the electrodes. Greater than 10 k $\Omega$  contact impedance prevents acquiring EEG signals. Before

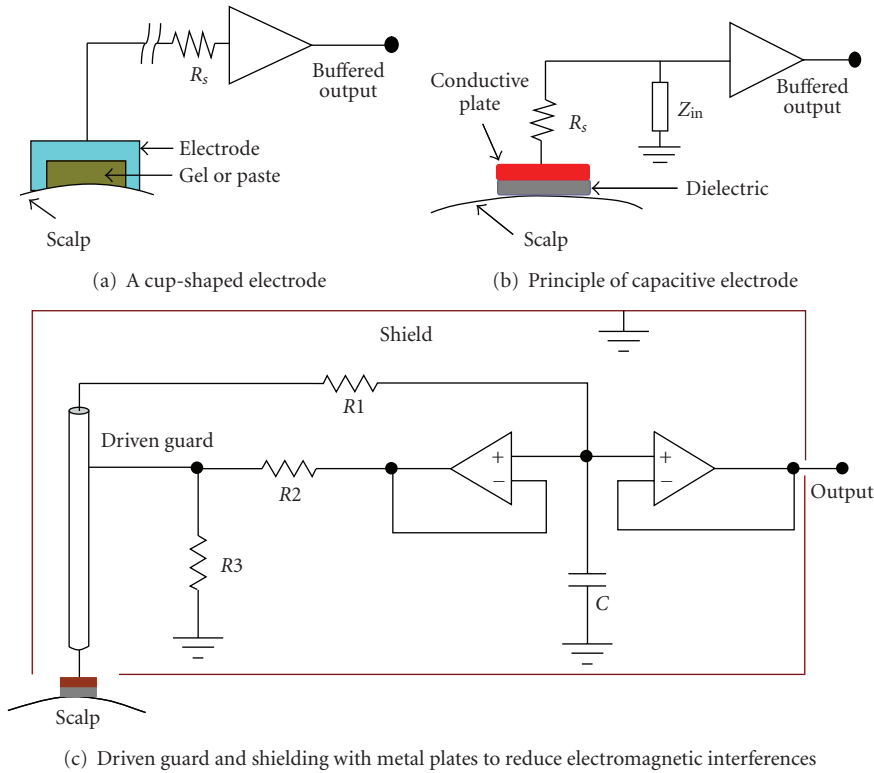


FIGURE 5: EEG electrode connections.

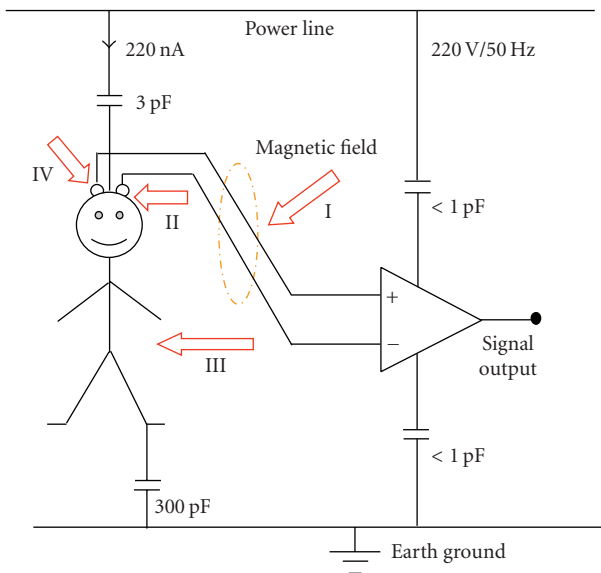


FIGURE 6: Electromagnetic interference (EMI) ways (for the capacitance values [9]). Arrows show the interference currents. (I) Voltage due to magnetic field to electrode cable loop is illustrated. (II) Displacement current on subject head due to electrical field causes voltage drop across electrodes. (III) Displacement current on subject body due to electrical field causes voltage drop across electrodes. (IV) Additionally, this current causes voltage between measurement electrode and amplifier common pin [24].

measurement, contact impedance should be measured, and EEG trace should be observed while recording. Using today's technology, high input impedance ( $>1\text{ G}\Omega$ ) amplifier chips and active electrode approaches decrease dependency of the contact impedance. To acquire proper signal, electrodes should not be moved. Otherwise it causes fluctuation of the EEG signal, and spikes on it.

(viii) *Noise Immunity*. Noise reduction techniques must be considered in electronic circuitry and printed circuit board design. Electronic cards and connection cables should be placed in a metal box to reduce electronic noise as much as possible. Using twisted, braided, and driven signal cables gives good results. Because EEG signals are low amplitude  $\mu\text{Vs}$ , they are very sensitive to electronic noise. Electronic noise should be less than  $2\text{ }\mu\text{V}$  (peak-to-peak).

(ix) *Environmental Conditions*. If the EEG system is combined with magnetic resonance imaging, it must be compatible for operating under a high magnetic field. Similarly, if the EEG system is used in an operation room while surgery, it should not be affected under high electronic noise conditions such as electro-cautery. Recording must be stable and ambient temperature should not affect system performance. System performance should be independent of reasonable temperature fluctuations.

(x) *Reduction for Common Mode Signals*. To reduce common mode signals, it is necessary to use instrumentation amplifier having greater than  $80\text{ dB CMRR}$ . This is important for high SNR signal acquisition.

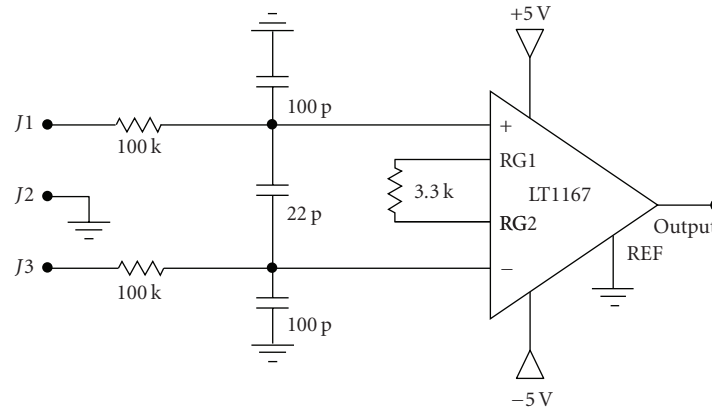


FIGURE 7: Suggested input amplifier circuit.

(xi) *Recording Mode.* Designer or user should decide the recording mode regarding their applications. EEG recordings can be bipolar (differentiated two close electrode signal), unipolar (differentiated common reference), or using averaged reference. Clinical or research applications require different recording modes.

(xii) *Reference and Ground Electrode Position.* Especially reference electrode placement is important for some applications. In general reference electrode is placed on vertex; ground electrode is placed on left or right (or together) ear.

(xiii) *Preserving the Biosignal Originality.* Linear and distortionless amplification must be provided. Otherwise signal processing (detection, pattern recognition, feature extraction, classification, and averaging, etc.) performances may decrease.

(xiv) *Avoiding Amplifier Saturation.* If the amplifier circuits saturate, analog signal loss is inevitable. Amplifier saturation is caused by high input signal, mainly due to electrode movements. In ac amplification, amplifier which is used before high-pass filtering must be fixed for optimum gain to avoid saturation level. If dc amplification is preferred, there is no amplifier saturation risk; on the other hand, number of efficient bit resolution is decreased.

(xv) *Cross-Talk Rejection.* For multichannel systems, cross-talk rejection must be high enough. Otherwise, channels can be affected from other channels; therefore, artifact exists.

(xvi) *Input Impedance.* Input impedance of the circuit must be high enough. For dc signals greater than  $1\text{ G}\Omega$  input impedance value gives good results. Low input impedance causes load of bio-signal source, and it causes damaging of the signal.

(xvii) *Input Bias Current.* Input bias current of the input amplifier must be as low as possible (pA). If bio-signal sources are loaded by input amplifier, it also causes distortion.

(xviii) *Frequency Band.* Selecting the proper filter band (at least band width must be  $0.5\text{ Hz}-70\text{ Hz}$ ) is important to acquire signal. This is also important for digitizing and data storing. Sufficient (and optimum) sampling rate ( $>140\text{ Hz}$ ) and transfer rate should be provided. Dc level should

be removed for efficient signal conditioning/processing in hardware or in software.

(xix) *Digitization.* Sufficient (and optimum) digital resolution ( $>10$  bits for ac amplification,  $>20$  bits for dc amplification) must be provided for analog to digital converter (ADC). If low digital resolution is used, the quantization error increases.

(xx) *Same Sampling Instants.* If the multichannel system is designed (or used), there must be no time delay between channels. For an analog multiplier, this may be a problem, however, not for a digital multiplier. To sample at the same time instants, sample and hold circuits should be used. If each analog channel has its own ADC, this can be made with ADC control signal timing.

(xxi) *Recording Time.* Sufficient (and optimum) recording time is necessary. Long-time recording (more than 2 hours) causes artifacts due to drying gel, perspiration and creating of anxiety in subject/patient. On the other hand, insufficient recording time causes insufficient data acquisition.

(xxii) *User Friendly.* The system hardware and software must be well integrated and must have user friendly interface.

(xxiii) *Low Power Consumption.* This is important for especially battery-powered systems.

(xxiv) *Low Cost.* The system should be cost effective, and components must be available.

## 4. Conclusion

There are major points that should be considered to improve the measurement performance in the design of the bio-signal measurement system or recording session. Specifically choosing the correct electrode, skin preparation, and reduction of power line noise are the important issues for EEG recordings. To reduce electromagnetic interferences, a metal box for electronic circuits, a shielded (Faraday cage principle) recording room, and guarding (driven or not) for common mode signal reduction are the efficient methods. The performance of the bio-signal measurement system depends on the electrodes, electronic circuitry, and recording conditions. Choosing the correct electrode and successful

electronic design strategy are essential to acquire EEG signals, properly.

## References

- [1] C. M. Sinclair, M. C. Gasper, and A. S. Blum, "Basic electronics in clinical neurophysiology," in *The Clinical Neurophysiology Primer*, A. S. Blum and S. B. Rutkove, Eds., pp. 3–18, Humana Press, Totowa, NJ, USA, 2007.
- [2] D. Prutchi and M. Norris, *Design and Development of Medical Electronic Instrumentation*, John Wiley & Sons, Hoboken, NJ, USA, 2005.
- [3] M. Leach Jr., "Fundamentals of low-noise analog circuit design," *Proceedings of the IEEE*, vol. 82, no. 10, pp. 1515–1538, 1994.
- [4] H. W. Ott, *Noise Reduction Techniques in Electronic Systems*, John Wiley & Sons, New York, NY, USA, 2nd edition, 1988.
- [5] H. H. Jasper, "The ten–twenty electrode system of the international federation," *Electroencephalography and Clinical Neurophysiology*, vol. 10, pp. 367–380, 1958.
- [6] R. Oostenveld and P. Praamstra, "The five percent electrode system for high-resolution EEG and ERP measurements," *Clinical Neurophysiology*, vol. 112, no. 4, pp. 713–719, 2001.
- [7] Biosemi, Product catalog, 2009, [http://www.biosemi.com/active\\_electrode.htm](http://www.biosemi.com/active_electrode.htm).
- [8] Neuroscan, Product catalog, 2009, [http://www.neuroscan.com/quick\\_caps.cfm](http://www.neuroscan.com/quick_caps.cfm).
- [9] EGI, Product catalog, 2009, <http://egi.com/research-division-research-products/sensor-nets>.
- [10] O. J. Prohaska, F. Olcaytug, P. Pfundner, and H. Dragaun, "Thin-film multiple electrode probes: possibilities and limitations," *IEEE Transactions on Biomedical Engineering*, vol. 33, no. 2, pp. 223–229, 1986.
- [11] B. A. Taheri, R. T. Knight, and R. L. Smith, "A dry electrode for EEG recording," *Electroencephalography and Clinical Neurophysiology*, vol. 90, no. 5, pp. 376–383, 1994.
- [12] W. J. R. Dunseath and E. F. Kelly, "Multichannel PC-based data-acquisition system for high-resolution EEG," *IEEE Transactions on Biomedical Engineering*, vol. 42, no. 12, pp. 1212–1217, 1995.
- [13] A. C. MettingVanRijn, A. P. Kuiper, T. E. Dankers, and C. A. Grimbergen, "Low-cost active electrode improves the resolution in biopotential recordings," in *Proceedings of the 18th Annual International Conference of the IEEE Engineering in Medicine and Biology*, pp. 101–102, Amsterdam, The Netherlands, October–November 1996.
- [14] G. Litscher, "A multifunctional helmet for noninvasive neuromonitoring," *Journal of Neurosurgical Anesthesiology*, vol. 10, no. 2, pp. 116–119, 1998.
- [15] G. Gargiulo, P. Bifulco, R. A. Calvo, M. Cesarelli, C. Jin, and A. van Schaik, "A mobile EEG system with dry electrodes," in *Proceedings of IEEE-BIOCAS Biomedical Circuits and Systems Conference (BIOCAS '08)*, pp. 273–276, Baltimore, Md, USA, November 2008.
- [16] P. J. Rousche and R. A. Normann, "Chronic recording capability of the Utah intracortical electrode array in cat sensory cortex," *Journal of Neuroscience Methods*, vol. 82, no. 1, pp. 1–15, 1998.
- [17] B. B. Winter and J. G. Webster, "Reduction of interference due to common mode voltage in biopotential amplifiers," *IEEE Transactions on Biomedical Engineering*, vol. 30, no. 1, pp. 58–62, 1983.
- [18] R. Aston, *Principles of Biomedical Instrumentation and Measurement*, Prentice Hall, Columbus, Ohio, USA, 1990.
- [19] J. G. Webster, *Medical Instrumentation, Application and Design*, Houghton Mifflin, Boston, Mass, USA, 2nd edition, 1992.
- [20] G. Litscher, "A multifunctional helmet for noninvasive neuromonitoring," *Journal of Neurosurgical Anesthesiology*, vol. 10, no. 2, pp. 116–119, 1998.
- [21] I. Ulbert, E. Halgren, G. Heit, and G. Karmos, "Multiple microelectrode-recording system for human intracortical applications," *Journal of Neuroscience Methods*, vol. 106, no. 1, pp. 69–79, 2001.
- [22] A. B. Usakli and N. G. Gencer, "Performance tests of a novel electroencephalographic data-acquisition system," in *Proceedings of the 5th IASTED International Conference on Biomedical Engineering (BioMED '07)*, pp. 253–257, Innsbruck, Austria, February 2007.
- [23] A. B. Usakli and N. G. Gencer, "USB-based 256-channel electroencephalographic data acquisition system for electrical source imaging of the human brain," *Instrumentation Science & Technology*, vol. 35, no. 3, pp. 255–273, 2007.
- [24] A. B. Usakli and S. Gurkan, "Design of a novel efficient human-computer interface: an electrooculogram based virtual keyboard," Accepted in *IEEE Transactions on Instrumentation and Measurement*.

## Research Article

# DTI Parameter Optimisation for Acquisition at 1.5T: SNR Analysis and Clinical Application

M. Laganà,<sup>1,2</sup> M. Rovaris,<sup>3</sup> A. Ceccarelli,<sup>3</sup> C. Venturelli,<sup>2</sup> S. Marini,<sup>2</sup> and G. Baselli<sup>2</sup>

<sup>1</sup> Polo Tecnologico, Fondazione Don Gnocchi ONLUS, IRCCS S. Maria Nascente, 20148 Milano, Italy

<sup>2</sup> Department of Bioengineering, Politecnico di Milano, 20133 Milan, Italy

<sup>3</sup> U.O. Sclerosi Multipla, Fondazione Don Gnocchi ONLUS, IRCCS S. Maria Nascente, 20148 Milano, Italy

Correspondence should be addressed to M. Laganà, mlagana@dongnocchi.it

Received 13 July 2009; Accepted 7 October 2009

Academic Editor: Fabio Babiloni

Copyright © 2010 M. Laganà et al. This is an open access article distributed under the Creative Commons Attribution License, which permits unrestricted use, distribution, and reproduction in any medium, provided the original work is properly cited.

**Background.** Magnetic Resonance (MR) diffusion tensor imaging (DTI) is able to quantify in vivo tissue microstructure properties and to detect disease related pathology of the central nervous system. Nevertheless, DTI is limited by low spatial resolution associated with its low signal-to-noise-ratio (SNR). **Aim.** The aim is to select a DTI sequence for brain clinical studies, optimizing SNR and resolution. **Methods and Results.** We applied 6 methods for SNR computation in 26 DTI sequences with different parameters using 4 healthy volunteers (HV). We choosed two DTI sequences for their high SNR, they differed by voxel size and b-value. Subsequently, the two selected sequences were acquired from 30 multiple sclerosis (MS) patients with different disability and lesion load and 18 age matched HV. We observed high concordance between mean diffusivity (MD) and fractional anisotropy (FA), nonetheless the DTI sequence with smaller voxel size displayed a better correlation with disease progression, despite a slightly lower SNR. The reliability of corpus callosum (CC) fiber tracking with the chosen DTI sequences was also tested. **Conclusion.** The sensitivity of DTI-derived indices to MS-related tissue abnormalities indicates that the optimized sequence may be a powerful tool in studies aimed at monitoring the disease course and severity.

## 1. Introduction

Magnetic Resonance (MR) diffusion tensor imaging (DTI) allows in vivo examination of the tissue microstructure, obtained by exploiting the properties of water diffusion. The DT computed for each voxel allowed us to calculate the magnitude of water diffusion, reflected by the mean diffusivity (MD) and the degree of anisotropy, which is a measure of tissue organization, expressed as an a-dimensional index, such as fractional anisotropy (FA) [1]. The pathological elements of multiple sclerosis (MS) have the potential to alter the permeability or geometry of structural barriers to water diffusion in the brain. Consistent with this, several in vivo DTI studies have reported increased MD and decreased FA values in T2-visible lesions, normal-appearing (NA) white matter (WM), and grey matter (GM) from patients with MS [2]. Combined with fibre tractography techniques, DTI reveals WM fibers characteristics and connectivity in the brain noninvasively. In MS, tractographic reconstruction has to deal with a general FA reduction in normal appearing

white matter (NAWM) and a high FA reduction in lesions with high structural loss [2–5].

The best acquisition and postprocessing strategies for DTI sequences in the disease, especially in MS, are still a matter of debate [2, 6, 7].

The Signal-to-noise ratio (SNR) of an image is a fundamental measure of MRI-scanner hardware and software performances, because it provides a quantitative evaluation and comparison among signal and noise levels of different imaging and reconstruction methods, sequence parameters, radio frequency coils, gradient amplitudes, and slew rates. Since DT is reconstructed through evaluations of loss of signal in diffusion-weighted images in comparison with reference  $b = 0$  s/mm<sup>2</sup> images, this technique is vulnerable to poor SNR values: the background noise level close to the low diffusion weighted signal would overestimate the signal itself and consequently underestimate the magnitude of diffusion. The SNR of the  $b = 0$  s/mm<sup>2</sup> images should be at least 20 to obtain unbiased DTI-derived measures. Many methods for SNR evaluation in MR images are available and they differ

for the estimation of the noise variance. They are commonly subdivided into two classes: single magnitude image methods derive the noise from a large, uniform background region [8, 9]; pair of images methods are based on two acquisitions of the same image [10–13]. The latter methods estimate the noise in the image obtained as the difference of the two acquired images, in a region positioned in the background or in the object of examination. These methods were not used for diffusion weighted evaluations, but only for conventional (T1,T2) imaging and validated on phantoms.

Against this background, the first aim of this study is the optimization of DTI sequence parameters, in order to produce images with high SNR, with a short acquisition time and a voxel size appropriate for tractography. The SNR was computed in brain images obtained with different DTI sequence parameters.

The second aim is the choice of the DTI sequence giving the best differentiation between HV and patients with MS.

The third aim is to ascertain whether these sequences enable us to track the corpus callosum (CC) fibers in MS patients [14–16].

A preliminary validation of the method will be shown on a group of MS patients with varying progression levels of the disease compared with an age-matched group of HV.

## 2. Material and Methods

**2.1. Subjects.** To obtain the optimization of SNR parameters, we performed a preliminary analysis on 4 HV (male/female = 2/2), mean age (range) = 44.75 (28–61) years).

To obtain the DTI sequence with the best differentiation between HV and MS patients we acquired 18 HV (male/female = 10/8, mean age (range) = 43.11 (24–50) years) and 30 MS patients (male/female = 8/22, mean age (range) = 45.03 (26–68) years, median EDSS (range) = 5.0 (2–8), median (range) disease duration = 13.5 (2–34) years), of whom 13 with relapsing-remitting (RR) MS and 17 with secondary progressive (SP) MS.

**2.2. MRI Acquisition.** MR scans were performed using a 1.5 T Siemens Magnetom Avanto scanner (Erlangen, Germany) in the Radiology Department of Fondazione Don Gnocchi ONLUS, IRCCS S. Maria Nascente, Milano (Italy).

Twenty-six DTI sequences with different parameters were tested on 4 HV for the preliminary analysis. Changed parameters were pixel size (from 1.87 to 2.5 mm<sup>2</sup>), slice thickness (from 1.9 to 2.8 mm), *b*-value (900 s/mm<sup>2</sup>, 1000 s/mm<sup>2</sup>, 1500 s/mm<sup>2</sup>, 2000 s/mm<sup>2</sup>), echo time (TE) (from 83 to 110 ms), and repetition time (TR) (from 6500 ms to 7800 ms).

The following reference sequences were applied on all 48 subjects of the study:

- (a) dual-echo turbo spin echo (TSE) (TR = 2650 ms, TE = 28/113 ms, echo train length (ETL) = 5; flip angle = 150; 50 interleaved, 2.5 mm-thick axial slices, matrix size = 256 × 256 and a field of view (FOV) = 250 mm);

- (b) three-dimensional (3D) T1-weighted magnetisation-prepared rapid acquisition gradient echo (MP-RAGE) (TR = 1900 ms, TE = 3.37 ms, TI = 1100 ms, flip angle = 15°, 176 contiguous, axial slices with voxel size = 1 × 1 × 1 mm<sup>3</sup>, matrix size = 256 × 256, FOV = 256 mm, slab tick = 187.2 mm).

The following two DTI sequences were also applied, as a consequence of the previous screening on 4 HV:

- (i) (DTI-A): pulsed-gradient spin-echo echo planar pulse sequence without SENSE (TR = 7000 ms, TE = 94 ms, 50 axial slices with 2.5 mm slice thickness, acquisition matrix size = 128 × 96; FOV = 320 × 240 mm) with diffusion gradients (*b*-value = 900 s/mm<sup>2</sup>) applied in 12 noncollinear directions;
- (ii) (DTI-B): pulsed-gradient spin-echo echo planar pulse sequence without SENSE (TR = 6500 ms, TE = 95 ms, 40 axial slices with 2.5 mm slice thickness, acquisition matrix size = 128 × 128; FOV = 240 × 240 mm) with diffusion gradients (*b*-value = 1000 s/mm<sup>2</sup>) applied in 12 noncollinear directions. Two acquisitions for each set of diffusion gradients were performed, in order to improve SNR. Acquisition time is compatible with clinical protocols: 3'09'' for the first sequence (DTI-A) and 2'56'' for the second (DTI-B).

The main differences between the first and the second DTI sequences were *b*-value (900 s/mm<sup>2</sup> versus 1000 s/mm<sup>2</sup>), pixel size (2,5 mm × 2,5 mm versus 1,88 mm × 1,88 mm), and TR (7000 ms versus 6500 ms).

DTI-B had 10 slices less than DTI-A; so it covered 25 mm less in the craniocaudal direction. Since our clinical aim is to analyze the microscopic changes of CC due to the MS pathology, we positioned DTI-B group of slices (slab) with the same centre and orientation of DTI-A slab, and then we moved it upward of 12,5 mm (25/2 mm) in the cranial direction. So, the two DTI had the last slice with the same position and orientation.

**2.3. Methods for SNR Computation.** All the 26 sequences were automatically analyzed with a home-made Matlab script, which computed SNR with six different methods for every slice of every volume (two *b*<sub>0</sub> volumes, not diffusion-weighted, and twenty-four diffusion-weighted volumes) and plotted SNR-to-slice (Figure 2).

In all of the 6 methods, the signal (*S*) is evaluated as the 2D mean intensity in a region of interest (ROI) of 10 × 10 = 100 pixels with maximum uniform brain signal, automatically extracted for every slice (red ROI, Figure 1(a)). Instead, for the estimation of noise, single and multiple images methods were used. Even if the multiple images ones are relatively insensitive to structured noise such as ghosting, ringing, and direct current (DC) artifacts, a perfect geometrical alignment of the images and temporal steadiness of the imaging process are strict requirements. For this reason, corresponding volumes of the two subsequent acquisitions were previously coregistered with statistical parametric mapping (SPM)5 (<http://www.fil.ion.ucl.ac.uk/spm/>).

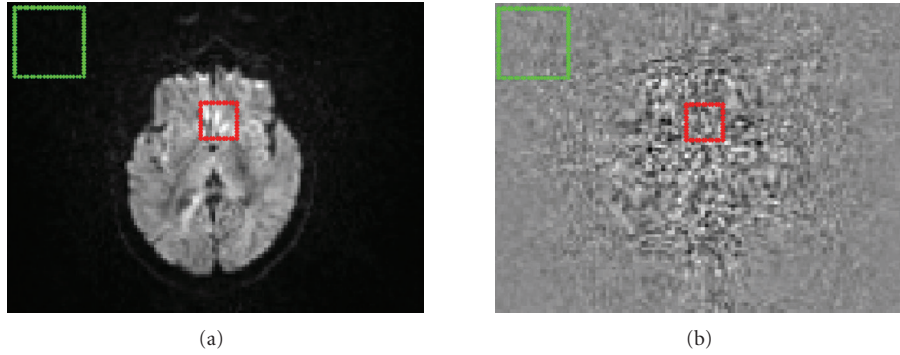


FIGURE 1: ROIs superimposed on 25th slice of the DTI-A 6th diffusion direction (a) and on image obtained by the difference of two acquisitions of the same image (b). The red ROI is for the evaluation of signal (for all the methods) and for the evaluation of noise standard deviation in methods 1 and in double image methods 2, 5; the green ROI is for the evaluation of noise in single image methods 3, 4, 6.

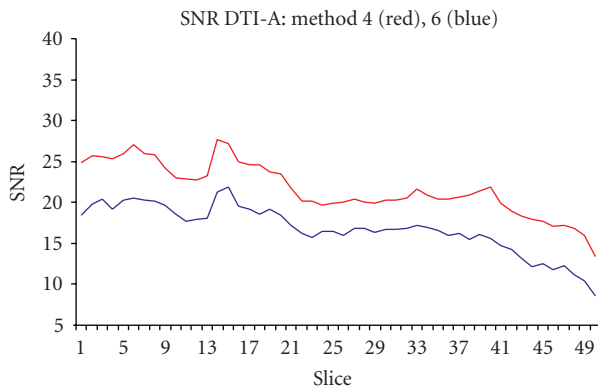


FIGURE 2: Comparison of DTI-A SNR obtained with method 4 and method 6. The mean SNR for  $b \neq 0$  s/mm<sup>2</sup> images is plotted for every slice.

*Method 1—Single ROI for Signal and Noise, Single Image.* The noise was evaluated in the same ROI used for the S (see above). SNR is computed with (1) [17]:

$$\text{SNR}_1 = \frac{S}{\sigma}, \quad (1)$$

where  $\sigma$  is the 2D standard deviation (SD) of pixel intensity in the ROI.

*Method 2—Single ROI for Signal and Noise, Difference of Images.* The noise was evaluated in the image obtained from the difference of two subsequent acquired images as the 2D SD of the intensities in the same ROI used for the signal S. Noise ROI must be positioned in tissue with sufficiently high SNR and not in the image background, because the noise within the ROI in the difference image is assumed to be Gaussian distributed.

SNR was then computed with (2) [17–21], where the factor  $\sqrt{2}$  is due to the property of the addition of the variances when two images are added or subtracted:

$$\text{SNR}_2 = \sqrt{2}S/\sigma, \quad (2)$$

where  $\sigma$  is the 2D SD of pixel intensity in the ROI.

*Method 3—Noise Estimated on Air (SD), Single Image.* The noise was estimated in a ROI of  $20 \times 20 = 400$  pixels, extracted from background (air) (Figure 1(a)), paying attention to put it far from ghosting and filter artifacts, visible as an increased signal near image edges. Since MRI noise in the air follows Rayleigh distribution, the apparent SD of the noise underestimates the true SD by approximately 0.655. Therefore, the SNR was obtained by (3) [9, 20, 22] as

$$\text{SNR}_3 = \frac{S}{\text{SD}(\text{true.noise})} = 0.655 \frac{S}{\text{SD}(\text{apparent.noise})}. \quad (3)$$

*Method 4—Noise Estimated on Air (Mean Value), Single Image.* The standard deviation of noise was estimated from a ROI of  $20 \times 20 = 400$  pixels, extracted from background (air). Since MR noise in the air follows Rayleigh distribution, the mean value of the signal in the second ROI ( $\mu_{\text{air}}$ ) is equal to the SD of the noise, multiplied for the coefficient  $\sqrt{\pi/2}$ . So, SNR was computed with (4) [17, 20]:

$$\text{SNR}_4 = \sqrt{\frac{\pi}{2}} \cdot \frac{S}{\mu_{\text{air}}}. \quad (4)$$

*Method 5—Single ROI for Signal and Noise, Difference of Images.* This method was similar to the method 2. We considered two images (A and B) obtained from two subsequent acquisitions of the same slice. The signal was the mean value of the pixels in a ROI on the first image (A). Then, we considered a second ROI on the second image (B), located as the first ROI in the first image. The SD of the noise was evaluated in the same ROI position and computed as suggested by Ogura et al. [17] with (5):

$$\sigma = \sqrt{\tau_{\text{ROIA-ROIB}}^2 + \tau_{\text{ROIB-ROIA}}^2 + 2 \cdot \nu_{\text{ROIB-ROIA}} \cdot \nu_{\text{ROIA-ROIB}}}, \quad (5)$$

where  $\tau$  was the standard deviation and  $\nu$  was the mean value of the pixel in an image obtained as the difference of image A minus image B (ROIA-ROIB) or vice versa.

*Method 6—Estimation of Noise Variance from the Background Histogram Mode, Single Image.* Since MRI noise in the air

follows Rayleigh distribution, the noise variance can be estimated by searching for the magnitude ( $m$ ) value at which the background histogram attains a maximum ( $m_{\max\text{air}}$ ): noise SD was estimated as the mode of the Probability Density Function histogram [12, 23] in a background ROI of  $20 \times 20 = 400$  pixels and the SNR was computed with (6):

$$\text{SNR}_6 = \frac{S}{\sigma_{\text{air}}} = \frac{S}{m_{\max}(\text{air})}. \quad (6)$$

**2.4. Postprocessing of Conventional Imaging.** Lesions were segmented on proton-density(PD)-weighted images, using the corresponding T2-weighted images to increase confidence in lesion identification. Then, lesion volume (ml) was calculated and segmented lesions were used for masking DTI (see Section 2.5), using Jim software package (Jim 5.0, Xinapse System, Leicester, UK).

3D-T1 MP-RAGE images were automatically segmented to GM, WM and cerebrospinal fluid (CSF), using SPM5 (<http://www.fil.ion.ucl.ac.uk/spm/>) and maximum image inhomogeneity correction [24]. An home-made Matlab script was used to classify each pixel as GM, WM or CSF, dependent on which map had the greatest probability at that location: this produced mutually exclusive masks for each tissue.

**2.5. Post Processing of Diffusion Tensor Imaging.** DTI data were corrected for eddy-current distortion by FSL package, which registered the 12 diffusion-weighted volumes to the  $b_0$ -volume, with a Mutual Information- (MI-) based non-linear transformation. Then diffusion gradient directions were corrected for scanner settings (i.e., slice angulation, slice orientation, etc.) and diffusion tensor was determined for each voxel using the freely available Diffusion Toolkit software, version 0.4.2 (<http://www.trackvis.org/>) with linear least-squares fitting method [25]. The tensors were then diagonalized, obtaining eigenvectors, eigenvalues, MD, and FA maps.

ROIs of lesions individuated on T2-images were masked out from MD and FA maps, in order to estimate NAWM damage.

GM and WM mutual exclusive masks were superimposed to MD and FA maps, and the corresponding histograms were produced. The erosion of the first-line outer voxels from the mutual exclusive masks excluded the contribution of partial volume effect from the surrounding CSF to the observed GM and WM diffusivity changes and WM anisotropy changes. Average MD was computed for GM and NAWM. Average FA was derived only for the NAWM, since no preferential direction of water molecular motion is expected to occur in the GM, due to the absence of a microstructural anisotropic organization of this tissue compartment.

**2.6. Fiber Tracking.** The reliability of fiber tracking with the 2 DTI sequences was tested using Diffusion Toolkit v0.4.2 (<http://www.trackvis.org/>) and visualized by the freely available software TrackVis v0.4.2 (<http://www.trackvis.org/>). The brute force approach and deterministic streamline-based fiber tracking were used, with FA-map as masking image and angle termination of  $35^\circ$ . For track selection, the one-ROI

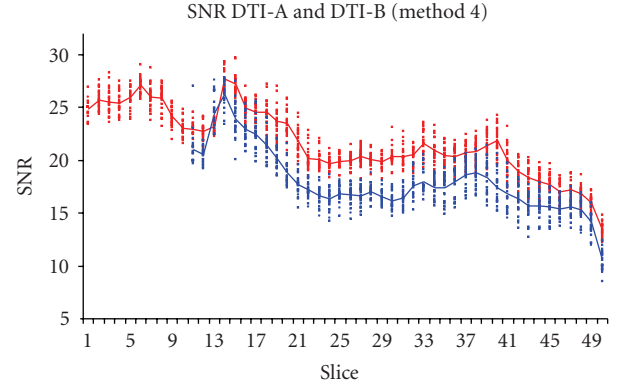


FIGURE 3: SNR computed with method 4 for images obtained with two repetitions of 12 DTI gradient directions. DTI-A ( $b$ -value =  $900 \text{ s/mm}^2$ , 50 slices) (red) is compared with DTI-B ( $b$ -value =  $1000 \text{ s/mm}^2$ , 40 slices) (blue). Note that DTI-B has been obtained with the last slice ( $z$  direction from feet to head) positioned as the last slice of DTI-A slice group.

approach was used: CC was identified and segmented in the three mid-sagittal adjacent slices of FA-map [26].

FA and MD histograms were derived for CC fiber tracts (CC-FA and CC-MD).

**2.7. Statistical Analysis.** A graphical display allowed to compare the six methods of SNR estimation and the quality of the sequences in terms of SNR.

We estimate the intraclass-correlation coefficients between the 2 DTI sequences used in the study, regarding the values of NAWM-FA, NAWM-MD, and GM-MD of all the 48 subjects (HV and MS patients).

Spearman's correlation coefficient (SCC) was assessed to estimate the correlation between DTI-derived measures (NAWM-FA, NAWM-MD, GM-MD, CC-FA, and CC-MD) and the subjects' condition (HV, RRMS, SPMS).

### 3. Results

**3.1. Analysis of SNR.** As expected, the six SNR evaluation methods gave different absolute numerical values. Nevertheless, the changes through slices (Figure 2) and through different volumes were in good agreement, as the ranking of the performances of the different sequences (Figures 3, 4).

SNRs were plotted for sequences ordered by ascending voxel size and with the same  $b$ -value, TE and TR: this kind of graphical representation showed clearly the increase of SNR with the increase of the voxel size. A similar representation was done for sequences with the same parameters but the  $b$ -value, giving the result of SNR decreasing with the increasing of the diffusion-sensitivity coefficient, in particular the SNR estimated on images obtained from sequences with  $b$ -value of  $1500 \text{ s/mm}^2$  was 20% less than the SNR of sequences with  $b$ -value of  $1000 \text{ s/mm}^2$ . The same analysis confirmed that the minimum TE feasible for the MR-scanner had to be selected, as expected, since DTI is T2 weighted.

The sequence with the highest SNR by all methods was DTI-A, which is characterized by parameters in the range

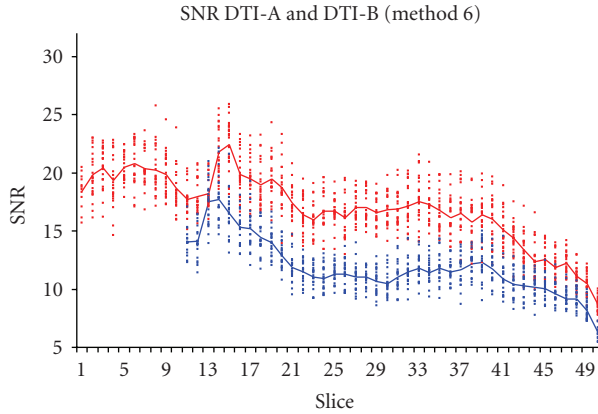


FIGURE 4: SNR computed with method 6 for images obtained with two repetitions of 12 DTI gradient directions. DTI-A ( $b$ -value =  $900 \text{ s/mm}^2$ , 50 slices) (red) is compared with DTI-B ( $b$ -value =  $1000 \text{ s/mm}^2$ , 40 slices) (blue). Note that DTI-B has been obtained with the last slice ( $z$  direction from feet to head) positioned as the last slice of DTI-A slice group.

TABLE 1: Intraclass correlation coefficient between measures derived from DTI-A and DTI-B.

| DTI-derived metric | Intraclass correlation coefficient |
|--------------------|------------------------------------|
| GMMD               | 0.95                               |
| NAWMMD             | 0.99                               |
| NAWMFA             | 0.91                               |

recommended by Pagani et al. [27] for multicentre MS trials.

Another sequence (DTI-B) was selected for the high SNR between those of pixel size of about  $1 \times 1 \text{ mm}^2$ . DTI-B SNR is lower than DTI-A SNR, less than 15%.

The SNR comparison of the two selected sequences is shown in Figures 3 and 4: only two SNR computational methods are shown (method 4 in Figure 3 and method 6 in Figure 4), but in both figures it is clear that DTI-A produces images with higher SNR, with near constant differences among slices.

**3.2. Statistical Comparison of Microstructural Indices of Fiber Integrity, Derived from Two Sequences.** The intraclass-correlation coefficients ranged from 0.91 to 0.99, showing high concordance of the parameters derived from DTI-A and DTI-B (Table 1).

The SCC showed that both DTI sequences separated HV from RRMS and SPMS patients, but that SCCs between DTI-B were higher than those between DTI-A ( $P < .01$ ) and subjects' condition as shown in Table 2.

**3.3. Fiber Tracking.** (i) Tractography algorithm was obtained with both the selected DTI sequences for all HV (in Figure 5 an example of CC tractography obtained with DTI-A is shown).

(ii) Tractography algorithm was obtained with both the selected DTI sequences for 28 of the 30 MS patients

TABLE 2: Spearman's Correlation Coefficient between DTI-derived measures and the subjects' condition.

| DTI-derived metric | Spearman's Correlation Coefficient |       |
|--------------------|------------------------------------|-------|
|                    | DTI-A                              | DTI-B |
| GMMD               | 0.57                               | 0.68  |
| NAWMMD             | 0.47                               | 0.64  |
| NAWMFA             | -0.60                              | -0.70 |
| CC-MD              | 0.63                               | 0.78  |
| CC-FA              | -0.80                              | -0.84 |

(Figure 6) but failed in two patients with a high number of lesions in CC.

## 4. Discussion

In this study we improved the quality of DTI sequences, looking for a compromise between SNR and spatial resolution. SNR values computed with different methods showed different bias and sensitivity to the noise level: this observation has to be further investigated. Despite that, at the aim of the present work, all methods were in accordance with the whole data set in pointing sequences DTI-A and DTI-B as the best ones without exception (SNR DTI-A > SNR DTI-B). These concordant evaluations allowed us to produce an automatic DTI sequences quality evaluation and to preliminary select two DTI sequences among 26. The two selected sequences had the best trade-off between SNR, voxel size, and diffusion sensing. Even if DTI-B has a lower SNR compared to DTI-A, the loss of maximum 15% in SNR was compensated by a higher resolution, which is a key element in determining tractographic reconstruction quality [7]. Both DTI sequences chosen through SNR-based evaluation are feasible for clinical protocols because of the acceptable acquisition time (about 3').

The optimum result is the production of CC individual-based tractography in 28 of 30 patients, with fiber tracts reconstructed even if they passed through a lesion. Both focal and diffuse alterations of tissue organization, which result in a decreased anisotropy and a consequent increase in uncertainty of the primary eigenvector of the DTI, are the well-known cause of the failure of tractography in MS in the previous studies [2, 28]. As previously described [7], the number of fibers decreases and tractography stops erroneously when SNR decreases. The improvement of SNR contributed on making possible the fiber bundles reconstruction. The high SNR is also fundamental for a better evaluation of MD and FA. Indeed, both of them are underestimated when SNR is low [29].

In order to increase SNR, more than one average is usually acquired, but too many averages amplify coregistration errors and raise acquisition time and subject movements. In our DTI protocol we choose to acquire 2 averages (runs) for every diffusion sequence. In Figure 1(b) the image is shown obtained by the difference between the first run and the second run (coregistered to the first one), which reveals that the ROI for the noise SD estimation (red) is put in a region

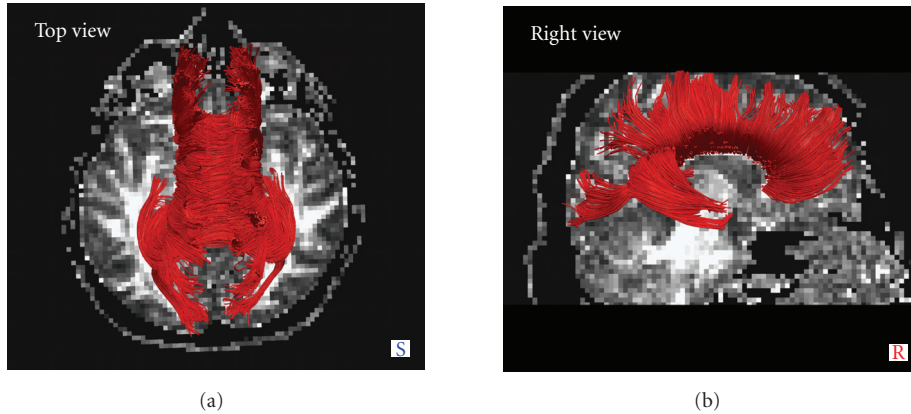


FIGURE 5: Top and right view of corpus callosum tractography for a 50-year-old healthy male subject.

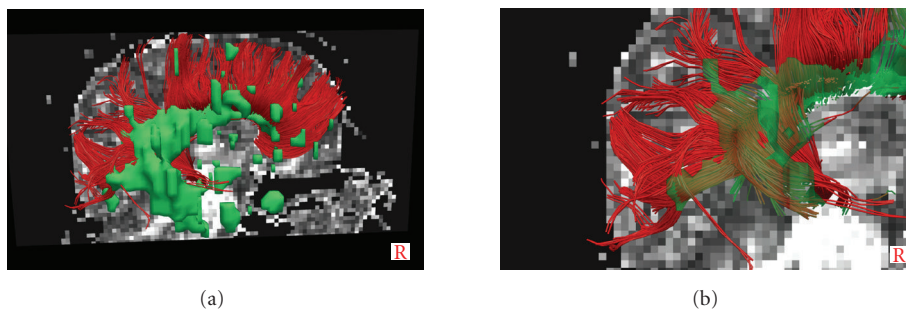


FIGURE 6: (a) Corpus callosum tractography for a 48-year-old relapsing remitting multiple sclerosis patient with lesional load of 16.4 mL. Lesions are superimposed on tractography and visualized with green blobs. (b) Zoom of posterior tracts which pass through the lesions of the same patient.

with minimum error due to mismatch of coregistration: the difference image is uniform and does not have ringing or border artifacts.

The noise, estimated with different methods, is almost constant over the slices (Figure 7): for example, the DTI-A noise computed with method 4 has mean value (range) = 9.2 (8.2–10.2) over an image with mean (range) intensity of 33.7 (0–585); DTI-B noise computed with method 4 has mean value (range) = 8.6 (7.7–9.3) over an image with mean (range) intensity of 40.8 (0–681). Therefore, the SNR slices dependency (Figures 3 and 4) is mainly due to the mean signal differences for the various tissues acquired slice by slice.

Besides SNR examinations, even resolution has to be considered in DTI sequence parameters selection. Indeed, FA and MD are also influenced by the voxel size, due to the increment of the radial eigenvalues in a large voxel [30]. Furthermore, tissue with different diffusion properties can be inside a large voxel, bringing biased diffusion results [29]. This problem is known as partial volume effect and it causes an altered evaluation of DTI-derived measures, with a higher influence on FA than MD, due to the increase of the radial eigenvalues in a large voxel [30]. It is also known that the presence of crossing fibers within a large voxel influences the estimation of diffusion properties, since the apparent principal DT eigenvector is obtained as an average of the two crossing fibers' directions with a consequent reduction in the FA [7, 30].

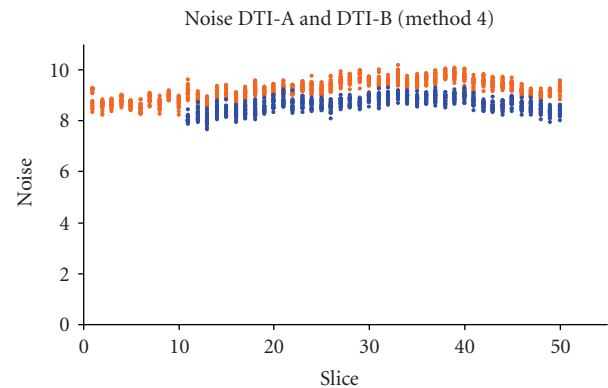


FIGURE 7: Comparison of Noise computed with method 4 for the two repetitions of 12 DTI gradient directions ( $b$ -value = 900  $s/mm^2$ , 50 slices) of DTI-A (orange dots) and the two repetitions of 12 DTI gradient directions ( $b$ -value = 1000  $s/mm^2$ , 40 slices) of DTI-B (blue dots).

For the above reasons we included also DTI-B in the clinical protocol, due to the smaller voxel size, even if DTI-A had the higher SNR.

Accurate FA and MD estimations improve the reliability of tractography, which is prone to errors: some of them are subjective (e.g., how the ROI for tracking selection is drawn, etc.) and some are intrinsic in the DTI sequence used.

Indeed, bias in the estimation of diffusion tensor eigenvectors and eigenvalues damaged fiber tracking because it causes false or missing fibers [28, 30]. Several studies have been performed to reduce the errors on fiber tracking [30–33], but these methodologies are still being developed, none are used routinely, and most of them are time consuming and require strong computational power.

## 5. Conclusion

The results about SNR computed with different methods (Figures 3 and 4) showed that even those methods applied only on phantoms in previous studies [17, 21], or on mouse brain [12] or human abdomen [20] conventional MRI, can be successfully used also for DTI on human brain.

Both our selected DTI sequences were able to quantify a tissue damage in MS, leading to distinguish between MS patients and HV and between the different MS phenotypes. However, the sequence with higher resolution and higher  $b$ -value (DTI-B) achieved a better correlation with the presence of MS disease. Even if DTI-B sequence has less slices than DTI-A, it covered the entire CC tracts due to the acquired slab position. Appropriate positioning of the acquisition slab should be evaluated in further studies in order to analyze other fiber bundles.

Finally, the proposed sequence and procedure showed higher reliability for fiber tracking and were able to discriminate the presence of MS disease even when severe lesional patterns were observed and may therefore be considered a potential powerful tool for studies to monitor the disease course and severity.

## References

- [1] P. J. Basser, J. Mattiello, and D. LeBihan, "Estimation of the effective self-diffusion tensor from the NMR spin echo," *Journal of Magnetic Resonance B*, vol. 103, no. 3, pp. 247–254, 1994.
- [2] M. Rovaris, F. Agosta, E. Pagani, and M. Filippi, "Diffusion tensor MR imaging," *Neuroimaging Clinics of North America*, vol. 19, no. 1, pp. 37–43, 2009.
- [3] M. Cercignani, G. Lannucci, and M. Filippi, "Diffusion-weighted imaging in multiple sclerosis," *The Italian Journal of Neurological Sciences*, vol. 20, supplement 2, pp. S246–S249, 1999.
- [4] D. H. Miller, A. J. Thompson, and M. Filippi, "Magnetic resonance studies of abnormalities in the normal appearing white matter and grey matter in multiple sclerosis," *Journal of Neurology*, vol. 250, no. 12, pp. 1407–1419, 2003.
- [5] M. Rovaris, A. Gass, R. Bammer, et al., "Diffusion MRI in multiple sclerosis," *Neurology*, vol. 65, no. 10, pp. 1526–1532, 2005.
- [6] D. K. Jones, M. A. Horsfield, and A. Simmons, "Optimal strategies for measuring diffusion in anisotropic systems by magnetic resonance imaging," *Magnetic Resonance in Medicine*, vol. 42, no. 3, pp. 515–525, 1999.
- [7] X. Liu, T. Zhu, T. Gu, and J. Zhong, "Optimization of in vivo high-resolution DTI of non-human primates on a 3T human scanner," *Methods*. In press.
- [8] R. M. Henkelman, "Measurement of signal intensities in the presence of noise in MR images," *Medical Physics*, vol. 12, no. 2, pp. 232–233, 1985.
- [9] L. Kaufman, D. M. Kramer, L. E. Crooks, and D. A. Ortendahl, "Measuring signal-to-noise ratios in MR imaging," *Radiology*, vol. 173, no. 1, pp. 265–267, 1989.
- [10] R. M. Sano, *MRI: Acceptance Testing and Quality Control: The Role of the Clinical Medical Physicist*, Medical Physics, Madison, Wis, USA, 1988.
- [11] B. W. Murphy, P. L. Carson, J. H. Ellis, Y. T. Zhang, R. J. Hyde, and T. L. Chenevert, "Signal-to-noise measures for magnetic resonance imagers," *Magnetic Resonance Imaging*, vol. 11, no. 3, pp. 425–428, 1993.
- [12] J. Sijbers, A. J. den Dekker, D. Poot, et al., "Robust estimation of the noise variance from background MR data," in *Medical Imaging 2006: Image Processing*, vol. 6144 of *Proceedings of SPIE*, pp. 1–11, San Diego, Calif, USA, February 2006.
- [13] J. Sijbers, A. J. den Dekker, J. Van Audekerke, M. Verhoye, and D. Van Dyck, "Estimation of the noise in magnitude MR images," *Magnetic Resonance Imaging*, vol. 16, no. 1, pp. 87–90, 1998.
- [14] S. Mori, B. J. Crain, V. P. Chacko, and P. C. M. van Zijl, "Three-dimensional tracking of axonal projections in the brain by magnetic resonance imaging," *Annals of Neurology*, vol. 45, no. 2, pp. 265–269, 1999.
- [15] T. E. Conturo, N. F. Lori, T. S. Cull, et al., "Tracking neuronal fiber pathways in the living human brain," *Proceedings of the National Academy of Sciences of the United States of America*, vol. 96, no. 18, pp. 10422–10427, 1999.
- [16] P. J. Basser, S. Pajevic, C. Pierpaoli, J. Duda, and A. Aldroubi, "In vivo fiber tractography using DT-MRI data," *Magnetic Resonance in Medicine*, vol. 44, no. 4, pp. 625–632, 2000.
- [17] A. Ogura, A. Miyai, F. Maeda, H. Fukutake, and R. Kikumoto, "Accuracy of signal-to-noise ratio measurement method for magnetic resonance images," *Japanese Journal of Radiological Technology*, vol. 59, no. 4, pp. 508–513, 2003.
- [18] National Electrical Manufacturers Association (NEMA), *Determination of Signal-to-Noise Ratio (SNR) in Diagnostic Magnetic Resonance Imaging*, NEMA Standard Publication no. MS 1-2001, National Electrical Manufacturers Association, Rosslyn, Va, USA, 2001.
- [19] S. B. Reeder, B. J. Wintersperger, O. Dietrich, et al., "Practical approaches to the evaluation of signal-to-noise ratio performance with parallel imaging: application with cardiac imaging and a 32-channel cardiac coil," *Magnetic Resonance in Medicine*, vol. 54, no. 3, pp. 748–754, 2005.
- [20] O. Dietrich, J. G. Raya, S. B. Reeder, M. F. Reiser, and S. O. Schoenberg, "Measurement of signal-to-noise ratios in MR images: influence of multichannel coils, parallel imaging, and reconstruction filters," *Journal of Magnetic Resonance Imaging*, vol. 26, no. 2, pp. 375–385, 2007.
- [21] H. Imai, T. Miyati, A. Ogura, et al., "Signal-to-noise ratio measurement in parallel MRI with subtraction mapping and consecutive methods," *Nippon Hoshasen Gijutsu Gakkai Zasshi*, vol. 64, no. 8, pp. 930–936, 2008.
- [22] D. Weber, "Quality Control Issues in MRI," 1998.
- [23] J. Sijbers, D. Poot, A. J. den Dekker, and W. Pintjens, "Automatic estimation of the noise variance from the histogram of a magnetic resonance image," *Physics in Medicine and Biology*, vol. 52, no. 5, pp. 1335–1348, 2007.
- [24] J. Ashburner and K. Friston, "Multimodal image coregistration and partitioning—a unified framework," *NeuroImage*, vol. 6, no. 3, pp. 209–217, 1997.
- [25] P. J. Basser, J. Mattiello, and D. LeBihan, "MR diffusion tensor spectroscopy and imaging," *Biophysical Journal*, vol. 66, no. 1, pp. 259–267, 1994.
- [26] M. Catani and M. Thiebaut de Schotten, "A diffusion tensor imaging tractography atlas for virtual in vivo dissections," *Cortex*, vol. 44, no. 8, pp. 1105–1132, 2008.

- [27] E. Pagani, M. Rovaris, J. G. Hirsch, et al., “Optimising diffusion measurements for large-scale, multicentre multiple sclerosis trials: a pan-European study,” *Journal of Neurology*, vol. 255, no. 3, p. 342, 2008.
- [28] O. Ciccarelli, M. Catani, H. Johansen-Berg, C. Clark, and A. Thompson, “Diffusion-based tractography in neurological disorders: concepts, applications, and future developments,” *The Lancet Neurology*, vol. 7, no. 8, pp. 715–727, 2008.
- [29] D. K. Jones and P. J. Basser, ““Squashing peanuts and smashing pumpkins”: how noise distorts diffusion-weighted MR data,” *Magnetic Resonance in Medicine*, vol. 52, no. 5, pp. 979–993, 2004.
- [30] Y. Assaf and O. Pasternak, “Diffusion tensor imaging (DTI)-based white matter mapping in brain research: a review,” *Journal of Molecular Neuroscience*, vol. 34, no. 1, pp. 51–61, 2008.
- [31] D. S. Tuch, T. G. Reese, M. R. Wiegell, N. Makris, J. W. Belliveau, and V. J. Wedeen, “High angular resolution diffusion imaging reveals intravoxel white matter fiber heterogeneity,” *Magnetic Resonance in Medicine*, vol. 48, no. 4, pp. 577–582, 2002.
- [32] D. S. Tuch, T. G. Reese, M. R. Wiegell, and V. J. Wedeen, “Diffusion MRI of complex neural architecture,” *Neuron*, vol. 40, no. 5, pp. 885–895, 2003.
- [33] K. M. Jansons and D. C. Alexander, “Persistent Angular Structure: new insights from diffusion MRI data. Dummy version,” in *Information Processing in Medical Imaging*, vol. 2732, pp. 672–683, Springer, Berlin, Germany, 2003.

## Research Article

# Exploring Cortical Attentional System by Using fMRI during a Continuous Performance Test

**M. G. Tana, E. Montin, S. Cerutti, and A. M. Bianchi**

*Department of Bioengineering, IIT Unit, Politecnico di Milano, Milan, Italy*

Correspondence should be addressed to M. G. Tana, mariagabriella.tana@polimi.it

Received 14 June 2009; Accepted 20 August 2009

Academic Editor: Fabio Babiloni

Copyright © 2010 M. G. Tana et al. This is an open access article distributed under the Creative Commons Attribution License, which permits unrestricted use, distribution, and reproduction in any medium, provided the original work is properly cited.

Functional magnetic resonance imaging (fMRI) was performed in eight healthy subjects to identify the localization, magnitude, and volume extent of activation in brain regions that are involved in blood oxygen level-dependent (BOLD) response during the performance of Conners' Continuous Performance Test (CPT). An extensive brain network was activated during the task including frontal, temporal, and occipital cortical areas and left cerebellum. The more activated cluster in terms of volume extent and magnitude was located in the right anterior cingulate cortex (ACC). Analyzing the dynamic trend of the activation in the identified areas during the entire duration of the sustained attention test, we found a progressive decreasing of BOLD response probably due to a habituation effect without any deterioration of the performances. The observed brain network is consistent with existing models of visual object processing and attentional control and may serve as a basis for fMRI studies in clinical populations with neuropsychological deficits in Conners' CPT performance.

## 1. Introduction

Sustained attention is defined as the ability to maintain a high vigilance level for a long time, allowing the subject to respond against presentation of infrequent and unpredictable events. One of the most widely used neuropsychological tests for the study of sustained attention is the Conners' Continuous Performance Test (CPT) [1]. The Conners' CPT is derived from the original CPT of Rosvold [2], which was developed to assess vigilance. In the Rosvold CPT, the stimuli are letters which are presented visually one at a time, at a fixed rate and the subject's task is to respond whenever the letter representing the target stimulus appears and to inhibit a response when any other letter appears. The letter chosen as target stimulus is typically X and the Rosenov test is therefore, also known as the "X-CPT."

Several neuropsychological tests are derived from the X-CPT and the fundamental paradigm on which all these are based is the serial presentation of target and nontarget stimuli and the subject's task is to respond or inhibit response to infrequent visual target stimuli.

In Conners' CPT, also known as "not-X-CPT", the target stimuli are the letters X like in the Rosvold's test, but the

subject's task is to respond to nontarget stimuli and to inhibit response to target stimuli [3]. Although the Conners CPT is designed to evaluate attention; it has been shown that task performance relies on diverse motor, sensory, and cognitive functions (e.g., maintenance of task instructions, visual perception of stimuli, target identification, and manual response) [4].

For this reason, abnormal performance on the CPT in clinical population may be caused by primary attention deficits or damages to neural systems that are engaged by the task. Therefore, it is of primary importance to identify and localize the brain regions forming the neural networks activated by CPT in healthy subjects to better understand the relationships between performance deficits and developmental or acquired disruption of brain networks in clinical populations [5].

The first aim of our work is to study the neural networks of brain regions involved during the Conners CPT paradigm, by using functional magnetic resonance imaging (fMRI) in order to identify the different contributors to task performance coming from different brain regions.

Another open issue in the investigation of cortical attentional system is understanding the temporal trend of

the brain response while performing the CPT task in the fMRI scanner system. The second objective of this work is, therefore, to investigate how fMRI activation in brain regions that are engaged during the performance of Conners' CPT task, evolve during the entire duration of the sustained attention test.

## 2. Materials and Methods

*2.1. Subjects.* Eight right-handed healthy adult volunteers participated in the study, 7 of them are male, and 1 is female with a mean age of 18.8 years (SD 2.9). Participants were recruited among the staff and students working in the "Ospedale Maggiore Policlinico, Milan, Italy" in which the experiment was performed.

All the subjects had normal vision and they had not history of neurological or psychiatric disorders.

*2.2. Continuous Performance Test (CPT).* The task used in the present study is the classical Conner's CPT test. It consists of 26 different letters, of the English alphabet, presented sequentially in random order, on goggle system used by the subject during fMRI scanning procedure. The instructions about the test are given before the test by means of a headphone system. Subjects were asked to press the response button with the forefinger of their right hand as fast as possible when any letter other than X appeared ("Go" event) and to withhold the response when the letter X was displayed ("No-Go" event). Letters were presented with interstimulus interval (ISI) of 1 or 2 s and remained on the screen for 250 milliseconds (stimulus duration). The attention task was 10 minutes long and a total of 450 letters were presented. An initial baseline lasting 2 minutes and a final recovery period lasting 2 minutes were also recorded. During baseline and recovery, meaningless images (differently oriented geometrical lines) were presented to the subjects.

The CPT test was implemented with the software "Presentation, version 0.81, build" (Neurobehavioral Systems). The package "Presentation" is able to produce the stimulus and to synchronize it with the MR scanner (mripulse function). Moreover, it is possible to obtain a logfile with the onset times of stimuli and the response times of the subject. The logfile information allows to compute the number of omission errors and of commission errors. An omission error is committed whenever the subject does not respond to the nontarget stimulus; a commission error is committed whenever he gives a response to a target stimulus.

*2.3. Data Acquisition.* MRI scans were performed into an 1.5T scanner (Eclipse Marconi—Philips system) at the Department of Diagnostic and Interventional Neuroradiology, Ospedale Maggiore Policlinico, IRCCS, Milan, Italy, using a standard head coil. Functional MRI images were acquired with an echo-planar imaging (EPI) sequence using axial orientation (TE = 60 milliseconds, TR = 3 seconds, flip angle = 90°). Most of the brain was covered by 26 slices (parallel to the line linking the anterior and posterior

commissures CA and CP) obtained with an in-plane resolution of 64 × 64 and 3.97 mm × 3.97 mm × 4 mm voxels. During the Conners' CPT fMRI data were collected in one run of 290 images. The first 10 volumes (30 seconds) were discarded from the following analysis, to allow steady state to be reached. Hence 280 volumes were used: the volumes from 11 to 50 (2 minutes) are the first rest time, the volumes from 51 to 250 (10 minutes) are the active time, the volumes from 251 to 290 (2 minutes) are the second rest time. Duration of the test was approximately 14 minutes.

### 2.4. Data Analysis

*fMRI Data Preprocessing.* The fMRI images were motion corrected and spatially smoothed with a 10 mm × 10 mm × 10 mm full width at half maximum Gaussian kernel by using SPM8b software package (<http://www.fil.ion.ucl.ac.uk/>). fMRI images were then spatially normalized to the neuroanatomical atlas of Talairach and Tournoux (using a 12 parameter affine approach and a T2\* weighted template image).

*First Level Analysis.* At a first stage of analysis fMRI data of each participant were analyzed using the mass univariate approach based on General Linear Model (GLM) Theory implemented in SPM8b.

First level analysis was performed using a block design in which five regressors (length 2 minutes 40 images volume) were used to model the BOLD response during the time in which the CPT task was executed by subjects. The regressors were built by convolving the SPM canonical haemodynamic response function (HRF) [6] with five box car functions of 2 minutes duration each, in such a way to cover the entire duration of the sustained attention test (10 minutes).

The parameters of motion correction resulting by image realignment are also included in the first level design matrix, as unwanted-effect regressors in order to remove residual movement artifacts [7].

The whole set of regressors modeling the effects of interest and the unwanted effects forming the first level design matrix is then fitted to the image data of each subject involved in the experiment. After the estimation of the regression coefficients, inference on relevant contrasts of their estimates was performed using a *t*-Student statistic. A set of first-level *t*-contrasts was specified, each contrast including a weight of one for a particular regressor of interest and a weight of zero for all other regressors. This results in five *t*-contrasts for each participant.

*Second Level Analysis.* At a second stage of analysis, the contrast images obtained at the single subject-level were included into a second level design matrix in order to compute a within-subjects one-way analysis of variance (ANOVA).

The second level design matrix was built by defining a single factor with five levels (each level corresponding to one temporal block of two minutes). Therefore, each level of

TABLE 1: Summary of BOLD activations during the first block (0–2 minutes, where 0 is the beginning of the execution of the task);  $xyz$  are Talairach coordinates and Max  $t$  is the maximum value of the  $t$ -statistic in the cluster ( $P = .05$  FDR corrected).

| Region  | $x$ | $y$ | $z$ | Max $t$ | Volume (mm <sup>3</sup> ) |
|---|-----|-----|-----|---------|---------------------------|
| Right Cingulate gyrus (anterior division)                 | 3   | 17  | 34  | 8.16    | 3204                      |
| Left cerebellum   | -3  | -70 | -11 | 4.89    | 216                       |
| Right insular cortex                                      | 39  | 11  | -5  | 5.09    | 882                       |
| Left insular cortex                                       | -45 | 8   | -5  | 4.70    | 297                       |
| Left lateral occipital cortex, left middle temporal gyrus | -45 | -64 | 2   | 1.76    | 153                       |
| Left lingual gyrus, Left intracalcarine occipital cortex  | -6  | -67 | 4   | 3.93    | 45                        |
| Right precentral gyrus, right postcentral gyrus           | -6  | -16 | 52  | 4.03    | 53                        |
| Right supramarginal gyrus, right superior temporal gyrus  | 63  | -34 | 25  | 3.87    | 54                        |

ANOVA design included the set of first level contrast images from all participants relative to a certain temporal block.

Within the one-way ANOVA design, we computed Student  $t$ -test obtaining five statistical maps, one for each block of 2 minutes. The spatial  $t$ -maps so obtained were thresholded for significance both at  $P = .001$  without correction for multiple comparison and at  $P = .05$  with False Discovery Rate correction.

Regions of interest (ROIs) were defined as clusters of contiguous voxels with a  $t$ -stat above the threshold.

In order to investigate how magnitude and extent of activation in brain regions evolve while performing the CPT task, we measured the volume of the ROIs identified for each temporal block of 2 minutes and averaged across subjects the spatial mean of the time courses of the voxels within each ROI.

### 3. Results

Table 1 illustrates the fMRI activations during the first 2 minutes of the CPT task. Brain areas associated with the task performance were located in the cingulate, temporal, and occipital cortical regions and in the cerebellum. BOLD activation in the cingulate cortex is almost entirely located in the anterior division and the greatest brain activation, in terms of volume extent of BOLD response and magnitude (maximum value of  $T$ -statistic in the cluster), is located in the right anterior cingulate cortex (ACC).

In Figure 1 it is shown how the fMRI activation evolves across the five temporal blocks: comparing with the first block, in the second block (2–4 minutes) and in the third block (4–6 minutes) of the attention test we observed a progressive decreasing of the volume of the activated areas and of the magnitude of their BOLD response. In the fourth block (6–8 minutes), instead, an increasing of the brain activity is observed and in the fifth block (8–10 minutes), there is a new decreasing.

Figure 2 represents the time course of the BOLD response in the ACC ROI during the entire duration of fMRI acquisition comprising the baseline period before the beginning of the attention task, the period in which the test was performed, and a final recovery period after the task (2–12 minutes).

In Figure 2 we can observe the initial increasing of the BOLD signal after the beginning of the test (forty-first volume), a subsequent decreasing until about the one-hundred-sixtieth volume, a newly increasing during the 4th block (160–200 volumes) and a decreasing during the 5th block and the final recovery period (201–280 volumes).

For the other areas, not shown in the papers, we observed a similar temporal trend of fMRI response during the test.

Figure 3 illustrates the temporal evolution during the test of the numbers of errors committed by the subjects. In each temporal block, we averaged the numbers of errors over each time interval of 2 minutes, and then we averaged the results obtained for each block across the population of healthy subjects. We considered the number of total errors calculated as the sum of omission and commission errors.

Since in the Conners CPT test, the subject’s task is to inhibit the response whenever the letter X representing the target stimulus appears (“No-Go event”) and to respond when any letters appear “Go event,” the omission errors are defined as the lacking responses to “Go-event,” and the commission errors are defined as the responses to “No-Go event.”

On the basis of the graphic shown in Figure 3 we can observe that the number of errors remains substantially unchanged if we compare the first block (0–2 minutes) and the second one (2–4 minutes), while the number of errors increases in a remarkable way in the third block (4–6 minutes) and in more slightly way in the fourth block (6–8 minutes), and then it decreases in the last temporal block (8–10 minutes). The largest number of errors are committed in the third period of the test, in line with previous clinical literature [8] and with the Conners’ C-CPT-II standard [9], which reported a fall in subjects’ attentional performance in the middle of the Conners’ CPT test.

### 4. Discussion

In this study we identified the network of activated brain regions in a group of healthy subjects by using fMRI during a sustained attention task. This network includes frontal, temporal and occipital and insular areas and the cerebellum. The largest cluster of activation was found in the frontal

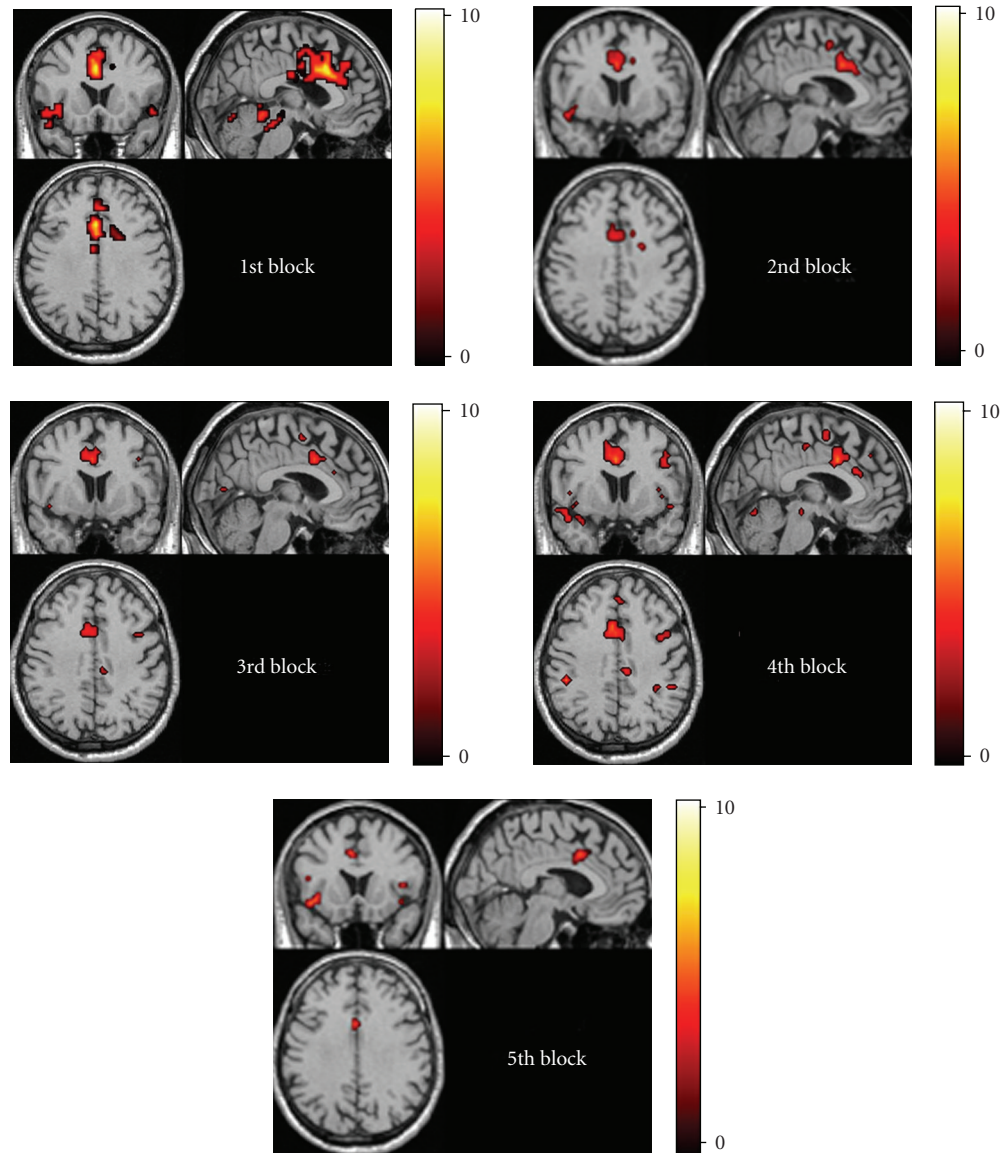


FIGURE 1: Brain activity during the five blocks of the sustained attention task.

lobe and, in particular, in the anterior cingulate cortex (ACC). The ACC plays a central role in attentional processing by modulating target selection (i.e., focusing attention) [10], motor response selection [11], error detection, and performance monitoring [12, 13].

Activation in left occipital and temporal cortex was located in the ventral visual pathway and it is involved in visual letter recognition as reported in previous studies [14]. The activation of right insular cortex is not documented in previous studies and it is not yet interpreted.

The cerebellum activation confirms results found by the attention study performed by [15], in which it has been shown the lateralization of the attention-related activity to the left cerebellum.

The results relative to the temporal trend of BOLD signal during the sustained stimulation show an initial increasing in fMRI activation in the first part of the test and a subsequent

decrease that can be explained by the theory of prolonged stimulation [16], and by the habituation phenomenon that is very frequently encountered in the study of sustained attention [17, 18].

It is widely accepted in literature that brain activity is associated with an increasing in regional cerebral blood flow (rCBF) not matched by a proportional increase in oxygen consumption or cerebral metabolic rate for oxygen (CMRO<sub>2</sub>) [19, 20]. As a consequence of this mismatch, the augmented rCBF requested by brain activity exceeds the augmented oxygen consumption resulting in an initial decreasing of deoxy-Hb and therefore an increasing of the BOLD signal within a few seconds after the onset of stimulation [21, 22].

Therefore, the initial rising of BOLD signal shown in our findings is well explained by this transient pronounced decoupling of rCBF and CMRO<sub>2</sub>.

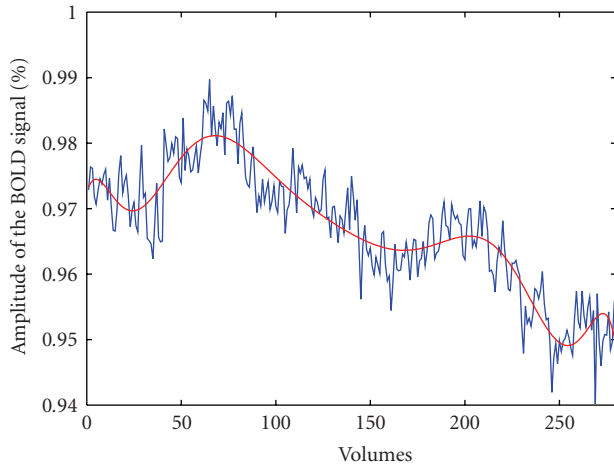


FIGURE 2: Time course of the BOLD signal of the activated region in the anterior cingulate cortex averaged across the voxels of the ROI and across subjects. The graphics shows the raw signal (blue line) and an interpolated signal by using polinomial fitting (red line). The volumes from 1 to 40 (2 minutes) are the first rest time, the volumes from 41 to 240 (10 minutes) are the active time, the volumes from 241 to 280 (2 minutes) are the second rest time.

After the initial increasing, we observed a slow decreasing in activation until reaching the baseline. This decreasing can be interpreted as a consequence of a restoration of the equilibrium between the cerebral flow and the oxidative metabolism and so the reduction of the BOLD signal could be partially explained by a restored coupling between cerebral flow response and metabolic demand [16].

The further decreasing after the reaching of the baseline is not documented in literature but can be interpreted on the basis of the habituation effect that is widely encountered in the study of sustained attention.

Since the phenomenon of the habituation, the brain progressively automates the carrying out of the task and gradually reduces the energetic request. This reduction in metabolic demand causes a rapid return of blood flow to basal level not immediately paralleled by the much slower recovery of the metabolic rate for oxygen. This results in a “negative” uncoupling between CBF and  $CMRO_2$  which could explain our findings. The presence of a “negative” uncoupling has been already proposed in previous studies in order to interpret the reduction of cerebral haemoglobin oxygenation below the basal level immediately after the end of stimulation [16, 23].

The “negative” recoupling is probably prevented by a new increasing of the brain activity that interrupt the habituation phenomenon and is due to a reaction of the subject to a reduction of the behavioral performance.

In particular, the light increasing of the fMRI response observed in the next to last block (6–8 minutes) followed by a decreasing of oxygenation level in the last block of the test (8–10 minutes) is probably related to the immediately previous (4–6 minutes) reduction of the behavioral performance of the subjects resulting in an increasing of the numbers of errors that we observed in the third block (4–6 minutes).

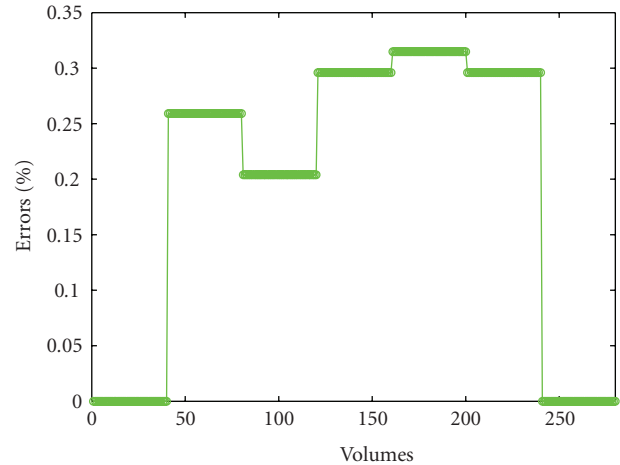


FIGURE 3: Time course of the number of errors averaged across subjects. The number of errors is expressed in percentage with respect to the number of stimuli.

At a behavioral level, it can be supposed that as a consequence of the increasing of the numbers of errors, the subjects make effort to limit the numbers of errors in order to improve their performances. This results in an increasing of the cerebral activity that, in turn, causes an initial rising of the cerebral oxygenation deriving from an initial decoupling of flow and metabolic demand and a following decreasing deriving from the recoupling of haemodynamic response and metabolic request.

After task cessation a further decreasing of the BOLD signal was found in our data followed by a rising of oxygenation level. This is in accordance with the results showed in [16, 23], and can be interpreted as transient deoxygenation resulting from a “negative” uncoupling between the decreasing of the cerebral flow and of the oxygen consumption.

The incompleteness of the recovery of the BOLD signal after this initial decreasing can be probably due to the shortness of time interval (2 minutes) during which the post-task is recorded. This assertion is suggested by Near Infrared Spectroscopy (NIRS) studies on the sustained attention that documented a complete recovery of the basal cerebral oxygenation level at about 8 minutes after the end of the test, that is, a recovery time longer than that typical of the motor and purely visual stimulation [24].

## 5. Conclusion

This study is aimed to the identification of the cerebral activations patterns during a sustained attention task in a group of healthy subjects. It also attempts to investigate how haemodynamic activation in brain regions involved in fMRI response to a sustained attentive task, evolves during the entire duration of the test and to understand the relationships between the cerebral activation and the behavioral performance.

Using the neuroimaging fMRI method we identified a complex network of brain regions involved in the sustained attention task. The activations are consistent with the existing models of visual object processing and attentional control and the results of clinical literature obtained with other neuroimaging techniques.

Timing analysis has shown a progressive decreasing of BOLD response during the CPT task due to the habituation effect and an increasing of the activation in the second half of the test probably correlated with the deterioration of the performance that occurs at the middle of the test.

This work can be a starting point for future investigation of the alteration of the pattern and of the dynamical behavior of cerebral network associated to neuropsychological deficits in clinical population. The relationships between specific patterns of activation and behavioral deficits may help us to identify targets for behavioral or pharmacological intervention.

## References

- [1] C. K. Conners, *Conners' Continuous Performance Test*, Multi-Health Systems, Toronto, Canada, 1995.
- [2] H. E. Rosvold, A. F. Mirsky, I. Sarason, E. D. Bransome Jr., and L. H. Beck, "A continuous performance test of brain damage," *Journal of Consulting Psychology*, vol. 20, no. 5, pp. 343–350, 1956.
- [3] J. C. Ballard, "Assessing attention: comparison of response-inhibition and traditional continuous performance tests," *Journal of Clinical and Experimental Neuropsychology*, vol. 23, no. 3, pp. 331–350, 2001.
- [4] J. C. Ballard, "Computerized assessment of sustained attention: a review of factors affecting vigilance performance," *Journal of Clinical and Experimental Neuropsychology*, vol. 18, no. 6, pp. 843–863, 1996.
- [5] C. J. Price and K. J. Friston, "Functional imaging studies of neuropsychological patients: applications and limitations," *Neurocase*, vol. 8, no. 5, pp. 345–354, 2002.
- [6] K. J. Friston, P. Fletcher, O. Josephs, A. Holmes, M. D. Rugg, and R. Turner, "Event-related fMRI: characterizing differential responses," *NeuroImage*, vol. 7, no. 1, pp. 30–40, 1998.
- [7] K. J. Friston, S. Williams, R. Howard, R. S. J. Frackowiak, and R. Turner, "Movement-related effects in fMRI time-series," *Magnetic Resonance in Medicine*, vol. 35, no. 3, pp. 346–355, 1996.
- [8] S. Homack and C. A. Riccio, "Conners' continuous performance test (2nd ed., CCPT-II)," *Journal of Attention Disorders*, vol. 9, no. 3, pp. 556–558, 2006.
- [9] C. K. Conners, *Conners' Continuous Performance Test*, Multi-Health Systems, Toronto, Canada, 1994.
- [10] M. I. Posner, S. E. Petersen, P. T. Fox, and M. E. Raichle, "Localization of cognitive operations in the human brain," *Science*, vol. 240, no. 4859, pp. 1627–1631, 1988.
- [11] R. D. Badgaiyan and M. I. Posner, "Mapping the cingulate cortex in response selection and monitoring," *NeuroImage*, vol. 7, no. 3, pp. 255–260, 1998.
- [12] W. J. Gehring and R. T. Knight, "Prefrontal-cingulate interactions in action monitoring," *Nature Neuroscience*, vol. 3, no. 5, pp. 516–520, 2000.
- [13] P. Luu, T. Flaisch, and D. M. Tucker, "Medial frontal cortex in action monitoring," *Journal of Neuroscience*, vol. 20, no. 1, pp. 464–469, 2000.
- [14] E. Temple, R. A. Poldrack, J. Salidis, et al., "Disrupted neural responses to phonological and orthographic processing in dyslexic children: an fMRI study," *NeuroReport*, vol. 12, no. 2, pp. 299–307, 2001.
- [15] G. Allen, R. B. Buxton, E. C. Wong, and E. Courchesne, "Attentional activation of the cerebellum independent of motor involvement," *Science*, vol. 275, no. 5308, pp. 1940–1943, 1997.
- [16] H. R. Heekeren, H. Obrig, R. Wenzel, et al., "Cerebral haemoglobin oxygenation during sustained visual stimulation—a near-infrared spectroscopy study," *Philosophical Transactions of the Royal Society B*, vol. 352, no. 1354, pp. 743–750, 1997.
- [17] G. Horn, "Neuronal mechanisms of habituation," *Nature*, vol. 215, no. 5102, pp. 707–711, 1967.
- [18] R. F. Thompson and W. A. Spencer, "Habituation: a model phenomenon for the study of neuronal substrates of behavior," *Psychological Review*, vol. 73, no. 1, pp. 16–43, 1966.
- [19] P. T. Fox and M. E. Raichle, "Focal physiological uncoupling of cerebral blood flow and oxidative metabolism during somatosensory stimulation in human subjects," *Proceedings of the National Academy of Sciences*, vol. 83, pp. 1140–1144, 1986.
- [20] M. Ueki, F. Linn, and K.-A. Hossmann, "Functional activation of cerebral blood flow and metabolism before and after global ischemia of rat brain," *Journal of Cerebral Blood Flow and Metabolism*, vol. 8, no. 4, pp. 486–494, 1988.
- [21] P. A. Bandettini, E. C. Wong, R. S. Hinks, R. S. Tikofsky, and J. S. Hyde, "Time course EPI of human brain function during task activation," *Magnetic Resonance in Medicine*, vol. 25, no. 2, pp. 390–397, 1992.
- [22] J. Frahm, H. Bruhn, K. D. Merboldt, and W. Hanicke, "Dynamic MR imaging of human brain oxygenation during rest and photic stimulation," *Journal of Magnetic Resonance Imaging*, vol. 2, no. 5, pp. 501–505, 1992.
- [23] J. Frahm, G. Krüger, K.-D. Merboldt, and A. Kleinschmidt, "Dynamic uncoupling and recoupling of perfusion and oxidative metabolism during focal brain activation in man," *Magnetic Resonance in Medicine*, vol. 35, no. 2, pp. 143–148, 1996.
- [24] M. Butti, D. Contini, E. Molteni, et al., "Effect of prolonged stimulation on cerebral hemodynamic: a time-resolved fNIRS study," *Medical Physics*, vol. 36, no. 9, pp. 4103–4114, 2009.

## Research Article

# EEG Analysis of the Brain Activity during the Observation of Commercial, Political, or Public Service Announcements

**Giovanni Vecchiato,<sup>1,2</sup> Laura Astolfi,<sup>1,2,3</sup> Alessandro Tabarrini,<sup>2,3</sup> Serenella Salinari,<sup>3</sup> Donatella Mattia,<sup>2</sup> Febo Cincotti,<sup>2</sup> Luigi Bianchi,<sup>2</sup> Domenica Sorrentino,<sup>2</sup> Fabio Aloise,<sup>2</sup> Ramon Soranzo,<sup>1</sup> and Fabio Babiloni<sup>1,2</sup>**

<sup>1</sup> Department of Physiology and Pharmacology, University of Rome "Sapienza", P.le A. Moro 5, 00185 Rome, Italy

<sup>2</sup> IRCCS Fondazione Santa Lucia, Laboratory of Neuroelectrical Imaging, Via Ardeatina 354, 00179 Rome, Italy

<sup>3</sup> Department of Computer Science and Informatics, University of Rome "Sapienza", Via Ariosto 25, 00100 Rome, Italy

Correspondence should be addressed to Fabio Babiloni, [fabio.babiloni@uniroma1.it](mailto:fabio.babiloni@uniroma1.it)

Received 24 July 2009; Accepted 29 September 2009

Academic Editor: Fabrizio De Vico Fallani

Copyright © 2010 Giovanni Vecchiato et al. This is an open access article distributed under the Creative Commons Attribution License, which permits unrestricted use, distribution, and reproduction in any medium, provided the original work is properly cited.

The use of modern brain imaging techniques could be useful to understand what brain areas are involved in the observation of video clips related to commercial advertising, as well as for the support of political campaigns, and also the areas of Public Service Announcements (PSAs). In this paper we describe the capability of tracking brain activity during the observation of commercials, political spots, and PSAs with advanced high-resolution EEG statistical techniques in time and frequency domains in a group of normal subjects. We analyzed the statistically significant cortical spectral power activity in different frequency bands during the observation of a commercial video clip related to the use of a beer in a group of 13 normal subjects. In addition, a TV speech of the Prime Minister of Italy was analyzed in two groups of swing and "supporter" voters. Results suggested that the cortical activity during the observation of commercial spots could vary consistently across the spot. This fact suggest the possibility to remove the parts of the spot that are not particularly attractive by using those cerebral indexes. The cortical activity during the observation of the political speech indicated a major cortical activity in the supporters group when compared to the swing voters. In this case, it is possible to conclude that the communication proposed has failed to raise attention or interest on swing voters. In conclusions, high-resolution EEG statistical techniques have been proved to be able to generate useful insights about the particular fruition of TV messages, related to both commercial as well as political fields.

## 1. Introduction

Every day we are exposed to several solicitations for purchasing products, voting or supporting particular politicians and even improving our life style. Such pressure has become usual, being mediated by all the current media available, video, audio, and even internet. How and to what extent these messages could be detected and recognized by our brain is still not well understood. In fact, the study of brain responses to commercial and political announcements has been measured mainly by the hemodynamic responses of the different brain areas, by using the functional Magnetic Resonance Imaging devices (fMRI). However, both the stimuli and the relative brain responses have rapidly shifting

characteristics that are not tracked by the evolution of the hemodynamic blood flow, which usually lasts 4–6 seconds. Different brain imaging tools, mainly EEG and Magnetoencephalography, exhibit a sufficient time resolution to follow the brain activity at an expense of a coarse level of spatial resolution with respect to the fMRI. In fact, during those last ten years, the use of the high resolution EEG techniques has retrieved an increased amount of information related to the brain during activities related to complex cognitive tasks, such as memory, visual attention, short-term memory, and so forth [1–3].

Starting from the interesting characteristic of the high resolution EEG techniques for the tracking of brain activity, the present work would like to describe neuroelectric-based

methodology for the assessment of the efficacy of commercial, politic, and Public Service Announcements (PSAs).

The aim of the brain imaging techniques applied to the fruition of commercial advertizing is to understand mechanisms underlying customer's engagement with brand or company advertized [4–6]. In particular, the issue is to explain how the exposure of subsequent film segments is able to trigger in the consumer mind persisting stimuli leading to interest, preference, purchase, and repurchase of a given product. In the last decades, several authors have investigated the capability of subjects to memorize and retrieve sensible “commercial” information observed during a TV spot [7–12].

Recently, a growing number of research laboratories are involved in recognizing the cerebral areas activated during the observation of figures and videos showing politicians, a field that the most people call Neuropolicy. This intense scientific movement has encouraged some companies and universities to seriously take an interest about the cerebral activity during fruition of politicians' images and TV commercials [13, 14].

Local governments of European countries, and also across the world, are called to disseminate information about health risky habits promoting instead healthy life style in order to improve the health of their citizens. In this context PSAs are noncommercial broadcast advertizemnets intended to modify public behavior. PSAs are at the core of many public health campaigns against smoking, fatty foods, abuse of alcohol, and other possible threats for the health of citizens. But the content of these PSAs could be also directed for the promotion of “positive” social collective behavior, for instance, calling against racism, supporting the integration of different cultures in the country, or promoting a healthy drive style, for the road security. Therefor effective PSAs provide a great public health benefit [15, 16]. However, the lack of reliable, quantitative, and objective means of advertizement evaluation is one of the impediments to better PSA outcomes. In addition, not well-designed PSAs are going to have counter effects with respect to their desired goals [17].

The purpose of this paper is to illustrate the potential of the High Resolution EEG techniques when applied to the analysis of brain activity related to the observation of TV commercials, political advertizing, and PSAs to localize cerebral areas mostly emotionally involved. In particular, we would like to describe how, by using appropriate statistical analysis, it is possible to recover significant information about cortical areas engaged by particular scenes inserted within the video clip analyzed. The brain activity was evaluated in both time and frequency domains by solving the associate inverse problem of EEG with the use of realistic head models. Successively, the data analyzed were statistically treated by comparing their actual values to the average values estimated during the observation of the documentary. Statistical estimators were then evaluated and employed in order to generate representations of the cortical areas elicited by the particular video considered.

## 2. Materials and Methods

The whole dataset is composed by EEG registrations of 13 healthy subjects (mean age  $30 \pm 4$  years) watching a documentary of 30 minutes intermingled by a TV commercial [18], and 10 subjects were involved in the observation of a documentary of 15 minutes intermingled with a couple of video clips supporting the Italian Prime Minister (politic announcement) and a campaigns against smoking (PSA). Each subject is exposed to the observation of a same documentary. Subjects were informed about the fact that the EEG recordings will be related to the observation of the brain activity during the documentary and TV commercial, political, and PSAs videos. The entire procedure was authorized by the local ethical committee at the recording site, and informed written consensuses to the recording procedures were taken before the EEG recordings. Subjects were instructed to pay attention to the material showed on the screen during the entire projection. The videos related to products, political support, and PSAs were inserted at the middle of the documentary.

In order to enhance the poor spatial content of the EEG activity, we employed the High Resolution EEG technologies [19, 20] to detect cortical areas involved in the task. Basically, these techniques involve the use of a large number (64–256) of scalp electrodes and rely on realistic MRI-constructed head models [21, 22] and spatial deconvolution estimations, which are usually computed by solving a linear-inverse problem based on Boundary-Element Mathematics [23, 24]. Subjects were comfortably seated on a reclining chair, in an electrically shielded, dimly lit room. A 64-channel EEG system (BrainAmp, Brainproducts GmbH, Germany) was used to record electrical potentials by means of an electrode cap, accordingly to an extension of the 10–20 international system. In the present work, the cortical activity was estimated from scalp EEG recordings by using realistic head models whose cortical surfaces consisted of about 5000 triangles uniformly disposed. The current density estimation of each one of the equivalent electrical dipole of the underlying neuronal population was computed by solving the linear-inverse problem according to the techniques described previously in this papers [18, 25, 26]. Thus, a time-varying waveform relative to the estimated current density activity at each single triangle of the modeled cortical surface was obtained. Such waveform was then subjected to the time-varying spectral analysis by computing the spectral power in the different frequency bands usually employed in EEG analysis, that is, theta (4–7 Hz), alpha (8–12 Hz), beta (13–24 Hz), and gamma (24–45 Hz).

However, the estimation of the spectral power do not convey information about the significance or nonsignificance of what have been computed. This significance has to be brought to the analysis by taking into account the  $z$ -score transformation of the cortical power spectra source imaging obtained. In fact, if a cortical area shows an increased activity during the period of the video to be tested, this increment has to be contrasted with the average power spectra activity observed during the documentary period. The  $z$ -score variable is then obtained by computing the

differences between the estimated values (power spectra in the commercial advertizing, political announcement, or PSA) in the video and the average power spectra activity during the documentary. This difference is successively divided by the standard deviation of the power spectra estimated during the documentary period.

Together with the statistically significant cortical source imaging applied in all the investigated videos, we would like to track specifically the changes in the power spectral intensity of the EEG channels during the videos observation. In order to do that, first we selected the set of the frontal leads, including Fp1, Fp2, F1, F3, Fz, AFz, F2, F4, AF1, and AF2. Then, we filtered the observed EEG activity in two main frequency bands: theta (4–7 Hz) and beta and gamma bands (13–40 Hz) [27]. This filtering procedure was justified by the fact that the theta frequency band is mainly involved in the memorization processes, while the beta and gamma frequency bands are instead advocated for the attention engagement. To summarize the activity from all these electrodes, the Global Field Power (GFP) was then computed. This is a measurement introduced by Lehmann and Michel some decades ago to summarize the overall activity over the scalp surface. GFP is computed from the entire set of electrodes by performing the sum of the squared values of the EEG potential at each electrodes, resulting in a time-varying waveforms related to the increase or decrease of the global power in the analyzed EEG. Since the data were estimated from two EEG datasets, one filtered 4–7 Hz and the other filtered between 13–40 Hz, we obtained two time-varying waveforms: the GFP filtered in the 4–7 Hz and the GFP filtered in the 13–40 Hz. Successively, on these waveforms we apply the  $z$ -score transformation by estimating the average and the standard deviation of the GFP values during the documentary. Values of  $z$ -score transformation higher than 2 suggest statistical significance differences between the value of the variable estimated and the baseline considered, at the 5% level.

In order to present these results relative to the entire population, we needed a common cortical representation to map the different activated areas of each subject. For this purpose we used the average brain model available from the McGill University website to display the cortical areas that are statistically significantly activated during different experimental conditions in all subjects analyzed. In this case, we are able to average the single subject result of the  $z$ -score test. In fact, we highlighted in yellow a voxel of the average brain model if it was a cortical site in which a statistical significant variation of the spectral power between the experimental conditions was found in all the subjects; if such brain voxel was statistically significant in all but one of the subjects analyzed, we depicted it in red. In all the other cases, the voxel was represented with a gray color. Only the statistical significant variation of such spectral power when compared to the documentary period was highlighted in color. Statistical significance threshold was set at  $p < 0.05$ , which Bonferroni corrected for multiple comparisons.

*2.1. Commercial Advertizing.* After the EEG registration related to the commercial advertizements each subject was

recalled in laboratory where an interview was performed asking if he/she usually drinks beer or light alcohol at least once per week. If yes, subjects were considered within the dataset of “drinkers” in opposition to the dataset of “no drinkers”. In order to increase the sensitivity of the analysis performed, only the EEG spectral analysis for the “drinkers” was analyzed and presented here.

### 3. Results

Of the 13 subjects recorded, only seven are “drinkers”. Hence, the successive analysis and results are presented for seven of such subjects. We summarized all results for the “drinkers” group in a couple of figures showing the statistically significant differences of cortical activation concerning this dataset in the theta frequency band (4–7 Hz), being the data regarding the alpha frequency band equivalent to the theta band. Figure 1 presents the  $z$ -score average activity of the drinkers population during the observation of a couple of frames of the commercial advertizing proposed, at time:  $T1 = 10$  seconds and  $T2 = 28$  seconds (the entire duration of the spot is 30 seconds). Note in the left lower panel the different brain views are relative to the brain seen from the back (1), left (2), front (3), and right (4). It is possible to note that the brain is presented from different perspectives in the lower panels, while in the upper panels there are the video frames observed by the subjects. The gray color represents the absence of the statistical differences between the cortical activity in the analyzed frequency band (theta in this case) during the video clips observation and the documentary. The color zones instead presented the cortical areas in which such spectral activity differs in the population analyzed.

By examining this strip, it results evident how the temporal evolution of the mean cortical activity changes according to the images viewed by the subjects. In particular, an enhancement of cerebral activity is suggested by the result of the application of the statistic tests at the beginning ( $T1$ ) and at the end of the commercial presented ( $T2$ ). The final part of the commercial spot attracts the interest in all the population analyzed, as the large cortical areas depicted in yellow and red suggested. It could be hypothesized that the initial part of the TV spot presented fails to attract the attention of the experimental group, as the brain activity result is similar to that generated during the observation of the documentary. This could be used in future to better tailor the TV spots by removing the parts of them that were unable to attract the attention of the audience.

The applications of the abovementioned technology to the evaluation of a TV speech of the Italian Prime Minister are shown in Figure 2.

Such figure shows the cerebral activity observed in two groups of people divided as swing voters (panel a) and the “supporters” of the Italian Prime Minister (panel b). The figure presents the statistically significant activity in the analyzed groups in the theta frequency band for a particular time frame of the speech. The brain activity is presented as seen from different perspectives (left, right, front, and back). The brain activity observed for the supporters (panel b) was

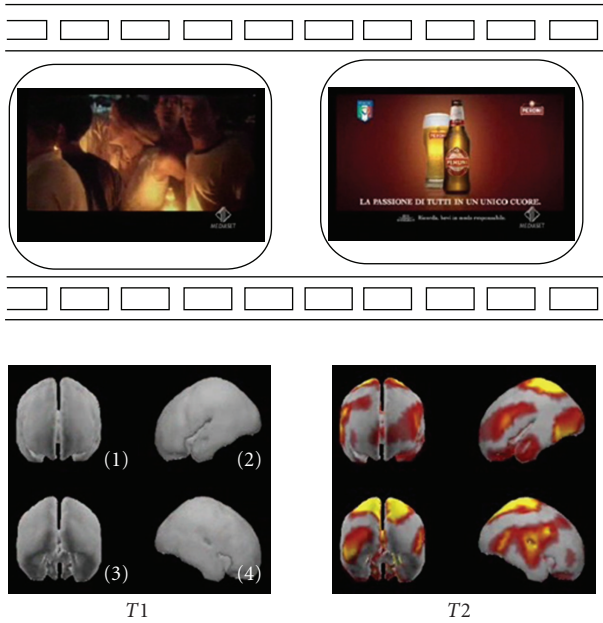


FIGURE 1: The track of the mean cortical activity of the group of “drinkers” in the theta frequency band spot. The statistical significant activity in this population is shown in 2 panels each representing subsequent film segments of a TV spot with corresponding brain activity. Temporal axes beat the spot in correspondence to the beginning ( $T1$ ) and the end ( $T2$ ) of the entire film sequence: time in seconds. Note in the left lower panel the different brain views are relative to the brain seen from the back (1), left (2), front (3), and right (4).

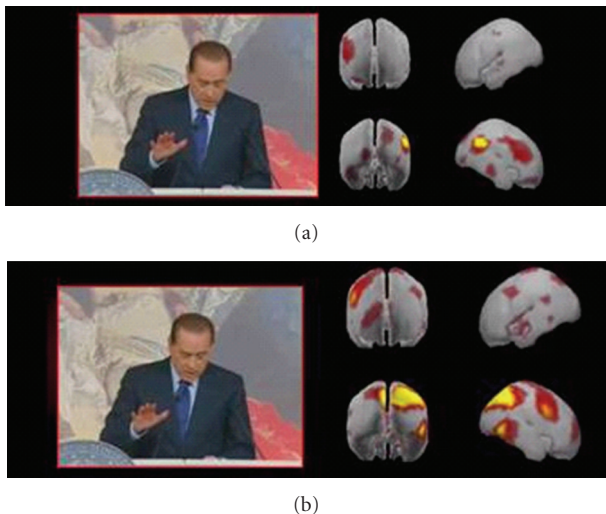


FIGURE 2: Analysis of a speech by the Italian Prime Minister: panel (a) presents the cerebral activity related to the population of swing voters in the theta frequency bands. Note the four brains depicted at the right of each frame are relative to the four different views of the brain surface from different points of view; same convention of Figure 1, panel (b) shows the cortical activity in the same frequency band for the supporters of the Prime Minister. Cortical areas depicted in red and yellow highlight those zones in which there is an enhancement of cerebral activity, when compared to a resting state.

characterized during all the speech by power spectral activity significantly larger than those obtained in the documentary. On the contrary, swing voters are relatively less attracted by the speech, since they had the brain activity not different from that of the documentary for the major part of the speech.

Hence, the results would suggest an overall efficacy of the communication generated by the video for the second group of subjects (panel b) with respect to the “perceived” communication offered by the prime minister’s speech by the first one (panel a). A possible interpretation of these results is that analyzed speech could only intensify the supporters’ idea leaving the swing voters neutral.

Another example of the application of the neuroelectric brain imaging technology applied to the case of the commercial and PSAs is represented in Figure 3. In such figure the time-varying changes of the filtered GFP in the theta (4–7 Hz) and in the beta and gamma bands (13–40 Hz) during the observation of a 30-second spot related to a commercial (row a) and a PSA against smoking (row b) are presented. It is interesting to note how in both cases the spectral activity of the frontal leads showed values of  $z$ -score over 2 for many instants. In such a case it could be suggested that the spectral activity in those time frames exceeds statistically the spectral activity observed during the vision of the documentary.

The brain activity observed during this PSA spot is instead presented in Figure 4, in which two cortical maps of the differences between the spectral activities during the spot when compared to those of the documentary are represented. Figure 4 shows the  $z$ -score maps during the PSA, where it is possible to note a precise activation of the frontal lobes during the 30 seconds of the spot. Also in this case it is interesting to note that the brain activity during the PSA is relevant in the prefrontal areas, and it is symmetrical in the beta and gamma frequency bands while located in the right frontal hemisphere for the theta band.

## 4. Discussions

Thanks to the high resolution EEG techniques, we tracked subjects’ brain activity during visualization of a commercial: in such manner, it has been possible to obtain a global measure of the reconstructed cortical signals by means of a simple graphic tool which allows us to distinguish the activity of different cortical areas. The abovementioned results allow us to comment on temporal and spatial events observed. In fact, it is worth noticing that the principal areas of statistical differences in power spectra in the “drinkers” condition are located almost bilaterally in the prefrontal BAs 8 and 9 as well as in the parietal BA 7. As presented in previous works performed both with EEG analysis [18] and MEG recordings [8], the observed phenomena suggest an active role of the prefrontal and parietal areas in coding of the information that will be retained by users from the TV commercials. In particular, activations of these cortical areas can be associated with attentional and memorization processes. The present work intends to stress the useful properties of the high resolution EEG technologies: this tool is able to help us in

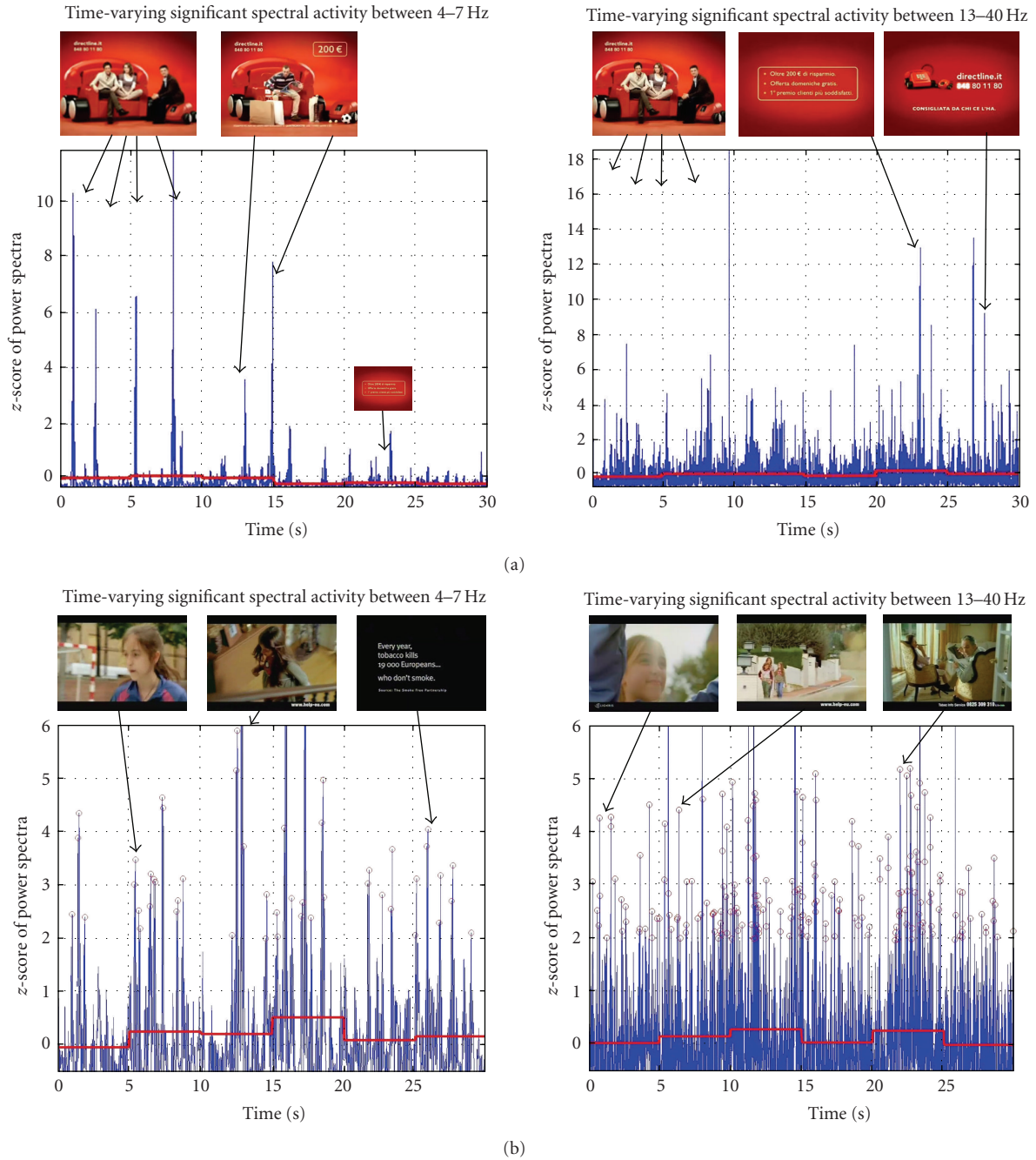


FIGURE 3: Representation of the filtered GFP related to frontal electrodes in the theta band (left panel) and beta and gamma bands (right panel) for the analyzed population during the observation of a commercial (row a) and a Public Service Announcement (row b) against the smoking. On the  $x$ -axis, there is the time duration of the spot; on the  $y$ -axis there is the  $z$ -score value of the GFP considered. Values greater than 2 mean a difference in power spectral activity during the PSA when compared to those of the documentary that are statistically significant at 5%. The red line is the average  $z$ -score values of the GFP in blocks of five seconds of spot.

observing and analyzing the temporal trend of the cortical activities thanks to a high-temporal and spatial resolution allowing us to distinguish changes of activation of ROIs corresponding to different cortical areas. The reconstruction of the cortical activity by means of the high resolution EEG technique and by combining the above statistic treatment of our data allowed us to track subjects' brain activity during

visualization of the commercial. In such a way for each film segment of the clip it was possible to distinguish cortical areas that were differently activated when compared to those of the observation of the documentary. This could be useful in the evaluation of the cortical responses to particular types of visual solicitations, performed by film, commercial clips, or faces of politicians, which at the moment is a field largely

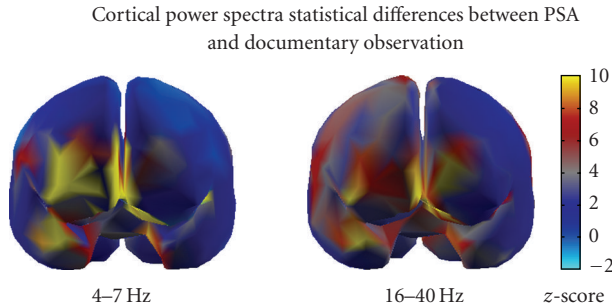


FIGURE 4: Brain activity related to the observation of the PSA when compared to that of the documentary. The brain is viewed from a frontal view. The color map is relative to the z-score values of the power spectra EEG activity during the PSA when compared to the documentary. Z-score values different from the blue means significant statistically activity. It is possible to note that in the theta frequency band, the right prefrontal cortex is activated while in the beta and gamma frequency bands the activation is rather symmetrical.

unexplored by the neuroscience. In fact, the big attention paid to political scenes originates from the experimental result that decisions based on “superficial” observation could predict the elections’ results, linearly correlated with the candidate’s margin of victory with a precision of 68.8% [28]. The consequence of this observation is that the recognition and liking of the politician’s face is a principal factor for the choice of the citizen more than “rational” considerations. Such phenomenon has been also confirmed by subsequent studies published in international scientific literature [29] and newspapers [30] suggesting that the scenic presence by itself mostly influences the decision of voting besides the fact that men and women can elicit a different kind of engagement according to the figure they saw. These results are surprising if we think about the USA midterm elections of 2006 when candidates and their supporting groups spent about 1 billion dollars in advertizements in order to inform electors about their political affiliations, qualities, and ideas. After predicting the electoral results [28, 29], the subsequent pass of this research has been to understand whether in this immediate decision the positive effects were prevailing (i.e., face pleasantness as well as his/her adaptation to particular a priori requirements demanded by the candidate) when compared to the negative ones. This was then studied in literature [29] and its result was that the effect of an emotionally “negative” judgement towards a candidate is an prevailing reason in his/her defeat (even in a contest of simulated elections) with respect to the fact of simply being “less attractive” than the other candidate. These data could also suggest that the cerebral activity, generated from an emotional state of “rejection” of the candidate, is completely different from the one generated from an emotional state of acception or satisfaction of the same one. Another interesting aspect is that results obtained by means of analyses performed on behavioral data reveal how decision makers sometimes have already made up their minds at an unconscious level, even when they consciously

indicate that they have not yet decided. From the traditional political research, that is, performed without using cerebral measurements techniques, it was already known that the negative vote plays also an important role in the final vote decision. In this contest, having a measure of the emotional state of people observing a candidate’s face assumes always more importance.

## 5. Conclusions

We employed advanced techniques for the tracking of brain activity during the observation of videos of different emotional natures: commercial, PSAs, and even political speech. The techniques here employed encompass the use of descriptors of the frequency contents of the EEG signals up to the statistical mapping of the cortical activity, during the observation of the proposed clips [31–36]. In all the cases presented here, it is possible to localize rather precisely the cortical areas involved in the processing of the particular video material proposed. The application of these techniques to the PSAs and to the political speech is still in its infancy, but in a near future could bring a neuroscience perspective in an already mature communication field.

## References

- [1] P. L. Nunez, *Electric Fields of the Brain: The Neurophysics of EEG*, Oxford University Press, New York, NY, USA, 1981.
- [2] P. L. Nunez, *Neocortical Dynamics and Human EEG Rhythms*, Oxford University Press, New York, NY, USA, 1995.
- [3] F. De Vico Fallani, L. Astolfi, F. Cincotti, et al., “Cortical network topology during successful memory encoding in a lifelike experiment,” in *Proceedings of the 30th Annual International Conference of the IEEE Engineering in Medicine and Biology Society (EMBS ’08)*, pp. 4007–4010, 2008.
- [4] T. Ambler, S. Braeutigam, J. Stins, S. P. R. Rose, and S. Swithenby, “Salience and choice: neural correlates of shopping decisions,” *Psychology and Marketing*, vol. 21, no. 4, pp. 247–261, 2004.
- [5] S. Braeutigam, S. P. R. Rose, S. J. Swithenby, and T. Ambler, “The distributed neuronal systems supporting choice-making in real-life situations: differences between men and women when choosing groceries detected using magnetoencephalography,” *European Journal of Neuroscience*, vol. 20, no. 1, pp. 293–302, 2004.
- [6] J. Cappel, *The Future of Advertising: New Media, New Clients, New Consumers in the Post-Television Age*, McGraw-Hill, New York, NY, USA, 2005.
- [7] H. E. Krugman, “Brain wave measures of media involvement,” *Journal of Advertising Research*, vol. 11, pp. 3–10, 1971.
- [8] A. A. Ioannides, L. Liu, D. Theofilou, et al., “Real time processing of affective and cognitive stimuli in the human brain extracted from MEG signals,” *Brain Topography*, vol. 13, no. 1, pp. 11–19, 2000.
- [9] T. Ambler and T. Burne, “The impact of affect on memory of advertising,” *Journal of Advertising Research*, vol. 39, no. 2, pp. 25–34, 1999.
- [10] M. Rotschild and J. Hyun, “Predicting memory for components of TV commercials from EEG,” *Journal of Consumer Research*, pp. 72–78, 1989.

- [11] J. R. Rossiter, R. B. Silberstein, P. G. Harris, and G. A. Nield, "Brain-imaging detection of visual scene encoding in long-term memory for TV commercials," *Journal of Advertising Research*, vol. 41, no. 2, pp. 13–21, 2001.
- [12] C. Young, "Brain waves, picture sorts<sup>®</sup>, and branding moments," *Journal of Advertising Research*, vol. 42, no. 4, pp. 42–53, 2002.
- [13] Sands Research, <http://sandsresearch.com/>.
- [14] Emory University, Centre For Neuropolicy, <http://www.neuropolicy.emory.edu/>.
- [15] L. Biener, J. E. Harris, and W. Hamilton, "Impact of the Massachusetts tobacco control programme: Population based trend analysis," *British Medical Journal*, vol. 321, pp. 351–354, 2000.
- [16] S. Emery, M. Wakefield, Y. Terry-McElrath, G. Szczypka, P. M. O'Malley, L. D. Johnston, et al., "Televized state-sponsored anti-tobacco advertising and youth smoking beliefs and behavior in the United States, 1999–2000," *Archives Pediatric Adolescent Medicine*, vol. 159, pp. 639–645, 2005.
- [17] M. Wakefield, B. Flay, M. Nichter, and G. Giovino, "Effects of anti-smoking advertising on youth smoking: a review," *Journal of Health Communication*, vol. 8, pp. 229–247, 2003.
- [18] L. Astolfi, F. De Vico Fallani, S. Salinari, et al., "Brain activity related to the memorization of TV commercials," *International Journal of Bioelectromagnetism*, vol. 10, no. 3, pp. 1–10, 2008.
- [19] J. Le and A. Gevins, "Method to reduce blur distortion from EEG's using a realistic head model," *IEEE Transactions on Biomedical Engineering*, vol. 40, no. 6, pp. 517–528, 1993.
- [20] A. Gevins, J. Le, N. K. Martin, P. Brickett, J. Desmond, and B. Reutter, "High resolution EEG: 124-channel recording, spatial deblurring and MRI integration methods," *Electroencephalography and Clinical Neurophysiology*, vol. 90, no. 5, pp. 337–358, 1994.
- [21] F. Babiloni, C. Babiloni, F. Carducci, et al., "High resolution EEG: a new model-dependent spatial deblurring method using a realistically-shaped MR-constructed subject's head model," *Electroencephalography and Clinical Neurophysiology*, vol. 102, no. 2, pp. 69–80, 1997.
- [22] F. Babiloni, C. Babiloni, L. Locche, F. Cincotti, P. M. Rossini, and F. Carducci, "High-resolution electro-encephalogram: source estimates of Laplacian-transformed somatosensory-evoked potentials using a realistic subject head model constructed from magnetic resonance images," *Medical and Biological Engineering and Computing*, vol. 38, no. 5, pp. 512–519, 2000.
- [23] A. M. Dale, A. K. Liu, B. R. Fischl, et al., "Dynamic statistical parametric mapping: combining fMRI and MEG for high-resolution imaging of cortical activity," *Neuron*, vol. 26, no. 1, pp. 55–67, 2000.
- [24] R. Grave de Peralta Menendez and S. L. Gonzalez Andino, "Distributed source models: standard solutions and new developments," in *Analysis of Neurophysiological Brain Functioning*, C. Uhl, Ed., pp. 176–201, Springer, New York, NY, USA, 1999.
- [25] L. Astolfi, F. Cincotti, D. Mattia, et al., "Comparison of different cortical connectivity estimators for high-resolution EEG recordings," *Human Brain Mapping*, vol. 28, no. 2, pp. 143–157, 2006.
- [26] F. Babiloni, F. Cincotti, C. Babiloni, et al., "Estimation of the cortical functional connectivity with the multimodal integration of high-resolution EEG and fMRI data by directed transfer function," *NeuroImage*, vol. 24, no. 1, pp. 118–131, 2005.
- [27] W. Klimesch, M. Doppelmayr, and S. Hanslmayr, "Upper alpha ERD and absolute power: their meaning for memory performance," *Progress in Brain Research*, vol. 159, pp. 151–165, 2006.
- [28] A. Todorov, A. N. Mandisodza, A. Goren, and C. C. Hall, "Inferences of competence from faces predict election outcomes," *Science*, vol. 308, pp. 1623–1626, 2005.
- [29] C. C. Ballew II and A. Todorov, "Predicting political elections from rapid and unreflective face judgments," *Proceedings of the National Academy of Sciences of the United States of America*, vol. 104, no. 46, pp. 17948–17953, 2007.
- [30] M. Iacoboni, J. Freedman, J. Kaplan, et al., "This is your brain on politics," *The New York Times*, November 2007, <http://www.nytimes.com/2007/11/11/opinion/11freedman.html?pagewanted=1&.r=2&sq=marco%20iacoboni&st=cse&scp=8>.
- [31] F. De Vico Fallani, L. Astolfi, F. Cincotti, et al., "Cortical functional connectivity networks in normal and spinal cord injured patients: evaluation by graph analysis," *Human Brain Mapping*, vol. 28, no. 12, pp. 1334–1346, 2007.
- [32] L. Astolfi, F. De Vico Fallani, F. Cincotti, et al., "Imaging functional brain connectivity patterns from high-resolution EEG and fMRI via graph theory," *Psychophysiology*, vol. 44, no. 6, pp. 880–893, 2007.
- [33] L. Astolfi, F. Cincotti, D. Mattia, et al., "Tracking the time-varying cortical connectivity patterns by adaptive multivariate estimators," *IEEE Transactions on Biomedical Engineering*, vol. 55, no. 3, pp. 902–913, 2008.
- [34] M. Oliveri, C. Babiloni, M. M. Filippi, et al., "Influence of the supplementary motor area on primary motor cortex excitability during movements triggered by neutral or emotionally unpleasant visual cues," *Experimental Brain Research*, vol. 149, no. 2, pp. 214–221, 2003.
- [35] C. Babiloni, F. Babiloni, F. Carducci, et al., "Mapping of early and late human somatosensory evoked brain potentials to phasic galvanic painful stimulation," *Human Brain Mapping*, vol. 12, no. 3, pp. 168–179, 2001.
- [36] A. Urbano, C. Babiloni, P. Onorati, and F. Babiloni, "Dynamic functional coupling of high resolution EEG potentials related to unilateral internally triggered one-digit movements," *Electroencephalography and Clinical Neurophysiology*, vol. 106, no. 6, pp. 477–487, 1998.

## Research Article

# On the Use of Electrooculogram for Efficient Human Computer Interfaces

A. B. Usakli,<sup>1,2</sup> S. Gurkan,<sup>2</sup> F. Aloise,<sup>1</sup> G. Vecchiato,<sup>1</sup> and F. Babiloni<sup>1</sup>

<sup>1</sup>IRCCS Fondazione Santa Lucia, Via Ardeatina, 306, 00179, Rome, Italy

<sup>2</sup>Department of Technical Sciences, The NCO Academy, 10100 Balikesir, Turkey

Correspondence should be addressed to A. B. Usakli, ausakli@yahoo.com

Received 13 June 2009; Accepted 28 July 2009

Academic Editor: Fabrizio De Vico Fallani

Copyright © 2010 A. B. Usakli et al. This is an open access article distributed under the Creative Commons Attribution License, which permits unrestricted use, distribution, and reproduction in any medium, provided the original work is properly cited.

The aim of this study is to present electrooculogram signals that can be used for human computer interface efficiently. Establishing an efficient alternative channel for communication without overt speech and hand movements is important to increase the quality of life for patients suffering from Amyotrophic Lateral Sclerosis or other illnesses that prevent correct limb and facial muscular responses. We have made several experiments to compare the P300-based BCI speller and EOG-based new system. A five-letter word can be written on average in 25 seconds and in 105 seconds with the EEG-based device. Giving message such as “clean-up” could be performed in 3 seconds with the new system. The new system is more efficient than P300-based BCI system in terms of accuracy, speed, applicability, and cost efficiency. Using EOG signals, it is possible to improve the communication abilities of those patients who can move their eyes.

## 1. Introduction

An efficient alternative channel for communication without speech and hand movements is important to increase the quality of life for patients suffering from Amyotrophic Lateral Sclerosis or other illnesses that prevent correct limb and facial muscular responses. In this respect, the area of study related to the Human Computer Interaction and Brain Computer Interface (BCI) is very important in hopes of improving the medium term quality of the life for such patients.

In eye movements, a potential across the cornea and retina exists, and it is source of electrooculogram (EOG). EOG can be modeled by a dipole [1], and these systems can be used in medical systems. There are several EOG-based HCI studies in literature. A wheelchair controlled with eye movements is developed for the disabled and elderly people. Eye movement signals and sensor signals are combined, and both direction and acceleration are controlled [2]. Using horizontal and vertical eye movements and two and three blinking signals a movable robot is controlled [3]. Because the EOG signals are slightly different for the each subject, a dynamical threshold algorithm is developed [4]. In this approach, the initial threshold is compared with the dynamic range; the threshold value is renewed after each

difference. According to this threshold the output signal is made 1 or 0 and afterwards it is processed. EOG, EEG and electromyogram (EMG) signals are classified in real time, and movable robots are controlled by using artificial neural network classifier [5, 6]. Investigating possibility of usage of the EOG for HCI, a relation between sight angle and EOG is determined [7].

The human-machine interface which provides control of machines for disabled people is called the Man Machine Interface (MMI). Generally, if the control is computer-based, it is called the Human Computer Interface (HCI) instead of MMI. If the assistive system is based on electroencephalogram (EEG), it is called BCI, and its applications are increasing for severely disabled people. BCI is a direct communication pathway between the brain and an external device. The BCI systems translate brain activity into electrical signals that control external devices. Thus they can represent the only technology for severely paralyzed patients to increase or maintain their communication and control options [8]. Because EEG signals are characterized by low amplitude ( $\mu V$ ), their measurement is more difficult than EOG.

As a contribution in this area of research, in this study, we present an HCI device that is able to recognize the subject's

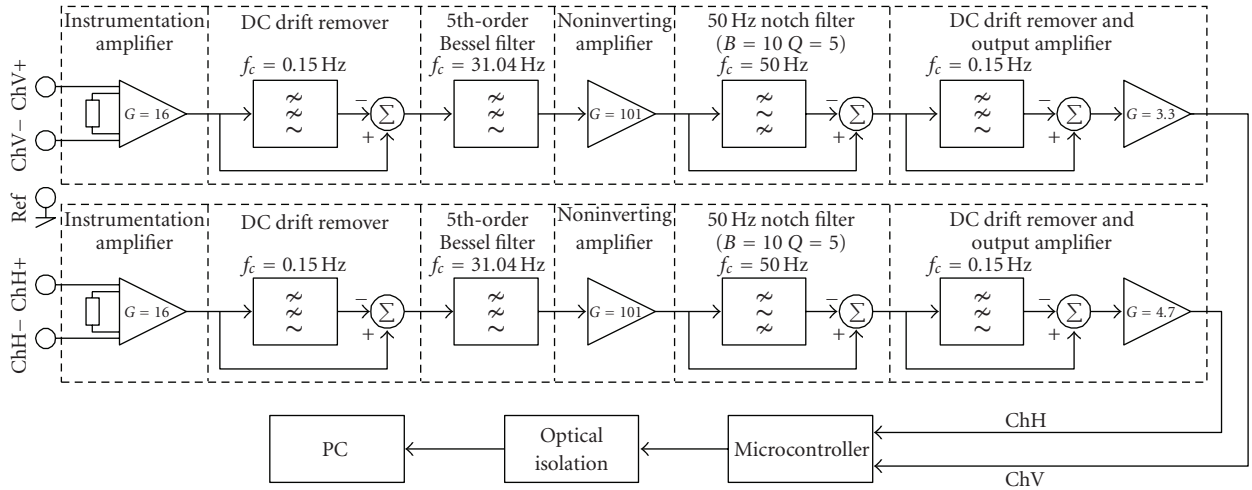


FIGURE 1: The new EOG system block diagram.

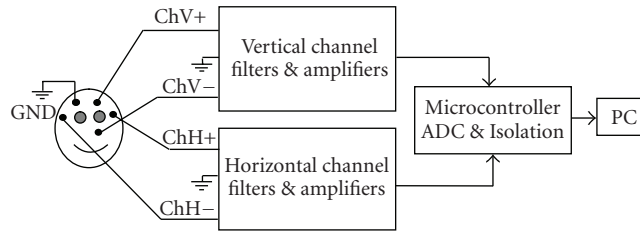


FIGURE 2: The EOG electrode configuration.

eye movements by using the collection of the electrical activity generated by the eye, that is, EOG. This device allows the patients to generate decisions on a screen by means of simple eye movements and the electroencephalogram (EEG) electrodes, without the need of sophisticated infrared cameras. Then, patients could be able to select letters on the screen, or even to communicate basic needs (food, drinks, etc.) to the caregiver with a simple movement of their eyes.

In this study, to make experimental comparison, we made two experiments with the BCI system and realized EOG system (the design rationale presented in [9]). For each device the subjects wanted to write a five-letter word. The performance of the EOG system is relatively good, since a five-letter word can be written by the patient on average in 25 seconds and in 105 seconds with the EEG-based device. Giving message such as “clean up” could be performed in 3 seconds. The experiments’ details are presented in the experimental results.

The paper is organized as follows: first, the new EOG-based HCI device will be presented. In this section the design in detail is briefly explained. Successively, experimental results will be illustrated.

## 2. Materials and Methods

**2.1. The New EOG-Based HCI Device.** In this subsection, as an HCI device, a novel EOG measurement system design is proposed. Horizontal and vertical eye movements are measured with two passive electrodes usually employed for

the EEG acquisition. The system block diagram is presented in Figure 1, and its electrode configuration in Figure 2. The system is microcontroller-based and battery powered. The CMRR is 88 dB, electronic noise is  $0.6 \mu\text{V}$  ( $p-p$ ), and sampling rate is 176 Hz. 5 Ag/AgCl electrodes are used (two for each channel and one is for ground). In order to remove the DC level and 50 Hz power line noise, the differentiate approach is used. This approach is much more successful than classical methods.

**2.2. The Design Details.** After filtering and the amplification stages, the EOG signals are digitized (10 bit) and then transferred to the PC. The EOG signals are then processed by a classification algorithm which is based on the nearest neighborhood (NN) relation, with a classification performance of 95%. The EOG measurement system, as an HCI, allows people to communicate with their environment, only by using eye movements, successfully and economically (180 USD). The system’s initial electronic circuitry (Figure 3) can be used for EOG, EMG, and EEG. After digitizing, horizontal and vertical EOG signals are then transferred to the PC serial port. Microcode Studio program is used to write the embedded code; Winpic800 is used to program the microcontroller ( $\mu\text{C}$ ). The data transfer rate is enough for the sampling rate (176 Hz), which is sufficient to process the EOG signals.

It is preferred to use the NN algorithm to classify the EOG signals since in this way they can be easily discriminated. The time cost of this algorithm is shorter than

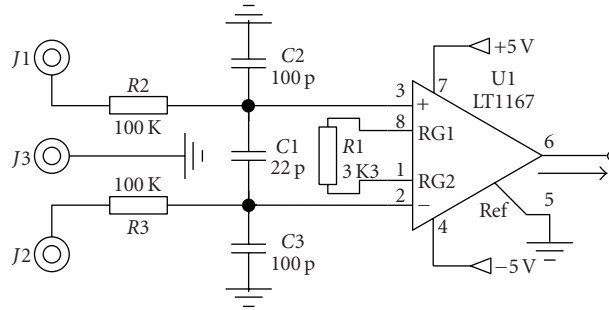


FIGURE 3: Input amplifier circuit.



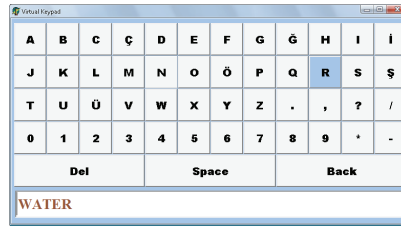
(a) Electrode montage



(b) Placed in metal box



(c) User interface main menu. At the top line horizontal and vertical EOG signals can be observed online. The other options for virtual keyboard, needs, and movement control can be selected



(d) Virtual keyboard with special characters



(e) Virtual keyboard (like P300 speller applications)

FIGURE 4: The realized EOG-based device.

the other, more complex, classification ones. Regarding the NN, the Euclidean distance formula is used as follows:

$$L(x, y) = \sqrt{\sum_{i=1}^d (x_i - y_i)^2} \quad (1)$$

As for the classification, 5 classes (each having 20 members) are used. Each member consists of 251 samples. To increase the classification performance, both channels are applied together to the classifier. The classification performance is 95%. System software transfers the data and classifies it in real time.

Summarizing, the realized system (Figure 4) is based on the following features:

- (i) horizontal and vertical eye movement signals are acquired,

- (ii) Ag/AgCl electrodes are used,
- (iii) DC level and power line noise signals are removed with a subtraction approach,
- (iv)  $\mu$ C-based,
- (v) battery powered,
- (vi) the NN algorithm is used for the classification,
- (vii) user-friendly interface.

### 3. Experimental Results

To compare the systems we made experiments with the BCI system (8 channels, Guger Technology) and new EOG system. The P300-based BCI speller based on the detection of P300 waveforms from the array of 8 electrodes returned

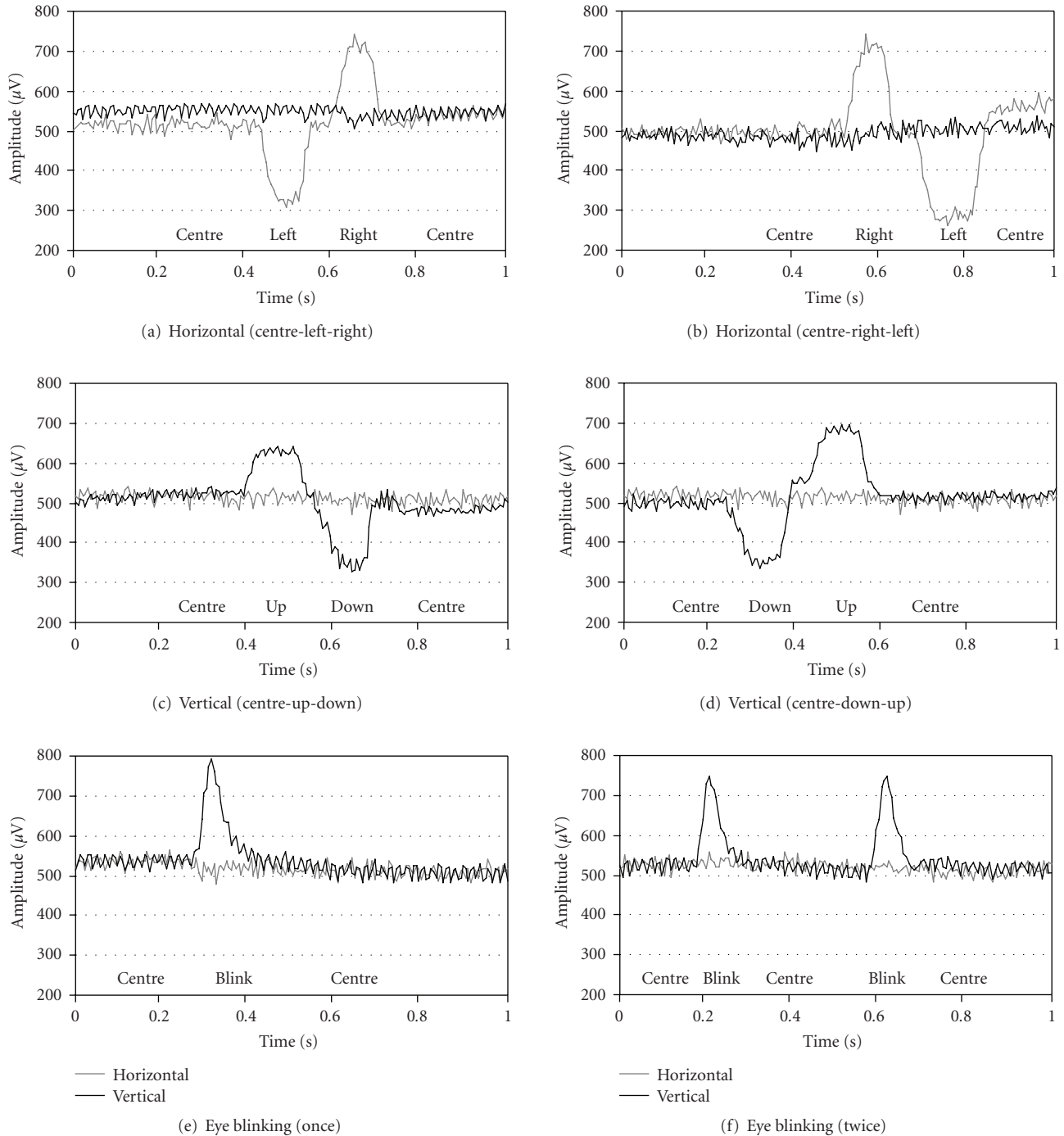


FIGURE 5: The EOG recording samples.

in 21 seconds (105 seconds for 5 letters) for the selection of the word “water” in the experimental group (10 subjects) employed. In addition, the accuracy of the letter selection on average was 81% in the same group, with a standard deviation of 14%. Controls were then able to master the P300 BCI system after a session of 30 minutes at the reported level of accuracy.

The group of 10 subjects that selected the word “water” with the EOG-based device employed an average time of

24.7 seconds, with 3.2 seconds as a standard deviation. The accuracy percentage in this group was 100%, regarding writing of the selected word. Also in this case the subjects were able to master the device after a session of 5 minutes. Notifying a need message (clean up) could be performed in 3 seconds.

As seen from the recordings in Figure 5, after considering noise reduction measures in designing of the biopotential data acquisition system, the EOG system performance is

good. Electronic noise reduction is also successful. The circuit can be easily adapted for EMG and EEG measurements.

#### 4. Conclusion

In this paper we proposed a new system to use the EOG signals for the realization of an HCI device able to restore some communication abilities to patients not able to move their limbs and facial muscles. After our experiments, it is observed that the new EOG-based system can be used for HCI, efficiently. From a technical point of view the highlights of the presented system are the following.

- (a) Horizontal and vertical EOG signals are measured successfully. CMRR is 88 dB, sampling rate is 176 Hz, and electronic noise is  $0.6 \mu\text{V}$  ( $p-p$ ). According to the specifications, the present system can measure the EOG signals properly.
- (b) The EOG signals, for different eye movements, are classified on-line. The NN algorithm (with Euclidean distance) is used. The signals do not need complex and time-costly classification algorithms.
- (c) The realized virtual keyboard allows the user to write messages and to communicate other needs relatively in an efficient way.

The EOG-based system seems more efficient than EEG-based (P300 BCI). It must be noted that the solution for the EOG system is extremely cheap when compared to the EEG solution (one order of magnitude) and then can be used as a first step for the hybrid device for the final users. A hybrid device is to familiarize the patient with a unique interface while he/she could switch with the biosignal more useful for him/her in that particular moment in time for the communication or for the control of the external devices. In this respect there will be the possibility to change the control signals without the need to relearn the user interfaces, as usually happen today with the use of different interfaces.

The realized system will be now tested by several patients in order to improve the quality of the graphic interface for a better and quick selection of the interesting items by using the EOG signals. As a future work, our research group will investigate using combined EOG and EEG and other inputs [10–15] for efficient configuration of a multi-input hybrid HCI.

#### References

- [1] S. Venkataramanan, P. Prabhat, S. R. Choudhury, H. B. Nemade, and J. S. Sahambi, "Biomedical instrumentation based on Electrooculogram (EOG) signal processing and application to a hospital alarm system," in *Proceedings of the 2nd IEEE International Conference on Intelligent Sensing and Information Processing (ICISIP '05)*, pp. 535–540, Chennai, India, January 2005.
- [2] R. Barae, L. Boquete, and M. Mazo, "System for assisted mobility using eye movements based on electrooculography," *IEEE Transaction on Neural Systems and Rehabilitation Engineering*, vol. 10, no. 4, pp. 209–218, 2002.
- [3] Y. Kim, N. L. Doh, Y. Youm, and W. K. Chung, "Robust discrimination method of the electrooculogram signals for human-computer interaction controlling mobile robot," *Intelligent Automation and Soft Computing*, vol. 13, no. 3, pp. 319–336, 2007.
- [4] Z. Lv, X. Wu, M. Li, and C. Zhang, "Implementation of the EOG-based human computer interface system," in *Proceedings of the 2nd International Conference on Bioinformatics and Biomedical Engineering (ICBBE '08)*, pp. 2188–2191, Shanghai, China, May 2008.
- [5] C. K. Young and M. Sasaki, "Mobile robot control by neural network EOG gesture recognition," in *Proceedings of the 8th International Conference on Neural Information Processing*, vol. 1, pp. 322–328, 2001.
- [6] Y. Chen and W. S. Newman, "A human-robot interface based on electrooculography," in *Proceedings of the IEEE International Conference on Robotics and Automation (ICRA '04)*, pp. 243–248, New Orleans, La, USA, April 2004.
- [7] D. Kumar and E. Poole, "Classification of EOG for human computer interface," in *Proceedings of the 2nd Joint IEEE Annual International Conference of the Engineering in Medicine and Biology Jointly with the 24th Annual Conference of the Biomedical Engineering Society (BMES/EMBS '02)*, vol. 1, pp. 64–67, Houston, Tex, USA, October 2002.
- [8] F. Cincotti, D. Mattia, F. Aloise, et al., "Non-invasive brain-computer interface system: towards its application as assistive technology," *Brain Research Bulletin*, vol. 75, no. 6, pp. 796–803, 2008.
- [9] A. B. Usakli and S. Gurkan, "Design of a novel efficient human computer interface: an electrooculogram based virtual keyboard," submitted to *IEEE Transactions on Instrumentation and Measurement*.
- [10] F. De Vico Fallani, L. Astolfi, F. Cincotti, et al., "Cortical Functional Connectivity Networks In Normal And Spinal Cord Injured Patients: Evaluation by Graph Analysis," *Human Brain Mapping*, vol. 28, no. 12, pp. 1334–1346, 2007.
- [11] L. Astolfi, F. De Vico Fallani, F. Cincotti, et al., "Imaging Functional Brain Connectivity Patterns From High-Resolution EEG And fMRI Via Graph Theory," *Psychophysiology*, vol. 44, no. 6, pp. 880–893, 2007.
- [12] L. Astolfi, F. Cincotti, D. Mattia, et al., "Tracking the time-varying cortical connectivity patterns by adaptive multivariate estimators," *IEEE Trans on Biomedical Engineering*, vol. 55, no. 3, pp. 902–913, 2008.
- [13] M. Oliveri, C. Babiloni, M. M. Filippi, et al., "Influence of the supplementary motor area on primary motor cortex excitability during movements triggered by neutral or emotionally unpleasant visual cues," *Exp Brain Res*, vol. 149, no. 2, pp. 214–221, 2003.
- [14] C. Babiloni, F. Babiloni, F. Carducci, et al., "Mapping of early and late human somatosensory evoked brain potentials to phasic galvanic painful stimulation," *Human Brain Mapping*, vol. 12, no. 3, pp. 168–179, 2001.
- [15] A. Urbano, C. Babiloni, F. Carducci, L. Fattorini, P. Onorati, and F. Babiloni, "Dynamic functional coupling of high resolution EEG potentials related to unilateral internally triggered one-digit movements," *Electroencephalography and clinical Neurophysiol*, vol. 106, pp. 477–487, 1998.

## Research Article

# Online Detection of P300 and Error Potentials in a BCI Speller

**Bernardo Dal Seno,<sup>1</sup> Matteo Matteucci,<sup>1</sup> and Luca Mainardi<sup>2</sup>**

<sup>1</sup>IIT-Unit, Department of Electronics and Information, Politecnico di Milano, Piazza Leonardo da Vinci 32, 20133 Milano, Italy

<sup>2</sup>IIT-Unit, Department of Bioengineering, Politecnico di Milano, Piazza Leonardo da Vinci 32, 20133 Milano, Italy

Correspondence should be addressed to Bernardo Dal Seno, [bernardo.dalseno@polimi.it](mailto:bernardo.dalseno@polimi.it)

Received 12 July 2009; Accepted 24 November 2009

Academic Editor: Sara L. Gonzalez

Copyright © 2010 Bernardo Dal Seno et al. This is an open access article distributed under the Creative Commons Attribution License, which permits unrestricted use, distribution, and reproduction in any medium, provided the original work is properly cited.

Error potentials (ErrPs), that is, alterations of the EEG traces related to the subject perception of erroneous responses, have been suggested to be an elegant way to recognize misinterpreted commands in brain-computer interface (BCI) systems. We implemented a P300-based BCI speller that uses a genetic algorithm (GA) to detect P300s, and added an automatic error-correction system (ECS) based on the single-sweep detection of ErrPs. The developed system was tested on-line on three subjects and here we report preliminary results. In two out of three subjects, the GA provided a good performance in detecting P300 (90% and 60% accuracy with 5 repetitions), and it was possible to detect ErrP with an accuracy (roughly 60%) well above the chance level. In our knowledge, this is the first time that ErrP detection is performed on-line in a P300-based BCI. Preliminary results are encouraging, but further refinements are needed to improve performances.

## 1. Introduction

A brain-computer interface (BCI) is an interface that does not entail muscle movements, but it bypasses any muscle or nerve mediation and connects a computer directly with the brain by picking up signals generated by the brain activity.

Among the different kinds of brain activity that can be used in a BCI, the P300 phenomenon has been known [1] and investigated for many years. It is an event-related potential (ERP), traditionally described as a positive peak visible in an EEG recording at approximately 300 ms from an event. It follows unexpected, rare, or particularly informative stimuli, and it is typically stronger in the parietal area. The shape of the P300 depends on the characteristics of the stimuli and their presentation.

For BCI applications, the “exact” shape of the P300 is not so important as having a way to detect it. Detecting a P300 in a single trial is very difficult and, therefore, repeated stimuli are normally used to facilitate the selection of the one that has generated a P300. The number of repetitions can be predetermined for each user to get the best trade-off between speed and accuracy.

In [2], Donchin and colleagues presented the first P300-based BCI, called also P300 speller, which permits to spell

words. A grid of letters and symbols is presented to the user, and entire columns or rows are flashed one after the other in random order (see Figure 1 for an example). When the column/row containing the desired letter is flashed, a P300 is elicited. In Donchin’s work, classification is made through stepwise discriminant analysis (SWDA) applied to averages of samples from epochs relative to the same stimulation (same row or same column).

Other BCI interfaces using the P300 protocol have been developed since then. In [3], a virtual-reality system is presented where subjects operate objects selected through the P300. Classification is made by comparing the correlation of single responses with the averages of all target and nontarget responses. In [4], subjects (healthy and impaired ones) control a cursor by choosing among four commands (up, down, left, right) via the P300. In this case, single-sweep detection is performed: independent component analysis (ICA) is used to decompose the EEG signal, a fuzzy classifier identifies a candidate P300 component among the ones extracted by ICA, and a neural network classifies it as target or nontarget. The system is more effective with healthy subjects, though no exact reason could be pinpointed. Finally, in [5], an initial attempt at using a BCI in a home environment is reported: a person with

amyotrophic lateral sclerosis uses a P300 speller on a daily basis.

Another relevant event-related potential is the *error potential* (ErrP hereafter), which is generated when a subject makes a mistake, and, more interestingly for BCI applications, when the machine behaves differently from the user intent. Known since the late 1980s [6, 7], ErrPs were described as a negative shift in the electric potential over the fronto-central region (from Fz to Cz of the 10–20 system) occurring 50–100 ms after an erroneous response (*error negativity*—Ne or *error-related negativity*—ERN) and a subsequent positive shift in the parietal region, whose maximum occurs between 200 and 500 ms after the error (*error positivity*—Pe). A high variability in shape, size, and delay of the Ne and Pe components has been observed as the effect of different underlying mechanism, whose nature is not yet certain [8].

In [9] the presence of ErrPs in a BCI paradigm (cursor movement by mu and beta rhythms) was revealed, as a positive peak at Cz 40 ms after the end of erroneous trials. This finding suggests an interesting application: the automatic detection of the errors made by a BCI in recognizing the user’s intent and a way to improve its performances. Millán and colleagues [10, 11] made experiments with ErrPs found in a motor-imagery BCI. They trained a Gaussian classifier to automatically recognize ErrPs, reaching an accuracy of about 80%.

In this work we present our experience in detecting P300 and ErrP in a P300-based speller with an integrated automatic error-correction system (ECS) based on the single-sweep ErrP detection.

## 2. Experimental Setting

We developed a classical BCI based on P300, the P300 speller, and integrated the use of ErrP in it. Our P300 speller is very similar in appearance and in functioning to the paradigm described by Donchin et al. [2]: 36 symbols are disposed on a 6×6 grid, and entire rows and columns of symbols are flashed one after the other in random order. The grid of symbols is visible in Figure 1. There are the letters from the alphabet, some digits, the space, and the *backspace*, represented as BS in the right bottom corner. The intensification of rows and columns lasts for 125 ms and the matrix remains blank for 125 ms between two consecutive flashes. Each row and column is flashed exactly once in the first 12 stimulations (a block of 12 consecutive stimulations is called a *repetition*); then another round of 12 stimulations is repeated, with flashing of rows and columns done in a new random order. We used 5 repetitions with no pause between repetitions. Please note that the number of repetitions is lower than usual. The choice is instrumental to stress the system under an unfavorable situation, thus soliciting a substantial number of misspelled letters.

After the fifth repetition, the P300 system detects the row and the column that are more likely to have elicited a P300, and selects the letter at their intersection. After a pause of 1 s, the letter is presented to the user in a big rectangle that pops up in front of the grid (see Figure 1). The presentation of the



FIGURE 1: Graphical interfaces of the P300 spellers used in the experiments, showing the moment of the letter feedback used for ErrP-based confirmation.

letter should elicit an ErrP if the letter predicted by the P300 system is different from the one the user intended.

An ErrP detection system figures out if any ErrP is elicited by the presentation of the selected letter, and in that case it overrides the P300 speller and cancels the last selection; otherwise, the letter is appended to the text at the top. After a 2–3 s pause (this parameter is tuned to each subject’s requirements), the speller starts a new series of stimulations for the next letter. A *trial*, in this context, is the whole series of 60 row/column flashes (12 flashes times 5 repetitions) together with the feedback of the speller selection made for each letter, that is, a single trial is composed of 60 P300 stimulations and 1 ErrP stimulation (a trial is about 15 s long).

In the online experiments, the users interact with the speller in two ways: in *copy mode* they are asked to select letters indicated by the BCI before each trial, so as to simplify the evaluation of the performance; in *free mode* subjects spell words of their own choosing. In *copy mode*, the system performs one trial for each letter, and it goes on to the next letter even when the P300 classifier is wrong; in this mode the ErrP correction system is not active. In *free mode* the ErrP correction system is active, and the user has to hit the *backspace* to correct a misspelled letter only when the error is not automatically recognized. During training, the speller is used in *copy mode* only. The GA and ErrP training was performed sequentially. In the ErrP training, in order to elicit error-related responses, the letter feedback is chosen wrongly in 20% of the times and correctly in 80% of the cases.

The speller we have implemented is based on BCI2000 [12], a general-purpose software system developed at the Wadsworth Center of the New York State Department of Health in Albany, New York, USA, for brain-computer interface (BCI) research. We developed three main components: a source module that acquires EEG data from our amplifier, an application derived from the built-in P300 speller, and a dual-classifier processing module to handle both P300 and ErrP classification. The application module implements the P300 speller with ErrP-based error correction, as described above, and a precise synchronization system (fully described

in [13]). The processing module splits the EEG signals in epochs synchronized on the stimulation instants, processes the data, and performs the classification of the epochs according to two separate processing chains, one for P300s and one for ErrPs, briefly described below.

### 3. Data Processing

EEG data are acquired with an EBNeuro BE Light amplifier at locations Fz, Cz, Pz, and Oz, and at a frequency of 512 Hz. Also, EOG is recorded from the right eye of the subject. EOG is not used for classification, but it is used to discard noisy epochs during training and is kept for future analysis. For P300 detection, a logistic classifier [14] is used, trained on features extracted through a genetic algorithm.

Genetic algorithms are a class of optimization algorithms that mimic the way natural evolution works. In a genetic algorithm, a set of possible solutions to an optimization problem are coded in strings called *chromosomes*; solutions are evaluated, and the best ones (those with highest *fitness*) are selected and combined together to form new possible solutions, in a process that mimics evolution among living beings. After some repetitions of the procedure, good solutions emerge.

In the genetic algorithm used in this work, each individual (chromosome) represents a set of possible features for discriminating the presence of a P300 in EEG recordings. Each gene encodes a feature and an EEG channel from which to extract it; a feature is obtained by multiplying the EEG channel by a weight function, whose exact shape is encoded by parameters in genes (see Figure 2 for examples of weight functions). Genetic operators are a variant of 1-point crossover and uniform mutation, and tournament selection with elitism is used. The fitness of a chromosome is the 4-fold cross-validated performance obtained by training a logistic classifier on the encoded features extracted from the training set. For a complete description of the algorithm, please see [15].

An analysis of the combination of the features extracted by the genetic algorithm and the classifier trained on the training set allows to compute weights assigned to individual EEG samples. In this way, the resulting classifier is very fast to apply online.

For ErrP detection, a simpler method is used, also because fewer training data are available (there is one ErrP stimulation per letter versus sixty for P300).

EEG data are segmented in epochs, whose extremes are found with the algorithm explained below. Epochs are then filtered in the band 1–10 Hz to improve the signal-to-noise ratio by eliminating frequency components extraneous to ErrPs. EEG samples are fed into a classifier trained through linear discriminant analysis (LDA).

On average, a difference between ErrP and non-ErrP epochs is observable only in some intervals of the segmented epoch, and these intervals depend on the subject. For these reasons we developed a way to automatically determine significant intervals in the ErrP for classification from the training data. Training data are first segmented in epochs

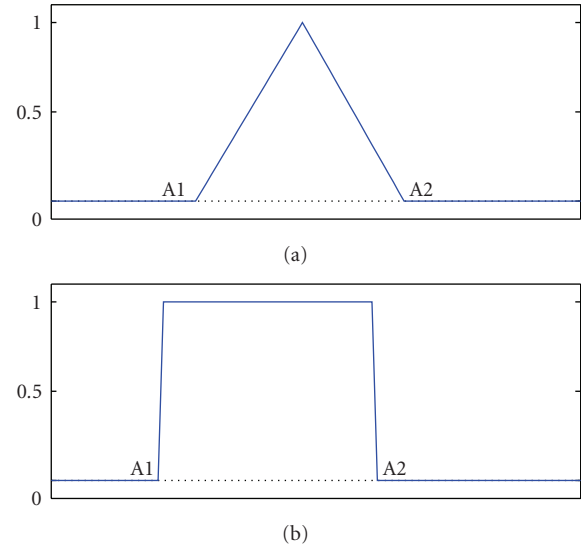


FIGURE 2: Weight functions used for feature extraction.

ranging from 100 ms before the stimulation instant (feedback onset) to 500 ms after it. Epochs containing strong EOG activity ( $>100 \mu V$  at any point) are automatically discarded before further analysis. A 1–10 Hz pass-band filter is then applied. For each channel  $c$  and time point  $t$ , the signals  $s_{c,1}(t)$  from ErrP epochs and  $s_{c,0}(t)$  from non-ErrP epochs can be viewed as two sets of random variables. A  $t$ -test is used to check if, for any given  $t$  and  $c$ , the mean of  $s_{c,1}(t)$  differs significantly from the mean of  $s_{c,0}(t)$ ; the significance level has been chosen to be 0.01, but much smaller  $P$ -values have been often found in analyzing data. The  $t$ -test is used only to find a time interval to use for classification, so the validity of its assumptions (Gaussian distributions with equal variance) is not very important; nevertheless, we ran some statistical tests on the data and they were satisfied.

The points detected by the  $t$ -test tend to lie in groups, because the filtered signals have a strong autocorrelation for short lags. However, many intervals of different sizes, with “holes” in between (see the top part of Figure 3 for an example), are usually detected, while we are interested only in finding one contiguous time interval containing all the interesting features of signals. We used DBSCAN [16], a clustering algorithm based on density, to fill holes and discard isolated points or small intervals. The biggest interval is selected and used for classification.

The training phase produces both a time interval and a linear classifier. During online classification, the procedure is very fast. EEG epochs are cut according to the interval found, and the classifier is applied to pass-band filtered epochs.

### 4. Results

Three subjects participated in a first set of online experiments. The P300 speller used 5 repetitions of each stimulation per letter; for Subject B1 we had to reduce the number of repetitions to 4 in order to have a reasonable

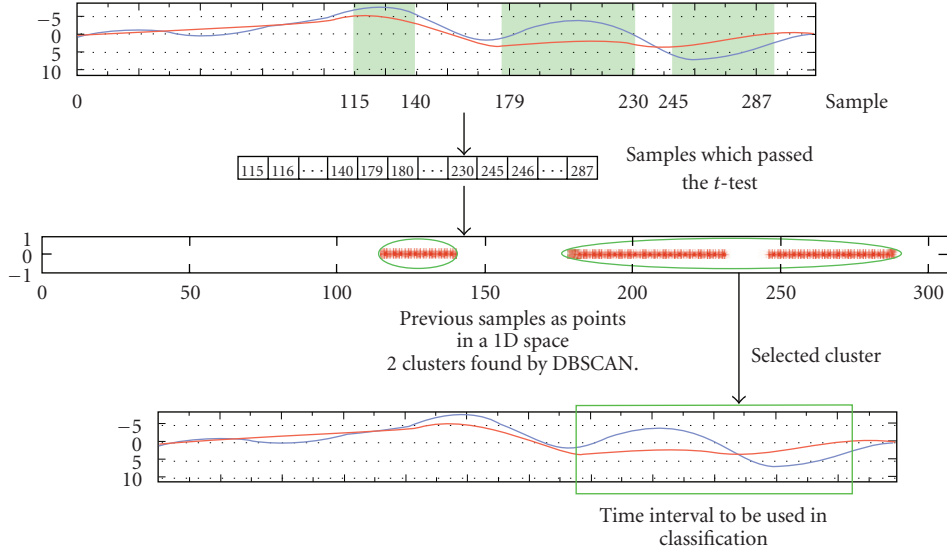


FIGURE 3: Procedure for the identification of significant intervals. Top: shadowed areas contain the samples that passed the  $t$ -test with a  $P$ -value of .01 or less. Middle: clustering of samples. Bottom: the interval used for classification.

TABLE 1: Results of the GA online in *free mode*. Training set size is the number of letters spelled in *copy mode* to collect training examples for the GA classifier. Performance is given as the number of correctly predicted letters over the total numbers of letters in the online usage.

| Subject | Training set size | No. repetitions | online performance |
|---------|-------------------|-----------------|--------------------|
| B1      | 196               | 4               | 74/109 (68%)       |
| B3      | 108               | 5               | 137/202 (68%)      |

number of errors (the online performance in *copy mode* for Subject B1 was 90% with 5 repetitions). On the other hand, Subject B2 had a poor performance mainly due to low concentration; the subject reported problems in focusing on the task, probably because of a failure of the brightness regulation of the computer screen that affected the online recordings. All results confirm the offline figures reported in [15], and confirm the validity of the GA-based classification method.

Subjects B1 and B3 also used the BCI to spell words in *free mode*, where the error correction mechanism was enabled. The results are shown in Table 1 and confirm that the classifier found by the GA can be used to really drive a BCI application. Subject B2 could have tried to use the speller by increasing the number of repetitions, but as the data was recorded also to evaluate error potentials, this would have made the recording sessions much longer.

Results of the online experiments are shown in Table 2. The classifiers were tested in sessions different from those used for training, so they are really indicative of a possible online use. For both users the classification performance is well above chance level, but this is not enough to say whether ErrP detection has been useful for such users. To test it, we computed the *gain* obtained by the inclusion

TABLE 2: Results of the online ErrP classification. Training size is the number of letters for each class from the ErrP *copy mode* session. Performance is the fraction of correct classification in the *free mode* experiment.

| Subject   | Train. Size | online performance |
|-----------|-------------|--------------------|
| B1 ErrP   | 84          | 23/35 (66%)        |
| B1 N-ErrP | 290         | 51/74 (69%)        |
| B3 ErrP   | 65          | 38/65 (58%)        |
| B3 N-ErrP | 193         | 91/137 (66%)       |

of an automatic ErrP correction system. The gain is based on the computation of the *Utility* metric we recently proposed (see [17] for details): for subject B1 we obtained a small improvement ( $\text{gain} = 1.0011$ ), while in subject B3 a detriment to the performance is observed ( $\text{gain} = 0.8733$ ).

## 5. Discussion

In this paper we have presented an experiment that—to the best of our knowledge—is the first attempt to use a P300 BCI with an integrated error-correction mechanism based on ErrPs. Although the number of subjects participating to the online study is quite limited, results are encouraging and confirm the feasibility of ErrP single-sweep detection already verified in more populated offline studies such as [18] or [13].

The use of a genetic algorithm for the definition of features to be used in P300 detection has proven its strength also in the online use, after good results in offline analysis [15]. In principle, the very same algorithm could be used for the ErrP feature design, but this is somehow prevented by the reduced number of examples that can be gathered in training sessions. A different strategy could be devised to collect ErrP

examples automatically during the use of our P300-based BCI application. Each back space in free mode can be treated as an explicit tagging of an ErrP by the user. With this strategy, data gathering would be still time consuming (we are not changing the odds for ErrP elicitation after all), but it could be more acceptable by the user, and it might enhance her experience with the speller as time passes.

The results presented are encouraging, but some additional work is still needed to improve the performance. In particular, it is important that ErrP detection reaches a high accuracy, higher than P300 detection. The reason is that ErrP stimulations are generated only once after each letter selection, and this is the only chance to detect an ErrP. An accuracy higher than chance is not sufficient to have a usable interface or a significant improvement as documented by the measured gain. In addition, to make the inclusion of ErrP corrections more profitable, the performances of the ErrP classifier should be tuned on a user-by-user basis. This could be done by maximizing the above mentioned gain. This was not done in the present paper, where we did not tune the ErrP classifier in favor of false positives (nor false negatives [19]).

In addition, to make the system more useful in practice, we plan to refine our processing methods and presentation interface (to better capture the subject attention) so as to increase the performance of the ErrP classifier; in a more extensive study with more subjects we will assess the online performance of the enhancement.

## Acknowledgments

This work has been partially supported by the Italian Institute of Technology (IIT), and by the grant “Brain-Computer Interfaces in Everyday Applications” from Politecnico di Milano and Regione Lombardia.

## References

- [1] S. Sutton, M. Braren, J. Zubin, and E. R. John, “Evoked-potential correlates of stimulus uncertainty,” *Science*, vol. 150, no. 3700, pp. 1187–1188, 1965.
- [2] E. Donchin, K. M. Spencer, and R. Wijesinghe, “The mental prosthesis: assessing the speed of a P300-based brain-computer interface,” *IEEE Transactions on Rehabilitation Engineering*, vol. 8, no. 2, pp. 174–179, 2000.
- [3] J. D. Bayliss, S. A. Inverso, and A. Tentler, “Changing the P300 brain computer interface,” *Cyberpsychology & Behavior*, vol. 7, no. 6, pp. 694–704, 2004.
- [4] F. Piccione, F. Giorgi, P. Tonin, et al., “P300-based brain computer interface: reliability and performance in healthy and paralysed participants,” *Clinical Neurophysiology*, vol. 117, no. 3, pp. 531–537, 2006.
- [5] T. M. Vaughan, D. J. McFarland, G. Schalk, et al., “The wadsworth BCI research and development program: at home with BCI,” *IEEE Transactions on Neural Systems and Rehabilitation Engineering*, vol. 14, no. 2, pp. 229–233, 2006.
- [6] M. Falkenstein, J. Hohnsbein, J. Hoormann, and L. Blanke, “Effects of crossmodal divided attention on late ERP components. II. Error processing in choice reaction tasks,” *Electroencephalography and Clinical Neurophysiology*, vol. 78, no. 6, pp. 447–455, 1991.
- [7] W. J. Gehring, B. Goss, M. G. H. Coles, D. E. Meyer, and E. Donchin, “A neural system for error detection and compensation,” *Psychological Science*, vol. 4, no. 6, pp. 385–390, 1993.
- [8] M. Falkenstein, “ERP correlates of erroneous performance,” in *Errors, Conflicts, and the Brain: Current Opinions on Performance Monitoring*, M. Ullsperger and M. Falkenstein, Eds., pp. 5–14, 2004.
- [9] G. Schalk, J. R. Wolpaw, D. J. McFarland, and G. Pfurtscheller, “EEG-based communication: presence of an error potential,” *Clinical Neurophysiology*, vol. 111, no. 12, pp. 2138–2144, 2000.
- [10] P. W. Ferrez and J. del R. Millán, “You are wrong!—automatic detection of interaction errors from brain waves,” in *Proceedings of the 19th International Joint Conference on Artificial Intelligence (IJCAI ’05)*, pp. 1413–1418, Edinburgh, UK, August 2005.
- [11] P. W. Ferrez and J. del R. Millán, “Simultaneous real-time detection of motor imagery and error-related potentials for improved BCI accuracy,” in *Proceedings of the 4th International Brain-Computer Interface Workshop & Training Course*, pp. 197–202, Graz, Austria, September 2008.
- [12] J. Mellinger and G. Schalk, “BCI2000: a general-purpose software platform for BCI research,” in *Towards Brain-Computer Interfacing*, G. Dornhege, J. del R. Millán, T. Hinterberger, D. J. McFarland, and K.-R. Müller, Eds., MIT Press, Cambridge, Mass, USA, 2007.
- [13] B. Dal Seno, *Toward an integrated P300- and ErrP-based brain-computer interface*, Ph.D. thesis, Politecnico di Milano, Milan, Italy, 2009.
- [14] S. le Cessie and J. C. van Houwelingen, “Ridge estimators in logistic regression,” *Applied Statistics*, vol. 41, no. 1, pp. 191–201, 1992.
- [15] B. Dal Seno, M. Matteucci, and L. Mainardi, “A genetic algorithm for automatic feature extraction in P300 detection,” in *Proceedings of the International Joint Conference on Neural Networks (IJCNN ’08)*, pp. 3145–3152, Hong Kong, 2008.
- [16] M. Ester, H.-P. Kriegel, J. Sander, and X.-A. Xu, “A density-based algorithm for discovering clusters in large spatial databases with noise,” in *Proceedings of the 2nd International Conference on Knowledge Discovery and Data Mining (KDD ’96)*, pp. 226–231, AAAI Press, Portland, Ore, USA, August 1996.
- [17] B. Dal Seno, M. Matteucci, and L. Mainardi, “The utility metric: a novel method to assess the overall performance of discrete brain-computer interfaces,” *IEEE Transactions on Neural Systems and Rehabilitation Engineering*. In press.
- [18] G. Visconti, B. Dal Seno, M. Matteucci, and L. Mainardi, “Automatic recognition of error potentials in a P300-based brain-computer interface,” in *Proceedings of the 4th International Brain-Computer Interface Workshop & Training Course*, pp. 238–243, Graz, Austria, September 2008.
- [19] B. Blankertz, G. Dornhege, R. Krepki, et al., “Boosting bit rates and error detection for the classification of fast-paced motor commands based on single-trial EEG analysis,” *IEEE Transactions on Neural Systems and Rehabilitation Engineering*, vol. 11, no. 2, pp. 127–131, 2003.

## Research Article

# Independent Component Analysis for Source Localization of EEG Sleep Spindle Components

Erricos M. Ventouras,<sup>1</sup> Periklis Y. Ktonas,<sup>2</sup> Hara Tsekou,<sup>2</sup> Thomas Paparrigopoulos,<sup>2</sup> Ioannis Kalatzis,<sup>1</sup> and Constantin R. Soldatos<sup>2</sup>

<sup>1</sup>Department of Medical Instrumentation Technology, Technological Educational Institution of Athens, Ag. Spyridonos Street, Egaleo, 12210 Athens, Greece

<sup>2</sup>Sleep Research Unit, Eginition Hospital, Department of Psychiatry, University of Athens, 74 Vas. Sophias Avenue, 11528 Athens, Greece

Correspondence should be addressed to Erricos M. Ventouras, ericvent@teiath.gr

Received 15 June 2009; Revised 24 November 2009; Accepted 19 January 2010

Academic Editor: Sara Gonzalez Andino

Copyright © 2010 Erricos M. Ventouras et al. This is an open access article distributed under the Creative Commons Attribution License, which permits unrestricted use, distribution, and reproduction in any medium, provided the original work is properly cited.

Sleep spindles are bursts of sleep electroencephalogram (EEG) quasirhythmic activity within the frequency band of 11–16 Hz, characterized by progressively increasing, then gradually decreasing amplitude. The purpose of the present study was to process sleep spindles with Independent Component Analysis (ICA) in order to investigate the possibility of extracting, through visual analysis of the spindle EEG and visual selection of Independent Components (ICs), spindle “components” (SCs) corresponding to separate EEG activity patterns during a spindle, and to investigate the intracranial current sources underlying these SCs. Current source analysis using Low-Resolution Brain Electromagnetic Tomography (LORETA) was applied to the original and the ICA-reconstructed EEGs. Results indicated that SCs can be extracted by reconstructing the EEG through back-projection of separate groups of ICs, based on a temporal and spectral analysis of ICs. The intracranial current sources related to the SCs were found to be spatially stable during the time evolution of the sleep spindles.

## 1. Introduction

Sleep spindles are characteristic transient oscillations that appear on the electroencephalogram (EEG) during nonrapid eye movement (non-REM) sleep. They are characterized by progressively increasing, then gradually decreasing waveforms with frequencies ranging from 11 to 16 Hz. Sleep spindles characterize sleep onset, being one of the defining EEG waveforms of stage 2 sleep. They are affected by medication, aging, and brain pathology and may be involved in learning processes [1]. Analyses of scalp-recorded sleep spindles have demonstrated topographic distinction between two sleep spindle classes: “slow” spindles, with spectral peak frequency at around 12 Hz, and “fast” spindles, with spectral peak frequency at around 14 Hz. Slow spindles are more pronounced over frontal scalp electrodes, while fast spindles exhibit mainly parietal and central scalp distribution [2–5].

Independent Component Analysis (ICA) is a statistical technique used for solving the Blind Source or Signal Separation (BSS) problem [6, 7]. Suppose that data measured in an experiment are expressed through an  $n$ -dimensional vector  $\mathbf{y}(k) = [y_1(k), \dots, y_n(k)]^T$ , for  $k = 1, \dots, N_{\text{sample}}$ , where  $N_{\text{sample}}$  is the number of measured data time samples. The BSS problem relates to recovering unknown “source” signals  $s_1(k), \dots, s_m(k)$  from their mixtures, that is, the measured data, without prior knowledge about the mixing mechanism producing the measured data. Sources and measured data are related through

$$\mathbf{y}(k) = \mathbf{M}\mathbf{s}(k), \quad k = 1, \dots, N_{\text{sample}}, \quad (1)$$

where  $\mathbf{M} = [\mathbf{m}_1, \dots, \mathbf{m}_m]$  is the unknown “mixing” matrix. It should be noted that, in the BSS context, the term “sources” does not refer to physical sources of the measured data, but to the mathematical entities that could satisfy (1).

The source signal, for each ICA source  $s_j$  ( $j = 1, \dots, m$ ), is assumed to represent a random variable, whose sample values are  $s_j(1), \dots, s_j(N_{\text{sample}})$ . The source signal random variables would be statistically independent if their joint probability density function (pdf)  $f(s_1 \cdots s_m)$  could be factored as follows:

$$f(s_1, \dots, s_m) = f_1(s_1)f_2(s_2) \cdots f_m(s_m), \quad (2)$$

where  $f_j(s_j)$  denotes the marginal pdf of  $s_j$ .

ICA tries to estimate sources as linear projections of the measured data, based on the criterion that the resulting source time courses  $s_j(1), \dots, s_j(N_{\text{sample}})$  ( $j = 1, \dots, m$ ), that is, the ICA source signal random variables, should be as statistically independent as possible [6]. Each estimated source is called an independent component (IC). In a more general aspect, in the case of time-series data, it is assumed that each ICA source is generated by a random process, which is independent of the random processes generating the other sources.

The solution is in the form

$$\mathbf{s}_{\text{est}}(k) = \mathbf{W}\mathbf{y}(k), \quad k = 1, \dots, N_{\text{sample}}, \quad (3)$$

where  $\mathbf{W}$  is called the “unmixing” matrix. ICs can be determined up to a multiplicative sign [8], which may vary across ICs. Due to this indeterminacy, ICs cannot be used for directly extracting quantitative measures from their values. Rather their characteristics, such as their waveform morphology, indicate that they represent original independent sources. Quantitative measures have to be extracted from “reconstructed” data, which are reprojections of ICs, through the mixing matrix [9].

When ICA is applied to electrical signals (mixtures) recorded from the human body, it would be interesting to investigate whether the current source regions of the recorded signals, inside the human body, remain spatially fixed for the duration of the recorded data. This characteristic of current source regions would have special importance for EEG data. It might be expressed through the qualification of “spatial stationarity” for the current sources, meaning that the EEG, reconstructed from a set of ICs, is generated by current sources which have stable locations for the duration of the recorded data [9, 10]. The spatial stationarity characteristic would be desirable because, if ICA could help in finding spatially stable intracranial current sources, it might shed light to the localization of various brain processes. ICA has been extensively used in EEG signal processing applications, including noise elimination, component extraction of Event-Related Potentials (ERPs), and single-trial ERP analysis [10, 11].

In the case of sleep spindles, in the time frame of a single spindle detected by a human scorer, there often seems to exist separate spindle “components” (SCs), with different frequency spectra and/or electrode distribution. Differentiating SCs in the context of investigating related intracranial current sources seems challenging, since SCs might overlap in space and time. In previous work, the extraction of such SCs has been investigated by applying ICA to sleep spindle EEG [12].

Techniques used for solving the inverse problem in order to detect intracranial current sources of scalp-recorded EEG, which assume a distributed current source model, have been extensively used in recent years [13]. In these models, extended brain areas are represented by a three-dimensional grid of solution points. Each point is a possible location of a current source. This approach does not pose restrictions on the number and focality of sources to be computed. It is suitable when there are no specific indications about source locations and extent. On the other hand, the number of source points can be much larger than the number of measurement points on the scalp surface. This makes the inverse problem a heavily undetermined one, resulting in source distributions that are rather diffuse and extended. Among the techniques assuming a distributed current source model, Low-Resolution Brain Electromagnetic Tomography (LORETA) is one of the most extensively used [14, 15]. LORETA solves the inverse problem by assuming that the orientations and strengths of neighboring neuronal sources are correlated, because neuronal activity in neighboring patches of cortex is expected to be correlated. Mathematically, this assumption is implemented by finding the “smoothest” of all possible source density distributions. The LORETA version presented by Pascual-Marqui et al. in [15] considered a three-shell spherical head model that was registered to the Talairach human brain atlas [16]. The solution space was restricted to the cortical gray matter and the hippocampus.

Based on recent research applying LORETA to visually detected sleep spindles, there exist indications that the difference in the frequency and topography of the two sleep spindle classes reflects electrical activity related to spindle oscillations at two broadly distinct cortical areas: fast spindling source activity found posteriorly and slow spindling source activity found anteriorly [17]. Concordant LORETA results were obtained in the study of Durka et al. [18], using multichannel matching pursuit as a preprocessing step for automatic detection and parameterization of sleep spindles. Furthermore, indications for the existence of different and independent cortical circuits generating the two classes of spindles have been provided by a study of electrocorticographic (EcoG) potentials from electrodes located in the prefrontal cortex [19]. On the other hand, the two frequency classes have also been attributed to a single mechanism, the duration of hyperpolarization-rebound sequence in thalamocortical neurons. Accordingly, long hyperpolarizations generate slower EEG frequencies, while short hyperpolarizations create faster EEG frequencies [20]. Indications for considering both slow and fast spindle activity as a single event in global thalamocortical coherence have been provided by a recent magnetoencephalographic (MEG) source localization study [21]. Also, the neuronal transition probability model proposed by Merica and Fortune [22] invokes oscillatory modes of different frequencies existing simultaneously in one fixed-size neuronal population source. The hypothesis that there is only one kind of sleep spindle and an anterior peak of alpha EEG activity during non-REM sleep has also been supported [1, 23, 24]. Therefore, the question as to whether there exist one or two

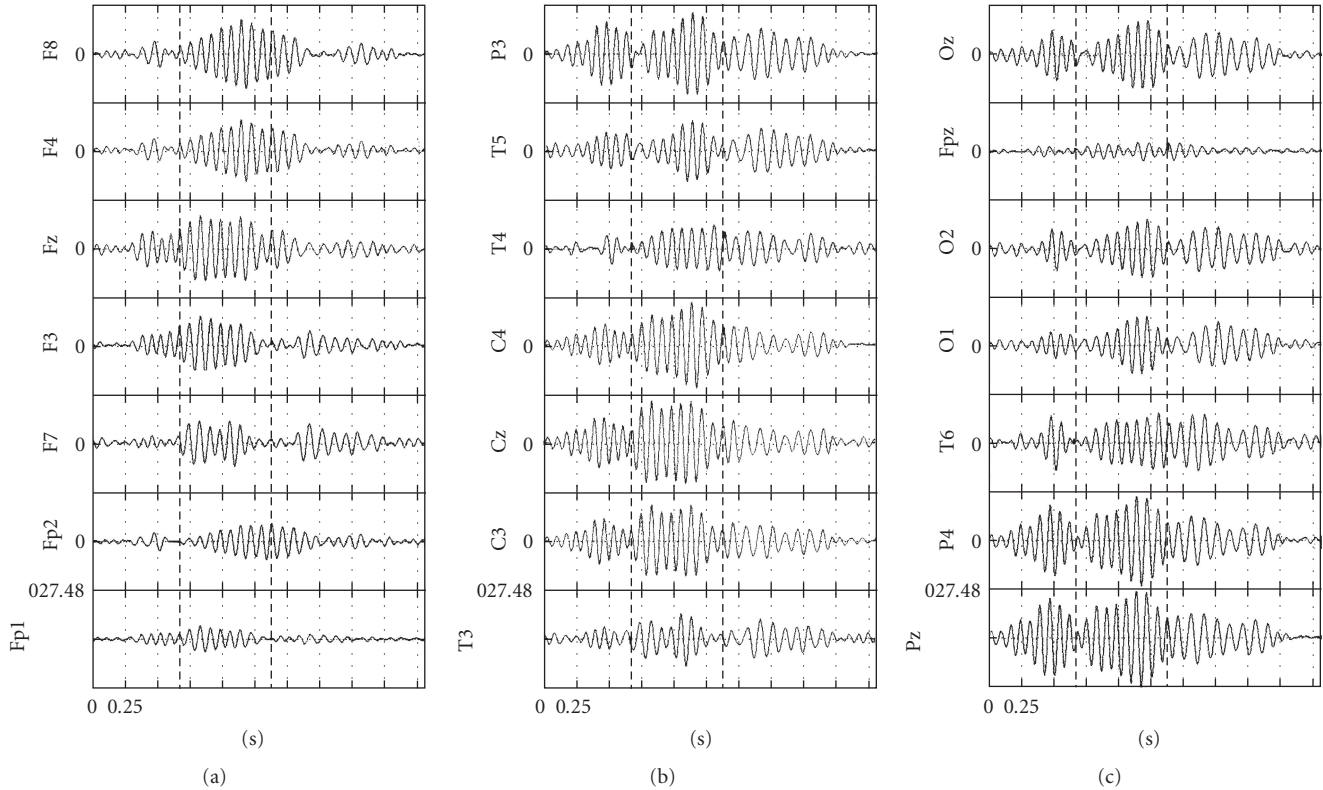


FIGURE 1: Bandpass-filtered 21-channel EEG sleep spindle recording. In each electrode recording plot the first (second) vertical dashed line indicates the time point of transition from part A (B) of the original single-spindle timeframe to part B (C). Potentials of EEG are in microvolts.

functionally separate sleep spindle generators, related to the fast and slow spindle classes, should be considered open.

The aim of the present study is to investigate the application of ICA to sleep spindle EEG, in order to enable the localization of intracranial current sources for SCs using LORETA. The methodology that is proposed may contribute to the on-going research concerning the existence of distinct intracranial current sources for the slow and fast spindle classes. Furthermore, an investigation is carried concerning whether SCs are generated by intracranial current sources with stable locations, that is, whether the current sources for SCs possess a “spatial stationarity” characteristic for the whole duration of the sleep spindle.

## 2. Material and Methods

**2.1. Sleep EEG Recording Procedure and Preprocessing.** A healthy 27-year-old male subject slept for one night in the Sleep Research Unit of the Department of Psychiatry at the University of Athens Medical School. Informed consent was obtained from the subject, and the study protocol was approved as appropriate. The all-night polysomnogram was recorded digitally utilizing a Micromed/BrainQuick system. The EEG was recorded with 21 electrodes (referential montage, reference at G2), at positions F8, T4, T6, Fp2, F4, C4, P4, O2, Fpz, Fz, Cz, Pz, Oz, Fp1, F3, C3, P3, O1, F7,

T3, T5, of the International 10/20 EEG electrode positioning system, with sampling frequency 512 Hz. Visual evaluation of the sleep record was carried out by an experienced polysomnographer, utilizing standard procedures [25], and was verified by a second one. The sleep EEG record was divided into stages and sleep spindles were visually detected from sleep stage 2, because sleep spindles are more prevalent in this sleep stage [1]. The sleep spindles were filtered using a 128th-order finite impulse response (FIR) bandpass filter, with 3 dB cut-off frequencies at 10.5 and 16 Hz, using the software package Matlab (The MathWorks Inc.).

**2.2. Computation of Independent Components.** ICA was applied on the original bandpass-filtered EEG data (Figure 1), using the FastICA algorithm [26]. In order to check whether the number of time samples available was sufficient for providing stable Independent Components (ICs) [9], the bandpass-filtered EEG data were upsampled 2, 4, 8, and 16 times. For all sampling rates, no differences were found between the computed ICs.

The ICs, which were produced when a  $21 \times 21$  unmixing matrix was computed, were composed of short-duration wavelets, with no apparent spindle-like activity and/or correspondence to the EEG spindle activity [27]. It should be noted that this was not due to algorithmic reasons related to the FastICA algorithm, since the same picture

emerged for ICs when either the infomax [28] or JADE (Joint Approximate Diagonalization of Eigen-matrices) [29] algorithms were applied, using the EEGLAB package [30]. In addition, this was not due to the number of time samples available, since the phenomenon was present even when the signal was highly upsampled (see above). In order to overcome the problem described above, dimensionality reduction was applied. The original data were first “centered”; that is, the data vector was transformed to a zero-mean variable. Then, dimensionality reduction was applied, in which a subset of the eigenvalues of the covariance matrix of the “centered” data was retained [7, 27, 31]. The dimensionality reduction resulted in the computation of  $n_{\text{red}} (< 21)$  ICs.  $n_{\text{red}}$  was selected as the number of dominant eigenvalues which accounted for 99% of the total variance of the bandpass-filtered EEG signal. Consequently, an  $n_{\text{red}} \times 21$  unmixing matrix was computed instead of a  $21 \times 21$  matrix. This procedure has been previously applied in ICA studies, where the dimensionality of the problem was reduced, by computing a sub-set of the rows of the unmixing matrix [31, 32]. Extensive trials showed that the ICs which were computed through this dimension-reduction technique did not include the short-duration wavelets mentioned above. Instead, the ICs had waveforms with spindle-like morphology, that is, waveforms of gradually increasing and then decreasing amplitude, lasting for at least 0.5 second.

**2.3. Extraction of Spindle Components.** The next step in the analysis consisted of dividing the original single-spindle timeframe into parts that reflected different spindle-like patterns, within that spindle. The rationale for such a temporal division is based on the observation that, within a single spindle, different spindle-like patterns may appear sequentially. The division was based on the existence, in the EEG recordings, of distinct waxing-waning cycles and/or on the existence of sustained transitions in instantaneous spindle frequency from “low” ( $\leq 12$  Hz) to “high” ( $\geq 13$  Hz) frequencies (or vice versa). The division was done manually on the bandpass-filtered EEG recordings, before application of ICA. The “division” point was located at the middle of the transition either from one waxing-waning cycle to the next one or from a low to a high (or vice versa) instantaneous spindle frequency. Frequencies equal to or higher than 14 Hz were considered “high” and, together with the “borderline-high” frequency of 13 Hz, were considered as representing the fast spindle class. The 13 Hz frequency was included in the fast spindle class, since the “border” between the spectra of the two spindle classes has been shown to be in the 12-13 Hz band [5, 33]. Accordingly, frequencies equal to or lower than 12 Hz were considered “low”, representing the slow spindle class.

After the division of the single-spindle timeframe into parts according to the decision process stated above, an inspection of the computed ICs followed. The aim was to select those ICs which possessed spindle-like morphology and would best correspond to the previously selected parts

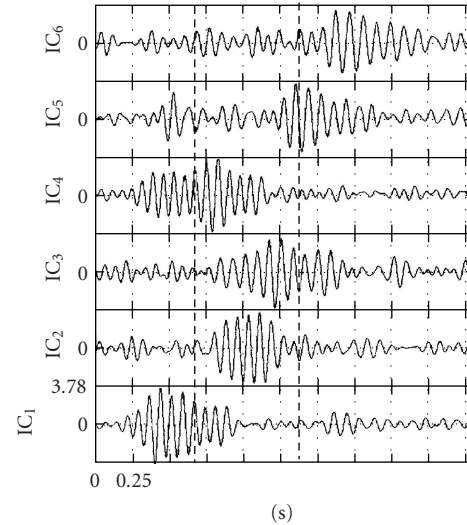


FIGURE 2: Independent Components (ICs) for the data in Figure 1. The exact IC values do not possess an interest, due to the sign and multiplicative constant indeterminacy of the results of ICA. The absolute maximum value of all ICs dictated a common magnitude range for the representation of the ICs. In each IC plot, the first (second) vertical dashed line indicates the time point of transition from part A (B) of the original single-spindle timeframe to part B (C).

of the single-spindle timeframe, as far as their time duration and their frequency content were concerned. For each EEG part, some ICs were grouped together and were considered as “representative” (main) ICs for that part, according to the following procedure: For ICs to be considered as representative of a spindle part, they should have had spindle-like waveform extending to at least two-thirds of the entire time length of the EEG part. Additionally, their maximum-power frequency should have been in the same spindle frequency class (slow or fast) as that of the EEG in that part. However, even if an IC’s spindle-like activity possessed temporal coincidence and had similar frequency content with an EEG part, it was not included in the representative IC group for that part if its spindle-like waveform extended significantly (i.e., for more than 0.5 second) into another part.

It should be noted that in the process of the approximate matching of the EEG parts to the spindle-like waveforms of the ICs, the initially chosen boundaries defining the EEG parts under examination could be modified. This modification was based on the information provided by the morphology of the ICs, because ICs could possess a much clearer starting and/or stopping point for the signal activity than the original filtered EEG.

After ICs had been selected as representative of the parts, the EEG was reconstructed, for the whole time duration of the spindle, based on the representative (main) ICs of each part. This led to the extraction, in the reconstructed EEG, of spindle components (SCs) corresponding to separate EEG activity patterns within the same spindle.

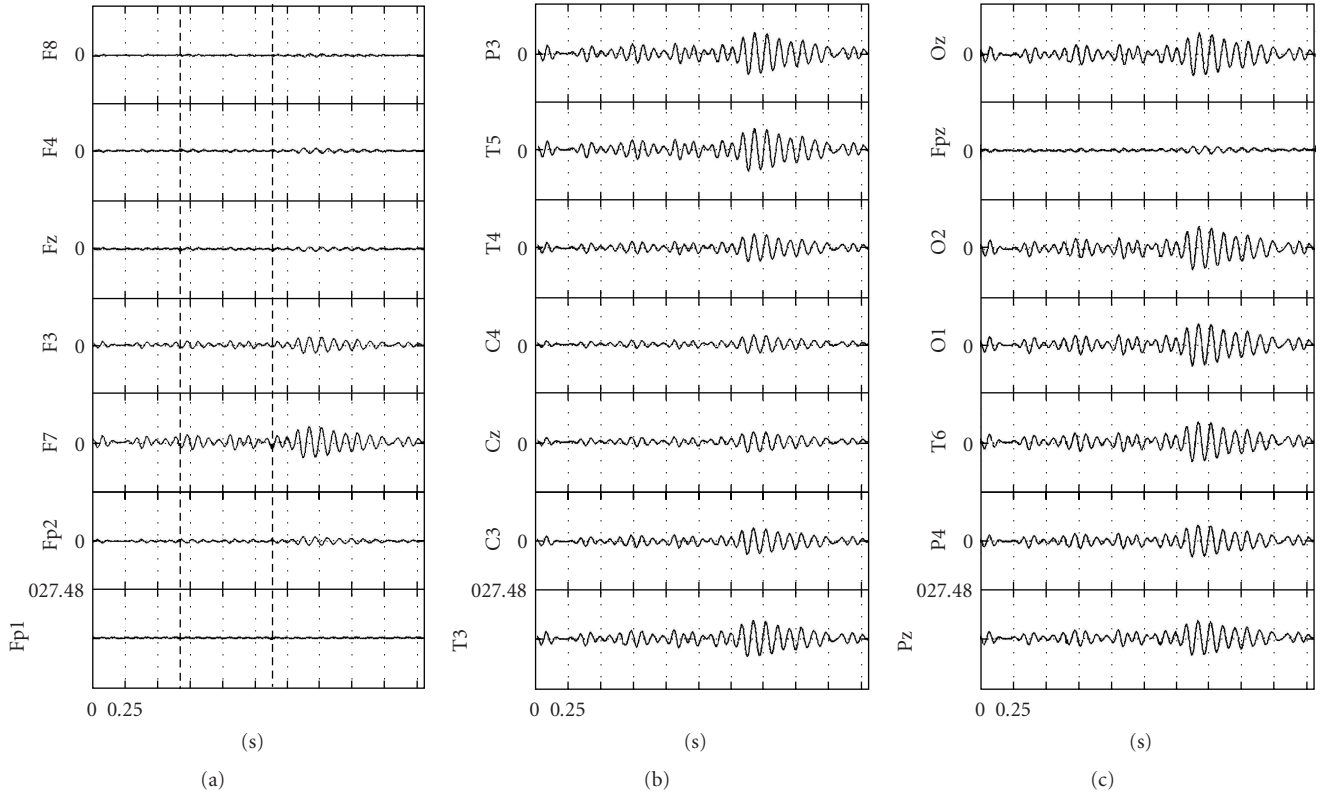


FIGURE 3: ICA-reconstructed EEG, based on IC6, corresponding to the SC (SC3), which is dominant in part C of the sleep spindle shown in Figure 1. In each electrode recording plot the first (second) vertical dashed line indicates the time point of transition from part A (B) of the original single-spindle timeframe to part B (C). Potentials of EEG are in microvolts.

**2.4. Computation of Intracranial Current Sources.** Numerous LORETA studies have used 19 or 21 electrodes of the 10/20 system [34–38]. Based on the results of these previous studies, the use of 21 electrodes in the present study was expected to provide acceptable localisation accuracy, despite the inevitable diffuseness in the current source locations produced by the method. However, we proceeded into an investigation of the lower limits of electrode use in LORETA-based inversions. Simulations were performed in order to check the extent to which the localization accuracy of the LORETA technique held, under the restriction of 8 and 16 electrodes available for the inversion. As expected, the computed current source distributions were extended over wide regions. Nevertheless, for the 16-electrode configuration, the positions of the local maxima of the computed source distributions, in conjunction with the topography of the surrounding “slopes”, corresponded to the correct current source locations.

The intracranial current sources were computed using LORETA, for each time sample, for both the original bandpass-filtered EEGs and the reconstructed ones. Accordingly, 3D distributions of source current density were estimated at the 2394 cortical locations utilized in LORETA [15]. The amount of information that was present in the current density signal sets, for all the time samples, was overwhelming and did not help in easily extracting information about the source distributions that corresponded to

the original EEGs and the SCs. In order to extract such information in a concise manner, while obtaining an average measure of the magnitude of the current source density at each source region, the temporal mean of the current density amplitude was computed for the whole duration of the respective spindle part, for each of the 2394 cortical locations. It was expected that these mean current density maps would represent faithfully the most active cortical regions, on the average, for the respective duration of each spindle part.

### 3. Results

**3.1. Spindle Components.** From the set of sleep spindles available for processing, special attention was paid to spindles which possessed a spectral bimodality, that is, exhibiting both slow and fast SCs. Figure 1 shows the multichannel recordings of such a spindle. The spindle started as a high-frequency one, with main frequency at 13–14 Hz, and then, at almost all electrodes, a transition to low frequencies took place, starting at 12 Hz and then moving to lower frequencies (10–11 Hz). Based on the visual inspection of the recordings, the activity at the majority of the electrodes presented three distinct parts or waxing-waning cycles, suggesting the existence of 3 SCs, termed hereafter SC1, SC2, and SC3. The approximate durations of the cycles were 0–0.675 second,

TABLE 1: Local maxima of LORETA current source density distributions for the original EEG, for the three parts (A, B, and C, resp.) into which the single-spindle timeframe was divided. The local maxima greater than or equal to 50% of the global maximum are shown (49% for the part C subtable). Coordinates are in mm. Origin at anterior commissure. For  $X$ , negative values represent left; positive values represent right. For  $Y$ , negative values represent posterior; positive values represent anterior. For  $Z$ , negative values represent inferior; positive values represent superior. Brodmann areas (BA) and both descriptions of the anatomical regions are shown.

| Part A        |                                |     |     |                    |                         |                     |   |
|---------------|--------------------------------|-----|-----|--------------------|-------------------------|---------------------|---|
| Local maximum | Coordinates in Talairach space |     |     | Brodmann area (BA) | Anatomical region 1     | Anatomical region 2 | Activity ( $*10^{-3}$ ) ( $\mu\text{A}/\text{mm}^2$ ) |
|               | $X$                            | $Y$ | $Z$ |                    |                         |                     |   |
| 1             | 4                              | -81 | 8   | 17                 | Cuneus                  | Occipital Lobe      | 15.96   |
| 2             | -52                            | -67 | 8   | 39                 | Middle Temporal Gyrus   | Temporal Lobe       | 13.14   |
| 3             | -45                            | -67 | 15  | 39                 | Middle Temporal Gyrus   | Temporal Lobe       | 13.14   |
| 4             | 46                             | -67 | 15  | 37                 | Middle Temporal Gyrus   | Temporal Lobe       | 13.08   |
| Part B        |                                |     |     |                    |                         |                     |   |
| Local maximum | Coordinates in Talairach space |     |     | Brodmann area (BA) | Anatomical region 1     | Anatomical region 2 | Activity ( $*10^{-3}$ ) ( $\mu\text{A}/\text{mm}^2$ ) |
|               | $X$                            | $Y$ | $Z$ |                    |                         |                     |   |
| 1             | 4                              | -81 | 8   | 17                 | Cuneus                  | Occipital Lobe      | 14.88   |
| 2             | 46                             | -67 | 8   | 37                 | Middle Temporal Gyrus   | Temporal Lobe       | 12.32   |
| 3             | -45                            | -67 | 15  | 39                 | Middle Temporal Gyrus   | Temporal Lobe       | 12.20   |
| 4             | -3                             | 52  | 1   | 10                 | Anterior Cingulate      | Limbic Lobe         | 7.80  |
| 5             | 53                             | 3   | -13 | 21                 | Middle Temporal Gyrus   | Temporal Lobe       | 7.76  |
| 6             | -59                            | -32 | 8   | 42                 | Superior Temporal Gyrus | Temporal Lobe       | 7.71  |
| Part C        |                                |     |     |                    |                         |                     |   |
| Local maximum | Coordinates in Talairach space |     |     | Brodmann area (BA) | Anatomical region 1     | Anatomical region 2 | Activity ( $*10^{-3}$ ) ( $\mu\text{A}/\text{mm}^2$ ) |
|               | $X$                            | $Y$ | $Z$ |                    |                         |                     |   |
| 1             | 4                              | -81 | 8   | 17                 | Cuneus                  | Occipital Lobe      | 6.90  |
| 2             | 46                             | -67 | 8   | 37                 | Middle Temporal Gyrus   | Temporal Lobe       | 6.17  |
| 3             | -45                            | -67 | 15  | 39                 | Middle Temporal Gyrus   | Temporal Lobe       | 6.00  |
| 4             | -59                            | -32 | 8   | 42                 | Superior Temporal Gyrus | Temporal Lobe       | 3.52  |
| 5             | -3                             | 52  | 1   | 10                 | Anterior Cingulate      | Limbic Lobe         | 3.44  |

0.675–1.375 second, and 1.375–2.3 second, respectively. The 1st cycle had a main frequency range of 13–14 Hz. The 2nd cycle presented an “intercycle” transition in many electrodes from 13 to 12 Hz. The 3rd cycle possessed a clear low-frequency content (10–11 Hz).

The dimensionality reduction process resulted in computing  $n_{\text{red}} = 6$  ICs, presented in Figure 2. Each IC possessed a visually discernible “main” waxing-waning cycle. By inspecting the starting and ending time of those cycles and their spectral content, and following the IC selection procedure described in Section 2.3, IC1, with main (i.e., maximum-power) frequency of its spindle-like waveform at 13 Hz, was selected as representative of part A and SC1. Its spindle-like waveform covered two-thirds of part A and its extension into part B was less than 0.5 second.

IC2, with main frequency of its spindle-like waveform at 13 Hz, was selected as representative of part B and SC2, since its waveform covered almost the entire time length of part B and did not extend to either parts A or C. IC3, with

main frequency of its spindle-like waveform at 12 Hz, was also selected as representative of part B and SC2, since its waveform covered almost the entire time length of part B and its extension into part C was less than 0.5 second. Finally, IC6, with main frequency of its spindle-like waveform at 11 Hz, was selected as representative of part C and SC3, since the waveform extended to more than two-thirds of part C and did not extend into part B. IC4 possessed a spindle-like waveform, with main frequencies at 13–14 Hz, spanning parts A and B. IC4 was not retained, because the waveform extended to 0.5 second in both parts A and B. IC5 possessed a spindle-like waveform, with main frequency at 12 Hz, spanning parts B and C. It was not included as a representative of either part B or C, since its spindle-like waveform did not extend to at least the two-thirds of the duration of part B or C. Figure 3 shows the reconstructed EEG, at 21 electrodes, based on IC6. The reconstructed EEG represents the spindle-like activity of SC3, which is the dominant SC in part C. In parts A and B, SC3 presented

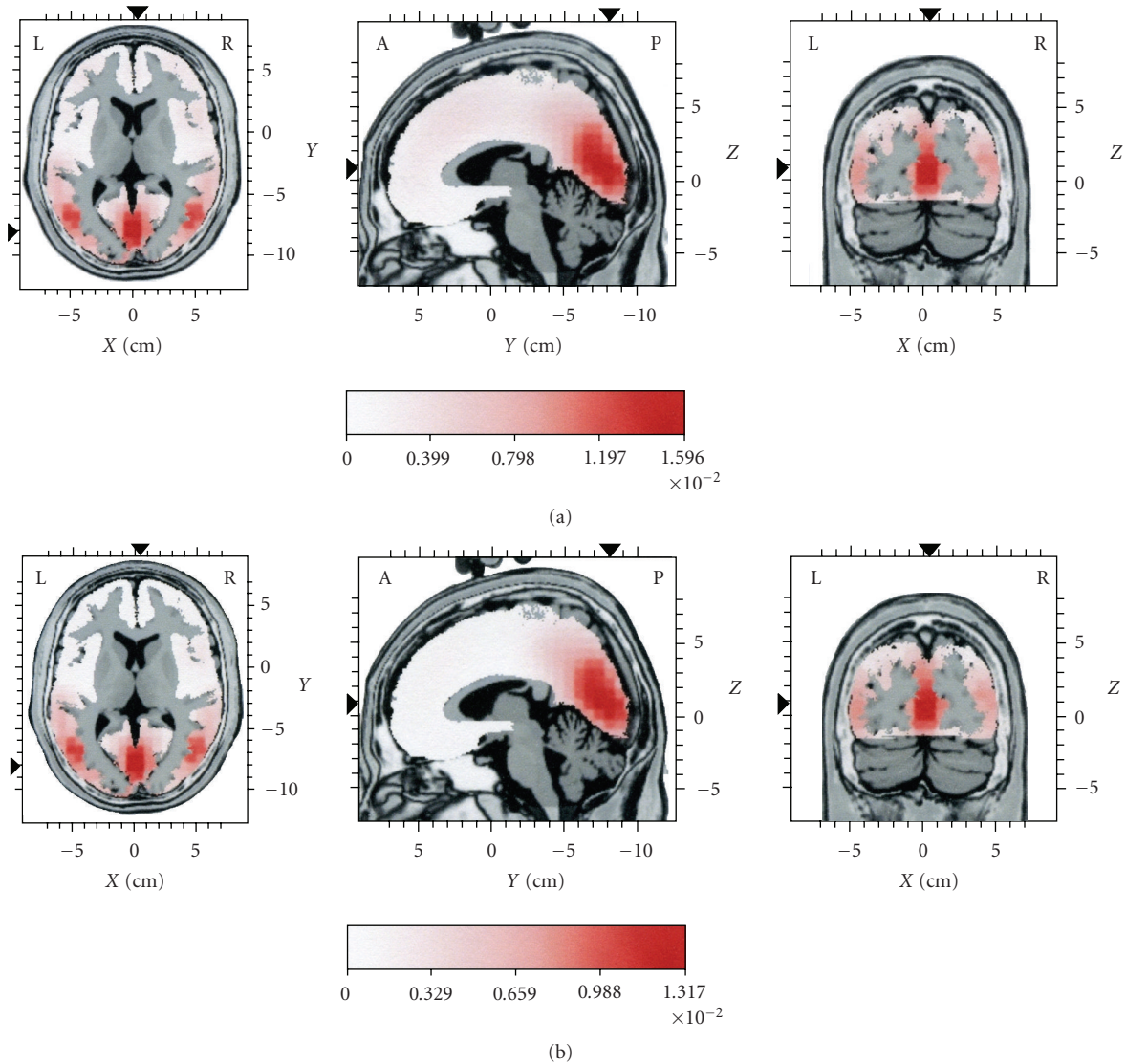


FIGURE 4: Distributions of mean current source activity for part A (see Figure 1). In (a) sources are given for the original EEG. In (b) sources are given for the reconstructed EEG, representing the dominant spindle component (SC1) in this part. The reconstruction of the EEG was based on IC1. Each distribution is displayed relative to its own maximum, using three slices (axial, sagittal, and coronal) intersecting at the point of global maximum of the distribution. Current density values are in  $\mu\text{A}/\text{mm}^2$ .

a much lower amplitude activity, which could hardly be characterized as spindle-like. Nevertheless, this activity could be a precursor to the clear emergence of SC3 in part C.

**3.2. Intracranial Current Sources.** Concerning the mean current source activity corresponding to the original EEG data for the three parts into which the single-spindle EEG was segmented, in all three parts the maxima were located at the cuneus (occipital lobe) and at the temporal lobes, bilaterally (Table 1). A frontal distribution, with local maximum at the anterior cingulate, with intensity at 52 and 49% of the global maximum, appeared in the mean current source activity maps for parts B and C, respectively (Table 1 parts B and C).

For part A, as mentioned above, the EEG frequency was high. Therefore, it was expected that the mean current source

activity should appear as activation mainly at posterior parts (Figure 4(a)). It should be noted that, in the context of the present work, the term “posterior” is used mainly in contradistinction to frontal lobes, and it denotes current sources not only in the occipital lobes but also in the limbic, parietal, and temporal lobes. The mean current source activity map (Figure 4(b)) corresponding to SC1 (i.e., the reconstruction of the EEG based on IC1, for part A, where IC1 was the main IC) showed the same loci of maximal activity at the cuneus (occipital lobe) and at the temporal lobes, bilaterally (Table 2), as those present in the current sources corresponding to the original EEG for part A.

For part B, the main current sources of the original EEG remained at the same posterior positions as for part A, namely, the cuneus and the middle temporal gyri, bilaterally (Figure 5(a) and Table 1 part B). However, a lower-intensity

TABLE 2: Local maxima of LORETA current source density distributions for spindle component SC1 for part A of the single-spindle timeframe. The local maxima greater than or equal to 50% of the global maximum are shown. Coordinates are in mm. Origin at anterior commissure. For X, negative values represent left; positive values represent right. For Y, negative values represent posterior, positive values represent anterior. For Z, negative values represent inferior, positive values represent superior. Brodmann areas (BA) and both descriptions of the anatomical regions are shown.

| Local maximum | Coordinates in Talairach space |     |   | Brodmann area (BA) | Anatomical region 1   | Anatomical region 2 | Activity ( $\times 10^{-3}$ ) ( $\mu\text{A}/\text{mm}^2$ ) |
|---------------|--------------------------------|-----|---|--------------------|-----------------------|---------------------|---|
|               | X                              | Y   | Z |                    |                       |                     |   |
| 1             | 4                              | -81 | 8 | 17                 | Cuneus                | Occipital Lobe      | 13.17   |
| 2             | -52                            | -67 | 8 | 39                 | Middle Temporal Gyrus | Temporal Lobe       | 11.06   |
| 3             | 46                             | -67 | 8 | 37                 | Middle Temporal Gyrus | Temporal Lobe       | 10.49   |

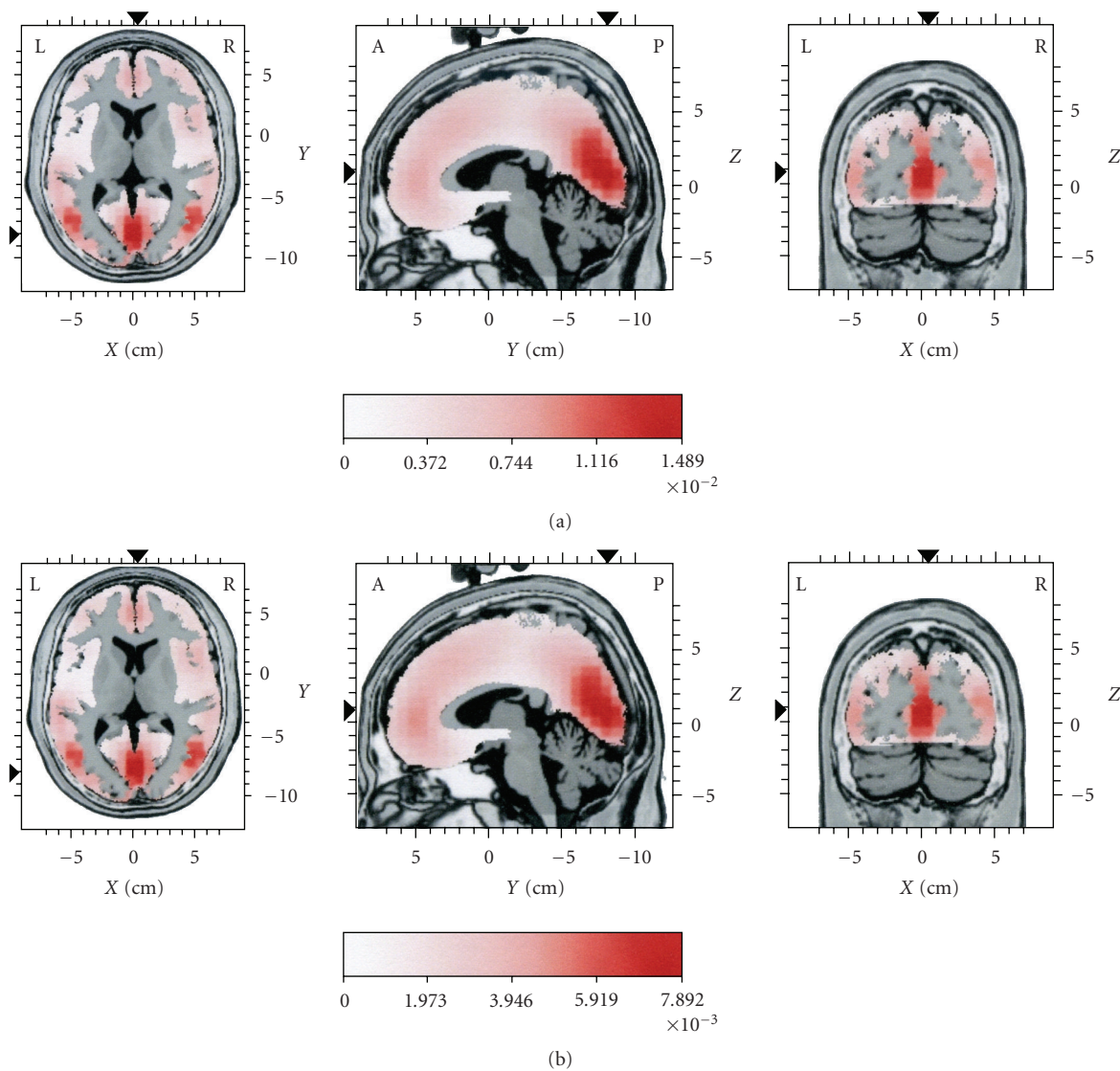


FIGURE 5: Distributions of mean current source activity for part B (see Figure 1). In (a) sources are given for the original EEG. In (b) sources are given for the reconstructed EEG, representing the dominant spindle component (SC2) in this part. The reconstruction of the EEG was based on IC2 and IC3. Each distribution is displayed relative to its own maximum, using three slices (axial, sagittal, and coronal) intersecting at the point of global maximum of the distribution. Current density values are in  $\mu\text{A}/\text{mm}^2$ .

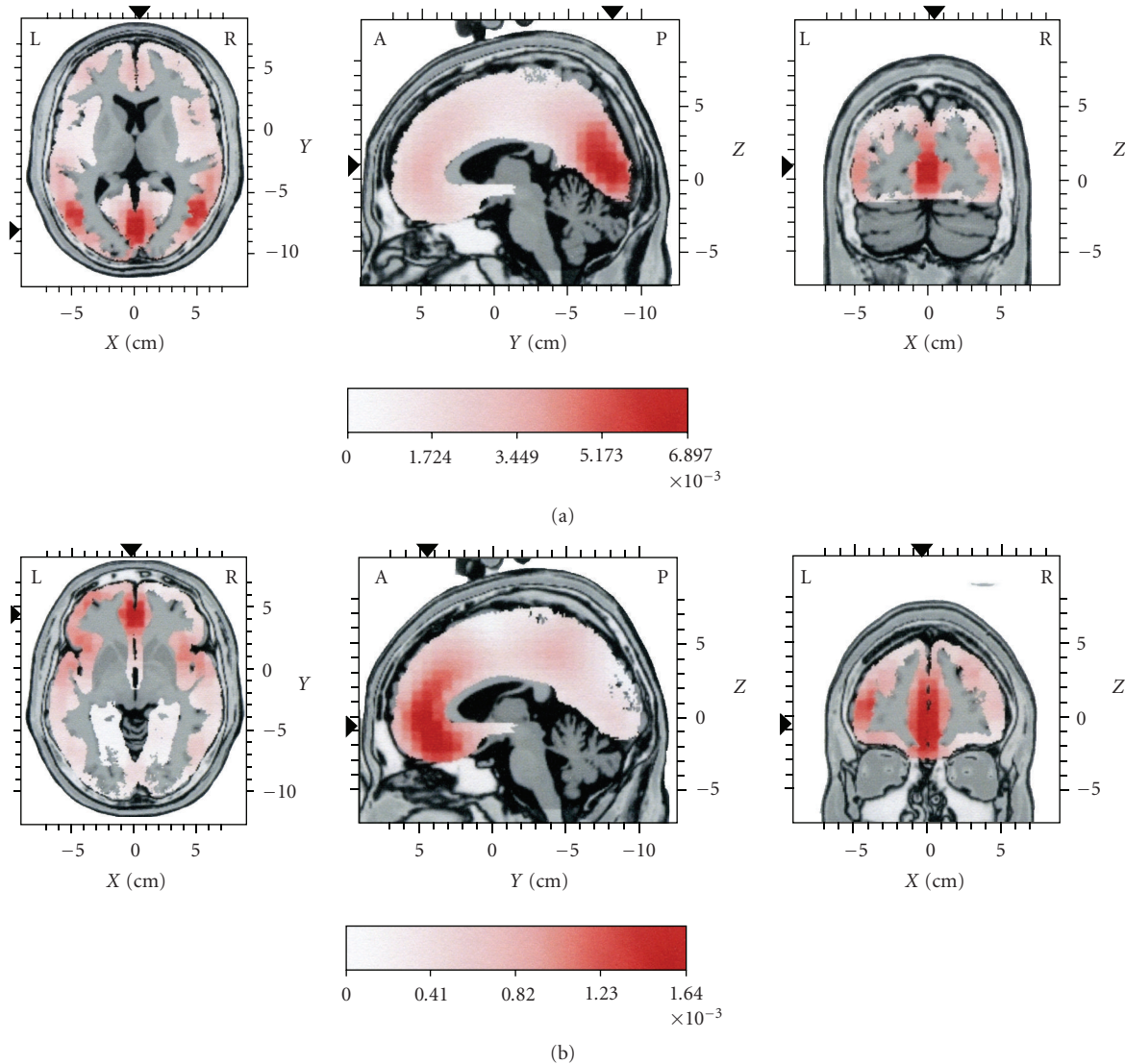


FIGURE 6: Distributions of mean current source activity for part C (see Figure 1). In (a) sources are given for the original EEG. In (b) sources are given for the reconstructed EEG, representing the dominant spindle component (SC3) in this part. The reconstruction of the EEG was based on IC6. Each distribution is displayed relative to its own maximum, using three slices (axial, sagittal, and coronal) intersecting at the point of global maximum of the distribution. Current density values are in  $\mu\text{A}/\text{mm}^2$ .

frontal component was also seen, at the anterior cingulate. As mentioned above, for part B the spindle frequency content remained high, although slower frequencies emerged. Therefore, the emergence of a lesser frontal source local maximum seems to be in agreement with the assumption that slow spindles tend to occur at frontal areas. The mean current source activity map (Figure 5(b)) corresponding to SC2 (i.e., the reconstruction of the EEG based on ICs 2 and 3, for part B, where ICs 2 and 3 were the main ICs) showed the same loci of maximal activity, at the cuneus, the temporal lobes, bilaterally, and the anterior cingulate (Table 3), as those present in the current sources corresponding to the original EEG for part B.

For part C, as mentioned above, the original EEG was of low frequency. Therefore, the observed dominance of

posterior sources for part C of the original EEG (Figure 6(a) and Table 1 part C) did not agree with the assumption that slow spindles tend to occur at frontal areas. Figure 6(b) presents the mean current source activity map corresponding to SC3 (i.e., the reconstruction of the EEG based on IC6, for part C, where IC6 is the main IC). A clear frontal maximal distribution emerged, with lesser activity at temporal and parietal areas (Table 4). This was consistent with the low frequency content of the spindle-like activity that existed in the reconstructed EEG for part C.

It should be noted that the local maxima of the current source distribution for the reconstructed EEG based on IC6 were at the same spatial location for each part of the reconstructed EEG. However, the amplitude of the current density of the sources was increasing from part A to B and

TABLE 3: Local maxima of LORETA current source density distributions for spindle component SC2 for part B of the single-spindle timeframe. The local maxima greater than or equal to 50% of the global maximum are shown. Coordinates are in mm. Origin is at anterior commissure. For X, negative values represent left; positive values represent right. For Y, negative values represent posterior; positive values represent anterior. For Z, negative values represent inferior; positive values represent superior. Brodmann areas (BA) and both descriptions of the anatomical regions are shown.

| Local maximum | Coordinates in Talairach space |     |     | Brodmann area (BA) | Anatomical region 1     | Anatomical region 2 | Activity ( $\times 10^{-3}$ ) ( $\mu\text{A}/\text{mm}^2$ ) |
|---------------|--------------------------------|-----|-----|--------------------|-------------------------|---------------------|---|
|               | X                              | Y   | Z   |                    |                         |                     |   |
| 1             | 4                              | -81 | 8   | 17                 | Cuneus                  | Occipital Lobe      | 7.89  |
| 2             | 46                             | -67 | 8   | 37                 | Middle Temporal Gyrus   | Temporal Lobe       | 6.65  |
| 3             | -45                            | -67 | 15  | 39                 | Middle Temporal Gyrus   | Temporal Lobe       | 6.34  |
| 4             | -3                             | 52  | 1   | 10                 | Anterior Cingulate      | Limbic Lobe         | 4.89  |
| 5             | 53                             | 3   | -13 | 21                 | Middle Temporal Gyrus   | Temporal Lobe       | 4.83  |
| 6             | -59                            | -32 | 8   | 42                 | Superior Temporal Gyrus | Temporal Lobe       | 4.39  |

TABLE 4: Local maxima of LORETA current source density distributions for spindle component SC3 for part C of the single-spindle timeframe. The local maxima greater than or equal to 50% of the global maximum are shown. Coordinates are in mm. Origin is at anterior commissure. For X, negative values represent left; positive values represent right. For Y, negative values represent posterior; positive values represent anterior. For Z, negative values represent inferior; positive values represent superior. Brodmann areas (BA) and both descriptions of the anatomical regions are shown.

| Local maximum | Coordinates in Talairach space |     |     | Brodmann area (BA) | Anatomical region 1      | Anatomical region 2 | Activity ( $\times 10^{-3}$ ) ( $\mu\text{A}/\text{mm}^2$ ) |
|---------------|--------------------------------|-----|-----|--------------------|--------------------------|---------------------|---|
|               | X                              | Y   | Z   |                    |                          |                     |   |
| 1             | -3                             | 45  | 6   | 10                 | Medial Frontal Gyrus     | Frontal Lobe        | 1.64  |
| 2             | -38                            | 52  | 8   | 10                 | Medial Frontal Gyrus     | Frontal Lobe        | 1.45  |
| 3             | 46                             | 10  | 36  | 9                  | Medial Frontal Gyrus     | Frontal Lobe        | 1.41  |
| 4             | -52                            | 3   | -20 | 21                 | Middle Temporal Gyrus    | Temporal Lobe       | 1.39  |
| 5             | 53                             | 10  | 8   | 44                 | Inferior Frontal Gyrus   | Frontal Lobe        | 1.35  |
| 6             | 46                             | 10  | 1   | 13                 | Insula                   | Sub-lobar           | 1.35  |
| 7             | -38                            | 17  | 1   | 13                 | Insula                   | Sub-lobar           | 1.23  |
| 8             | -45                            | -46 | 50  | 40                 | Inferior Parietal Lobule | Parietal Lobe       | 1.11  |
| 9             | -52                            | -60 | 36  | 40                 | Inferior Parietal Lobule | Parietal Lobe       | 1.00  |
| 10            | -52                            | -60 | 15  | 22                 | Superior Temporal Gyrus  | Temporal Lobe       | 0.89  |
| 11            | 32                             | 45  | 29  | 10                 | Medial Frontal Gyrus     | Frontal Lobe        | 0.87  |
| 12            | -59                            | -32 | 22  | 40                 | Inferior Parietal Lobule | Parietal Lobe       | 0.86  |
| 13            | 25                             | -4  | -27 | Amygdala           | Uncus                    | Limbic Lobe         | 0.86  |
| 14            | 25                             | 38  | 43  | 8                  | Superior Frontal Gyrus   | Frontal Lobe        | 0.84  |

finally C, corresponding to the emergence of SC3 as the dominant spindle component of part C. Spatial stability for the local maxima of the current source distribution across the three parts of the EEG occurred also for SC1, that is, the EEG that was reconstructed based on IC1, and for SC2, that is, the EEG that was reconstructed based on IC2 and IC3.

#### 4. Discussion

In the present study, the possibilities offered by ICA processing were explored for extracting sleep spindle com-

ponents (SCs), in order to study the structure of sleep spindles during their temporal evolution. Observation of morphological characteristics of the obtained ICs and definition of distinct groups of ICs based on these characteristics proved quite helpful in elucidating such SCs. The results provide indication that SCs which relate to a single-spindle EEG recording, and which may not be easily distinguishable in the original recording, may be separated using morphological and frequency spectrum criteria, when these criteria are applied to the original single-spindle EEG recording and its ICs. The EEGs reconstructed from the different IC groups clearly indicated

specific SCs active in consecutive parts of a single spindle. The sleep spindles were divided into consecutive time segments (parts) and at each segment the corresponding SC was found to provide the predominant spindle-like characteristics of the EEG. The above findings are in accordance to the feature of ICA processing related to the “unmixing” of the available recorded data into underlying components.

One of the benefits of this approach was that the contribution of the current sources for each SC to the total EEG current source distribution could be differentiated, with interesting results concerning the sources of slow and fast spindle classes. In accordance with previous findings, we observed that fast SC activity related to activation of principally posterior brain parts, whereas slow SC activity related to activation of mainly anterior parts. On the other hand, there existed cases where the amplitude maxima of the total EEG current sources for some time parts of the original EEG were located posteriorly, although the dominant frequency of the original EEG, at those parts, was slow.

A consistent finding in the spindles analysed in the present study was the spatial stationarity of the current sources for each SC, across consecutive reconstructed EEG parts of the same spindle. In conjunction with the results discussed in the previous paragraph, spatial stationarity of current sources provides an indication that slow and fast components of a single spindle (which may represent a frequency shift during its duration) may originate in different parts of the brain and reflect distinct groups of generators which remain active throughout the spindle duration. The intensity of these generators may be modulated in time, to reflect the changes in the frequency content of the spindle as a function of time.

Future research should include the application of the proposed technique of SC extraction and related current source estimation to a set of healthy young adults, and then to healthy subjects of all ages, in order to investigate possible age effects on SCs. Furthermore, taking into account the limitations of LORETA [13], current sources should be investigated with inversion techniques using different and/or more comprehensive methodological approaches than LORETA [39, 40], in order to check whether the present findings can be replicated with such techniques. An extensive investigation, from the point of view of inversion techniques, might also contribute in a more robust manner to the elucidation of the questions related to the existence and location of functionally separate sleep spindle generators, for the fast and slow spindle classes.

## References

- [1] L. De Gennaro and M. Ferrara, “Sleep spindles: an overview,” *Sleep Medicine Reviews*, vol. 7, no. 5, pp. 423–440, 2003.
- [2] J. Zeitlhofer, G. Gruber, P. Anderer, S. Asenbaum, P. Schimicek, and B. Saletu, “Topographic distribution of sleep spindles in young healthy subjects,” *Journal of Sleep Research*, vol. 6, no. 3, pp. 149–155, 1997.
- [3] H. Tanaka, M. Hayashi, and T. Hori, “Topographical characteristics and principal component structure of the hypnagogic EEG,” *Sleep*, vol. 20, no. 7, pp. 523–534, 1997.
- [4] J. S. Zygierevicz, K. J. Blinowska, P. J. Durka, W. Szelenberger, S. Niemcewicz, and W. Androsiuk, “High resolution study of sleep spindles,” *Clinical Neurophysiology*, vol. 110, no. 12, pp. 2136–2147, 1999.
- [5] E. Werth, P. Achermann, D.-J. Dijk, and A. A. Borbely, “Spindle frequency activity in the sleep EEG: individual differences and topographic distribution,” *Electroencephalography and Clinical Neurophysiology*, vol. 103, no. 5, pp. 535–542, 1997.
- [6] A. Hyvärinen, “Survey on independent component analysis,” *Neural Computing Surveys*, vol. 2, pp. 94–128, 1999.
- [7] C. J. James and C. W. Hesse, “Independent component analysis for biomedical signals,” *Physiological Measurement*, vol. 26, no. 1, pp. R15–R39, 2005.
- [8] P. Comon, “Independent component analysis, a new concept?” *Signal Processing*, vol. 36, no. 3, pp. 287–314, 1994.
- [9] S. Makeig, M. Westerfield, T.-P. Jung, et al., “Functionally independent components of the late positive event-related potential during visual spatial attention,” *Journal of Neuroscience*, vol. 19, no. 7, pp. 2665–2680, 1999.
- [10] J. Onton, M. Westerfield, J. Townsend, and S. Makeig, “Imaging human EEG dynamics using independent component analysis,” *Neuroscience and Biobehavioral Reviews*, vol. 30, no. 6, pp. 808–822, 2006.
- [11] B. Jervis, S. Belal, K. Camilleri, et al., “The independent components of auditory P300 and CNV evoked potentials derived from single-trial recordings,” *Physiological Measurement*, vol. 28, no. 8, pp. 745–771, 2007.
- [12] E. M. Ventouras, I. Alevizos, P. Y. Ktonas, et al., “Independent components of sleep spindles,” in *Proceedings of the 29th Annual International Conference of the IEEE Engineering in Medicine and Biology (EMBC '07)*, pp. 4002–4005, Lyon, France, August 2007.
- [13] C. M. Michel, M. M. Murray, G. Lantz, S. Gonzalez, L. Spinelli, and R. Grave de Peralta, “EEG source imaging,” *Clinical Neurophysiology*, vol. 115, no. 10, pp. 2195–2222, 2004.
- [14] R. D. Pascual-Marqui, C. M. Michel, and D. Lehmann, “Low resolution electromagnetic tomography: a new method for localizing electrical activity in the brain,” *International Journal of Psychophysiology*, vol. 18, no. 1, pp. 49–65, 1994.
- [15] R. D. Pascual-Marqui, D. Lehmann, T. Koenig, et al., “Low resolution brain electromagnetic tomography (LORETA) functional imaging in acute, neuroleptic-naive, first-episode, productive schizophrenia,” *Psychiatry Research: Neuroimaging*, vol. 90, no. 3, pp. 169–179, 1999.
- [16] J. Talairach and P. Tournoux, *Co-Planar Stereotaxic Atlas of the Human Brain*, Thieme, New York, NY, USA, 1988.
- [17] P. Anderer, G. Klosch, G. Gruber, et al., “Low-resolution brain electromagnetic tomography revealed simultaneously active frontal and parietal sleep spindle sources in the human cortex,” *Neuroscience*, vol. 103, no. 3, pp. 581–592, 2001.
- [18] P. J. Durka, A. Matysiak, E. M. Montes, P. V. Sosa, and K. J. Blinowska, “Multichannel matching pursuit and EEG inverse solutions,” *Journal of Neuroscience Methods*, vol. 148, no. 1, pp. 49–59, 2005.
- [19] M. Nakamura, S. Uchida, T. Maehara, et al., “Sleep spindles in human prefrontal cortex: an electrocorticographic study,” *Neuroscience Research*, vol. 45, no. 4, pp. 419–427, 2003.
- [20] M. Steriade and F. Amzica, “Coalescence of sleep rhythms and their chronology in corticothalamic networks,” *Sleep Research Online*, vol. 1, no. 1, pp. 1–10, 1998.

- [21] V. Gumenyuk, T. Roth, J. E. Moran, et al., "Cortical locations of maximal spindle activity: magnetoencephalography (MEG) study," *Journal of Sleep Research*, vol. 18, no. 2, pp. 245–253, 2009.
- [22] H. Merica and R. D. Fortune, "A neuronal transition probability model for the evolution of power in the sigma and delta frequency bands of sleep EEG," *Physiology and Behavior*, vol. 62, no. 3, pp. 585–589, 1997.
- [23] V. Knoblauch, W. L. J. Martens, A. Wirz-Justice, and C. Cajochen, "Human sleep spindle characteristics after sleep deprivation," *Clinical Neurophysiology*, vol. 114, no. 12, pp. 2258–2267, 2003.
- [24] L. De Gennaro, M. Ferrara, F. Vecchio, G. Curcio, and M. Bertini, "An electroencephalographic fingerprint of human sleep," *NeuroImage*, vol. 26, no. 1, pp. 114–122, 2005.
- [25] A. Rechtschaffen and A. Kales, Eds., *A Manual of Standardized Terminology, Techniques and Scoring System for Sleep Stages of Human Subjects*, Public Health Service, U.S. Government Printing Office, Washington, DC, USA, 1968.
- [26] A. Hyvärinen, "Fast and robust fixed-point algorithms for independent component analysis," *IEEE Transactions on Neural Networks*, vol. 10, no. 3, pp. 626–634, 1999.
- [27] E. M. Ventouras, P. Y. Ktonas, H. Tsekou, T. Paparrigopoulos, I. Kalatzis, and C. R. Soldatos, "Slow and fast EEG sleep spindle component extraction using Independent Component Analysis," in *Proceedings of the 8th IEEE International Conference on BioInformatics and BioEngineering (BIBE '08)*, Athens, Greece, October 2008.
- [28] A. J. Bell and T. J. Sejnowski, "An information-maximization approach to blind separation and blind deconvolution," *Neural computation*, vol. 7, no. 6, pp. 1129–1159, 1995.
- [29] J. F. Cardoso and A. Souloumiac, "Blind beamforming for non-Gaussian signals," *IEE Proceedings F*, vol. 140, no. 6, pp. 362–370, 1993.
- [30] A. Delorme and S. Makeig, "EEGLAB: an open source toolbox for analysis of single-trial EEG dynamics including independent component analysis," *Journal of Neuroscience Methods*, vol. 134, no. 1, pp. 9–21, 2004.
- [31] A. Hyvärinen and E. Oja, "Independent component analysis: algorithms and applications," *Neural Networks*, vol. 13, no. 4–5, pp. 411–430, 2000.
- [32] R. Vigario, J. Sarela, and E. Oja, "Independent component analysis in wave decomposition of auditory evoked fields," in *Proceedings of the International Conference on Artificial Neural Networks (ICANN '98)*, pp. 287–292, Skovde, Sweden, 1998.
- [33] I. Manshanden, J. C. de Munck, N. R. Simon, and F. H. Lopes da Silva, "Source localization of MEG sleep spindles and the relation to sources of alpha band rhythms," *Clinical Neurophysiology*, vol. 113, no. 12, pp. 1937–1947, 2002.
- [34] R. Ferri, O. Bruni, S. Miano, and M. G. Terzano, "Topographic mapping of the spectral components of the cyclic alternating pattern (CAP)," *Sleep Medicine*, vol. 6, no. 1, pp. 29–36, 2005.
- [35] M. Toth, B. Faludi, J. Wackermann, J. Czopf, and I. Kondakor, "Characteristic changes in brain electrical activity due to chronic hypoxia in patients with obstructive sleep apnea syndrome (OSAS): a combined EEG study using LORETA and omega complexity," *Brain Topography*, vol. 22, no. 3, pp. 185–190, 2009.
- [36] M. Saletu, P. Anderer, G. M. Saletu-Zyhlarz, M. Mandl, B. Saletu, and J. Zeitlhofer, "Modafinil improves information processing speed and increases energetic resources for orientation of attention in narcoleptics: double-blind, placebo-controlled ERP studies with low-resolution brain electromagnetic tomography (LORETA)," *Sleep Medicine*, vol. 10, no. 8, pp. 850–858, 2009.
- [37] A. Sinai and H. Pratt, "High-resolution time course of hemispheric dominance revealed by low-resolution electromagnetic tomography," *Clinical Neurophysiology*, vol. 114, no. 7, pp. 1181–1188, 2003.
- [38] M. J. Herrmann, J. Rommler, A.-C. Ehlis, A. Heidrich, and A. J. Fallgatter, "Source localization (LORETA) of the error-related-negativity (ERN/Ne) and positivity (Pe)," *Cognitive Brain Research*, vol. 20, no. 2, pp. 294–299, 2004.
- [39] R. Grave de Peralta Menendez, M. M. Murray, C. M. Michel, R. Martuzzi, and S. L. Gonzalez Andino, "Electrical neuroimaging based on biophysical constraints," *NeuroImage*, vol. 21, no. 2, pp. 527–539, 2004.
- [40] C. Phillips, J. Mattout, M. D. Rugg, P. Maquet, and K. J. Friston, "An empirical Bayesian solution to the source reconstruction problem in EEG," *NeuroImage*, vol. 24, no. 4, pp. 997–1011, 2005.

## Research Article

# Music Composition from the Brain Signal: Representing the Mental State by Music

Dan Wu,<sup>1</sup> Chaoyi Li,<sup>1,2</sup> Yu Yin,<sup>1</sup> Changzheng Zhou,<sup>1,3</sup> and Dezhong Yao<sup>1</sup>

<sup>1</sup>Key Laboratory for NeuroInformation of Ministry of Education, School of Life Science and Technology, University of Electronic Science and Technology of China, Chengdu 610054, China

<sup>2</sup>Shanghai Institutes for Biological Sciences, Chinese Academy of Sciences, Shanghai 200031, China

<sup>3</sup>Department of Students' Affairs, Arts Education Centre, University of Electronic Science and Technology of China, Chengdu 610054, China

Correspondence should be addressed to Dezhong Yao, dyao@uestc.edu.cn

Received 18 June 2009; Revised 29 September 2009; Accepted 22 December 2009

Academic Editor: Fabio Babiloni

Copyright © 2010 Dan Wu et al. This is an open access article distributed under the Creative Commons Attribution License, which permits unrestricted use, distribution, and reproduction in any medium, provided the original work is properly cited.

This paper proposes a method to translate human EEG into music, so as to represent mental state by music. The arousal levels of the brain mental state and music emotion are implicitly used as the bridge between the mind world and the music. The arousal level of the brain is based on the EEG features extracted mainly by wavelet analysis, and the music arousal level is related to the musical parameters such as pitch, tempo, rhythm, and tonality. While composing, some music principles (harmonics and structure) were taken into consideration. With EEGs during various sleep stages as an example, the music generated from them had different patterns of pitch, rhythm, and tonality. 35 volunteers listened to the music pieces, and significant difference in music arousal levels was found. It implied that different mental states may be identified by the corresponding music, and so the music from EEG may be a potential tool for EEG monitoring, biofeedback therapy, and so forth.

## 1. Introduction

Music is a universal human trait throughout the human history and across all cultures, and it is also a powerful tool for emotion and mood modulation [1]. Music is not only a kind of entertainment, but another kind of language; thus music composition may be conceived as a specific representation of human mind.

Along with the widespread of computer application, some researchers attempted to “teach” the computer to compose music, where a variety of mathematic algorithms [2] and fundamental music rules [3] were explored. In general, for such a computer composition, subjective algorithm design and artificial selection of music rules are crucial and difficult. To learn from the nature and ourselves, various signals from human body, such as the DNA [4], proteins [5], electromyograms (EMGs) [6], and brainwaves [7], have been utilized in computer composition in 1990s.

The brainwaves, the electroencephalograms (EEGs), are the visual plotting of the brain neural electric activities

projected to the scalp surface. The earliest attempt to hear brainwaves as music was made in 1934 [8]. In most of these early works, however, only the amplitude of the alpha waves or other simple and direct characters of EEG signals was utilized as the driving sources of the musical sound. In the 1990s, various new music generating rules were created from digital filtering or coherent analysis of EEG [9]. In general, these techniques may be classified into two categories. The first one is sonification, which aims at monitoring the brainwaves in an auditory way and includes various methods, such as the direct parameter mapping [10], the one based on the interictal epileptic discharges as triggers for the beginning of music tones [11], and rules worked on the scale-free phenomena which exists at both EEG and music [12]. The second one is the brainwave music which has involved musical theories in composition. The typical work is the application of brainwave music in Brain Computer Interface (BCI) [7].

In this work, we proposed a method to translate the mental signal, the EEG, into music. The goal is to represent

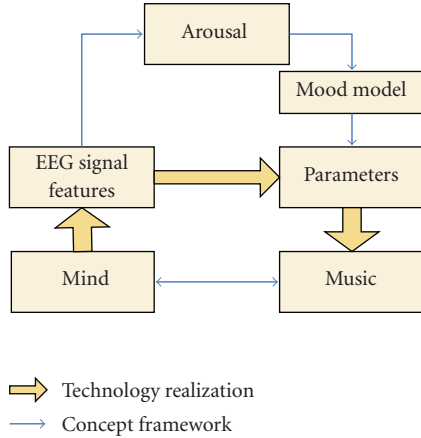


FIGURE 1: Overview of the brainwave music generation.

the mental state by music. The arousal levels corresponding to both the brain mental states and music emotion are implicitly used as the bridge between the mind world and music melody. EEGs during various sleep stages were tested as the example.

## 2. Material and Methods

**2.1. Sleep EEG Data.** To show the performance of the proposed mapping rules, we apply this method to the real EEG data recorded during the different sleep stages. The sleep stages were recognized by two of the authors according to the rules of Rechtschaffen and Kales (R&K). The data of rapid-eye movement sleep (REM) and nonrapid eye movement were utilized. For the nonrapid eye movement sleep data, we chose segments from both stage 2 (named NREM henceforth) and stages 3 or 4 (the slow-wave sleep (SWS)). The subject was a 25-year-old male, physically and mentally healthy, right-handed. The study was approved by the local Review Board for Human Participant Research. The subject signed an informed consent form for the experiment. The signals were recorded by a 32 channel NeuroScan system with a sampling rate of 250 Hz and were band-pass filtered from 0.5 Hz to 40 Hz. The data is referenced to infinity [13]. The data for music generation is acquired from the second night of the subject sleeping with the braincap. The following analysis was performed on the data at electrode Cz, which is at the central of the head and is a channel less affected by the body movement.

### 2.2. EEG, Music, and Arousal

**2.2.1. Sleep EEG and Mental Arousal Level.** It is believed that the arousal level in different sleep stages is associated with the brain activities; it means that a sleep stage, REM, NREM, or SWS, is a phenomenological representation of the underlying neural activities which are the electrophysiological reflection of a specific mental arousal state. For example, REM is considered to be deeply related to dreams, which involves

learning and memory [14]; thus it is considered being more alert than SWS; that is, it has a high arousal level than SWS.

The time-frequency EEG features are different among REM, NREM, and SWS. The REM stage shows small amplitude activities, similar to light drowsiness, and its alpha band (8–13 Hz) activity is slightly slower than in wakefulness. The brainwaves of SWS are of quite preponderant delta waves (1–4 Hz) and theta rhythm (4–7 Hz), thus typically of low frequency and high amplitude. And the wave amplitude and frequency of NREM are between REM and SWS. As the sleep stages can be identified by the features of EEG, which may be utilized as the physiological indexes of different mental states for music composition of various arousal levels.

**2.2.2. Music and Emotion Arousal.** As a representation of the internal emotion of a composer, music with some features can be adopted to evoke emotion and mood state. Some studies indicated that music emotion is able to be communicated with various acoustic cues, including tempo, sound level, spectrum, and articulation [15]. And musical structures or patterns usually have their inherent emotional expressions [16]. To evaluate music emotion, a popular one is the Thayer’s model, which describes emotion in two dimensions, the valence and the arousal. The valence indicates whether the music is pleasant or unpleasant, while the arousal represents the activity of the music, the activeness or passiveness of the emotion [17]. The two-dimension structure gives us important cues for computational modeling.

Therefore, the musical structure and some features such as pitch, tonality, rhythm, and volume played important roles in the emotion expression. For example, a fast tempo (dense rhythm cadence) usually represents a high arousal level, while a slow tempo (sparse rhythm cadence) indicates the low arousal emotion [18].

**2.3. Music Generation from EEG.** For music generation, the overview of the method is shown in Figure 1, where the blue arrow indicates the conceptual framework and the yellow arrow shows the actual realization in this work. Using arousal as a bridge, EEG features were extracted as a reflection of the mind state, and it was mapped to the parameters of music which had similar arousal level according to the two-dimension mood model.

The music generation consists of five steps, details shown in Figure 2. First, extract the EEG signal features; second, define the music segments (parameters: *main note*, *tonality*, and *rhythm cadence*) based on the corresponding EEG features; third, generate music bars (parameters: *chord* and *note position*) from the EEG features and music segment parameters; fourth, fix the values of notes (*timbre*, *pitch*, *duration*, and *volume*) according to the bar parameters; the last, construct the music melody by a software (Max/MSP) and a MIDI file is made.

**2.3.1. EEG Features and Music Segment.** For different mental states, EEGs are of distinct features in frequency and amplitude, that is, different time-frequency (T-F) patterns.

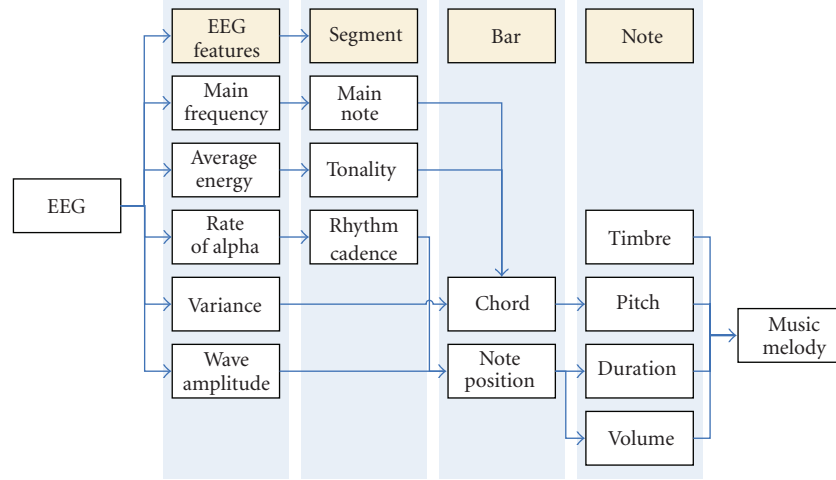


FIGURE 2: Mapping rules from EEG to music.

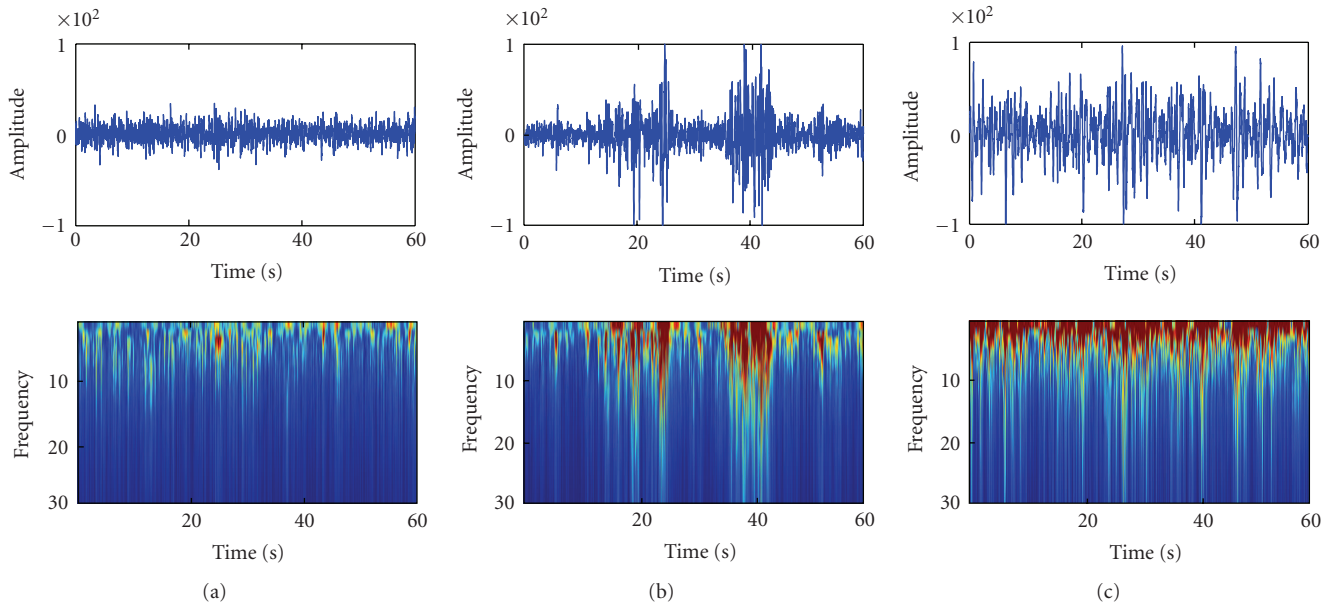


FIGURE 3: Sleep EEG and Wavelet analysis. (a) REM; (b) NREM; (c) SWS.

The *main frequency*, *rate of alpha*, and *variance* are obtained from the complex morlet wavelet coefficients, while the *wave amplitude* and *average energy* are estimated directly from the EEG signal.

The music sequence has the same time length as the real EEG. The segmentation is based on the following inequation (1), so that when it exists, a new segment is assumed:

$$\frac{|x(i) - \bar{x}|}{\bar{x}} > 1, \quad (1)$$

where  $x(i)$  denotes the value of the EEG signal at the current point  $i$ , and  $\bar{x}$  is the average of the data  $x(i)$  from the last segment ending to the current time.

In a segment, the three parameters, *main note*, *tonality*, and *rhythm*, are kept the same. As shown in Figure 2, the

*main note*, the most important note in a music melody, is based on the EEG *main frequency*. When the EEG *main frequency* is high, the *main note* is high, and vice versa.

According to music esthetic theory about *tonality*, a major music usually is utilized for a positive melody, while a minor is identified to be soft and mellow [18]. In this work, we defined an empirical threshold that when the average energy is lower than the threshold, we take the Major; else the Minor. Therefore, a deep sleep stage, SWS, would be represented by a minor key, and the REM stage would be matched with the major. The key transfer would make the music pieces have a rich variety, and the stage change can be identified by the music modulation.

The *rhythm cadence* is related to the *rate of alpha*. When it is high, the rhythm cadence is dense, which means that the number of notes in a fixed length is large. The result is that

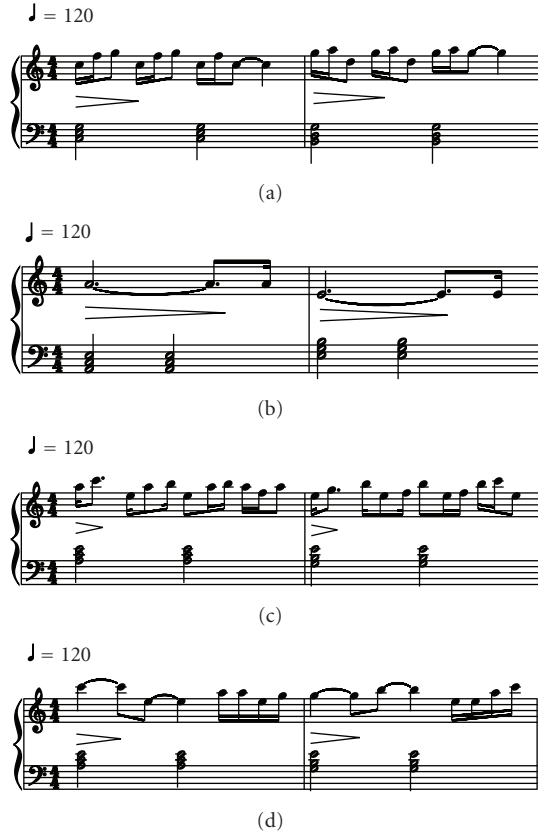


FIGURE 4: Music scores for REM (a), SWS (b), NREM segment 1 (c), and NREM segment 2 (d).

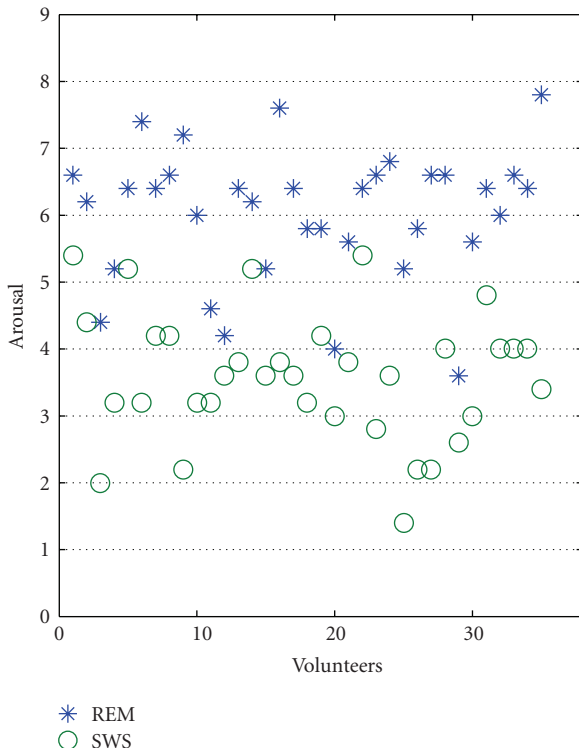


FIGURE 5: The distribution of the emotion arousal levels of the REM and SWS music.

a fast tempo corresponds to a high arousal level. When the rate is low, the condition is adverse.

**2.3.2. Music Generation: Bar.** In a music segment, the substructure is the bar, where the chord and note position are finally determined. As variance of the wavelet coefficients can represent the change of the frequency combination in the time-frequency domain, we use it to determine the chord. Since the chord is complex, here we simply assume that the stability of the chord and the change of EEG spectrum are consistent.

In this work, we take 4 beats in a bar and 4 positions in a beat. The parameter “note position” indicates a note on or off at a position. The *rhythm cadence* determines the number of notes on, and then the EEG amplitude over an empirical threshold for each bar determines the specific position for a note “on.”

**2.3.3. Music Generation: Note.** Music melody is the combination of notes, and for each note, there are four essential features: timbre, pitch, duration, and volume.

The *timbre* of the note is assumed to be piano in this work. And in general, we may have different timbres for different segments if necessary.

The *pitch* of a note is related to the chord. In our method, each bar has a chord, and the notes in a bar are selected from two families: the first family consists of the note pitches of the harmonic chord (chord tone) and the second includes the other note pitches of the scale (none chord tone). For example, when the chord is major C, the family of chord tone consists of C, E, G, while the none chord tone family includes D, F, A, B. To ensure the tonality of the melody, there are a few rules for pitch family choice; for example the chord notes are usually placed at the downbeat (the first beat of the bar); the pitch interval is limited to 7 semitones.

The *duration* of a note is represented by the note position. A note starts at the position of a note on and lasts until the next note-on position. However, the lasting must be in the same bar so that if the next note-on position is in the next bar, the current note’s duration will stop at the current bar end.

The *volume* of a note is indicated by the note position of the beat. A downbeat has a large volume, while an upbeat has a small volume.

**2.3.4. Music Emotion Evaluation Test.** In order to ascertain if the music of different sleep states can be identified, and to see the emotion dimensions when people listen to them, 35 healthy students (20 males, 15 females), ranging in age from 21 to 28 years (mean 22.49, SD 1.65), were asked to participate in this test. None of the volunteers reported any neurological disorders, psychiatric diseases, or were on medication. All had normal hearing. 94.3% of them had never received special musical education, and 5.7% of them (two subjects) had special musical training less than 2 years.

Since the waveforms of REM and SWS are more typical than NREM (see Figure 3), we designed a test with 10 music

TABLE 1: Music parameters of REM and SWS.

| Music parameters | Main note | Tonality | Rhythm cadence | Pitch | Duration | Volume |
|------------------|-----------|----------|----------------|-------|----------|--------|
| REM              | High      | Major    | Dense          | High  | Short    | Large  |
| SWS              | Low       | Minor    | Sparse         | Low   | Long     | Small  |

pieces consisting of 5 from REM and 5 from SWS with the proposed mapping rule. Each music piece lasted 60 seconds and they were randomly played to the volunteers. The volunteers were asked to focus on the emotions of the music pieces. After listening to each piece, they were required to mark a table for the arousal levels which had a 9-point scale from 1 to 9 (with “1 = very passive” and “9 = very excited” on the arousal scale).

### 3. Results

**3.1. Music of Sleep EEG.** Figure 3 shows the wavelet analysis results of REM, NREM, and SWS. Apparently, the REM and SWS data may be assumed to be one segment, while the NREM data should be segmented into five segments for its very clear variety of features in frequency and amplitude related to the spindle waves. For the data in Figure 3, we found that segment 1 of NREM was quite similar to REM, segment 2 is similar to SWS, and the reason is that the wave amplitude and frequency of NREM are between REM and SWS as noted above.

The music pieces of different sleep stages are of different features in music structure. Table 1 shows the music parameters of REM and SWS EEG. The REM music has high-pitch notes and dense rhythm; thus it indicates a high arousal state. The SWS music has notes of low pitch, and the rhythm is sparse; thus it denotes a low arousal state. Figure 4 shows the examples of the music scores of the sleep EEG.

**3.2. Music Emotion Evaluation.** In the music emotion evaluation test, the arousal level of REM and SWS is  $6.02 \pm 0.99$  and  $3.59 \pm 0.97$ , respectively. And the differences between them are significant ( $T(34) = 12.571$ ,  $P < .01$ ). Figure 5 showed the points from all the volunteers in the emotion space with blue stars and green circles for the REM and SWS music pieces, respectively. It is quite clear that the music of REM has high arousal level than SWS, which means that the music of REM is more active. Figure 5 demonstrates that our method can translate the different arousal mental state to the corresponding music arousal level. The arousal level of REM music is higher than SWS music for all the listeners, although their absolute arousal level points are different.

### 4. Discussions and Conclusion

There is growing interest in the relation between the brain and music. The approach to translate the EEG data into music is an attempt to represent the mind world with music. Although arousal has been a common topic in both brain

mental state and music emotion studies, it is a new attempt to use arousal as the bridge between the brain mental state and the music. The above results show that the approach is advisable and effective and that the music pieces of different sleep stages are of distinct music features corresponding to the different levels of arousal. The active state is represented by music pieces with high arousal level, while music for the calm state has a low arousal level.

In this EEG music generation, some basic music theories have been considered. As EEG is a physiologic signal, if we translate it into music directly, the music may be stochastic; if the music rules are too strictly followed, some detailed meaningful EEG information may be ignored. To keep a proper balance between the science (direct translation) and art (composition), only some important principles of music were involved in the program, and the features of the EEG were chosen carefully to maintain the most meaningful physiologic information. If some random parameters are utilized to replace these features, the music would show no specific patterns. In general, the choice of the feature extraction method would influence the meaning of the derived music, and any principle followed by both the brain activity and music would be an appropriate bridge between the brainwave and music.

In this pilot experiment, the method was evaluated on the sleep EEG data from one subject. Though individual EEG data is different from one subject to another, the basic features of sleep EEG with different mental states are quite steady, such as the characteristic waves of different sleep stages. That means, for the same sleep stage, that the music of different subjects would be different in details, but the main patterns would be similar.

To improve this work, other EEG signal processing methods can be adopted, such as complexity analysis, independent component analysis, and fractal analysis (power law [12]). In our current method, we just consider the arousal level of the brain and music while the other emotion dimensions, such as valence, can also be involved in the further music generation studies. Moreover, the program needs to be tested on more data to improve itself to adapt to various cases.

This method might be used potentially in an assistant sleep monitor in clinical applications because the music of different sleep stages can be identified easily and more comfortably. However, it needs further experimental studies before any practical application. Also, it can work as a musical analytical method for the ample states of EEG. Furthermore, this method can be utilized as a unique automatic music generation system, which enables those people who have no composition skills to make music through using their brainwaves. Therefore, it can be utilized as a bio-feedback tool in disease therapy and fatigue recovery.

## Acknowledgments

The fifth author was supported by the Natural Science Foundations of China (60736029) and the National High-Tech R&D Program of China (2009AA02Z301). The second author was supported by the Natural Science Foundations of China (90820301 and 60835005) and the Major State Basic Research Program (2007CB311001) of China. The authors thank Tiejun Liu for the EEG data supply and Xiaomo Bai who works in Sichuan Conservatory of Music for theoretical suggestions in music.

## References

- [1] I. Peretz, "The nature of music from a biological perspective," *Cognition*, vol. 100, no. 1, pp. 1–32, 2006.
- [2] A. Pazos, A. Santos del Riego, J. Dorado, and J. J. Romero Caldalda, "Genetic music composer," in *Proceedings of the Congress on Evolutionary Computation*, pp. 885–890, 1999.
- [3] R. L. Baron and S. H. L. Andresis, "Automatic music generating method and device," US patent no. 6506969, 2003.
- [4] A. S. Sousa, F. Baquero, and C. Nombela, "The making of the genoma music," *Revista Iberoamericana de Micología*, vol. 22, no. 4, pp. 242–248, 2005.
- [5] J. Dunn and M. A. Clark, "Life music: the sonification of proteins," *Leonardo*, vol. 32, pp. 25–32, 1999.
- [6] B. Arslan, A. Brouse, J. Castet, J. Filatriau, R. Lehembre, and Q. Noirhomme, "Biologically-driven musical instrument," in *Proceedings of the Summer Workshop on Multimodal Interfaces (eNTerFACE '05)*, 2005.
- [7] E. R. Miranda and A. Brouse, "Interfacing the brain directly with musical systems: on developing systems for making music with brain signals," *Leonardo*, vol. 38, no. 4, pp. 331–336, 2005.
- [8] E. Adrian and B. Matthews, "The Berger rhythms: potential changes from the occipital lobes in man," *Brain*, vol. 57, pp. 355–385, 1934.
- [9] D. Rosenboom, *Extended Musical Interface with the Human Nervous System*, International Society for the Arts, Sciences and Technology, San Francisco, Calif, USA, 1997.
- [10] T. Hinterberger and G. Baier, "Parametric orchestral sonification of EEG in real time," *IEEE Multimedia*, vol. 12, no. 2, pp. 70–79, 2005.
- [11] G. Baier, T. Hermann, and U. Stephani, "Event-based sonification of EEG rhythms in real time," *Clinical Neurophysiology*, vol. 118, no. 6, pp. 1377–1386, 2007.
- [12] D. Wu, C.-Y. Li, and D.-Z. Yao, "Scale-free music of the brain," *PLoS ONE*, vol. 4, no. 6, article e5915, 2009.
- [13] D. Yao, "A method to standardize a reference of scalp EEG recordings to a point at infinity," *Physiological Measurement*, vol. 22, no. 4, pp. 693–711, 2001.
- [14] R. Stickgold, J. A. Hobson, R. Fosse, and M. Fosse, "Sleep, learning, and dreams: off-line memory reprocessing," *Science*, vol. 294, no. 5544, pp. 1052–1057, 2001.
- [15] P. N. Juslin, "Cue utilization in communication of emotion in music performance: relating performance to perception," *Journal of Experimental Psychology: Human Perception and Performance*, vol. 26, no. 6, pp. 1797–1813, 2000.
- [16] P. N. Juslin and J. A. Sloboda, *Music and Emotion: Theory and Research*, Oxford University Press, New York, NY, USA, 2001.
- [17] R. E. Thayer, *The Biopsychology of Mood and Arousal*, Oxford University Press, New York, NY, USA, 1989.
- [18] H. Lin, *Course for Psychology in Music Aesthetic*, Shanghai Conservatory of Music Press, Shanghai, China, 2005.